

Fragmentation of Concrete Under Dynamic Loading – a Numerical Multiscale Approach

Christoph Grunwald

Dissertation zur Erlangung des Doktorgrades der Technischen
Fakultät der Albert-Ludwigs-Universität Freiburg im Breisgau

Fragmentation of Concrete Under Dynamic Loading – a Numerical Multiscale Approach

Christoph Grunwald

In Partial Fulfillment of the Requirements for the Degree of:

Doktor der Ingenieurwissenschaften (Dr.-Ing.)

Examination board

Chairman	Prof. Dr. habil. Dr. rer. nat. Oliver Ambacher
Primary Reviewer	Prof. Dr.-Ing. habil. Stefan Hiermaier
Secondary Reviewer	Prof. Dr.-Ing. habil. Carsten Könke
Assessor	Prof. Dr.-Ing. Frank Balle

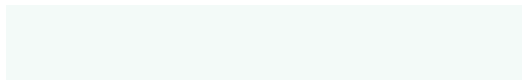
Date of Exam	June 30, 2023
--------------	---------------

Freiburg, June 30, 2023

Affidavit

I hereby confirm that this thesis is the result of my own work. I did not receive any help or support from commercial consultants. All sources and / or materials applied are listed and specified in the thesis.

Furthermore, I confirm that this thesis has not yet been submitted as part of another examination process neither in identical nor in similar form.



Christoph Grunwald

Freiburg, June 30, 2023

Acknowledgments

Life is nonlinear. I remember well the 13.03.2014, the day of my application interview at EMI with Prof. Alexander Stolz and Prof. Werner Riedel: Not being sufficiently stimulated by my tasks in the industry, I once stumbled upon an interesting-looking job description by EMI and without further reading wrote an email, asking whether an engineer having “only” a diploma from a university of applied science could be an appropriate choice. The affirming answer reached me within 24 hours and it was only then that I began reading the job description with care. I soon came to the firm conclusion that EMI surely does not need a *mechanical engineer* to simulate the behavior of *concrete*. Although I was very trained to build large and complicated finite element models, they were always limited to linear-elastic material behavior. When Werner asked me during the interview if I was interested in going “beyond” this sphere, I gladly agreed. From many perspectives, that was a life-changing moment for me and my family.

But Werner was not only the leading person at the beginning of my journey with EMI, it was him again who came up with the idea to give me the possibility of writing a dissertation. I am very grateful that he and Alex considered me for the task and that they did everything to get over the first sticking points: As I soon realized, being accepted for a doctorate at a German university with an “old” diploma of a university of applied science is way more difficult than getting a job at EMI. Two former professors of mine, Prof. Manfred Kruppa and Prof. Jürgen Schmitz, were willing to certify my ability for scientific work, for which I am much obliged.

Our director, Prof. Stefan Hiermaier, took on the next steps and strongly promotes my application at the university. He supported my thesis every moment, allowed me to hear the required lectures during working hours, and of course provided the necessary scientific and working environment. Prof. Carsten Könke from Bauhaus-University Weimar was willing to serve as secondary reviewer. I gladly remember his cordial welcome at Weimar and I am grateful that he took the effort to assess the thesis and traveled to Freiburg for the exam.

During the work on the dissertation, some colleagues helped me tremendously: While Werner oversaw the great story and kept me from distracting on by-roads, Dr. Martin Sauer was always there for detailed in-depth discussion, interested in every strange behavior of SOPHIA and always with good hints and recommendations. Benjamin Schaufelberger has been my day-to-day discussion partner, especially for strange material behavior, while Dr. Nathanaël Durr helped me with strange continuum mechanics. When listing all the strange things, I should not forget to mention our cluster and its MPI environment. It was Udo Ziegenhagel, who continuously tamed the beast. He (always almost immediately) took action if the cluster had something different in mind (or memory) than I. My current group leader, Dr. Kai Fischer, provided me with an almost perfect working environment and allowed me to work independently and freely, which I greatly appreciate! He accepted that I did a lot of thinking work on my road bike (no, not during work, but early in the afternoon). That I had ample time to work on my topic without disruption, I owe to Dr. Julia Rosin and Christoph Roller, who generously overtook some project work.

Several people read parts or the whole work to track errors, misrepresentations, nonsense and misleading paragraphs. Besides the already mentioned colleagues, I would like to thank Dr. Malte von Ramin, Dr. Jet Hoe Tang, my good friend Dr. William Kaal (who convinced me in 2014 to join Fraunhofer), my father Bernd Grunwald, and our librarian Johanna Holz. However, my brother Daniel deserves most of the credit in this respect: He did an outstanding job and worked his meticulous way through every sentence, equation and footnote to find errors nobody else noticed (and at times when nobody else was still awake). Thank you very much, Danny!

Nobody had to endure a bug-tracing, absent-minded candidate more than my family. My beloved spouse Susanne and my kids Annika, Julius and Johannes coped patiently with me in the last years, learned the basics of C++ during lunch and are now well aware that concrete is a nasty thing. Thank you my dears.

Life is nonlinear – with a single invariant: God. That I can write an acknowledgments section in a dissertation is completely his work. He graciously led me to this day through all nonlinear tweaks and undeserved achievements. To him be all glory and praise.

It is good to give thanks to the LORD,
to sing praises to your name, O Most High;
to declare your steadfast love in the morning,
and your faithfulness by night.

For you, O LORD, have made me glad by your work;
at the works of your hands I sing for joy.

Psalms 92,1.2.4

Abstract

Quantifying debris throw of concrete structures under abnormal loading conditions is of high importance for risk assessment analysis in certain settings. However, determining mass and initial velocities of dispersing debris is a unique challenge and not yet satisfyingly addressed. Experimental characterization is very cost-intensive, complicated, laborious and yet often not significant. Current simulation approaches consider mostly small to laboratory-sized specimens or employ modeling approaches either not accurate or not efficient enough to tackle the tenacious predicament of simulating the debris throw of real concrete structures.

It is therefore the aim of this thesis to develop a finite element based simulation approach that overcomes these limitations. A basic ingredient is the representation of concrete on its mesoscale. A three-phase modeling approach has been identified through an extensive literature study to capture all necessary effects in the fragmentation of concrete sufficiently: explicitly resolved, spherical inclusions represent the stiff aggregates embedded in a softer mortar matrix; both constituents are modeled with the RHT plasticity model, which is furnished with an additional principal stress criterion for improved brittle behavior under tension. The contact zone between mortar and aggregate, the interfacial transition zone – prevalent locus of microcracks and faults – is represented by extrinsic cohesive zone elements. The employment of these elements only for this weakest material link limits the number of topology changes of the mesh to a moderate and manageable magnitude. Matrix and transgranular failure is in contrast considered by application of a smeared crack approach in combination with simple element removal. Three example simulations validate the approach in terms of crack propagation and branching as well as fragment sizes and velocities.

In order to keep the overall computational efforts for large structures manageable, it is proposed to model only specific regions of interest on the mesoscale. The surrounding structure should be represented by a macroscale homogenization, as is common today. For the connection between both scales, a novel weak staggered coupling for direct solution schemes with explicit time integration

(historically often denoted as “hydrocodes”), is presented. Within this scheme, the macro interface movement serves as boundary condition on the micro- (or meso-)scales’ interface. An averaged stress state of a finite microscale volume in the vicinity of the interface is then used to determine the resistance of this lower-level scale against deformation. Equivalent forces are derived in virtual macro elements and returned to the macro interface nodes to update their kinematic state. It is shown that this coupling achieves equivalent results to an established standard coupling based on Lagrange multipliers, while simultaneously possessing advantages regarding computational performance: The amount of data to be communicated between the scales is less, the number of additional operations for the coupling is of linear order with respect to the coupled degree of freedoms, and – most importantly – changing mesh topologies at the interface can be handled intuitively with ease. The parallel implementation, discussed at the end of the thesis, exhibits outstanding scalability and sets simulation of large structures within reach.

After discussing some remaining limitations, results from fragmentation simulations are used to highlight the usefulness of the modeling approach by determining potential flight distances for each fragment considering individual aerodynamic factors depending on its unique shape.

Zusammenfassung

Die Quantifizierung des Trümmerwurfs von Betonstrukturen unter außergewöhnlichen Belastungen ist für die Risikobewertung in bestimmten Situationen von großer Bedeutung. Die Bestimmung von Masse und Anfangsgeschwindigkeit der sich herauslösenden Trümmerteile stellt jedoch eine besondere Herausforderung dar und ist bislang noch nicht zufriedenstellend gelöst. Die experimentelle Charakterisierung ist sehr kostenintensiv, aufwendig und dennoch oft nicht aussagekräftig. Aktuelle Simulationsansätze werden meist nur auf kleine oder mittelgroße Geometrien angewandt oder verwenden Modellierungsansätze, die entweder nicht genau oder nicht effizient genug sind, um die anspruchsvolle Simulation der Trümmerbildung an realen Betonstrukturen zu bewältigen.

Ziel dieser Arbeit ist es daher, einen auf der Finite Elemente Methode basierenden Simulationsansatz zu entwickeln, der diese Einschränkungen überwindet. Ein grundlegender Bestandteil dabei ist die Abbildung von Beton auf der Mesoskala. In einer umfangreichen Literaturrecherche wurde ein dreiphasiger Modellierungsansatz identifiziert, der alle notwendigen Effekte der Fragmentierung von Beton hinreichend erfasst: Explizit modellierte, kugelförmige Einschlüsse stellen die harte Gesteinskörnung dar, die in einer weicheren Mörtelmatrix eingebettet ist; für beide Bestandteile wird das RHT-Plastizitätsmodell verwendet, das um ein zusätzliches Hauptspannungskriterium für ein verbessertes Zugversagen erweitert wurde. Die Kontaktfläche zwischen Matrix und Zuschlagskorn – ein bevorzugter Ort für Mikrorisse und andere Defekte – wird mit extrinsischen Kohäsivzonelementen idealisiert. Die Verwendung dieser Elemente nur für dieses schwächste Bindeglied begrenzt die Anzahl der Topologieänderungen des Netzes auf ein moderates Maß. Matrix und transgranulares Versagen wird hingegen berücksichtigt, indem Elemente nach einem bestimmten Kriterium aus der Simulation entfernt werden. Drei Anwendungsbeispiele validieren den Ansatz hinsichtlich Rissausbreitung und -verzweigung sowie Fragmentgrößen und -geschwindigkeiten.

Um den gesamten Rechenaufwand für große Strukturen überschaubar zu halten, wird vorgeschlagen, nur bestimmte Regionen auf der Mesoskala zu modellieren.

Die umgebende Struktur sollte homogenisiert auf der Makroskala dargestellt werden. Für die Verbindung zwischen beiden Skalen wird eine neuartige Kopplung speziell für direkte Lösungsschemata mit expliziter Zeitintegration (sog. Hydrocodes) vorgestellt. In diesem Konzept dient die Bewegung der Makrogrenzfläche als Randbedingung für die Grenzfläche der Mesoskala. Ein gemittelter Spannungszustand eines begrenzten Mesoskalenvolumens in unmittelbarer Nähe der Grenzfläche wird verwendet, um den Widerstand dieser Materialregion gegen Deformation zu bestimmen. Entsprechende Kräfte werden in virtuellen Makroelementen ermittelt und an die Makro-Grenzflächenknoten zurückgegeben, um deren kinematischen Zustand zu aktualisieren. Es wird gezeigt, dass diese Kopplung äquivalente Ergebnisse zu einer etablierten Standardkopplung auf der Grundlage von Lagrange-Multiplikatoren erzielt, während sie gleichzeitig Vorteile hinsichtlich der Rechenleistung aufweist: Die Menge der zwischen den Skalen zu kommunizierenden Daten ist geringer, die Anzahl der zusätzlichen Operationen für die Kopplung ist von linearer Größenordnung in Bezug auf die gekoppelten Freiheitsgrade und – ein bedeutender Vorteil – eine sich verändernde Netztopologie an der Schnittstelle wird intuitiv berücksichtigt. Der am Ende der Arbeit diskutierte Vorschlag zur parallelen Implementierung der Kopplung weist eine hervorragende Skalierbarkeit auf und rückt die Simulation großer Strukturen in greifbare Nähe.

Nach der Erörterung einiger verbleibender Einschränkungen werden Ergebnisse von Fragmentierungssimulationen verwendet, um die Nützlichkeit des Modellierungsansatzes zu verdeutlichen. Dabei werden potenzielle Flugdistanzen für jedes Fragment unter Berücksichtigung individueller aerodynamischer Faktoren in Abhängigkeit von der jeweiligen Trümmerform bestimmt.

Notes on notation and list of abbreviations

Throughout this work, the following notation is used:

- Italic Roman and Greek letters are used to denote scalars, as a , α .
- Italic bold Roman and Greek letters are used to denote first- or second-order tensors, such as the displacement vector

$$\mathbf{u} = \begin{pmatrix} u_x \\ u_y \\ u_z \end{pmatrix}$$

or Cauchy's stress tensor:

$$\boldsymbol{\sigma} = \begin{pmatrix} \sigma_{xx} & \sigma_{xy} & \sigma_{xz} \\ \sigma_{yx} & \sigma_{yy} & \sigma_{yz} \\ \sigma_{zx} & \sigma_{zy} & \sigma_{zz} \end{pmatrix}$$

- Regular bold Roman letters denote arrays of entities or matrices – usually in the context of finite elements due to discretization – such as the array of discrete displacements of node k :

$$\mathbf{u}_k = \begin{bmatrix} u_{k,x} \\ u_{k,y} \\ u_{k,z} \end{bmatrix}$$

or the massmatrix \mathbf{M} . Due to the nonavailability of a well-performing (appealing) font for upright bold Greek symbols, the standard italic symbols are used for discretized arrays as well. In this case, the context decides.

The following tables declares frequently used symbols and abbreviations used in this thesis. Symbols which occur only once within a specific context are declared there and not listed here.

Symbol	Explanation
$a_{j,x}, a_{j,y}, a_{j,z}$	Weight factors in Gauss integration for integration point j
B	Discrete symmetric gradient operator
c_D	Aerodynamic drag coefficient
c_S, c_B	Speed of sound, Bulk speed of sound
C	Coupling matrix for LM coupling
d	Dimension (Chapter 5.2)
D, D_R, \mathcal{D}	Damage factor RHT, damage factor Rankine, combined damage factor
D, D	Rate of deformation tensor / matrix
$DIF_{t,c}$	Dynamic increase factor tension, compression
e, \dot{e}	Internal energy, rate of internal energy
E	Young's modulus
\mathcal{E}	Symbol denoting a finite element
f_c	Compressive strength
f_d	Damping factor of the SPML approach
f_s, \hat{f}_s	Shear strength and normalized shear strength
f_t, \hat{f}_t	Tensile strength and normalized tensile strength
$F_R, F_R^{c,t}$	RHT strain rate factor and corresponding value for compression/tension
F	Array of internal forces
$\tilde{\mathbf{F}}_{\mathcal{J}}^m$	Array of coupling forces derived from the microscale
$\circ_{\mathcal{F}}, \circ^{\mathcal{F}}$	Sub- or superscript \mathcal{F} denotes variables of the filter region (SPML approach)
G	Shear modulus
G_F	Fracture energy
H, H₀	Interface operator LM coupling
i, j, k	Sum indices
\circ_I, \circ^I	Sub- or superscript I denotes variables of the macro interface region

Symbol	Explanation
\circ_i, \circ^i	Sub- or superscript i denotes variables of the micro interface
\mathbf{I}, \mathbf{I}	Identity tensor / matrix
$[j]$	Fractional time increment in subcycling
\mathbf{J}	Jacobian matrix
$\circ_{\mathcal{J}}, \circ^{\mathcal{J}}$	Sub- or superscript \mathcal{J} denotes variables of the macro interface
J_2	Second invariant of the deviatoric stress tensor
K	Bulk modulus
\mathbf{K}	Stiffness matrix
l_c	Critical or characteristic length of a finite element
\mathbf{L}, \mathbf{L}	Spatial gradient of velocity tensor / matrix
\circ_m, \circ^m	Sub- or superscript m denotes variables on the microscale
\circ_M, \circ^M	Sub- or superscript M denotes variables on the macroscale
\circ_{MI}, \circ^{MI}	Sub- or superscript MI denotes variables of the combined macro- and interface domain
\mathbf{M}	Mass matrix
\mathbf{M}_{LH}	Combined mass and coupling matrix (Chapter 5.2)
$n_{\mathcal{E}}^i$	Number of elements in the micro domain covered by the interface domain
$n_i, n_{\mathcal{J}}$	Number of nodes on the micro, respectively macro interface
n_M, n_m, n_I	Number of nodes in the macro domain, micro domain, interface domain
(n)	Step / cycle designator
\mathbf{N}	Matrix of FE interpolation functions
\mathcal{N}	Symbol denoting a node
\mathbb{N}	Matrix of FE interpolation functions of macro discretization in the micro domain (SPML approach)
p, \hat{p}	Pressure, normalized pressure (by f_c)
\hat{p}_t, \hat{p}_0	RHT failure cutoff pressure, RHT root pressure
\mathbb{P}_m	Unique microscale displacement projector
\mathcal{P}	Designator of partition or computational processing unit
q	Artificial viscosity
\mathbb{Q}_M	Compatible macroscale displacement projector

Symbol	Explanation
\mathbf{R}	Array of external forces
R_3	RHT third invariant factor
$\mathbf{s}, \mathbf{s}, \dot{\mathbf{s}}, \dot{\mathbf{s}}$	Deviatoric stress tensor / matrix and corresponding rates
$\Delta t, \Delta t_h, \Delta t_c$	Time step, half time step and critical time step
t, t_0, t_e	Time, start- and endtime
\mathbf{t}, \mathbf{t}	Vector / array of tractions
$\delta \mathbf{u}$	Vector of test functions
$\mathbf{u}, \dot{\mathbf{u}}, \ddot{\mathbf{u}}$	Vector of displacement, velocity and acceleration
$\mathbf{u}, \dot{\mathbf{u}}, \ddot{\mathbf{u}}$	Array of displacement, velocity and acceleration
$\mathbf{u}_m, \mathbf{u}_M, \dot{\mathbf{u}}_m, \dot{\mathbf{u}}_M$	Unique microscale displacement and compatible macro displacement field and associated velocity field
v	Velocity
\mathbf{W}, \mathbf{W}	Spin tensor / matrix
\mathbf{W}_2	Array of kinematic variable in the LM coupling (Chapter 5.2)
w/c	Mass ratio of water to cement in concrete mixes
\mathbf{x}, \mathbf{x}	Spatial coordinate
∇	Nabla operator
$\hat{\circ}$	Denotes the normalization of the variable \circ with f_c
$\tilde{\circ}$	Symbols with the tilde refer to virtual entities in the WS coupling (Chapter 5.3)
$\langle \circ \rangle$	Denotes an averaging of variable \circ
$\ \circ\ $	Euclidian norm of \circ
$\Gamma, \Gamma_I, \Gamma_i$	Interface, macro domain interface, micro domain interface
δ, δ_c	Crack opening, critical crack opening
$\varepsilon, \dot{\varepsilon}$	Uniaxial strain and corresponding rate
$\varepsilon_{eff}, \dot{\varepsilon}_{eff}$	Effective strain and corresponding rate
ε_{cr}	Rankine crack strain
$\varepsilon_{eff}^{pl}, \dot{\varepsilon}_{eff}^{pl}$	Effective plastic strain and corresponding rate

Symbol	Explanation
$\varepsilon, \dot{\varepsilon}_v$	Volumetric strain and corresponding rate
$\varepsilon, \dot{\varepsilon}$	Strain tensor and strain rate tensor
ε_{pl}	Plastic strain tensor
$\epsilon, \dot{\epsilon}$	Deviatoric strain tensor and deviatoric strain rate tensor
ζ_L, ζ_Q	Artificial viscosity parameter
θ	Angle of similarity (or Lode) angle
λ	Vector of Lagrange multipliers
ν	Poisson's ratio
ξ	Local (elemental) coordinates of a finite element
ρ	Density
ω	frequency, eigenfrequency
σ	Uniaxial stress
σ	Cauchy stress tensor
σ_I, σ_i	Principal stress tensor and its components $i = 1 \dots 3$
$\langle \sigma_m \rangle$	Averaged micro domain stress
σ_y, σ_y	Yield stress
σ_{eff}	Effective stress
σ_{vM}	von Mises equivalent stress
$\hat{\sigma}_f, \hat{\sigma}_r$	RHT failure stress, residual limit stress
Φ	Yield function
Ω	Body or domain Ω
$\partial\Omega$	Surface or boundary of body Ω

Abbreviation	Explanation
ATC	Atomistic to continua
CZE	Cohesive zone elements
DOF	Degree of freedom
EOM	Equation of motion
EOS	Equation of state
FE	Finite elements
FEM	Finite element method
FPZ	Fracture process zone
HPC	High-Performance Computing
ITZ	Interfacial transition zone
MD	Molecular dynamics
LM	Lagrange multiplier
RHT	Riedel-Hiermaier-Thoma material model for concrete
RVE	Representative volume element
SHB	Split-Hopkinson-Bar
(S)PML	(Selective) perfectly matched layer
WS	Weak staggered

Contents

1	Introduction	1
1.1	Current state of fragment determination	3
1.2	Aim and scope of this thesis	5
1.3	Structure of the dissertation	7
2	Numerical fundamentals	9
2.1	Momentum balance: continuous description	9
2.2	Spatial discretization with finite elements	10
2.3	Temporal discretization	12
2.4	Wave propagation codes	15
	2.4.1 Classification of dynamic problems	15
	2.4.2 Overview of the Lagrangian simulation cycle	16
	2.4.3 Codes used in this thesis	20
2.5	Summary	22
3	Relevant aspects of concrete material and mesomechanical modeling – a review	23
3.1	Constituents and structural features	23
	3.1.1 Constituents	23
	3.1.2 Structure	26
3.2	The general behavior of concrete under loading	31
	3.2.1 Static loading	31
	3.2.2 Dynamic loading	39
3.3	Modeling concrete	45
	3.3.1 Relevant material scale	47
	3.3.2 Geometric representation	49
	3.3.3 The role and consideration of the ITZ	54
	3.3.4 Discretization and mesh resolution	56
3.4	Concluding choice of a suitable mesomechanical representation	58

4	Development of a robust and efficient mesomechanical modeling approach for fragmentation simulation	59
4.1	Modeling cracking and fragmentation with FE	60
4.2	Modeling the bulk material response	65
4.2.1	Original formulation of the RHT model	66
4.2.2	Critique on the RHT model	73
4.2.3	Formulation of an improved yield criterion for brittle failure	75
4.2.4	Correction of the residual failure surface	86
4.2.5	Equation of state	87
4.3	Validation examples	88
4.3.1	Crack propagation and branching	89
4.3.2	Fragment velocities and momentum transfer	92
4.3.3	Fragment mass distribution	96
4.4	Summary and way forward	101
5	Formulation of a multiscale framework for wave propagation codes	103
5.1	Review of multiscale approaches	104
5.1.1	Hierarchical approaches	105
5.1.2	Concurrent approaches	107
5.1.3	Wave propagation in multiscale methods	109
5.2	An existing coupling based on Lagrange multipliers	111
5.3	Development of an efficient weak staggered coupling	116
5.3.1	Governing equations	118
5.3.2	Discretization	119
5.3.3	Establishing the virtual interface domain	121
5.3.4	Interface coupling procedure	122
5.3.5	Averaging the micro model	124
5.3.6	Estimation of efficiency	126
5.4	Abating pathological wave reflections	128
5.4.1	Remedies in literature	130
5.4.2	The SPML approach of <i>Marchais</i> et al.	131
5.4.3	Adaption of the SPML approach to the WS coupling	135
6	Validation and application of the weak staggered coupling and outlook on trajectory determination	141
6.1	Validation examples and comparison between coupling approaches	141
6.1.1	Example 1 – homogeneous microscale	141
6.1.2	Example 2 – heterogeneous microscale	143
6.1.3	Example 3 – wave propagation parallel to the interface	144

6.1.4	Example 4 – embedded microdomain	146
6.2	Development of a parallel framework for simulations in 3D	147
6.2.1	Introduction	147
6.2.2	Parallel set-up	149
6.2.3	Exemplified scalability of the WS coupling	152
6.3	Application example: internal explosion in a confined chamber	154
6.3.1	Model and set-up	154
6.3.2	Results	156
6.3.3	A critical note on remaining limitations	157
6.4	Outlook – detailed trajectory determination	159
7	Closing remarks	163
7.1	Main achievements of the present work	163
7.2	Topics for further investigation	165
	Bibliography	169
A	Appendix	205
A.1	Generation of mesomechanical models – geometric representation	205
A.2	Subcycling	210
A.2.1	Overview on existing subcycling algorithms	210
A.2.2	Proposed subcycling algorithm for the WS coupling	214
A.2.3	Subcycling of the LM approach	216
A.2.4	Stability of subcycling	218
A.3	Cement reaction	219
A.4	Strain rate enhancement formulas	219
A.5	Loading conditions of the validation examples	223
A.6	Material parameter for the mesomechanical simulations within this work	225
A.6.1	RHT model parameter for mortar matrix	225
A.6.2	Aggregate material model	230
A.6.3	ITZ data	231

1 Introduction

It was a matter of a few milliseconds only, less than a visual impression needs from perception to processing in the brain. All that was left of the solid reinforced concrete structure were several buckets of larger and almost uncountable smaller fragments, spread over a radius of up to four hundred meters. Inferring the initial velocities roughly from the mass and distance, it was found that the debris had been propelled up to some hundred meters per second. The simple iron-made door was later found far away within a swampy area. Severely distorted, half sunken; the other half sprawling diagonally towards the sky. Yet nobody was hurt. A miracle? Definitely, if the explosion of the stacked ammunition within this storage facility had occurred at its designated location in a military camp. Luckily, the described scenario was only a field test, although an impressive one.¹ Indeed, it brings the threat which occurs due to debris throw of structures under high dynamic loading home to everybody involved.

In scenarios involving the detonation of explosive substances, the first major threat to humans and structures is the blast wave. However, an accurate prediction of its propagation, the resulting pressure field, and its consequences is well done with today's analytical and numerical methods. A different picture emerges regarding what should be considered the second major threat after the impact of a shock wave on structures: debris throw.² Especially brittle materials are susceptible to considerable fragmentation and resulting debris throw, even beyond the hazard range of the blast wave, and are both harmful to humans and facilities [3, 4]. But not only military applications, such as the ammunition storage structure described above, should be kept in mind: the calm summer day of August 20th, 1997, changed the life of eleven families forever. Whether it was a mechanical impact

¹ The actual test was done in Singapore and presented during a meeting that the author attended. A public report is not available, but similar tests have been carried out by the Swedish Defense Research Agency and have been reported, e.g., in [1], Figure 1.1, left.

² Depending on the field of interest, the term "fragments" is reserved for metallic fragments that originate from ammunition casings, and the term "debris" or "secondary fragments" is exclusively used for those that emerge from structures, e.g., [2]. In this thesis, both terms are used interchangeably and refer *always* to the concrete structure.

or friction within the fan of the dust removal unit – nobody knows. Yet the resulting dust explosion at the grain storage facility located on the Atlantic coast in Bayle, France, destroyed the humongous silos within a wink. Debris pieces of around 1 kg were found still 140 meters away and it is reported that the eleven victims were primarily killed by debris [5]. And what about nuclear power plants, exposed to a malicious (terrorist) act, where one might consider a pipeline with contaminated water directly behind a wall or below a floor? What consequences might occur if high-velocity debris hits – and potentially perforates – such a pipeline? What about people in exposed environments, such as embassies or buildings housing religious minorities?

But blast events are only one example. Indeed, on a more general level, every dynamic loading situation of structures might lead to the gross emergence of lethal or destructive fragments. For instance, the impact of objects with high velocities – such as airplane parts – may evoke strong debris throw due to invoked spallation phenomena, see Figure 1.1, right. Surely, there is a warranted quest not only to quantify the effects of the blast wave but likewise the threats due to flying fragments, presuming that most people and objects worth protecting might be *behind* walls exposed to abnormal loading conditions.

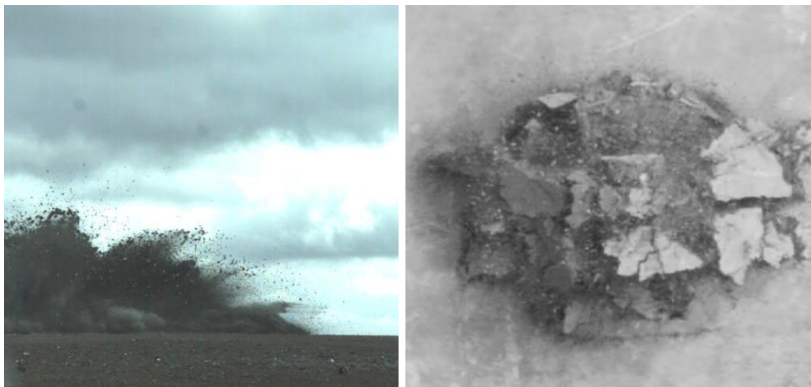


Figure 1.1: Serious debris throw from structures under extreme loading. Left: Break-up of a reinforced concrete ammunition storage [1]. Right: Rear face of a fiber-reinforced concrete slab subjected to the impact of a scaled airplane-turbine model (snap-shot from high-speed recordings of an experimental series detailed in [6]). The impactor did not penetrate the slab. Nevertheless, the space behind it is not a safe place either.

To assess the actual threat, one needs to know the initial conditions of the dispersing debris. Having *mass* and the *initial velocity* vector, the subsequent flight phase can be predicted by applying an equation of motion. However, depending on the assumptions made, very different final positions and kinetic energies might be determined. The reason is the strong dependence of the trajectory on aerodynamic coefficients ruling drag, lift, and even rotation and flipping of irregularly shaped fragments. Comparing only the drag coefficient for a sphere³, which is approximately $c_D^s \approx 0.42$, with those for a cuboid – ranging between $c_D^c \approx 0.6 \dots 1.2$ [8] – highlights that these assumptions considerably affect the resulting flight distance. Besides the initial kinematics, therefore, the actual *shape* of the emerging fragments is a third important piece of information.

1.1 Current state of fragment determination

This stated, the impression that the threat of debris throw is not considered in today's risk analysis should be strictly dismissed. Actually, this is part of a sober risk analysis (see, e.g., [5]) and is subject to current standards and guidelines.⁴ But the underlying data and methods rely almost solely on empirical data. The fact that such a situation is not satisfying should be clear if one considers the immense problems involved in conducting and evaluating such experiments. Not alone that a test area has to be available, the characterization of fragments necessitates the logging of the debris during flight or even better during emergence. In the case of concrete, this is almost impossible with optical systems, simply due to the large amount of dust and debris [9]. Furthermore – if these limitations may be bypassed somehow – the observation with cameras, laser interferometer, and other suitable measurement techniques allows only the observation of the structures' surface, while it is on hand that spalling effects lead to beginning fragmentation in the inner part of the structure.

The main information about the debris is obtained by post-mortem analysis, presuming the manual collection and recording of every fragment found after the experiment (no comment about the tediousness of this painstaking work). Even in the very unlikely case that the complete mass of the subject is recovered, the picked debris pieces may differ from those which will in reality hit persons or

³ E.g., used substitutional for the determined fragments in [7].

⁴ E.g., national safety rules, such as the DGUV 113-017 in Germany or military standards, such as the NATO guidelines for the storage of military ammunition and explosives [2].

installations, since larger debris may have been again divided during impacting and bouncing along the ground.

There is a further restriction, which stymies the direct application of experimental results in the quantification of debris throw – the extraordinary scatter. Even small and uncontrollable fluctuations in the detonation of explosives may lead to a different loading of the structure and influences fragmentation and dispersal of debris. Indeed, in any case small changes in the setup entail a different pattern of fragmentation. Even if one might be able to control all aspects in every detail: the heterogeneous material structure of concrete induces in each experiment a diverse outcome, claiming several, statistically meaningful, repetitions of the same experiment.

Scaled experiments are often in many respects a less expensive option. But while blast effects scale well, debris throw does not. Besides the size effect of concrete structures, where the failure of a concrete member strongly depends on its size, the aerodynamic forces and the vertical force component due to gravitation do not scale. Consequently, not only the initial break-up conditions of scaled experiments are of inferior significance, the resulting flight distances and final impact velocities are simply not transferable. Full-scale experiments remain the only possibility.

Therefore, a simulation approach is needed that can model the initiation and propagation of cracks under dynamic conditions, which could then be used in a second step to evaluate fragments and debris throw. Until now, it has undoubtedly been possible to precisely predict the failure of concrete structures under abnormal loading with its accompanying high strain rates and pressures. Sophisticated material models have been developed in recent decades, which reliably predict the amount and location of highly damaged areas. In addition, more and more attempts have been published with explicit reference to the evaluation of fragment data. Examples reach from applications in the mining industry, e.g., [10, 11], over general protection concerns, such as masonry buildings against blast [12], to military applications, e.g., [13–15], to mention just a few references. The numerical methods and approaches used differ significantly, however, with works relying on the finite element method (FEM) preponderating. Yet finite element meshes describe continuous bodies and the separation of elements is not straightforward. Instead of separating elements, some authors derive analytical descriptions based on internal state variables and determine fragment distributions parallel to or after simulations [7, 10, 16]. Other researchers convert finite elements into meshless particles, based on damage criteria [17, 18],

others directly rely on meshfree methods, e.g., [19–21], or on a Eulerian material description [14, 22].

However, all these approaches are not free from disadvantages. Simulations based on the Eulerian framework suffer in the accurate delineation of material interfaces. Furthermore, meshes required to resolve small fragments and dispersing debris lead to high computational demands. The latter is also a limitation to meshless methods; certainly a reason why this method was applied only to small structures or in 2D until now. Moreover, the size information is lost, or at least difficult to estimate, if elements are converted to particles. At the structural level, attempts have been made to apply different element separation techniques to simulate fragment generation, such as node splitting, erosion, and cohesive zone elements; refer, for instance, to [7, 23–25]. In these cases, however, computational constraints limit the mesh resolution and, therefore, bound the fragment distribution at a relatively large minimum size. Depending on the element separation technique, a lot of material is removed, and the results are reduced to well-informed estimates. Finally, the resulting fragments – if resolved – are often only rough approximations. But as mentioned above, determining the trajectories depends then on several assumptions relating especially to the acting drag and lift forces leading to high uncertainty.

1.2 Aim and scope of this thesis

This thesis aims to develop a numerical approach capable of simulating the fragmentation process from emergence to dispersion of debris in concrete structures, overcoming the above mentioned limitations and being hence suitable for the application in large 3D models. It is hypothesized here that two basic ingredients are necessary to accomplish this goal: a suitable description of concrete and the coupling of this description with a common homogenized macromechanical scale. The detailed development and combination of these are the major contributions of this work.

Since concrete fragmentation is a process triggered and driven by its structure as a heterogeneous composite material, a simulation approach that attempts to describe fragmentation accurately must explicitly consider the structure of the underlying material on an appropriate scale. This scale will be later introduced as “mesoscale”. Currently, this scale is only used for the simulation of laboratory-sized

specimens to understand the behavior of the material or to limit the number of specific experiments by replacing them with simulations. But attempts to exploit mesomechanical descriptions for fragmentation analysis in larger structures are still missing. The reason might be the accompanying computational efforts, which let researchers and engineers hesitate to utilize this description. In fact, not all attempts to model concrete on the mesoscale are capable of delivering fragments in reasonable computational time. While, e.g., the application of cohesive zone elements renders cracking phenomena and dispersing material regions with high accuracy, the computational burden in 3D is extremely high. On the other hand, smeared crack approaches are potentially not accurate enough. It will be argued in Chapter 4 that a combination of both approaches with a fine mesh and an apt representation of concrete constituents provides a powerful and robust modeling paradigm able to capture the basic phenomena within acceptable computational times. Therefore, the choice and formulation of a suitable mesomechanical modeling approach for concrete constitute the first key component of this work.

However, discretization of complete structures on the mesoscale will still be not feasible in the foreseeable future. This fact motivates the appropriation of multiscale analysis, where two scales simultaneously exist and the mesoscale is utilized only for relevant parts of the structure. The second major contribution of this thesis is therefore the development of a method which allows a strong coupling of two disparate finite element meshes with wave propagation in both domains. Again, applicable couplings already exist, as will be shown in Chapter 5. Yet none of the existing ones respects the classical “direct” solution scheme, employed in wave propagation codes with explicit time integration. Application and implementation of such schemes in these codes is nevertheless possible, but will either lead to considerably increased computational efforts or to an intricate handling of changing mesh topologies at the interface due to emerging cracks in the lower scale. In contrast, the coupling approach proposed here respects the given solution scheme, adds only a few additional operations, and is consequently highly efficient. Thereby, the way should be paved for the simulation of fragmentation and debris throw in regions of interest, while simultaneously considering the effects of the surrounding structure – an important aspect in some scenarios.

The two major subjects of this work will be sustained by the following individual contributions:

- Identification and application of a suitable description of concrete on its mesoscale, capable of covering element separation with robustness, but sufficient accuracy.
- Enhancing and improving a widely used material model for concrete under dynamic loading with a rate-dependent, regularized principal stress criterion.
- Exploiting the mesoscale description beyond the simulation of failure to actual determination and analysis of fragments – utilizing their individual shapes to determine unique aerodynamic coefficients.
- Developing a two-scale coupling approach for direct solution schemes with explicit time integration and comparison with an existing method based on Lagrange multipliers.
- Application of a “selective perfectly matched layer” to the coupling interface to dwindle pathological wave reflections.

If one follows reference [26] in the principal differentiation of (a) fragments’ emergence, (b) their dispersal, and finally (c) their effects, this thesis is mainly concerned with the first issue. The subsequent trajectories of the debris will be only briefly discussed for one application scenario, while the effects of fragments on human bodies or structures are completely out of the scope. But even the emergence of fragments will be covered within this thesis only to a certain extent. Focus is on the overall *framework*, the identification of necessary ingredients, less on the perfect solution in every detail. Nevertheless, some application examples will clearly show that the aim of predictive fragmentation simulation is within reach.

1.3 Structure of the dissertation

The structure of this dissertation is as follows: Chapter 2 commences with a review of the numerical fundamentals necessary for the understanding of this thesis. Its focus is on the description of wave propagation codes. Chapter 3 deals with the material concrete – its composition and behavior under loading – and the different options for numerical idealization on the macro- as well as the mesoscale in the literature. Subsequently, a specific modeling approach

– a combination of a plasticity model for the matrix and distinctly modeled aggregates and cohesive zone elements for the interfacial failure between the two constituents – is formulated and applied in Chapter 4, which is the first main pillar of this thesis. The second one is the following Chapter 5, in which a novel two-scale coupling approach is introduced. While this chapter contains more or less the theoretical basis and specific issues, such as pathological wave reflections, validation and application of the coupling is deferred to Chapter 6. Finally, Chapter 7 summarizes this thesis and discusses open issues for future research.

2 Numerical fundamentals

The purpose of this chapter is to equip the reader with the necessary numerical peculiarities employed in this thesis, which is mainly the solution of dynamic problems with wave propagation codes. It is assumed that the reader is familiar with the basic idea and discretization of the finite element method, which will not be elaborated on in detail.

2.1 Momentum balance: continuous description

Let Ω be a continuous body and \mathbf{x} the representation of a material point in \mathbb{R}^3 . The local momentum balance for this body – Cauchy's first law of motion – then reads in the spatial (deformed) configuration [27, 28]:

$$\rho \ddot{\mathbf{u}}(\mathbf{x}, t) - \rho \mathbf{k}(\mathbf{x}, t) - \nabla \cdot \boldsymbol{\sigma}(\mathbf{x}, t) = \mathbf{0} \quad (2.1)$$

The symbols in equation (2.1) denote the density ρ , the second derivative of displacements $\mathbf{u}(\mathbf{x}, t)$ with respect to time t – accelerations $\ddot{\mathbf{u}}(\mathbf{x}, t)$, body forces \mathbf{k} , the nabla operator ∇ , and the Cauchy stress tensor $\boldsymbol{\sigma}(\mathbf{x}, t)$. The multiplication operator \cdot implies the scalar product. For legibility, the explicit dependence on the spatial coordinate \mathbf{x} will be omitted from now on. Together with the initial conditions

$$\mathbf{u}(t_0) = \mathbf{0} \quad (2.2a)$$

$$\dot{\mathbf{u}}(t_0) = \mathbf{0} \quad (2.2b)$$

and potential kinematic and traction boundary conditions on the body's surface $\partial\Omega$

$$\dot{\mathbf{u}}(t) = \dot{\mathbf{u}}^e(t) \text{ on } \partial\Omega_u \quad (2.3a)$$

$$\mathbf{t}(t) = \mathbf{t}^e(t) \text{ on } \partial\Omega_t \quad (2.3b)$$

the problem forms an initial boundary value problem, with $\partial\Omega = \partial\Omega_u \cup \partial\Omega_t$ and $\partial\Omega_u \cap \partial\Omega_t = \emptyset$. \mathbf{t} denotes the traction vector. In the following, body forces are neglected for simplicity throughout, i.e. $\rho\mathbf{k}(t) = \mathbf{0}$. However, it poses no difficulty to consider body forces.

Using the virtual work principle, a weak formulation of the momentum balance with an admissible test function $\delta\mathbf{u}$ reads after some transformations (see, e.g., [29]):

$$\int_{\Omega} \delta\mathbf{u} \cdot \rho\ddot{\mathbf{u}} d\Omega + \int_{\Omega} \nabla\delta\mathbf{u} : \boldsymbol{\sigma}(t) d\Omega - \int_{\partial\Omega_t} \delta\mathbf{u} \cdot \mathbf{t}(t) d\partial\Omega = \mathbf{0} \quad (2.4)$$

The test functions $\delta\mathbf{u}$ have to vanish on $\partial\Omega_u$ and are to be sufficiently smooth with respect to \mathbf{x} .

2.2 Spatial discretization with finite elements

In order to solve the weak formulation of the momentum balance, equation (2.4) has to be discretized in space and time. For spatial discretization, finite differences or finite elements (FE) are often employed. A detailed derivation of the discretization is omitted here for the sake of brevity and the reader is referred to standard textbooks, such as reference [29]. In this thesis, only Lagrangian FE will be used.

Discretizing the body Ω now with $n_{\mathcal{E}}$ finite elements \mathcal{E} and $n_{\mathcal{N}}$ nodes \mathcal{N} , the semi-discretized (spatially discretized) equation of motion (EOM) reads then⁵:

$$\mathbf{M}\ddot{\mathbf{u}}(t) + \mathbf{K}(t)\mathbf{u}(t) = \mathbf{R}(t) \quad (2.5)$$

⁵ Please note that \mathbf{u} is now the *array* of displacements, which has one entry for each degree of freedom, i.e. $\mathbf{u} = [u_{1,x} \ u_{1,y} \ u_{1,z} \ u_{2,x} \ \dots \ u_{n_{\mathcal{N}},z}]^T$.

with the mass matrix \mathbf{M} , the stiffness matrix \mathbf{K} and the vector of outer forces \mathbf{R} which are defined by:

$$\mathbf{M} = \sum_{j=1}^{n_{\mathcal{E}}} \int_{\Omega_j^{\mathcal{E}}} \rho \mathbf{N} \mathbf{N}^T d\Omega_j^{\mathcal{E}} \quad (2.6a)$$

$$\mathbf{K}(t) = \sum_{j=1}^{n_{\mathcal{E}}} \int_{\Omega_j^{\mathcal{E}}} \mathbf{B}^T \mathbf{C}_E(t) \mathbf{B} d\Omega_j^{\mathcal{E}} \quad (2.6b)$$

$$\mathbf{R}(t) = \sum_{j=1}^{n_{\mathcal{E}}} \int_{\partial\Omega_{t,j}^{\mathcal{E}}} \mathbf{N} \mathbf{t}(t) d\partial\Omega_{t,j}^{\mathcal{E}} \quad (2.6c)$$

with $\Omega_j^{\mathcal{E}}$ being the volume of the j -th element and \mathbf{N} the array of shape or interpolation functions. $\mathbf{B} = \partial \mathbf{N} / \partial \mathbf{x}$ is the discrete symmetric gradient operator (or “strain-displacement matrix”) and \mathbf{C}_E the elasticity matrix.

The product of stiffness matrix and displacement vector is a force vector, designated as “internal” forces, \mathbf{F} . From elementary equilibrium considerations, one can show that:

$$\mathbf{F}(t) = \mathbf{K}(t) \mathbf{u}(t) = \sum_{j=1}^{n_{\mathcal{E}}} \int_{\Omega_j^{\mathcal{E}}} \mathbf{B}^T \boldsymbol{\sigma}(t) d\Omega_j^{\mathcal{E}} \quad (2.7)$$

Then the equation of motion finally reads:

$$\mathbf{M} \ddot{\mathbf{u}}(t) = \mathbf{R}(t) - \mathbf{F}(t) \quad (2.8)$$

This equation can be solved by left multiplication with \mathbf{M}^{-1} . However, the inversion is costly and – although \mathbf{M} is sparse, \mathbf{M}^{-1} is not. Reducing \mathbf{M} to a diagonal matrix, one can avoid the inversion and equation (2.8) expresses then an array of independent equations – one for each degree of freedom (DOF). For each DOF k , the solution is then simply determined by:

$$\ddot{u}_k = \frac{R_k - F_k}{m_{\mathcal{N}}} \quad (2.9)$$

with m_N being the mass of the corresponding node.⁶ Together with the fact that \mathbf{F} is a vector that can be filled by looping through the element assembly, there is no need to store or factorize global matrices. Consequently, this scheme is very efficient and robust – even the loss of elements can be inherently covered (in the following the diagonalization of \mathbf{M} is presupposed if the opposite is not explicitly mentioned). Since the elemental contribution to the inner force vector is accomplished “directly” at the element level, this scheme was labeled “direct” by Belytschko [32, 33]. However, the effectiveness of this scheme depends strongly on the choice of the time integration algorithm, which is touched on next.

2.3 Temporal discretization

A natural discretization of a second-order differential equation $\ddot{u} = f(u)$ would be the application of central differences. Defining the (time) increment, the “time step”, from step (n) to $(n + 1)$ as Δt , one finds:

$$\dot{\mathbf{u}}^{(n)} = \frac{1}{2\Delta t} \left(-\mathbf{u}^{(n-1)} + \mathbf{u}^{(n+1)} \right) \quad (2.10a)$$

$$\ddot{\mathbf{u}}^{(n)} = \frac{1}{\Delta t^2} \left(\mathbf{u}^{(n-1)} - 2\mathbf{u}^{(n)} + \mathbf{u}^{(n+1)} \right) \quad (2.10b)$$

The displacements for the next step $(n + 1)$ can be determined with the second line by formulating:

$$\mathbf{u}^{(n+1)} = -\mathbf{u}^{(n-1)} + 2\mathbf{u}^{(n)} + \Delta t^2 \ddot{\mathbf{u}}^{(n)} \quad (2.11)$$

The accelerations $\ddot{\mathbf{u}}^{(n)}$ are determined by solving the EoM:

$$\ddot{\mathbf{u}}^{(n)} = \mathbf{M}^{-1} \left(\mathbf{R}^{(n)} - \mathbf{F}^{(n)} \right) \quad (2.12)$$

Note that the EOM is formulated for *current step* (n) ; thus, the solution advances to the next step simply based on already known values. This integration scheme

⁶ Besides the pure computational advantage of this representation, there are physical arguments why a diagonal mass matrix delivers more accurate results under impulsive loading. In case of a consistent mass matrix, the whole system/mesh will perceive the loading of a single node immediately, which is not physical. For a diagonal mass matrix, only the nodes where the impulsive loading is applied feel the load, and neighbored nodes are not affected before the next cycle. This leads to a correct shock propagation [30, 31].

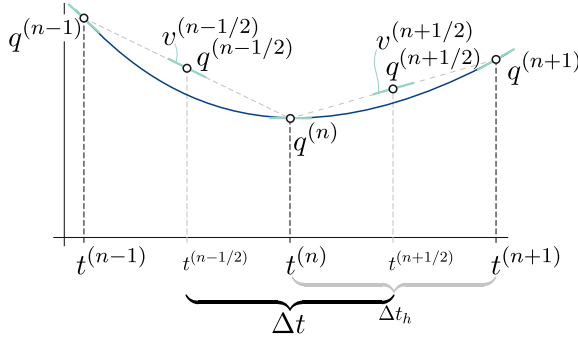


Figure 2.1: Leapfrog time integration scheme of a one dimensional function $q(t)$, $v = \dot{q}$. Derivatives are approximated by central difference quotients on a staggered time grid. The definition of the time steps as Δt and Δt_h follows the convention in SOPHIA. Figure redrawn from [34].

is labeled “explicit”. In practice, a slightly more complex scheme is applied to achieve second-order accuracy. In this so-called “Leapfrog-scheme”⁷, the first derivatives are determined at a staggered grid, refer to Figure 2.1. From this figure, one can easily derive the following definitions for moving from $t^{(n)}$ to $t^{(n+1)}$:

$$\dot{\mathbf{u}}^{(n-1/2)} = \frac{1}{\Delta t_h} \left(\mathbf{u}^{(n)} - \mathbf{u}^{(n-1)} \right) \quad (2.13a)$$

$$\dot{\mathbf{u}}^{(n+1/2)} = \frac{1}{\Delta t_h} \left(\mathbf{u}^{(n+1)} - \mathbf{u}^{(n)} \right) \quad (2.13b)$$

$$\ddot{\mathbf{u}}^{(n)} = \frac{1}{\Delta t} \left(\dot{\mathbf{u}}^{(n+1/2)} - \dot{\mathbf{u}}^{(n-1/2)} \right) \quad (2.13c)$$

leading to the update equations:

$$\dot{\mathbf{u}}^{(n+1/2)} = \dot{\mathbf{u}}^{(n-1/2)} + \Delta t \ddot{\mathbf{u}}^{(n)} \quad (2.14a)$$

$$\mathbf{u}^{(n+1)} = \mathbf{u}^{(n)} + \Delta t_h \dot{\mathbf{u}}^{(n+1/2)} \quad (2.14b)$$

⁷ The scheme inherits its name due to its staggered characteristics. In molecular dynamics, the scheme is known as the “Verlet” algorithm, whereas the terms “Störmer”- or “Encke”-method are also known. Störmer has used the scheme already 1907, Encke even around 1860 and – most remarkably – Richard Feynman noted in 1965 that the underlying idea is already used by Isaac Newton in his *Principia*, see [34] for a brief historic review.

As previously written, this scheme has the advantage of having all the values for the evaluation of the next step at hand. On the other hand, it is only conditionally stable. Its integration operator has to be bound by a critical time integrator to prevent instability. One can show that this critical time step can be derived from the highest eigenfrequency of the whole element assembly, ω_{max} :

$$\Delta t_c \leq \frac{2}{\omega_{max}} \quad (2.15)$$

Since ω_{max} is not necessarily constant, evaluation of the critical time step would necessitate the solution of the general eigenvalue problem of the FE assembly in each computational cycle, which of course is not feasible. Therefore, in practice, an approximation of this value is used. Based on the analytical solution of a linear 1D bar element, where the natural frequency is $\omega = 2c_S/l$ (with $c_S = \sqrt{E/\rho}$ the speed of sound, E the Young's modulus, ρ the density, and l the length of the bar), the observation is that Δt has to be less than the time it takes for an elastic wave to travel the distance from one node to the next. This descriptive approximation can be easily extended to other finite elements and is hence formulated as

$$\Delta t_c \leq \frac{l_c}{c_S} \quad (2.16)$$

in which l_c is an – element dependent – critical length. Strictly speaking, the above argumentation holds only for linear systems, but as *Belytschko* notes: “[T]here is considerable empirical evidence that these stability limits are valid for non-linear problems if the current highest frequency or wave speed is used in the equations” ([32, p.25]).

For comparison, consider now a different time integration, the widely used Newmark scheme. This scheme can be achieved by a truncated Taylor series expansion of \mathbf{u} and $\dot{\mathbf{u}}$. Newmark proposed the following two expressions:

$$\mathbf{u}^{(n+1)} = \mathbf{u}^{(n)} + \Delta t \dot{\mathbf{u}}^{(n)} + \Delta t^2 \left[(1/2 - \beta) \ddot{\mathbf{u}}^{(n)} + \beta \ddot{\mathbf{u}}^{(n+1)} \right] \quad (2.17a)$$

$$\dot{\mathbf{u}}^{(n+1)} = \dot{\mathbf{u}}^{(n)} + \Delta t \left[(1 - \gamma) \ddot{\mathbf{u}}^{(n)} + \gamma \ddot{\mathbf{u}}^{(n+1)} \right] \quad (2.17b)$$

with $0 \leq \gamma \leq 1$ and $0 \leq \beta \leq 1$ being two numerical parameters. Now for the evaluation of the displacements and velocities at $(n + 1)$, the accelerations at

$(n + 1)$ have to be at hand.⁸ It follows that the EOM has to be formulated at $(n + 1)$:

$$\ddot{\mathbf{u}}^{(n+1)} = \mathbf{M}^{-1} \left(\mathbf{R}^{(n+1)} - \mathbf{F}^{(n+1)} \right) \quad (2.18)$$

The crucial point is that the vector of internal forces \mathbf{F} depends then on unknown values and an iterative solution is necessary. Such a scheme is said to be “implicit”. Depending on the choice of γ and β , the scheme becomes unconditionally stable, which is an important advantage. In contrast to explicit integration, large time steps are possible. Since, however, the solution of each step involves several iterations until equilibrium is found, these time steps are computationally much more expensive than a comparable explicit one and may fail in situations where strong nonlinearities are involved. Additionally, the vector of internal forces $\mathbf{F}^{(n+1)}$ would in this case not be constituted by direct recourse to element stresses, as written in equation (2.7). Instead, the product of the current stiffness and the current displacement would be used, which requires factorization of the stiffness matrix in each step. This again is a costly operation.

2.4 Wave propagation codes

2.4.1 Classification of dynamic problems

The EOM is the fundamental basis of all problems that describe the deformation of bodies under dynamic loading. However, there exists a wide variety of solution options, each with its unique advantages and disadvantages. In order to choose a suitable strategy, it is therefore beneficial to distinguish two broad dynamic problem classes. E.g. *Belytschko* et al. differentiate broadly between “wave propagation problems” and “inertial problems” with the following rule of thumb: “[If the] rise time and duration of the load [...] exceed several traversal times, the problem is often in the inertial category” ([35, p.17]) or even more general: An inertial problem is “everything, which is not a wave problem”. *Nickell* labels inertia problems more specific as “structural vibration problems [...] which] are almost always dominated by low-frequency components of the response” ([36, p. 303]). *Dokainish* et al. use the meanwhile dominant term “structural dynamics” for this problem class. In contrast, wave propagation problems are such problems

⁸ Admittingly this depends on the values of γ and β . Commonly, $\gamma = 1/2$ and $\beta = 1/4$ or $1/6$ are chosen. But if instead $\beta = 0$, the scheme renders to an explicit scheme.

“in which the behavior at the wave front is of engineering importance, and in such cases it is the intermediate and high-frequency structural modes that dominate the response throughout the time span of interest” ([37, p.1371]), while *Combes* et al. differentiate between “dynamic vibration” and “fast dynamic” problems [38]. Analysis of high- and hypervelocity impacts and effects of explosions and blast waves are typical examples of the latter.

The resolution of stress waves necessitates very small (and therefore many) timesteps. Furthermore, often highly nonlinear material behavior must be considered which renders explicit time integration for this class of problems superior compared to implicit methods. Indeed, dedicated wave propagation codes, or “hydrocodes”, to use the historical term, are the preferred choice⁹ [31, 40, 41]. In these codes, the detailed direct scheme described above is used during each “cycle”.

2.4.2 Overview of the Lagrangian simulation cycle

Starting with the initial conditions of the current time t at the current cycle (n), the kinematic variables \mathbf{L} (spatial gradient of velocity tensor), \mathbf{D} (rate of deformation or stretching tensor) and \mathbf{W} (spin or vorticity tensor) are determined for each element \mathcal{E} individually, based on the velocity field of its nodes. They are written here in tensorial notation and only later in the summarizing listing expressed for the discretized system. In general:

$$\mathbf{L}^{(n-1/2)} = \nabla \mathbf{u}^{(n-1/2)} \quad (2.19)$$

The rate of deformation tensor \mathbf{D} is equal to the symmetric part of the spatial gradient of the velocity tensor \mathbf{L} :

$$\mathbf{D}^{(n-1/2)} = \frac{1}{2} \left(\mathbf{L}^{(n-1/2)} + \left(\mathbf{L}^{(n-1/2)} \right)^\top \right) \quad (2.20)$$

⁹ A further term found in literature is “Lagrangian shock hydrodynamics code”, e.g. in [39]. Throughout the thesis, the term “hydrocode” is used as a generic *terminus technicus* synonymously to “wave propagation code”. This short form of “hydrodynamic computer codes” stems from the fact that the shear strength of condensed matter can be neglected in cases of very high compression and the matter behaves consequently like a fluid [40].

Since an updated Lagrangian formulation with small strain increments is used, the strain rate equals the deformation rate tensor [42]¹⁰:

$$\dot{\epsilon}^{(n-1/2)} = \mathbf{D}^{(n-1/2)} \quad (2.21)$$

with its volumetric part, defined by the trace of the tensor:

$$\dot{\epsilon}_v^{(n-1/2)} = \text{tr} \left(\mathbf{D}^{(n-1/2)} \right) \quad (2.22)$$

The vorticity tensor is equal to the antisymmetric part of the spatial gradient of the velocity tensor $\mathbf{L} = \mathbf{D} + \mathbf{W}$, with:

$$\mathbf{W}^{(n-1/2)} = \frac{1}{2} \left(\mathbf{L}^{(n-1/2)} - \left(\mathbf{L}^{(n-1/2)} \right)^\top \right) \quad (2.23)$$

The current specific energy, e , is determined by integrating its rate, \dot{e} :

$$\dot{e}^{(n-1/2)} = \frac{1}{\rho^{(n-1)}} \boldsymbol{\sigma}^{(n-1)} : \mathbf{D}^{(n-1/2)} \quad (2.24a)$$

$$e^{(n-1/2)} = e^{(n-1)} + \frac{1}{2} \Delta t_h^{(n-1/2)} \dot{e}^{(n-1/2)} \quad (2.24b)$$

And for the density ρ :

$$\dot{\rho}^{(n)} = -\rho^{(n-1)} \mathbf{L}^{(n-1/2)} \quad (2.25a)$$

$$\rho^{(n)} = \rho^{(n-1)} + \Delta t_h^{(n-1/2)} \dot{\rho}^{(n)} \quad (2.25b)$$

Noting that so far only variables based on the velocity field and not on specific material parameters have been determined, now a constitutive model comes into play to determine the elements' stress state $\boldsymbol{\sigma}$. Historically, hydrocodes take advantage of the split of the total stress state into a hydrostatic contribution, the pressure p , and the remaining deviatoric stress tensor \mathbf{s} :

$$\boldsymbol{\sigma}^{(n)} = \mathbf{s}^{(n)} - p^{(n)} \mathbf{I} \quad (2.26)$$

with \mathbf{I} being the identity tensor. Both contributions are determined separately, which simplifies the application of complex, nonlinear relationships for pressure and deviatoric stress. In scenarios with very high pressure or non-viscous fluids

¹⁰ The difference is that \mathbf{D} is based on the derivatives with respect to the spatial coordinates \mathbf{x} , while in $\dot{\epsilon}$ with respect to the material coordinates \mathbf{X} . In the updated Lagrangian case $\mathbf{X} \approx \mathbf{x}$ [42, p.150].

only, the shear strength might even be negligible and only the pressure state has to be calculated.

The current pressure is computed employing an equation of state (EOS). An EOS is – in general – an arbitrary relationship between pressure p , density ρ , and specific internal energy e of a material portion:

$$p = f(\rho, e) \quad (2.27)$$

Equations of state in the form above are labeled “incomplete”, since they do not take into account heat conduction effects, for which a relation based on a Gibbs potential would be necessary [43]. Since in most cases (shock) wave propagation is only of very short duration, adiabatic conditions can be assumed and incomplete EOS are fully valid. On the other hand, a set of further parameters, κ , including, e.g., porosity, can be considered in the EOS for appropriate material modeling. Within the computational cycle, the pressure is therefore determined by:

$$p^{(n)} = f(\rho^{(n)}, e^{(n)}, \kappa^{(n)}) + q \quad (2.28)$$

Shock waves represent a sharp discontinuity in the field variables, which cannot be properly described in a finite mesh. Therefore, an additional pressure term, q , labeled “artificial viscosity”, has already been considered above. Its effect is to “smear” the shock front over several elements:

$$q = \rho l_c \nabla \cdot \dot{\mathbf{u}} (c_B^2 l_c \nabla \cdot \dot{\mathbf{u}} - \zeta_L \zeta_Q) \quad (2.29)$$

Unless stated otherwise, all simulations within this work contain this additional pressure term, based on the two input parameters ζ_L and ζ_Q and the materials bulk speed of sound, c_B .

Based on Hooke’s law, the deviatoric stress rate can be derived through the shear modulus G :

$$\dot{\mathbf{s}}^{(n-1/2)} = 2G\dot{\boldsymbol{\epsilon}}^{(n-1/2)} \quad (2.30)$$

in which $\dot{\boldsymbol{\epsilon}}$ denotes the deviatoric portion of the strain rate tensor:

$$\dot{\boldsymbol{\epsilon}}^{(n-1/2)} = \dot{\boldsymbol{\epsilon}}^{(n-1/2)} - \frac{1}{3} \dot{\epsilon}_v^{(n-1/2)} \mathbf{I} \quad (2.31)$$

Simply integrating the stress rate to yield deviatoric stresses is not sufficient since the above-stated stress rate is not objective with respect to rotation. This means that rigid body rotation would lead to contributions to the final stress

tensor, which of course is unphysical. Therefore, objective stress rates have to be employed. Different rates have been proposed, in most cases the Jaumann rate is used due to its simplicity:

$$\mathbf{s}^{(n)} = \mathbf{s}^{(n-1)} + \Delta t_h^{(n-1/2)} \left(\dot{\mathbf{s}}^{(n-1/2)} - \mathbf{W}^{(n-1/2)} \mathbf{s}^{(n-1)} + \mathbf{s}^{(n-1)} \mathbf{W}^{(n-1/2)} \right) \quad (2.32)$$

Equation (2.26) is then used to assemble the full stress tensor if necessary.

In many cases, materials should be modeled which have a limited capacity to withstand stresses and consequently fail if stressed above. This limit – or yield – stress is hence an upper bound of the physical admissible stress state. In order to derive this limit stress, a strength model describes the yield stress σ_y as a function of different material and internal variables – depending on the complexity of the model:

$$\sigma_y^{(n)} = f(\dots) \quad (2.33)$$

A yield function $\Phi(\sigma_y, \sigma)$ is used to check whether the current stress state σ , derived so far, is admissible or not. Therefore, this state is labeled as “elastic trial stress”. If the trial stress is above the yield criterion, it has to be mapped back on the limit surface. After updating the stress state, the energy is corrected with the current stress:

$$\dot{e}^{(n)} = \frac{1}{\rho^{(n)}} \sigma^{(n)} : \mathbf{D}^{(n-1/2)} \quad (2.34a)$$

$$e^{(n)} = e^{(n-1/2)} + \frac{1}{2} \Delta t^{(n-1/2)} \dot{e}^{(n)} \quad (2.34b)$$

Whereas the above equations have been written for a material point in the continuum, their application is in the context of a FE discretization. Consequently, these equations have to be applied to nodal (\mathcal{N}) or element (\mathcal{E}) values, which is achieved by replacing all variables with their discretized matrix form. Element values are further determined at the elements integration points.

Having the updated stress at hand, the inner element forces can then be computed by standard Gaussian integration with weight factors $a_{g..}$ at n_g Gauss points and the elements' Jacobian matrix \mathbf{J} :

$$\mathbf{F}^{(n)} = \sum_{g=1}^{n_g} \mathbf{B}_g^T \sigma_g^{(n)} \det \mathbf{J}_g a_{g,x} a_{g,y} a_{g,z} \quad (2.35)$$

Summing up all external forces, e.g., due to boundary conditions, contact or cohesive forces for each nodal DOF in the vector of external loads \mathbf{R} , the updated acceleration is yielded by reformulating the momentum balance:

$$\ddot{\mathbf{u}}^{(n)} = \mathbf{M}^{-1} \left(\mathbf{R}^{(n)} - \mathbf{F}^{(n)} \right) \quad (2.36)$$

Note that – as mentioned above – it is tacitly assumed here that \mathbf{M} is a diagonal matrix and that equation (2.36) can be therefore solved for each DOF independently by applying equation (2.9). With the updated accelerations, new velocities and displacements are derived:

$$\dot{\mathbf{u}}^{(n+1/2)} = \ddot{\mathbf{u}}^{(n)} \Delta t^{(n)} + \dot{\mathbf{u}}^{(n-1/2)} \quad (2.37a)$$

$$\mathbf{u}^{(n+1)} = \dot{\mathbf{u}}^{(n+1/2)} \Delta t_h^{(n+1/2)} + \mathbf{u}^{(n)} \quad (2.37b)$$

Finally, the time is increased, and a new admissible time step is determined. The process starts over again. For reference use, the scheme is summarized in Algorithm 1.

2.4.3 Codes used in this thesis

The developments detailed in this thesis were mainly developed for use in the 3D research code SOPHIA, a wave propagation code for Lagrangian finite elements and smooth hydroparticles (SPH). It was originally developed as a particle code at the University of the German Armed Forces [44], and was later extended to cover finite elements [45]. Meanwhile, the code is maintained and further developed at EMI, where it is used mainly as research code. To investigate some aspects of the two-scale coupling, especially to compare the developed weak staggered coupling with an existing coupling based on Lagrange multipliers, a 2D code was written from scratch, following the scheme detailed above, but with restriction to 2D solid elements.

Algorithm 1 Overview computational cycle. (n) denotes the current cycle/time.

while $t < t_e$ **do**

$\Delta t^{(n)}, \Delta t_h^{(n-1/2)}, \dot{\mathbf{u}}^{(n-1/2)}$ ▷ Initial values for step (n)

for all Elements \mathcal{E} **do**

for each integration point **do**

$$\mathbf{L}^{(n-1/2)} = \mathbf{B} \dot{\mathbf{u}}^{(n-1/2)}$$

$$\dot{\epsilon}^{(n-1/2)} = \mathbf{D}^{(n-1/2)} = 1/2 \left(\mathbf{L}^{(n-1/2)} + \mathbf{L}^{T(n-1/2)} \right)$$

$$\mathbf{W}^{(n-1/2)} = 1/2 \left(\mathbf{L}^{(n-1/2)} - \mathbf{L}^{T(n-1/2)} \right)$$

$$e^{(n-1/2)} = e^{(n-1)} + 1/2 \Delta t_h^{(n-1/2)} \left(\rho^{-1(n-1)} \boldsymbol{\sigma}^{(n-1)} : \mathbf{D}^{(n-1/2)} \right)$$

$$\rho^{(n)} = \rho^{(n-1)} - \Delta t_h^{(n-1/2)} (\rho^{(n-1)} \mathbf{L}^{(n-1/2)})$$

$$p^{(n)} = f(\rho^{(n)}, e^{(n)}, \dots)$$

$$\dot{s}^{(n-1/2)} = 2G \dot{\epsilon}^{(n-1/2)}$$

$$\mathbf{s}^{(n)} = \mathbf{s}^{(n-1)} + \Delta t_h^{(n-1/2)} \left(\dot{\mathbf{s}}^{(n-1/2)} - \mathbf{W}^{(n-1/2)} \mathbf{s}^{(n-1)} + \mathbf{s}^{(n-1)} \mathbf{W}^{(n-1/2)} \right)$$

$$\boldsymbol{\sigma}^{(n)} = f(\mathbf{s}^{(n)}, p^{(n)}, \dot{\epsilon}^{(n-1/2)}, \dots)$$

$$e^{(n)} = e^{(n-1/2)} + 1/2 \Delta t_h^{(n-1/2)} \left(\rho^{-1(n)} \boldsymbol{\sigma}^{(n)} : \mathbf{D}^{(n-1/2)} \right)$$

end for

$$\mathbf{F}^{(n)} = \sum_{g=1}^{n_g} \mathbf{B}_g^T \boldsymbol{\sigma}_g^{(n)} \det \mathbf{J}_g a_{g,x} a_{g,y} a_{g,z}$$

end for

for all nodes \mathcal{N} **do**

$$\ddot{\mathbf{u}}_{\mathcal{N}}^{(n)} = \left(\mathbf{R}_{\mathcal{N}}^{(n)} - \mathbf{F}_{\mathcal{N}}^{(n)} \right) / m_{\mathcal{N}}$$

$$\dot{\mathbf{u}}_{\mathcal{N}}^{(n+1/2)} = \ddot{\mathbf{u}}_{\mathcal{N}}^{(n)} \Delta t^{(n)} + \dot{\mathbf{u}}_{\mathcal{N}}^{(n-1/2)}$$

$$\mathbf{u}_{\mathcal{N}}^{(n+1)} = \dot{\mathbf{u}}_{\mathcal{N}}^{(n+1/2)} \Delta t_h^{(n-1/2)} + \mathbf{u}_{\mathcal{N}}^{(n)}$$

end for

$$\Delta t^{(n+1/2)} = \Delta t_c^{(n)}, \Delta t^{(n+1)} = 1/2 \left(\Delta t^{(n-1/2)} + \Delta t^{(n+1/2)} \right)$$

$$t^{(n+1)} = t^{(n)} + \Delta t^{(n-1/2)}$$

$$n \rightarrow n + 1$$

end while

2.5 Summary

With regard to the developments expounded later in this thesis, let the key findings of this chapter be briefly summarized:

- Using explicit time integration, a solution is achieved by progressing in time with very small but numerous time steps.
- Each time step is in general very cheap since no global matrices have to be built, stored, or inverted.
- Since the investigation of wave propagation problems requires in any case small time steps, explicit schemes are a natural choice for these problems.
- The explicit, direct scheme even allows the removal of elements during run time with no difficulties.
- Highly nonlinear problems can be easily treated with this scheme since no iterations are involved.
- Whereas the explicit scheme always achieves a solution, it is of limited stability, and a critical step size must not be exceeded.

3 Relevant aspects of concrete material and mesomechanical modeling – a review

The purpose of this chapter is to review the material concrete, its basic constituents, composition and resulting microstructure. This forms the foundation for the discussion of different concrete modeling approaches in the literature together with the advantages and shortcomings of the individual methods. Based on this deliberation, the next chapter proposes a robust approach for mesomechanical modeling, which allows the accurate simulation of fragmentation while being still efficient enough to be employed in large FE domains.

3.1 Constituents and structural features¹¹

3.1.1 Constituents

Ordinary concrete consists mainly of (portland) cement, coarse and fine aggregates, and water. In addition to these three constituents, small amounts of other substances are possible to control specific properties of hardened concrete, but can be elided here.

Cement Cement is the basic constituent of concrete; it binds the aggregates together to form a hard solid. Originally, the name “portland cement” was a trade name: the material was patented by Joseph Aspdin, in England, 1824, and

¹¹ If not explicitly mentioned, the information contained within this section is taken from references [46–49].

got its name due to its similarity with natural limestone, quarried near Portland. Today “portland cement” designates a group of closely related cement types and is by far the most widely used cementitious binder [50]. For the purpose of this thesis, it is sufficient to give in the following only a very brief and concise overview of its ingredients and hydration, since the primary focus is on hardened cement and its mechanical behavior.

In an unreacted dry state, cement is a fine, gray powder. It is obtained mainly by vitrification of dehydrated limestone with small amounts of clay, marl, chalk, and shales at very high temperatures (1400–1500° C). During the burning, complex chemical processes take place, passing different phases and intermediate products. The final product that leaves the kiln is called “clinker”, dark gray porous nodules, with diameters between 6 and 50 mm. After cooling, the clinker is ground to a fine powder and small amounts of gypsum are added to control early reactions of tricalcium silicate during hydration. The final mixture of clinker and gypsum is labeled “cement” and consists basically of five different calcium oxide compounds listed in the appendix, Page 219.

When mixed with water, “hydration” begins – an exoergic reaction between the water and the cement constituents – resulting in several “hydration products” by diffusion of water through the oxides. The final, hardened reaction product is commonly designated as “cement paste”. Again, the different reactions are very complex involving distinguished phases and reaction products over time. It suffices here to note that out of the hydration of the two predominant compounds tricalcium and dicalcium silicate (C3S and C2S), two phases, namely calcium silicate hydrates (C-S-H) – or cement gel – and calcium-hydroxide (CH) – or portlandite, emerge. Together with water, these are the main constituents on the microscale. Gradually, the hydration products fill the room previously occupied by water. Broadly simplifying, longer needles or thin sheets evolve first (C-S-H from C3S reaction) and later, shorter ones take up the remaining space (C-S-H from less reactive C2S reaction). Hexagonal shaped oriented CH crystals with poor mechanical properties fill the abiding room and occupy up to 25 % space. In contrast, the amorphous, porous C-S-H phase with indifferent morphology predominates and constitutes 50–60 % of the final hydration products. Although many issues are still unresolved and the complex reaction process is even today not yet fully understood in all its diversity, it is widely believed that the nanostructure of cement gel dominates the mechanical properties of concrete [51].

The amount of water in relation to the cement mass, the w/c mass ratio, strongly influences the chemical reaction. It is therefore one of the most important factors

with regard to concrete's strength, since this ratio determines the final porosity and therefore the mechanical properties. After complete hydration, the added water is either chemically bound ("hydration water"), physically adsorbed or free [52]. The physically adsorbed water is attracted to surfaces of other particles without forming further reaction products and occupies especially the gel pores. Complete hydration of cement requires approximately 25 % of its mass as water, but since roughly one third of the added water is adsorbed and therefore not available for reaction, in general around 40 % water (related to the cement mass) must be supplied for a complete reaction. However, even in this case, the water may not reach the core of all cement particles and some unhydrated remnant abides.¹² If less than 40 % water (i.e. $w/c < 0.4$) is supplied, unhydrated cement grains remain in the final mix. If – on the other hand – more water is added, the excess water stays in capillary pores. During drying, they may drain and increase overall porosity.

Aggregates Cement is generally combined with a large amount of filler material, the aggregates. In fact, only the combination of (hardened) cement and large aggregates qualifies for the designation "concrete". In standard cases up to roughly 70–80 % of the total volume of the final blend is constituted by aggregates; not only for economical reasons, but further to increase the dimensional stability and wear resistance. These filler particles are mainly from natural rocks and either as gravel or as crushed particles added to the blend. However, any chemically pure material that is free from impurities on its surface can be used to achieve good cohesion with cement. The shape and material of deployed aggregate in real concrete has mainly pragmatic consequences; fresh concrete is more workable with round, almost spherical aggregates. Round particles have furthermore less surface to volume ratio and need less cement to be covered. Finally, simply the source of supply may be decisive.

One commonly distinguishes between "coarse" and "fine" aggregates. There are different definitions which specify the limit between 4.0 and 4.75 mm.¹³

¹² The reaction begins on the outer surface of cement grains and soon builds up a hardly permeable sheet with growing thickness. The subsequent reaction is then controlled by diffusion and slows down considerably. In fact, hydration never stops completely. Strictly speaking, it continues throughout the lifetime of concrete, explaining its strength increase with time [53].

¹³ For ASTM, coarse aggregates are those passing sieve openings in the range of 4.75 to 50 mm and fine aggregates from 0.075 to 4.75 mm. The European standard differentiates between "rock flour" – particles passing a sieve opening of 0.063 mm; "fine" with an upper

Hardened cement paste with fine aggregates only is commonly labeled “mortar” or “grout”, but this term is not infrequently used in a more narrow sense for cement paste with sand only.

Although mainly intended as an inexpensive filler material, the type and grading of aggregates have an influence on the properties of concretes. While there are direct effects on overall dimensional stability, wear resistance, workability¹⁴ and the elastic properties of hardened concrete, the effects on concretes *strength* are more indirect¹⁵: since the amount of aggregates dictates the necessary quantity of water, the hydration and consequently the strength may be influenced. The use of finer aggregates entails a lower porosity, while larger aggregates with flat shape promote a reduced cohesion between cement paste and aggregate. Aggregates bind a water film around their surface which may accumulate under larger, elongated particles as filled pockets of water. This effect, known as “bleeding”, is abetted by poor mixing and engenders strongly reduced bonding properties in these regions and shrinkage cracks. *Structural* effects may influence the post-peak behavior. In experiments an increase of fracture energy with maximum aggregate size was observed and an increased brittleness of such concretes ascertained. The reason seems to be aggregate interlocking, as well as crack bridging and branching, as will be detailed below.

3.1.2 Structure

Hydration and the mixture of cement paste and aggregates yield a very specific micro structure, which features porosity, a weak transition zone on the aggregate-matrix interface, and promotes microcracks and residual stresses, as detailed below.

sieve opening not larger than 4 mm; and “coarse” aggregates with the lower sieve opening not less than 2 and the upper sieve opening not less than 4 mm, acc. to EN 12620.

¹⁴ Ease of flow, consistency, filling of small gaps.

¹⁵ Actually, contradictory findings exist in the literature. Whereas, e.g., [54] observe an increase of tensile strength with increasing aggregate size, they refer to other works in which the opposite was observed. In [55] an enhancement of the tensile strength is reported up to a maximum diameter of 8 mm, for larger values the strength remains constant. Concerning compression, [56] document a growth of strength with larger particle size. On the other side [57] and [58] observe again an antipodal effect. In the same way, [59] cites early research results that confirm the decrease in compressive strength with increasing aggregate diameter. Their particle based mesomechanical model support this position.

Porosity Concrete is a porous material and its porosity exerts a major influence on its strength. Three levels of pores have to be distinguished:

1. **Gel porosity** The cement gel is not a dense structure, but has in contrast a porosity of up to 25 % and is more an “interconnected network of void” ([60, p.509]). Gel pores occur in the size of 1×10^{-7} to 1×10^{-5} mm. Being an inherent property of the cement gel, they are independent of the w/c ratio and cannot, or only marginally, be influenced. Water is adsorbed in the voids and remains within the material, even under ideal conditions.
2. **Capillary porosity** These pores, in the size of 1×10^{-5} to 1×10^{-1} mm, are highly depended on the w/c ratio. If too much water is available, water-filled spaces remain after hydration. For $w/c > 0.6$ even a continuous capillary system evolves, which, after draining, allows the intrusion of fluids and gases into the concrete. Capillary voids are irregular in shape and are usually filled by “pore solution”, a solution of alkali hydroxides.
3. **Air voids** Air voids emerge if air is *entrained* during pouring and mixing or if larger air is *entrapped* during pouring. While smaller entrained air voids have diameters of around 0.06 to 1 mm, entrapped air voids of irregular shape can be even larger. Especially these larger lacunae have a major impact on the strength, as was demonstrated in [61]. The authors investigated the flexural strength of beams with different degrees of macropore sizes and found a much higher flexural strength for beams without larger pores, showing simultaneously no dependence of the total porosity. It is ergo the existence of larger voids, and less the porosity of the microstructure, which leads to a drop-down of strength. The same fact was maintained additionally in [62].

Although porosity generally decreases mechanical strength, pores play a vital role in the resistance of concrete to freezing and thawing. For exposed concretes, a minimum amount of pores is therefore necessary and regulated in national standards.

Interfacial transition zone The interface between aggregates and hydration products – the so-called interfacial transition zone (ITZ) – has received a considerable amount of interest. It is meanwhile proven and accepted that this zone constitutes the weakest link in the material. For the rather small cement grains with a size between 1 and 100 μm , the much larger inclusion particles (diameter in mm range) form wall-like obstacles within the blend. Due to the “wall-effect”,

only small cement grains can be packed in the vicinity of the aggregates. This fact, together with the water film around aggregates due to adsorbed water and bleeding, leads to a higher w/c ratio in this region, while the ratio in the bulk matrix is therefore reduced.¹⁶ The increased w/c ratio results in a noticeably porous transition zone with a preference for oriented CH panel crystals that fill the space between small C-S-H crystals [47, 63, 64]. Whereas the thickness of this zone is initially up to 100 μm , within some time¹⁷ the zone of high porosity reduces to around 15–20 μm – corresponding to the average size of the cement grains [63, 64]. It should be emphasized here that the ITZ is de facto a *transition zone*, not a sharp, well definite layer with specific properties, but a nonuniform, heterogeneous zone with considerable statistical variance.

Of course, the actual properties and structure of the ITZ depends on the aggregate type. Despite the roughness of the surface of the particles [66], some aggregates, such as limestone, have been found to react with the hydration products and thus increase the local porosity. Although some pores are later filled with subsequent reaction products, the ITZ has still been found weaker than in other cases [67]. Besides the ITZ between cement and aggregates, further ITZs appear in concrete, e.g., between unhydrated and hydrated cement paste or additives and the hydrated cement paste. With regard to the macromechanical properties, however, the ITZ between cement and coarse aggregates is the most important one. If considering only mortar, here as well the ITZ between hydration products and sand particles is of major importance and has been claimed to be the dominating effect on the mortar strength [66].

Not only is it a region with poor strength properties, the ITZ is also a common location for flaws such as microcracks, which are especially present within these zones even before the concrete is strained. Under loading, these cracks propagate and coalesce. Post-mortem investigations in compressed cylinders revealed that the largest amount of cracks is found in the ITZ [68]. There are two main failure types, as stated by *Königsberger et al.*: (a) ITZ-aggregation separation, leading to a clean separation of matrix and aggregate, and (b) ITZ-failure, where a slight cover of cement is visible on the aggregates surface afterwards [69]. It seems that the bond between aggregate and cement paste plays a vital role in these cases. Especially for rough aggregates, typically ITZ-failure is observed.¹⁸ Focusing

¹⁶ It has been indeed shown by fluorescent light micrographs that bulk porosity decreases when more sand is added by simultaneously keeping the total w/c ratio constant [63].

¹⁷ 56 and 81 hours have been tested in [65], respectively [64].

¹⁸ *Guinea et al.* confirmed these findings by preparing aggregates with epoxy or bitumen to purposefully modify the bond strength. They show that bond strength is an important factor

on a single ITZ and not on complete structures, *Zimbelmann* already earlier observed the two mentioned failure mechanism, but related them to the age of the concrete. For young concrete (less than 80 days), ITZ-failure was observed more commonly; for older concretes typically the adhesion within the contact zone was lost [64]. These results indicate a change of the ITZ over time. Further research revealed that, over time, the amount of C-S-H in the ITZ increases, owing to slow chemical changes. Thereby, the ITZ eventually exhibits stronger properties than the bulk paste! Nevertheless, as a matter of fact, the ITZ should be regarded as the dominant limiting structural link of concrete.

Micro cracks and residual stresses Early research by *Hsu* et al. lead to the insight that pristine concrete specimens exhibit a large concentration of initial microcracks, see Figure 3.1. They may be traced back to thermal stresses during hydration and to shrinkage. Considerable heat is produced during hydration and thermal gradients appear in the hardened material. Under such circumstances, not only the substantial disparity of the thermal dilation coefficient between aggregates and cement paste, but also their different stiffnesses cause noticeable stresses. *Shrinkage* may be attributed to the change in moisture content (either due to environmental change or – here more important – self-desiccation), chemical reactions and physical interactions of the hydration products with the pore solution [71]. All these effects contribute to the internal stress distribution in the cement matrix and engender the initiation of visible surface cracks [72], and more importantly microcracks in the ITZ [73]. These should be regarded as a major factor of the limited capability of concrete to carry tensile stresses. Besides initial cracks, the aforementioned effects lead to residual stresses within the concrete [53], which potentially direct crack propagation [72]. Table 3.1 lists the main crack formation sources as given in [62].

for overall strength and failure behavior in three-point bending tests. With increasing bond strength, more particle itself break during loading, whereas debonding was the major failure mode for weak bonds. Weak interfaces have been found to reduce compressive strength to 30% of the normal value [70].

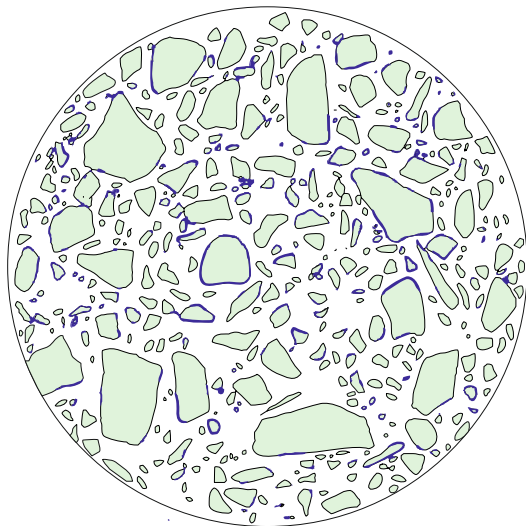


Figure 3.1: Microcrack map of a specimen before loading. Figure redrawn from Figure 2 in [68]. Dark blue bold lines indicate cracks. 12% of the aggregate perimeter is initially cracked.

Stage within strength development	Typical discontinuity
Pouring and compaction	Compaction pores
Fresh concrete	Bleeding cavities
Hardening concrete	Thermal cracks, chemical and capillary shrinkage cracks
Drying concrete	Hygral shrinkage cracks
Loaded concrete	Interfacial cracks, crack growth

Table 3.1: Crack formation at characteristic periods in concretes lifetime, according to [62].

3.2 The general behavior of concrete under loading

Two different aspects contribute mainly to the distinct material response of concrete under stress and strain: On the one hand, the interaction between stiff aggregates and a softer cement matrix leads to local structural effects such as stress concentrations and redistribution. On the other hand, microcracks play a vital role in the behavior. A thesis committed to the fragmentation of concrete is interested mainly in the failure behavior, which will be discussed in the following under the rubrics of loading rate and the most important stress states.

3.2.1 Static loading

Failure under tension

On a macroscopic perspective, the stress-strain curve of a concrete specimen loaded under tension, initially reveals a proportional increase of stress with strain, which becomes nonlinear only shortly before reaching a maximum value, Figure 3.2. This value marks the ultimate tensile load the specimen can bear and the corresponding nominal stress value is known as the tensile strength, f_t . It is reached roughly at 100 microstrain for standard concrete [74]. The initial inclination of the stress-strain path corresponds to the Young's modulus which is roughly around 35 GPa with a Poisson ratio between 0.15 and 0.25. Although f_t is widely taken as a material property, mesostructural effects, such as internal stress distribution, flaws, notches etc. hamper the hypothesis that the measured *macro* stress can be really regarded as a material parameter. Additionally, it has been widely observed that the experimental set up has a tremendous influence on this value.¹⁹ In general, the measured value of f_t is a "system parameter", a combination of material and structural response and esteemed to be lower than the actual material strength [49, 75–77]. Nevertheless, this value is commonly used as material property in design and modeling.

¹⁹ Kühn has shown in detail that the strength values show a significant scatter for different batches, degrees of dryness, specimen geometry and loading conditions [75]. For a discussion of the influence of the load application systems (plates, brushes etc.) see [49].

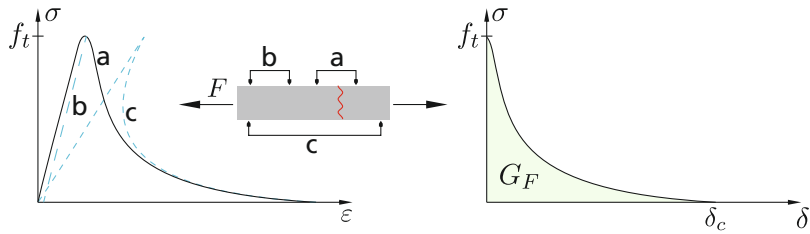


Figure 3.2: Schematic view of the stress-strain diagram under uniaxial tension, following [76].

At peak stress, or even just before, existing microcracks start to grow or to emerge from internal flaws. In some plane of the specimen the limit strength is eventually reached when several growing microcracks have coalesced to one (or more) discernible mesocracks – “geometrical discontinuit[ies] that separate the material” ([78, p. 45]). With further loading this crack grows continually to a macrocrack and eventually separates parts of the specimen.

In the basic understanding, crack growth is fueled in the “fracture process zone” (FPZ), a material region in front of the crack tip with an extension of around three times the maximum aggregate diameter [79]. Here progressive microcrack growth and fusion constantly prolongates the mesocrack towards the macrocrack; refer to Figure 4.2 on Page 63 for a schematic view. All further displacement measured in the specimen appears only in the FPZ – the cracking has “localized”. Whereas a continuing crack opening is measured (for gauge “a” in Figure 3.2), the rest of the specimen is unloaded (gauge “b”). If the experiment is done under displacement controlled conditions, one observes for increased displacements still the ability of the specimen to carry a diminishing load. This gradual loss of the mechanical resistance is marked by a decrease in the stress-strain diagram. It is labeled “tensile-softening” [80] and is a characteristic for concrete and comparable quasi-brittle materials. It can be related to the aggregate structure and mesoscopic crack patterns. Stress is transferred in this post-peak branch by friction between crack surfaces, aggregate interlocking, debonding and crack bridging [70, 72, 74]. Due to the fact that the post-peak branch is actually not a strain, but a crack opening which occurs only in a specific, local zone, it seems appropriate to handle this branch uniquely as a stress-crack opening displacement relation, see Figure 3.2, right. The crack opening, δ , is defined as

the total deformation minus the elastic portion.²⁰ The area below this curve is the energy dissipated during cracking and labeled appropriately as “fracture energy”. It is defined as the required quantity of energy necessary to generate one unit area of a continuous crack [81]:

$$G_F = \int_0^{\delta_c} \sigma d\delta \quad (3.1)$$

It has been observed that cracks propagate mainly around aggregates and group of aggregates. This explains the fact that the fracture energy increases with increasing aggregate diameter – the cracking is more tortuous. Interlocking and tilting of crack surfaces is more pronounced and more energy is dissipated [49].

Meanwhile, experimental findings by *van Mier* question the above described hypothesis of the crack growth in the FPZ [72]. Although the existence of microcracks has been indirectly measured in rock by acoustic emission technique, the dictum of a “cloud of microcracks” in front of stress-free cracks appears to be only partially correct. Instead, a more refined model includes a “bridging zone” between the original FPZ and the stress-free macrocrack. The actual crack process seems then to be best described by three stages:

1. growth of larger, isolated mesocracks in the vicinity of large aggregates, nurtured by local fracture process zones. It is this stage in which the most energy is released and which leads to the initial drastic drop in the $\sigma - \delta$ -curve.
2. growth of a continuous crack structure – the bridging zone – which consists of several (macro)cracks, which partly overlap, branch, combine, shield or are bridged. Planes of cracks branching off the main (final) fracture plane, have been experimentally observed, e.g., [82, 83].
3. failure of the crack interface grain bridges leads to “stress-free” macrocracks.

As a major implication, one has to maintain that localization occurs not in one direction, but is a complex three-dimensional phenomenon.

The fracture energy has become a vital parameter in the modeling of concretes failure. Again, this parameter is a mixed property of structural and material response and shows a large scatter. Furthermore, the maximum crack opening is

²⁰ For the more general case, δ is the accumulated crack opening displacement of all cracks within the fracture process zone [81].

more or less independent of the aggregate size, but in general difficult to obtain. Values between 400 and 500 μm for normal concrete have been measured [74]. Since the maximum crack displacement defines the fracture energy, this value depends to a noticeable amount on the assumptions of the experimenter and is consequently not directly comparable. Nonetheless, *Bažant* et al. compiled the results from a large number of published data. The mean value of 112 N/m fits well in the interval of 65 to 200 N/m mentioned in [74].

Failure under compression

Under uniaxial compression, in general a similar macroscopic behavior is observed as under tension, albeit with some noteworthy differences. A linear increase of stress with strain is observed only up to approximately 30 % of the limit load [87] with a Young's modulus more or less equal to tension [74]. After reaching this load level, especially the initial bond cracks evolve and propagate in a stable manner. Between 70 and 90 % matrix cracks develop. They bridge mainly between large aggregates and connect bond cracks. Besides further propagation, cracks may be even arrested if they run into zones with higher strength or less stress. For more than roughly 90 % ultimate load, unstable crack propagation occurs. From this point on, an increasing nonlinearity is measured up to the

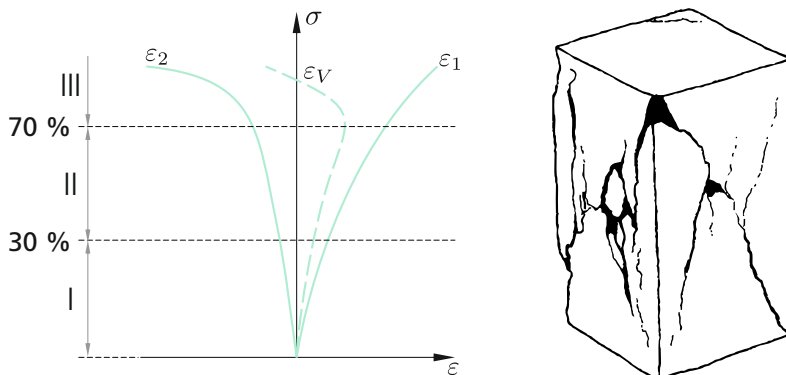


Figure 3.3: Evolution of strains under uniaxial strain, according to [85]. Right: Crack pattern in a 200 mm long specimen with frictional constraint (redrawn from Figure 6 in [86]).

peak from which a softening branch deploys, but less steep than under tension. Localization occurs frequently at several inclined cracks, not only one. The peak value in the stress-strain diagram is denoted as compressive strength, f_c .

With regard to the strains, an interesting phenomenon is observed, namely the dilation²¹ of the volumetric strain at some point, which has been identified as the onset of unstable crack propagation. Figure 3.3 shows a typical stress-strain diagram for a specimen loaded under uniaxial compression. In the first stages the total volume is reduced, whereas the lateral strain ε_2 suddenly increases. The resulting growth of volume – with Poisson's ratios around 0.5 – is ascribed to the onset of the development of the matrix cracks [68].

While the micromechanics under global tensile stress are relatively easy to understand, they are much more complicated under compression. Since macroscopical surface splitting and inclined shear planes occur as typical failure modes (Figure 3.3, right) and shear cones are retrieved if the specimen is manually disintegrated after testing [80], the existence of mode II cracking was postulated. However, this issue (and even more mode III) is strongly debated and there are cogent indicators that mode I cracking is the main failure mechanism in all cases, as discussed thoroughly in [72] and [89]. Indeed, attempts to achieve states of pure shear have failed, since as soon as slight tension is present, cracking is dominated by tensile cracks. Moreover, several hypothesis recurring to complex stress fields as a result of the heterogeneous microstructure, are able to explain a predominance of mode I failure, even in mixed-mode loading. E.g., Figure 3.4 shows the theoretical model developed by *Vile* [90]. Below and above an aggregate in loading direction, a zone of triaxial confinement emerges due to the different stiffness properties. The softer matrix “flows” around these conical zones and shear planes develop. But on an even smaller scale these shear planes have been identified as arrays of very small mode I cracks, which weaken the mortar matrix [91]. Subsequently, “shear fracture” along the oblique array path occurs as a secondary effect. Stepping back one length scale, the structural interplay of matrix and aggregates promotes again mode I cracking, as Figure 3.5 highlights. The stiffer aggregates transfer the load F to slightly displaced particles. As a result, tensile stresses develop in the matrix between these particles if the movement of the lower aggregates is not impeded by lateral confinement (i.e. $P = 0$ in Figure 3.5).

²¹ Although the term dilation is in most cases used synonymously with volumetric strain, it should be – to the opinion of some – reserved to the cause of increased volumetric strain, namely the approaching and eventually rolling over of aggregates [88].

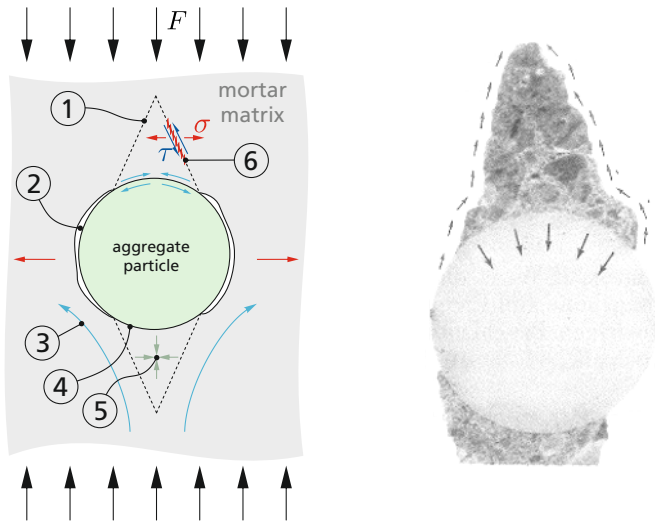


Figure 3.4: Left: Failure mechanism model for a single stiff aggregate particle embedded in a soft cement matrix under compressive load, after [90, 92]. (1) potential “shear” plane; (2) broken bond, either due to stress or initial microcracks; (3) “flow” of soft mortar past hard particle; (4) bond intact, mortar restrained by aggregate texture; (5) triaxial compression due to mismatch of Poisson’s ratio; (6) array of mode I cracks. Right: Experimental confirmation with steatite spheres by Stroeven [93, p. 469].

Multiaxial stress states

With regard to multiaxial stresses, it is obvious that a lateral force on the particles in Figure 3.5 has a positive impact on strength. It hampers the movement of the particles and thereby constraints the amount of tensile stresses in the matrix. If cracks are already present, the lateral confinement increases the frictional resistance against sliding crack surfaces and promotes aggregate interlocking [80]. Indeed, a considerable amount of test data clearly show an increased strength of concrete under confinement. Even if only small lateral pressure is applied, the stress approaches a constant value after a certain degree of softening. With increasing confinement, the softening part diminishes and the stress-strain curve exhibits characteristics of a plastic, i.e. ductile, material behavior. This phenomenon has been labeled “brittle-to-ductile-transition” and is an important

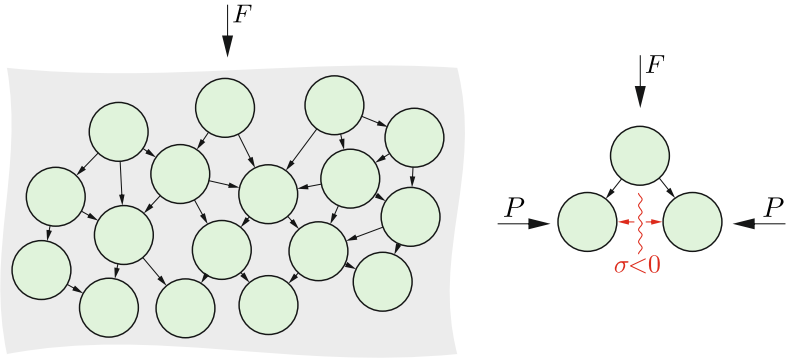


Figure 3.5: Left: Effect of particle stacking in concrete under compression. Right: Exerting confining pressures leads to a higher load-bearing capacity due to compressive stresses in the cement paste. (Both sketches after [49]).

aspect when considering high dynamic loading. Shock waves generally lead to very high pressures in the material and therefore to a completely different mechanical behavior of concrete than in unconfined states. For ease of discussion, let \hat{p} denote the normalized confining pressure, $\hat{p} = p/f_c$. Then the transition occurs in the interval of $\hat{p} = 0.6 \dots 1.5$ [94–96]. In combination, the failure pattern changes. Already for low confinements the number of cracks reduce drastically to “well individualized, open fractures” [95, 96]. For increasing confinement ($\hat{p} \approx 0.7$), the cracking is smeared, cracks less opened and slightly stronger inclined, whereas for higher confinement no visible mechanical damage was observable in the tests of *Jamet et al.* [96]. In this state diffuse microcracking is spread throughout the specimen. Obviously the cement matrix has lost its cohesive capabilities and disintegrates easily [97]; the material state resembles a powder with embedded (but debonded) larger aggregate particles. Not only for compressive, but likewise for tensile dominated states the “brittle-to-ductile” transition is observable [98].

Concerning the highest regime of confining pressures up to and more than 400 MPa – which can be achieved only by a few machines world-wide – discrepancies in the results of different working groups are discernible. Whereas a strength increase is observable even for high pressures in references [99] and [100], *Williams et al.* maintain that above $\hat{p} \approx 11.5$ a limit stress is achieved and no further increase visible beyond. With their own words, the material “is

approaching full saturation after which the strength remains essentially constant with increases in confining pressure. [...] Concrete will not continue to gain strength with increasing pressure when all of the air porosity in the concrete has been crushed out, i.e., when void closure is reached.” ([101, p. 17]) Currently, it is not clear how the discrepancy can be explained and it is perhaps a sagacious position to ignore this fact for now with the comment that this thesis is more interested in tensile stress states under low confinement.

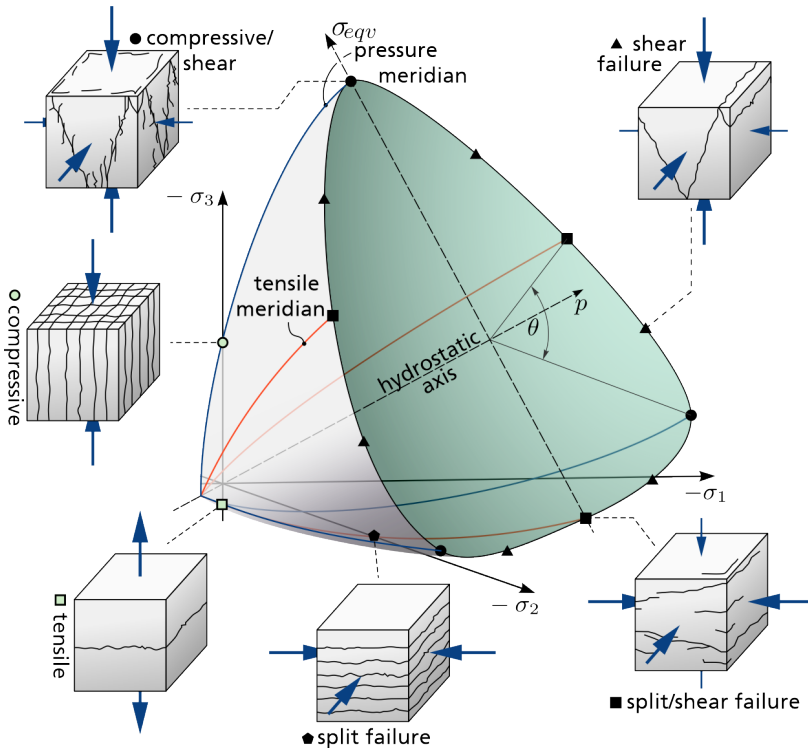


Figure 3.6: Schematic failure surface of concrete in the principal stress space together with typical failure modes and crack patterns under specific stress states. Figure redrawn from [102].

As an important stress state, especially hydrostatic compression has received considerable attention. Hydrostatic compression tests produce important data

for direct use in equation of states. Here, the results of *Poinard et al.* [97] shall be reviewed as representative for similar investigations, cited already above. Their tests show a strong nonlinear stress-strain path with three stages during hydrostatic compression, indicated by the development of the bulk modulus of the loading/unloading branches:

1. Elastic regime: Up to the elastic limit, \hat{p}_{el} , the behavior is dominated by the cement matrix and remains elastic.
2. “Crush-regime”²²: Reaching the elastic limit²³, a strong decrease of the tangential bulk modulus can be observed up to a certain second transition point, \hat{p}_{por} . Within this loading regime, i.e. $\hat{p}_{el} < \hat{p} < \hat{p}_{por}$, pores are irreversibly compressed and extensive microcracking of the cement matrix occurs.
3. Densified regime: If \hat{p}_{por} is reached, the stiffness again increases. This pressure marks the complete closure of voids. The material's internal structure is destroyed and it behaves as a granular stacking arrangement which densifies under external pressure.²⁴ Note that this point is hardly visible directly in the pressure-volumetric strain diagram, which exhibits a continuous increase in the tangential bulk modulus.

Numerical values for the transition points differ between tests and concretes, but may be – considering additionally the high-quality results of [101] and oedometer tests of mortar mentioned in [104] – given in the following range: $\hat{p}_{el} \approx 2/3 \dots 1$ (confirming the earliest reported value of 0.6 in [98]) and \hat{p}_{por} ranging between $\hat{p}_{por} \approx 5 \dots 9$.

Figure 3.6 schematically shows a failure envelope of concrete together with simplistic fracture patterns under different stress states.

3.2.2 Dynamic loading

It has been observed early that the behavior of concrete materials depends strongly on the rate of the applied load. While the effect on the elastic properties

²² Term from *Williams et al.* [101].

²³ While this point is distinct in the pressure-compression plots of some test results, e.g., [103, 104], it is less sharp in other tests.

²⁴ *Bažant et al.* give a different – or maybe supplementing – physical reasoning: Stage three is there assumed to be determined by closing of capillary voids [103].

(e.g., Young's modulus) is only moderate, the strength values, especially f_t , show a drastic increase under higher strain rates. Meanwhile a large body of test results exist, which undermine this fact. Commonly, this strength increase is expressed by the so-called "dynamic increase factor" (DIF), the ratio of the apparent dynamic strength to the quasi-static value:

$$DIF = \frac{f_{dyn}}{f_{stat}} \quad (3.2)$$

Figure 3.7 shows the available test data for DIF_t (tension) and DIF_c (compression) from literature.

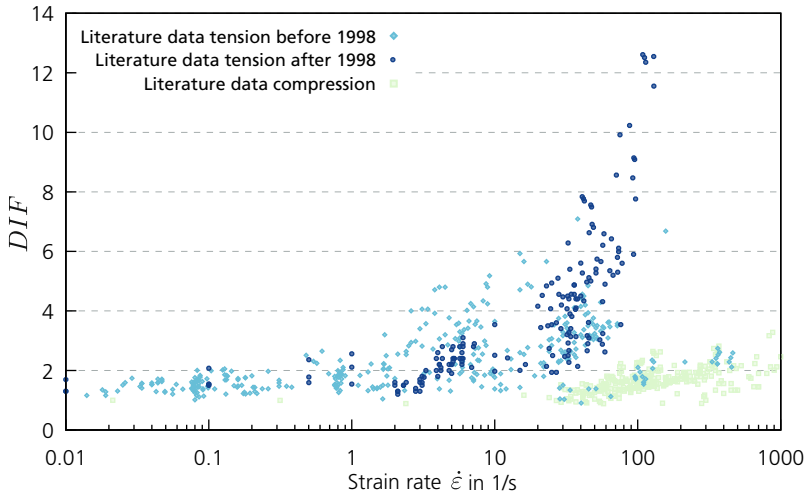


Figure 3.7: Dynamic increase factor for tension and compression. See Appendix A.4 for an enlarged figure with distinct symbols and literature sources.

While it is out of question that a strength enhancement is observed, it is still debated what its origin is. Is the strength increase an inherent material property? A system property, i.e. a combination of material and structural property, or even simply a pure artifact of the testing set-up? Explanations and reasoning for all views exist abundantly; most researchers take either the first or the second position. No efforts will be made to wade into the full scope of literature on this subject, but some major findings and interpretations should be given in the following paragraphs.

There are several effects that have been brought into play. They may be broadly distinguished into thermo-activated, viscous, and structural/inertial effects [105]. In the case of compressive tests, almost all researchers now accept a structural effect due to inertia confinement – the transition from uniaxial stress to uniaxial strain state, as brought forth by *Bischoff* et al. [106]. Due to inertia, a rapid radial extension is hampered by the Poisson effect. In turn, a hydrostatic pressure emerges around the core of the specimen, thereby effectually increasing its strength. Experiments with different geometric ratios and even hollow specimens confirmed the importance of these effects [107]. Additionally, frictional constraints between specimen and testing set-up may be a further source of confinement [108], as already known from static tests [49]. Recently, numerical investigations have been used to posit that volumetric plastic strains constrain emerging shear bands, thereby hindering the propagation and delaying failure [88].

While these effects are to be expected under compressive failure, they are not able to fully explain the strength increase in tensile mode. One major, but still poorly understood rubric, classified above as thermodynamic effects, concerns the role of microcracking. E.g., *Lu* et al. allege this to be the major factor and argue boldly for an intrinsic material property [109]. Their position is supported by several aspects brought up in literature, featuring the role of micro cracking:

- Failure occurs no longer at the “weakest link”. Instead, higher rates tend to produce a more even stress distribution in the specimen and to reduce stress intensities around micro defects [75, 110]. Overall, a strength value corresponding to the average strength of the specimen is measured [75, 111].
- Cracks propagate through stronger aggregates since the crack surfaces exhibit a higher momentum if loaded faster [112]. This effect explains why the strain rate effect is less pronounced in higher strength concrete, due to the smaller difference between strength values of aggregates and matrix.
- *Reinhardt* et al. argued on the basis of a linear elastic fracture mechanic model of a simplified cracking process that the energy supply to the crack processing eventually is too high to be absorbed, promoting an equilibrium around the crack tip. Energy is stored there as kinetic and deformation energy and changes the stress distribution. This concept further explains the difference between observed maximum crack propagation velocity and its theoretical limit. But if the crack propagation velocity is limited, the stress in the surrounding material further increases and additional cracks

are activated, or existing cracks branch more often²⁵ and leave a more tortuous crack surface [116].²⁶

Finally, since its first suggestion by *Rossi* [120, 121], the role of moisture has been widely acknowledged to constitute a viscous effect. Experimentally shown by *Reinhardt* et al. [122], and later by *Ross* et al. [123], *Rossi* referred to the “Stefan effect” as a qualitative explanation for the different strength enhancement of wet and dry samples. If two plates with a fluid film between are pulled apart, a reaction force proportional to the pull velocity will emerge. It is argued that free and adsorbed water within the pores behave similarly. This effect might explain why the *DIF* is less pronounced in concretes with higher strength, since the *w/c* ratio of such mixes is generally lower than in ordinary concrete. As a second argument, *Rossi* pointed to the increased occurrence of intergranular failure. Since the aggregates cannot be strengthened by the Stefan effect (due to absence of water), the difference in apparent strength between matrix and aggregates is reduced. The effect should (a) delay the creation and propagation of microcracks and (b) counter the advancement of macrocracks after localization. It seems, however, that the influence of moisture is restricted to a strain rate regime $\dot{\epsilon} < 1.0 \text{ 1/s}$ [124].²⁷

There might be further effects stemming from concretes micro structure, not yet understood, or even investigated intensively. Some results demonstrate a correlation between the material's porosity and the *DIF*, respectively energy absorption [126]. *Mayercsik* et al. conjecture that collapsing pores bring forth internal contact surfaces and a temporal change of stiffness. Even air flow in and between pores may play a role [127]. Other findings indicate an influence on the

²⁵ Replicated bifurcation of the main crack into multiple small microcracks along propagation has been shown to explain the apparent fracture energy increase in PMMA [114, 115] and might be a contributive factor for concrete as well, though much more difficult to prove experimentally.

²⁶ E.g., *Grote* et al. compared the behavior of cement paste, mortar and concrete and found that the strength enhancement of mortar is less than that of concrete, most likely due to the absence of aggregates. They have a “reinforcing” effect on concrete [117]. Numerically this finding was confirmed by mesoscale simulations of *Chen* et al. [118] and *Song* et al. [119]. The latter authors showed that the phase stresses in the aggregates increase considerably with strain rate, which – in their opinion – constitutes an inertia independent strength increase contribution.

²⁷ Relating to the humidity of concrete, *Cadoni* et al. refer to differences in stress wave propagation. In dry concrete, stress waves might be reflected at defects; multiple reflections then might increase the overall stress state, whereas the wave propagates with less interference in a wet specimen [125]. Although physical and inventive, this hypothesis has not been supported so far by other researchers.

DIF by the aggregate type used [128], but there is still much research to do before coming to firm conclusions.²⁸

Furthermore, some of the scatter of the data (Figure 3.7) may be well explained by the fact that measurement or derivation of the strain rate is quite delicate. Differing definitions, gauge positions, and approaches lead to noticeable disagreement between results [138]. Additionally, the rate of the assumed quasi-static strength differs among authors by several magnitudes [106] – not to mention the nonidentical experimental set-ups. *Kühn*, who devoted a considerable amount of work in a unique analysis of the Split-Hopkinson-Bar (SHB) test set-up, goes a step further and advocates the position, that the strength increase is purely a phenomenon evoked by the experimental set-up and inapplicable assumptions for evaluation.²⁹ Although surely an extreme position, he was able to show that alone by different evaluation methods, measurement errors, filtering of raw data etc. gross differences in the final values emerge. He insists that the different techniques used by the different groups make a direct comparison impossible. It is surely important to keep in mind that almost all tensile tests of concrete are *indirect* tests, relying sometimes on simple theoretical concepts. And though the work of *Forquin* et al. does not endorse the extreme view of *Kühn*, it puts

²⁸ The quantitative contributions of the different effects are likewise unresolved. E.g., *Grote* et al. assign roughly 60 % of rate enhancement to the effect of hydrostatic pressure and only 40 % to an intrinsic material property, whereas *Cotsovos* et al. vote for *purely* inertial effects [117, 129]. Others again insist that only the second, steeper increase of the *DIF* should be explained by structural reasons, e.g., [130]. Similarly doubtful is the strain rate range in which each effect should be dominant. As a limit rate beyond that inertial effects become dominant in pressure tests, *Cusatis*, as well as *Gary* et al., sets the limit already at 10 1/s, while *Bischoff* et al. mentions 30 and *Guo* et al. 40 1/s [106, 131–133]. Agreeing with most researchers that the unifying explanation for the rate enhancement is lateral confinement, *Flores-Johnson* et al. maintain it is responsible for the sharp increase only, and not relevant below rates of 100 1/s [108]. However, this pronounced limit – again – is located differently. For tension, *Malvar* et al., as well as *Levi-Hevroni* et al. define the transition point at 1/s, *Ross* et al. at 5 and the CEB bulletin at 30 1/s [123, 134–136], whereas in [137] two transition points are defined. Likewise, for compression, the CEB bulletin follows *Bischoff* et al. with the already mentioned 30 1/s, while [123] determines 60 1/s [123].

²⁹ In his words: “Der Autor [...] geht dabei davon aus, dass der klassische Dehnrateneffekt eine rein strukturelle Eigenschaft ist, die nichts mit einer stofflichen Kenngröße zu tun hat.” ([75, p. i]) and “Der Autor vermutet die Hauptursachen des vermeintlichen Dehnrateneffektes in diesem Wechselspiel aus Prüftechnik und Prüfobjekt und der zu starken Vereinfachung bei den den meisten Auswertemethoden zugrunde gelegten Annahmen. Die Folgen der lokalen Trägheit und der inhomogenen Spannungsverteilung können in den meisten Fällen nicht abgeschätzt werden. Dies beginnt bereits bei der korrekten Ermittlung statischer Kennwerte und verschärft sich mit zunehmender Prüfgeschwindigkeit. Die Ergebnisse sind entsprechend kritisch zu hinterfragen.” (p. 28)

likewise the validity of the standard evaluation of SHB results in question [138].³⁰ Consequently, the DIF_t seems to be generally overestimated.³¹ Indeed, it seems to be unnoticed in current literature that the DIF_t data compilation features a group of more recent data – indicated in the figure as dark blue dots – pointing to higher DIF_t than data before 1998. The newer data have been all generated by SHB set-ups, being the only technique available for this strain rate regime [87]. This observation nurtures further the assumption that the DIF_t is (at least partly) a system-property, depending on the complete experimental set-up – not only on the testing device, but surely as well on specimen size and shape [107, 140], hence obscuring the material property (if any).

Numerical analysis is certainly a possibility to gain more insight into the issue. But again, no clear picture emerges. If the strength increase is not a material property, a rate-independent model should be able to replicate experimental results sufficiently accurate. That this is the case is claimed by some for compressive SHB tests, e.g., in [108, 139, 141]. For tensile loading, results seem to preponderate, which indicate that rate dependency should be modeled as part of the constitutive model, e.g., [142–144]. Consensus exists at least to reckon the moderate strain rate enhancement below $\dot{\epsilon} \approx 1$ 1/s as a material inherent “rate sensitivity”, e.g., [131, 145, 146]. But it is very difficult, if not impossible, to come to a resolute conclusion. Modeling approaches, material model types and idealizations are too different to be compared one by one. As the only certainty currently one may hold that much more research has to be focused on this topic until the issue is finally settled. For now it can be summarized that it is important to validate ones own simulation models with experimental data. If the increase is observed in the results, it may be of lesser significance why.

Besides the strength increase, the evolution of the failure strain and fracture energy with strain rate is of importance for modeling fragmentation. While it seems that an increase of failure strain up to at least 50 % is probable [147] (some works indicate even a 3.5 fold increase [110]), comprehensive data is rare and not in unison [148]. Refer to [75] for further discussion and relevant references.

³⁰ The basic assumptions are: (a) linear acoustic approximation of waves, (b) linear elastic material up to the point of spallation, (c) velocity rebound, measured as rear free surface velocity, is generated by one single spall plane only. *Forquin* et al. furnish evidence that all three assumptions are violated to some degree.

³¹ Similar arguments for the compressive tests have been risen by *Song* et al. They showed with numerical analysis that the specimens exhibit a strong nonuniform stress and strain field for high strain rates (beyond 100 1/s). The standard evaluation process hence overestimates the DIF_c for this rate regime [139].

Regarding the increase of fracture energy, the available data will be presented and briefly discussed in Section 4.2.3 on Page 81. Concerning the cracking and fragmentation behavior, the experimental observations are clear. Increasing the strain rate, cracking becomes much more diffuse, cracks branch more frequently and the number of fragments aggrandizes considerably, see, e.g., [105, 149].

3.3 Modeling concrete

Having the complex micro structure and the different aspects of its mechanical behavior now on the page, it should be obvious that a comprehensive mathematical description, likewise suited for all load cases and applications, is extremely difficult – if not impossible. But with more specific situations in view, the macroscopic failure behavior of concrete can admittedly be modeled with remarkable success. Driven by the increasing computational power, rigorous formulations for numerical plasticity, and the growing field of continuous damage mechanics, a plethora of concrete material models emerged – mainly between 1980 and 2000. Starting with very simple descriptions, the models evolve more and more into sophisticated descriptions able to capture the necessary effects to even model the behavior under high dynamic loading.

Most models may be classified as *phenomenological*, which means that they try to reproduce the material behavior observed on the macroscale by suitable mathematical descriptions of state variables.³² Although powerful in many applications and (principally) accessible in their formulation, the choice, and parametrization of the state variables remains always subjective, a concern aptly expressed by Souza Neto et al.: “[D]ue to the difficulty involved in the identification of the underlying dissipative mechanisms, the choice of the appropriate set of internal variables is somewhat subtle and tends to be biased by the preferences and background of the investigator.” ([28, p.75])

Indeed, many models share similarities and use only different mathematical functions to fit the same observations. They lack in general fundamental micromechanical considerations. To cite two further important researchers in the

³² To mention just a few examples with focus (but not limited) to dynamic application: plasticity models: [104, 150–155], continuum damage models: [133, 156–160]. Since newer models tend to combine aspects from both descriptions, drawing a neat line between plasticity and continuum damage models is often hardly possible.

field: “[C]onstitutive models for concrete have been predominantly phenomenological in nature, rather than being based directly on first principles of mechanics. The feeling is gradually growing strong, however, that this situation is not ideal.” ([161, p. 67]) And: “[A]t present, this approach has probably entered a period of diminishing returns, in which a great effort yields only minor and insufficient improvements to the constitutive model. [...] Lacking a complete micromechanical model, one must partly rely on intuitive understanding of the physical mechanism involved. To a large extent, this is an art.” ([162, pp. 944, 947])

In order to consider micromechanical mechanisms inherently, the last decades have witnessed the raise of multiscale methods. While there are different motivations to apply multiscale techniques, one major advantage is the discrete resolution of different phases of the material and thereby explicitly modeling the interaction of the phases. As one of the pioneers in this field expresses: “the physics is *inherently* multiscale; that is the different scales interact strongly to produce the observed behavior” ([163, p. 2391]). Thus, instead of simply fitting chosen experiments, multiscale methods are powerful tools to deliver a more accurate and realistic behavior. *van Mier* et al. already 2002 forecast: “It would be no surprise if future development of such tools leads to an approach where large-scale concrete structures, at least critical components of such structures, are analyzed directly at the particle level.” ([164, p.245])

There have been analytical attempts to formulate closed models based on micromechanical considerations³³, but the fact that such models for concrete are rare, reflects the enormous challenges which come along with such an approach. A more widely embraced route is numerical multiscale approaches. Complex macroscopic models are replaced by a full resolution of a lower material level with less sophisticated material models. By the explicit consideration of different constituents, phenomena due to the interaction of the phases are resolved directly and have no longer been somehow considered in an analytical expression. Of course, the achieved simplification on the material level is bought by a strong increase in computational efforts and it can be maintained with some boldness

³³ The first who attempt to formulate a micromechanical model was *Ortiz* [161]. His model relies on the theory of mixed continua and the insight that an applied force leads to different phase stresses in cement and aggregate. The anisotropic damage model uses compliance tensor of aggregates and matrix as state variables, which describe the amount of microdamage. Similar developments are found later, e.g., in [165]. Indeed, the most successful micromechanical model, the “microplane model” by *Bažant* et al., should be in no case left unmentioned [162]. Even if it is seldom used in engineering practice (presumably due to lack of implementation in relevant commercial codes), several application examples, collecting static and dynamic problems, highlight the quality of the model [149, 166, 167].

that multiscale analyses are always computationally much more expensive than the application of homogenized material models. Besides the actual computational effort to solve the lower scale, the coupling of the scales always introduces a certain overhead in the computation, not to speak about the complexities of combining multiple different material scales.

Being appealing and seemingly simple at first glance, there are considerably different approaches for multiscale analysis concerning two aspects: a) How the lower material scale is resolved and b) how the different scales are numerically combined. The remainder of this chapter and the next one are dedicated to the first aspect with regard to concrete. After reviewing the different approaches in literature, the next chapter details a synthesis of the findings and presents an efficient description of concrete on the mesoscale. Chapter 5 then is dedicated to the second aspect and proposes a formulation of how to combine the meso- and the macroscale.

3.3.1 Relevant material scale

It was early recognized that a detailed and accurate description of concrete has to include the peculiarities of the lower length scales not only by a phenomenological description but by explicitly modeling the major constituents. This approach delivers hence a much more micromechanical orientated description of the behavior and one can expect higher accuracy in spite of utilizing less complex models – although the above-cited quest for “stepwise linear analysis” by *van Mier* et al. is still too optimistic for most applications. For the mechanical behavior of concrete, inclusions (i.e. aggregates), microcracks and pores, are the most important factors. These three elements are sufficiently resolved in the so-called “mesoscale”. As its cognates “micro” and “macro”, the term “meso” stems from classical greek, where the very common word $\mu\epsilon\sigma\sigma\omicron$ simply means “between”. In engineering or material science, the term “mesoscale” usually denotes a specific scale of observation, where the detailed *micro* structure of a material is not yet in view, but simultaneously the consideration of the material as homogeneous on the *macroscale* is no longer sufficient – which is commonly applicable for composite materials. Although the term “first-level microstructure”, used in [168], aptly defines the mesoscale as the first scale below the macroscale, the independent term mesoscale is meanwhile a commonly used terminus technicus

– however with blurred size limits.³⁴ For composite materials, it denotes the scale, where the main ingredients of the composite are discretely resolved, but are itself viewed as homogeneous. Figure 3.8 gives a descriptive overview of the scales and their unique resolved features.

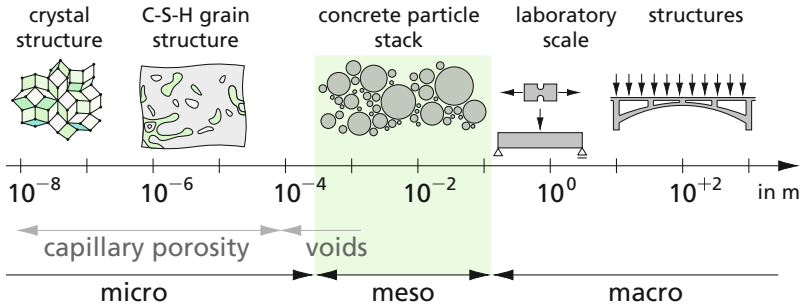


Figure 3.8: Definition of the three size levels of concrete after [62]. The specific sizes, as well as the composition of the figure, have been taken from [49] and [46]. Note that the transition between the three levels is blurred and not as specific as the figure may indicate.

Since the first attempts in the early 1980s, with very coarse meshes, static loading and 2D plane strain assumptions, the computational possibilities have considerably increased and mesomechanical modeling of concrete (and of course

³⁴ To the best knowledge of the author it were Zaitsev et al. who first mentioned the term “meso level” with regard to concrete [169]. They described concrete as a “multi-level hierarchy system” and distinguished between *four* scales: macro-, meso-, micro-, and nanoscale. They defined each scale with regard to the size of a representative volume element (RVE), which sufficiently describes the scale in view. Thus, the macroscale is seen as the scale, where main inhomogeneities, e.g., aggregates are “large”. The corresponding size of the RVE would be around 1×10^{-1} m – four times the dimension of the largest inhomogeneity. On the next smaller scale, the mesoscale, the mortar volume between the large inclusions is in view. A RVE has the size of around 1×10^{-2} m, encompassing fine inclusions, such as aggregate grains. The RVE of the microlevel consists of hardened cement paste and exhibits “big” pores, with a size of up to 1×10^{-4} m as main inclusions. Correspondingly, the RVE size for this level would be around 5×10^{-4} m. Lastly, the nano scale represents the material with capillary pores, with a diameter in the order of magnitude of 1×10^{-7} m. Today this division is no longer used; instead only three scales – macro-, meso- and microscale – are commonly referred to. (At least with respect to the structural behavior. E.g., in [51, 170], reference is still made to four levels, by dividing the micro level into Level I – the crystalline structure of C-S-H with two different properties – and Level II, the C-S-H matrix as shown in Figure 3.8. They have been given in this form by Wittmann already 1983, however, without mentioning specific scale limits [62].)

other materials, such as sandstone [171], and alumina foam [172], to mention just two examples) was used extensively by different researchers and working groups. In almost all cases two (mortar and coarse aggregates) or three (mortar, coarse aggregates, and ITZ) phases are resolved in the models, and until now it seems that further subdivisions into more than these is not necessary [173]. However, besides the actual objectives of the different researchers, the modeling approaches still differ strongly.

In the following an attempt is made to adumbrate what seems to be the most effective way to accurately describe concrete on the mesoscale, considering the main conclusions of other researchers. Although the finite element method is by no way the only option to solve the underlying problem³⁵, it is still the most widely used; definitely one of the most versatile, available, and efficient methods and naturally employed for considering (shock) wave propagation. It is therefore the method of choice in this work. Due to the large number of works, the following overview is by no means exhaustive but should provide the interested reader with a broad picture of the different possibilities, while the next chapter describes the approach taken in this thesis. *Thilakarathna* et al. have reviewed the state of the art of concrete mesoscale modeling up to the year 2020 [187]. Besides the references mentioned in the present work, the reader is referred to further works cited in this exhaustive review paper. Although following basically the same (natural) distinctions as in [187], a slightly different emphasis, additional reasoning, and unmentioned aspects are added in the following review, while trying to be as concise as possible where the reference to [187] suffices.

3.3.2 Geometric representation

The fact that simulating real engineering structures is the final aim, makes modeling in 3D inevitable. Still today some researchers limit their models to two

³⁵ The lattice grid method has been – especially with regard to concrete – applied successfully. In these models, lattice grids – a network of beam elements – approximate the underlying volume. Failure is made possible by simply removing single beams. One of the pioneering works in this context was done by *Schlengen* et al. More sophisticated descriptions have been used later, e.g., in [175–180]. Besides lattice models, models based on the discrete element method (DEM), e.g., [80, 181–184], or related methods, such as the Rigid Body Spring Method [185] and even combinations of DEM and lattice [186], have been successfully used to analyze the failure behavior of concrete. [187] contains a detailed overview and a discussion of unique (dis)advantages.

dimensions, mostly with the assumption of plain strain conditions to reduce computational and modeling efforts, e.g., [188–192], to name only a few. However, there are severe restrictions with regard to structural behavior. Whereas *Häfner* et al. maintained that no significant difference in the case of the effective linear material properties is observable [191], *Hain* et al. directly compared the homogenized elastic properties of hardened cement paste obtained from 2D and 3D simulations. Their findings indicate that only the 3D representation of the micro structure yields valid results [193]. Surely stress states with reference to the third axes, as failure under biaxial and triaxial stresses, cannot be modeled within a 2D representation [194]. But even in the case of uniaxial stress states, the inability of 2D models to resolve complicated cracking networks entails a potential underestimation of crack density and dissipated fracture energy [195], an effect more pronounced for lower strain rates [144]. Yet in the case of high rates a clear difference was shown in [173] and [196] for the case of compressive loading. Here, the 2D model failed to account appropriately for the lateral inertia confinement and hence wrongly predicted the dynamic increase factor. As mentioned above, localization is not only in one direction, but a three-dimensional phenomenon [49, 76], affirming the remark of *Zohdi* et al. that in case of micro-macro mechanics “three-dimensional simulations are unavoidable for reliable results” ([197, p.6]).

Aggregate shape

As mentioned above, there are mainly two types of aggregates: *gravel/rounded* and *crushed*. Whereas gravel aggregates are smooth and of round shape, crushed ones exhibit sharp edges. Most researchers rely on simple ideal geometric representations of aggregates, see Figure 3.9. For *gravel* stones, spherical aggregates with only one parameter, are the simplest ones to generate and model and are frequently used. More realistic are ellipsoids [190, 191, 198]. This shape is still easy to describe mathematically, but the actual modeling process is more involved since aggregates must not interfere, and contact checks during placing are more complex than in the case of spheres. Even more realistic roundish shapes may be generated by an overlay of spherical harmonic functions or frequency distribution over a radius [188, 199]. *Crushed* aggregates may be resembled by randomly generated polygons [173, 189, 196, 200], or by Voronoi discretizations, as in [142]. Again, the actual complexity lies in the contact search between the aggregates during the filling process, especially in 3D.

In rare cases, aggregates are modeled based on image analysis [201–203]. It seems, however, that there is no real advantage of this complicated process since only 2D slices are processed. Much more realistic models would surely be achieved by CT image processing with 3D models, which is, however, time-consuming, costly, and does not necessarily promise a real advantage. As a final position, *Contrafatto* et al. even refrains from a geometrical representation of the different phases [204]. They simply randomly assign the material properties of the phases to Gauss integration points of their elements. By consideration of the volumetric portions, a realistic distribution of phases is impressed on the mesh. The advantage is that the mesh is very simple and no geometric checks or constraints have to be considered. Hence, the creation is very effective. On the other hand, only “smeared” models can be used and it is hardly possible to track the damage at interfaces of the aggregates/mortar or similar effects.

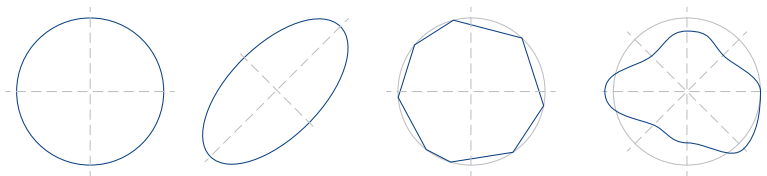


Figure 3.9: Different aggregate shapes for mesomechanical models. From left to right: Spherical, elliptical, polygonal and smooth roundish.

Regarding the effect of the shape on the mechanical behavior, opposite positions can be found abundantly. While it is perspicuous that different shapes *have* an effect³⁶, it is more questionable whether this effect can be quantified satisfactorily. In other words: misrepresent models with simple spherical inclusions the actual failure behavior of concrete? That this might not be the case – at least in confined conditions – is indicated by the experimental results of *Poinard* et al. [205]. Utilizing X-ray pictures of different slices of a specimen after specified loading/unloading cycles, they optically observed the mesostructural changes and quantified the porosity content between two concrete batches. Apart from using round in the first and crushed aggregates in the second, the concrete receipt was identical. No significant differences in the stress-strain response, nor in the optical

³⁶ E.g., the shape influences the mechanical bond and the larger surface of crushed aggregates may affect positively the tensile strength due to an increased area for bonding available [46, p. 125]. The surface itself may influence the bond behavior due to its roughness and finally due to chemical interaction.

investigation of the slice pictures were observed – indicating that the shape of the aggregates does not matter.

Nevertheless, several *numerical* investigations exist and come to different conclusions. E.g., in [206] it is claimed that the aggregate form can significantly change the properties of concrete, however, without further proving this statement; whereas Häfner et al. demonstrated that at least the elastic properties of concrete remain more or less equal – regardless whether elliptic or spherical aggregates are used [191]. In contrast, a better agreement between measured and computed elastic properties for spherical aggregates was reported in [207]. However, both works reveal higher stress concentrations in the surrounding concrete matrix for ellipsoid forms, which indicates an influence of the aggregate shape in crack initiation and damage accumulation. Leite et al. indeed found that elliptical shapes with a ratio of the shortest to the longest axis of $r = 0.75$ yield an increase in fracture toughness when compared to spherical inclusions [175]. They assume that this effect is the result of an interplay between crack path orientation and a potential larger crack surface. The overall strength and the width of the fracture process zone of a specimen was maintained to be only slightly affected by the aggregate shape in [208], whereas the shape of the localization zone depended strongly on it. Kim et al. considered circular, hexagonal, pentagonal, tetragonal, and arbitrary polygonal shapes in two dimensional representative volume elements under tensile loading [209]. While the shape does only marginally influence the ultimate tensile strength – with spherical inclusions delivering the highest values due to the absence of stress concentrations – it significantly affects crack initiation, propagation, and distribution. However, one has to remark that alone the position of aggregates is in reality a pure random factor, and consequently crack patterns and distributions are a less significant parameter than more objective values such as ultimate strength and fracture energy. Actually, the maximum difference in ultimate strength was given by the authors to be only roughly 5 %. Although the authors of [210] as well affirm that the aggregate shape is “crucial” to reproduce three-point bending tests, the differences seem to be even less than 5 %. Indeed, the differences in the reported load deflection curves are well within the expected scatter of different model realizations, as, e.g., shown in [211], and hence do not support this bold statement. Pedersen et al. observed in a dynamic context even no significant difference in the overall stress-strain response of their 2D samples at all. For both, spherical and sharp particles, the same fracture planes were activated and the fracture process zone had almost an identical width. Again in the context of dynamic analysis, Hao et al. refer to the works of [118, 213] and conclude that models with spherical aggregates represent sufficiently accurate experimental

findings [145]. Summarizing this discussion, it seems reasonable and justified to consider only spherical inclusions, thereby simplifying the modeling process considerably – an important point for large 3D domains. Potentially the strength of the specimens is thereby slightly overestimated, but well within acceptable ranges.

Pores

As detailed above on Page 27, the bulk of pores is to be found on concretes microscale and therefore not resolved in mesomechanical models. It is clear that the chosen mesh resolution has a direct impact on the ability to explicitly consider pores or not. But even larger air voids are rarely modeled in literature, although these features may have a significant impact on the material response. An exception is reference [192]. One objective of this study was especially to investigate the influence of the pores concerning energy dissipation and load-bearing capacity. A very fine discretization was necessary to resolve even tiny pores. Further works including pores are [214] and [215]. Both report a strong adverse effect on the tensile strength with increasing porosity. Generally, cracks are attracted by and propagate through pores. One could assert without hesitation that this aspect is more dominant than the effect of different aggregate shapes. On the other side, the consideration of pores is not as easy as it sounds. Pores are generally smaller than aggregates; therefore only a certain amount of pores can be discretized reasonably, as discussed in the next paragraph. Problems may occur if compressive loading is applied and contact algorithms are not robust enough to handle complex interpenetration conditions. In tensile-dominated scenarios, this issue does not emerge and the consideration of pores is definitely a step toward realistic material description and should not be avoided.

Inclusion size

A further issue relates to the size of the smallest inclusion. The term mesolevel is only loosely defined, hence there is no common agreement of how detailed the structure has to be resolved.³⁷ From a mechanical point of view, coarse

³⁷ Even in the textbook of *van Mier* [49], the level is once defined to range from 1×10^{-4} to 1×10^{-2} m, whereas the dissenting range given in Figure 3.8 on Page 48 is shown in Figure 1.3 in the book.

aggregates have the most decisive influence on the composites behavior, since bond cracks start to develop there [68]. They serve as stress concentrators and crack barriers [80]. On the other hand, one might expect an influence of the smaller aggregates as well. Several numerical investigations have been conducted, indicating that one should strive to discretize the smallest inclusions possible.³⁸ In practice, one is limited by an affordable element size, the resulting time step, and computational power. A prominent lower limit of discretized inclusions, therefore, lies around 1 to 3 mm [104, 143, 160, 215, 218], a range, which will be applied here as well.

3.3.3 The role and consideration of the ITZ

The ITZ is the weakest link in the composite concrete. Not only are the strength values lower in this transition region, but – as shown in Figure 3.1 – microcracks prevail here, even before loading. Attempts to include the ITZ properties in a mesomechanical model can be traced down to two approaches: (a) Adding an *element layer* around the aggregates with reduced strength, as done, e.g., in [139, 173, 196, 219] or (b) the use of *cohesive zone elements* or strongly related methods; references are, among others, [142, 189, 198, 201, 220]. Bringing the two ITZ-failure modes back in mind, it is clear that approach (a) is restricted to the

³⁸ E.g., Gangnani et al. analyzed a 2D notched specimen under tension with a varying number of aggregate classes. For each omitted class, the matrix behavior was appropriately homogenized. Furthermore, a differentiation between mortar and concrete was done. In the case of mortar, it was found that the peak strength and fracture energy decreases with decreasing number of particles. For concrete, the peak strength remains constant, but the fracture energy was considerably overestimated. The authors observe that damage is more widely spread since it cannot emerge from the nonexistent small particles, more elements participate in damage (leading to increased fracture energy) and large aggregates promote a more tortuous fracture path. According to their opinion, small particles should consequently be included in the model [216]. Snozzi et al. kept the aggregate content of 2D samples under dynamic tension constant, while changing the size of the aggregates. Under high strain rates, the overall peak strength was slightly higher in case of large aggregates ($\dot{\epsilon} = 1000$ 1/s, difference: $\approx 5\%$) than for lower rates ($\dot{\epsilon} = 10$ 1/s, difference: $\approx 20\%$). For smaller aggregates, propagating cracks are more likely to find a way along ITZ of smaller particles, whereas the crack propagates through the aggregates if large inclusions are present [142]. A statistic model to predict the compressive strength of concrete under consideration of the aggregate grading was developed in [59]. This model shows that an increase in small particles leads in general to higher strength. With regard to homogenized shock properties of a mesomechanical RVE, Riedel showed that the size of the aggregates is no decisive factor [104, 217].

ITZ-failure, while (b) is only capable of modeling the more common ITZ-aggregate separation.

Only a few works are dedicated to investigate the influence of the ITZ in mesomechanical simulations, and again, the findings appear to be indistinct. E.g., *Bernard et al.* claim in [221] that only a slight influence of the ITZ on the compressive strength can be found, a finding supported by [222, 223]. On the other hand, *Hartmann* used the first approach to model concrete specimens under tension and compression. He yields very satisfying results for 2D samples with high resolution and hence a very thin ITZ (0.1 mm). In contrast, the results for much coarser 3D models (ITZ width 0.2 mm) are not very realistic [218]. The effect of the ITZ thickness, strength, and amount of ITZ regions was later investigated more systematically by *Kim et al.* with approach (a). In their study, the ultimate load under quasi-static uniaxial tension was only marginally influenced by the ITZ thickness, slightly more by the number of transition regions in the model³⁹, but heavily by the ITZ strength properties. The thickness range studied was 0.1 to 0.8 mm – indicating that the resolution may not be the main reason for the poor 3D results of *Hartmann*.

A brief comparison between simulation with and without explicit consideration of the ITZ with approach (b) is mentioned in [198]. The authors show that the model with ITZ is better able to reproduce the experimentally observed pre-peak nonlinearity and is in general more ductile than the one without ITZ. *Tu et al.* compared both approaches directly. For tensile loading, they got comparable results, but for compressive loading, the behavior of the model with cohesive zone models was simply faulty. They associated this with the incapability of the cohesive zone elements to capture shear failure under compressive states [219].

From the reviewed works, one might conclude that both approaches yield satisfying results for tensile loading if the parameters are adjusted properly. Thus said, approach (a) with added layers, has the considerable restriction that it is applicable only to very fine and simple meshes, ideally structured ones (see Section 3.3.4). In 3D models with free meshes, such as the complex simulations in [143], it is virtually impossible to achieve an adequate regular mesh layer of realistic thickness. For such models idealization (b) – cohesive zone elements – appears to be a more appropriate and pragmatic choice, simplifying the model generation process considerably.

³⁹ Change of aggregate volume content by 30 % leads to a change of the ultimate strength of approximately 5 %.

One final comment regarding the role of the ITZ should point to a difficulty inherent in both approaches: As *Kim et al.* and others correctly remark: the mechanical properties of the ITZ are simply unknown and difficult to determine [75, 187, 209]. Few attempts have been made to characterize strength values experimentally for use in simulation models (e.g., in [75]) and the uncertainty is still large. Most researchers therefore simply take values that are below the ones for the cement matrix – usually 50 % [219] – but the exact reduction level is unsettled.

3.3.4 Discretization and mesh resolution

A distinction can be drawn between works utilizing a *structured* grid, e.g., [99, 104, 160, 216, 224], to name just a few, and *free* or *aligned* meshes. In the first case, each regular cell/element is filled with a specific material model for either matrix or aggregate. The advantages of this kind of mesh are its simple generation and the very regular shaped elements with equal size. Especially in the context of dynamic simulations with explicit time integration, these meshes deliver stable time steps and are computationally efficient. Depending on the analysis, these qualities may be more important than an accurate depiction of the particle's shape, whose round geometry is projected on the grid and consequently only roughly approximated, see Figure 3.10.

On the other hand, considerable disadvantages exist with this approach: As just mentioned, shapes of inclusions are only coarsely approximated, unless the mesh resolution is very high. As *Dupray et al.* remark, the possibility exists that aggregates occupy neighboring cells if the overall amount is high [99]. Hence, no cement film between the aggregates may be present, which obstructs the sliding of aggregates. Finally, taking the ITZ into account is possible, but limited. Cohesive zone elements are a potential choice, but the stepwise idealization of round corners will lead to alternating opening directions of the cracks. Simply altering the mechanical properties of the first element layer around the aggregates is possible, but overestimates the width of the ITZ in most cases considerably, see the discussion above. Unstructured, free, or aligned meshes may follow the shape of the particles very closely and allow for sufficient space between the particles. Cohesive zone elements to consider the ITZ are oriented normal to the aggregate surface. The use of irregular meshes may even reduce the influence of the discretization on the results, as observed in [176]. However, especially in 3D, the meshing process itself is very demanding and a high number of elements are

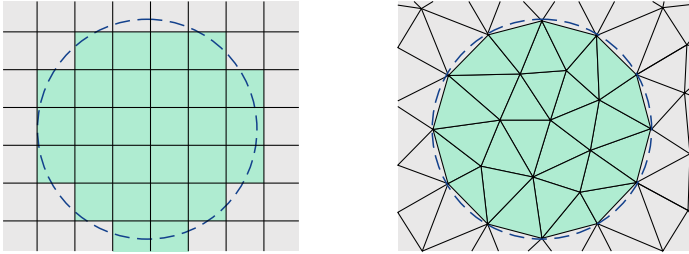


Figure 3.10: The two principal mesh types exemplified for a single spherical particle: structured or grid mesh (left) and free or aligned mesh (right).

likely to be generated for realistic samples. Furthermore, elements with adverse geometries, such as highly skewed or elongated elements, are likely to emerge and the topological structure – the connectivity between nodes and elements – is very complex, with a high number of elements connected to each node. Having the involved models in mind, the approach furthermore necessitates in 3D the use of tetrahedral elements. Since in wave propagation codes only linear shape functions are used, these elements tend to be too stiff. Special precautions must be taken against volumetric locking near the incompressible limit [225].

Several works conduct a convergence study to determine an optimal mesh resolution, e.g., [160, 201, 210, 215]. These studies concordantly report an element edge length between 0.5 and 1 mm as sufficiently small. *Chen et al.* as well as *Wang et al.* even show that for SHB simulations with 4 mm (respectively 2 mm) the force signal is still acceptable, while a qualitative crack pattern demands an edge length of 1 mm [118, 214]. Besides an accurate replication of the damage, even the volume content of the aggregates depends on the mesh size, due to deviation of the meshed aggregate shape from the perfect spherical shape.⁴⁰ As often, a balance has to be found between an appropriate resolution and the available computational power, which dictates an upper bound of the total number of elements, hence the size of the elements in a given model.

⁴⁰ This is noticeable, particularly, for small inclusions, where the diameter is only a little larger than the element edge. Then spherical shapes transform into diamonds during discretization, losing a considerable amount of their volume. In general, the loss of up to 10 % of the intended aggregate volume occurs frequently.

3.4 Concluding choice of a suitable mesomechanical representation

The preceding discussion has highlighted a large number of different options to represent the meso structure of concrete. Trying to find a way that in the end supports the aim of this thesis by capturing cracking and fragmentation under tensile-dominated loading accurately and efficiently, the following approach will be used herein:

- Aggregates are modeled as spherical particles only.
- Aggregates are surrounded by an ITZ that is considered by cohesive zone elements.
- Pores are explicitly modeled.
- The smallest aggregate/pore size depends on the current model but a diameter of less than 2 mm is unreasonable given the aspired minimal element edge length of 1... 1.5 mm to keep computational efforts within limits. Effects of smaller inclusions and defects are considered in the matrix behavior.
- A free mesh is used for a reliable geometric representation of the structural features.

As was found, cracking under mode I is the most prominent mode in the composite concrete, even if the overall applied stress state is not tension. The reason is the structural interplay between hard aggregates and soft matrix, delivering tensile stresses in the mortar. Consequently, the material model for this phase should be able to represent the tensile failure appropriately, while the overall approach should allow a dissection of the initially continuous finite element assembly. The next chapter covers these issues in detail.

4 Development of a robust and efficient mesomechanical modeling approach for fragmentation simulation

The previous chapter has expounded on the structure of concrete, its mechanical behavior, and a suitable mesomechanical modeling paradigm. In the present chapter, an appropriate mathematical description of the material behavior of the involved phases and the actual application of the whole approach is pursued. Starting the discussion on a suitable idealization of inter-matrix failure, a material model for mortar and aggregates is detailed subsequently and chosen application examples complete this first part of the thesis.

Wave propagation codes rely almost exclusively on phenomenological material models based on plasticity, sometimes furnished with a qualitative damage description. One reason may be the historical development. Strength of materials had not been considered in the first algorithms and was added only later as an additional aspect to the equation of state. A different reason may be considerations with regard to computational efficiency. As mentioned in Chapter 2, the computational costs are determined by the number of operations in each cycle. The more complex a material model, the more expensive a single cycle will be. Consequently, many material models are based on a straightforward von Mises yield criterion: while pressure remains constant, the inadmissible deviatoric stress states are simply scaled back to the elastic limit surface [226]. It will be discussed later that this assumption is untenable for brittle materials, and an extension of an existing plasticity model will be presented to be used for the mortar matrix.

The material models and categories mentioned above simulate the macromechanical behavior of concrete as a continuum. Explicitly accounting for cracks is beyond their capabilities, but this feature is necessary to achieve fragmentation.

Before delving into the material modeling, the next section briefly discusses the available options for dissolving the mesh assembly.

4.1 Modeling cracking and fragmentation with FE

The capability to represent discrete cracks is at first beyond the abilities of the finite element method, where the element assembly represents a continuum. However, all models that consider softening may lead in certain loading states to elements which completely “fail”, i.e., which do not exhibit any resistance in unconfined states. Therefore, these elements may be interpreted as finite, cracked material regions. Since the crack is not explicitly represented, the term “smeared crack” is often used, although this term originally designated a specific class of material models.⁴¹ The actual dissolution of the element assemblage can be achieved by removing failed elements. This technique is known as “*erosion*” and is widely used in hydrocode simulations. Originally invented to secure stable time steps by eliminating grossly deformed elements that do not further contribute to the system’s response, this approach has been used already for quasi-fragmentation, e.g., in [24, 145]. Whereas for the sake of stability, geometric strain thresholds are often used as deletion criteria, for these cases more physical-based measures have to be employed. *Chen et al.* used a principal strain threshold to model cracks in mesoscale simulations of spallation experiments [118]; other authors removed elements after dissipation of a defined fracture energy [231].

Surely, simply taking matter out of the model is not a physical mechanism and can be seen only as a rudimentary approximation to cracking. Besides violating the energy conservation (strain energy of eroded elements vanishes), mass conservation may be violated as well if nodal masses are reduced after element deletion or if finally free nodes are removed from the simulation. Additionally, especially under pressure, the stiffness change due to removed volume, may undesirably influence the local behavior. Furthermore, erosion alone is not able to accurately depict aggregate debonding and, finally, it is obvious that the crack

⁴¹ Basic idea of these models was the additive split of the strain state in a strain state of the uncracked bulk material and a strain state of a fictive crack within each element [78, 81, 89, 227, 228], which are related by operator matrices. Due to the frequent occurrence of “stress locking” – the ability of failed elements to transfer stresses due to a mismatch between crack orientation and element alignment [229] – the models did not hold sway. The only current advocating work known to the author is reference [230].

width depends on the element size. If, however, the global aim consists in a simulation that is able to separate an initial continuum to quantify fragments, erosion is, under the assumption of fine discretization and sound material models, a useful approach.

The concept of *embedded discontinuities* should be mentioned here for completeness and to account for the fact that this approach is often mentioned in the context of simulating fracture problems. It consists of enriching the shape functions of standard finite elements by discontinuous contributions, which are then able to account for the discontinuity in the displacement field [232, 233]. The most famous candidate of this technique is the “eXtended Finite Element Method” (XFEM). It is an attractive and interesting option to simulate crack and crack propagation – yet without really separating elements. Furthermore, a demonstration of a large, real-sized 3D problem with this technique is still missing (to the best knowledge of the author). It seems that this method is limited in this context, especially with regard to multiple cracks and severely damaged material regions [115], as common in scenarios under high dynamic loading.

A further, very simple technique used in rare cases is *node splitting*. For example, this technique is available as an option in the commercial code LS-Dyna. Here, each node is connected to one element only; coincident nodes are held together by an artificial constraint, which is released if a certain criterion is reached. Applications can be found, e.g., in [23, 234]. Although easily applicable, the disadvantages preponderate: Once the constraint is set free, all coincident nodes disassemble, leading to very brittle behavior. After release, the nodes no longer receive forces from the surrounding elements and, finally, the number of nodes involved is immense.

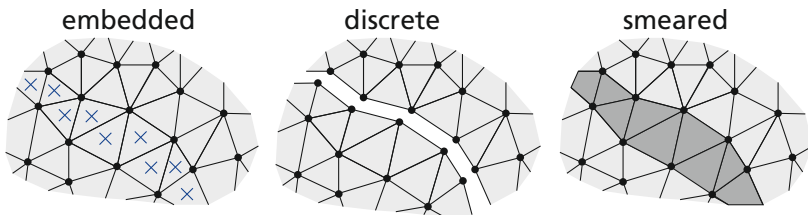


Figure 4.1: Different concepts to model displacement discontinuities with finite elements.

Although in some respects similar, but much more physical and mature, are *cohesive zone* methods. Based on the pioneering work of *Barenblatt* and *Dugdale* [235, 236], they have become the de facto standard for modeling element separation and fragmentation. The principal idea stems from the insight that cracks develop not in a single point, but emerge from a small region. In this zone, the voids grow and damage increases, but there are still ligaments bridging the separating material. In concrete, this zone may be well identified as the fracture process zone, where small aggregates can interlock and contribute to this mechanism. Consequently, stresses are still transferred, although the separation of material has begun. With increasing crack opening, the transferable stress reduces until a critical crack opening is reached and the crack is fully open and hence stress-free, see Figure 4.2. The idea was already applied to concrete at the end of the 1970s by *Hillerborg* et al. [237]. It is therefore also designated as “Hillerborg” or “fictitious crack” model in the context of concrete modeling.

The numerical realization of this idea is based on cohesive zone elements (CZE), whose breakthrough occurred mainly through the works of *Xu* et al., as well as *Camacho* et al. [238–240], although even earlier applied, e.g., in [241]. CZE are a special element type (also known as interface or contact elements), connecting standard continua elements. After activation or insertion of CZE, the corresponding nodes are split, and the nodal forces are determined by a traction-separation law. Using different laws, even sophisticated softening relations can be applied and interaction between the different crack modes established, although elementary traction-separation laws are mostly accurate enough. After a critical crack opening is reached, the CZE is deactivated or deleted, and the formerly connected continuum elements are separated. For the bulk material, an inexpensive linear-elastic model might be sufficient in many cases since damage is explicitly resolved by the CZE. Although cracks can emerge only on the edges/facets of continuum elements and crack propagation direction is thereby slightly limited, the method is a very physical and powerful approach to simulate fracture problems. *Knell* et al., for instance, simulated with CZE the spallation of concrete specimens [143]. While the results exhibit a slightly too brittle behavior, this work impressively demonstrated the principal ability of this approach to model concrete fracture.

On the other hand, the approach is not free of disadvantages:

- The computational effort is considerably. The fracture process zone should be resolved by a sufficient number of CZE, which – depending on the material scale – may result in a very high mesh resolution. *Zhou* et al. recommend two to five elements per cohesive zone [115], which for

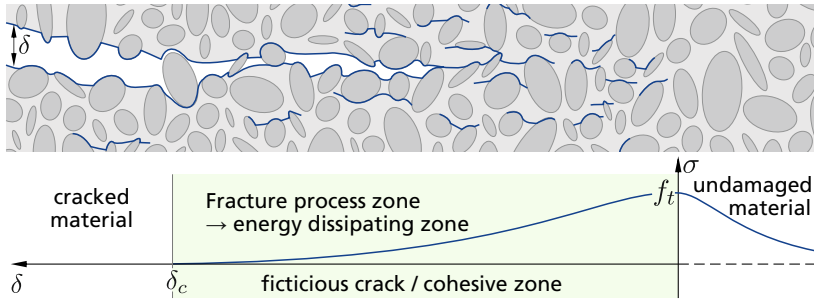


Figure 4.2: General principle of the fictitious crack or cohesive zone model. The crack is formed by coalescing microcracks. Due to aggregate bridging, interlocking, zigzag cracking, and crack branching, stresses are still transferred until a critical crack opening is reached. In the model, these bridging stresses are expressed as tractions on the crack surfaces.

concrete is only a few millimeter long [142]. If the resolution is already very high, e.g., in order to discretize a lower material scale, this disadvantage vanishes.

- There are two ways to implement CZE: Extrinsic elements are inserted dynamically as needed, whereas intrinsic elements are included in the mesh from the beginning at every potential failure locus. Application of extrinsic elements necessitate a new mesh topology and change of data structure after each nodesplit, which can be very complex, expensive and error-prone. Intrinsic elements, on the other hand, increase the total number of elements by a factor of four to six and potentially introduce spurious stiffness irregularities. Furthermore, measures against penetrations in case of compression have to be applied [219].
- Although simple activation criteria for CZE are available and sufficient, the decision on how the neighbored mesh topology should look after a nodesplit is not trivial, especially in 3D. Criteria based on geometric considerations, as, e.g., in [143] and [171], can be used, but lead in case of complex meshes to a dramatic increase of computational efforts and may fail if combined with erosion of surrounding continuum elements.⁴² In the FE models employed here (see Section 4.3), on average, 80 elements

⁴² The criterion searches for intact “paths” via all connected continua elements from one failed facet to the other. If such a path cannot be established because of other failed facets around the node, the node is split. However, the path criterion may fail if eventually some connected elements disappear due to erosion.

are connected to a single node – in rare cases even more than 120. The necessary time for the routines handling mesh reconfiguration after nodesplit and the functions for stabilization increases disproportionately to the number of elements per node. To express it differently: The approach is feasible, but not effective. If, as is the aim of this study, large parts of a concrete structure should be discretized on a lower material scale, then the approaches discussed so far are too costly and simpler ones must be found [231, 242].

- A further issue concerns parallelization of the nodesplit. If nodes of a boundary element of partition \mathcal{P} are split, one has to ensure that the corresponding node in neighboring process $\mathcal{P} + 1$ has to be split in the same manner, i.e. the mesh topology on the partition borders has to conform at all times. Although this is feasible, the necessary synchronization routines are complex and again take additional time.

It might be easily conceivable that these issues will eventually be resolved and more efficient formulations and algorithms be developed, which allow the comprehensive application of CZE for intermatrix failure in the simulation of large concrete structures. Yet, it seems that this is still a vision for the future and the use of CZE should for now be limited to the ITZ. In this case, the disadvantages still hold, but have a highly reduced impact.

Conclusion Massive damage that causes multiple fragments translates from a numerical point of view to dramatic changes in topology in an initially continuous mesh. This is almost irreconcilable with the basic demands of effectiveness, robustness, and accuracy of such a simulation. Especially the last requirement was scrutinized by *Song et al.* in a comparative study of the above-mentioned techniques (schematically shown in Figure 4.1) for a 2D model. The disenchanting result was expressed by the authors: “None of these methods are currently able to accurately predict crack propagation velocities and paths for all of the relatively simple problems that were tackled here.” ([119, p.249]) Especially erosion was commented as follows: “The element deletion method performed especially poorly for crack paths that are not coincident with meshlines. It is somewhat perplexing that this method is widely used in industry and has performed reasonably in predicting the gross features of certain experiments.”

Yet from a pragmatic perspective one has to state – despite the findings of *Song et al.* and all limitations of the approaches – that currently simply no better

methodologies are available which are suited to model complex cracking and fragmentation in larger domains *at all*. It is an undeniable fact that CZE, as well as erosion, have been used in the past successfully to at least give good estimates of crack paths in various contexts and problems. This should not shroud the limitations of these approaches, and certainly calls for scrutinizing the numerical results – but discarding the methods wholly would be similarly misleading. In terms of accuracy and physical legitimacy, the cohesive zone approach should be preferred. In terms of efficiency and robustness, erosion is the technique of choice. With regard to simulation on concretes mesoscale, therefore, a hybrid approach is proposed in which the weak transition zone between matrix and aggregates is modeled by CZE and erosion is used for fragmenting the bulk material. Since the success of erosion relies utterly on the underlying material model, it is important to deploy a suitable and proven description – an issue to which the next section now turns.

4.2 Modeling the bulk material response

A basic motivation to apply multiscale techniques is the potential reduction of the complexity of the material models involved. However, in the case of concrete, this advantage only partly holds. Both main phases, mortar and coarse aggregates, are by themselves materials with complex behavior. Mortar might be perceived as a “low scale concrete”, constituted of a cement matrix and fine inclusions, like sand and voids. Therefore, its material description necessitates again a homogenization step and has to account for the not explicitly modeled phases. Likewise, the aggregates: Although there is a huge variety in natural stones, even crystalline magmatic rocks, such as granite, exhibit many similar phenomena as concrete. It is therefore necessary to model both phases with a suitable description, which respects the basic failure phenomena as detailed in Section 3.2. The benefit arising from modeling concrete on the mesoscale in this context lies mainly in the fact that crack paths can be resolved very realistically and that the interaction of the matrix and aggregates locally influences the stress field.

As mentioned at the beginning of this chapter, plasticity models prevail in wave propagation codes. For concrete, quite a number have been proposed meanwhile. While the pioneering, well-known Drucker-Prager model [150] first described the expansion of the elastic limit surface under pressure influence, most current

models consider additionally the dependence of the limit stress on stress triaxiality, strain rate, and plastic strain, e.g., [153, 154, 159, 243, 244], to give only an arbitrary and easily extendable selection.

In this work, the Riedel-Hiermaier-Thoma (RHT) model is utilized for mortar and for aggregates. This model has been successfully applied to a variety of problems in which concrete is dynamically loaded and has been proven to deliver satisfactory overall results in a wide range of stresses. Nevertheless, it is not free from (legitimate) critique. The model is introduced below, followed by an extension to account for improved brittle material behavior. It should be noted, however, that the aim of this thesis is not to develop or calibrate a perfect mortar material model for mesomechanical simulations. Instead, the global aim is to establish a basic framework for the simulation of debris throw. Although the material model described below will yield satisfying results, some open issues and room for future improvement remain.

4.2.1 Original formulation of the RHT model

The RHT model was developed until 2000 by *Riedel* and published in several articles and a dissertation [104, 217, 245]. Since its implementation as standard concrete model in ANSYS Autodyn, and later as *MAT_273 in LS-Dyna by *Borrvall* et al. [246], it has been extensively used for simulating the macro response of concrete and related geological materials under dynamic loading. A review of applications of the Autodyn implementation has been summarized, for example, in [247]. The formulation of the model was inspired by the Holmquist-Johnson (HJ) model for concrete [155], but elaborates on several distinct aspects not covered in the original HJ model. In the following, the basic ingredients of the RHT model are briefly described, without going into too much detail, which has been done elsewhere, e.g., in [104, 248]. After presenting the original formulation of the model, points of critique are gathered, and improvements are suggested and discussed afterwards.

The basic idea of the RHT strength model is to describe the current yield stress based on two limit envelopes: The failure surface and the residual strength surface. Once the stress exceeds the failure limit, the current yield stress is linearly interpolated between these surfaces through a scalar damage factor stress. Prior to that, a plastic strain measure is used as a scaling variable to describe the

actual yield stress in a hardening regime.⁴³ The model description resorts to the invariants of the stress tensor in terms of pressure p , the second invariant of the deviatoric stress tensor J_2 , and the Lode angle (angle of similarity) θ :

$$p = -\frac{1}{3}tr(\boldsymbol{\sigma}) = -\frac{1}{3}(\sigma_1 + \sigma_2 + \sigma_3) \quad (4.1)$$

$$\sqrt{J_2} = \sqrt{\frac{3}{2}tr(\boldsymbol{s})} = \sigma_{vM} \quad (4.2)$$

$$\cos(3\theta) = 3\sqrt{6} \frac{\det(\boldsymbol{s})}{tr(\boldsymbol{s}^2)^{3/2}} = \frac{27 \det(\boldsymbol{s})}{2\sigma_{vM}^3} \quad (4.3)$$

Failure surface

The maximum distortion stress that the material can withstand is described as a function of pressure p , lode angle θ , and effective strain rate $\dot{\epsilon}_{eff}$:

$$\sigma_f = \sigma_f(p, \theta, \dot{\epsilon}_{eff}) = f_c \hat{\sigma}_f(\hat{p}, F_R(\dot{\epsilon}_{eff}, \hat{p})) R_3(\theta, \hat{p}) \quad (4.4)$$

$\hat{\sigma}_f$ denotes the normalized failure stress, \hat{p} the current normalized pressure; F_R is a strain rate increase factor detailed below, and R_3 the William-Warnke formulation to account for the angle of similarity. Note that the circumflex over a symbol denotes the normalization of the variable by f_c , the uniaxial unconfined cylindrical compressive strength: $\hat{\circ} \equiv \circ / f_c$.

A piecewise definition for $\hat{\sigma}_f$ is applied, interpolating bilinear for pressure below $p = F_R f_c / 3$ and expanding polynomial above:

$$\hat{\sigma}_f(\hat{p}, F_R(\dot{\epsilon}_{eff}, \hat{p})) = \begin{cases} A(\hat{p} - \hat{p}_0)^n & 3\hat{p} \geq F_R \\ \frac{F_R \hat{f}_s}{Q_1} + 3\hat{p} \left(1 - \frac{\hat{f}_s}{Q_1}\right) & F_R > 3\hat{p} \geq 0 \\ \frac{F_R \hat{f}_s}{Q_1} - 3\hat{p} \left(\frac{1}{Q_2} - \frac{\hat{f}_s}{Q_1 f_t}\right) & 0 > 3\hat{p} \geq 3\hat{p}_t \\ 0 & 3\hat{p}_t > 3\hat{p} \end{cases} \quad (4.5)$$

⁴³ Often this is referred to as an interpolation between a virgin elastic limit and the failure surface. However, this notion is strictly speaking not correct, since the operation is a scaling. Yet it is not completely wrong since the scaling factor is derived by interpolating between zero plastic strains and plastic strains at failure.

with $\hat{p}_0 = F_R/3 - (F_R/A)^{(1/n)}$. \hat{f}_s and \hat{f}_t denote the normalized shear and tensile strength, respectively; A and n are material parameters, \hat{p}_t is the normalized failure cutoff pressure, often denoted as Hugoniot tensile limit (HTL). In the original formulation this value is the root \hat{p}_0 of the exponential function used to describe the failure surface for $\hat{p} > F_R/3$. A second option – which has been approached in the LS-Dyna implementation – is to linearly extrapolate the failure surface between shear and tensile strength, by considering the projection on the pressure meridian:

$$\hat{p}_t = \frac{F_R Q_2 \hat{f}_s \hat{f}_t}{3 (Q_1 \hat{f}_t - Q_2 \hat{f}_s)} \quad (4.6)$$

Strength dependence on the stress triaxiality

Values Q_1 and Q_2 in equations (4.5) and (4.6) reflect the influence of the third invariant on the failure stress; namely the fact that concrete can sustain higher deviatoric stresses on the compressive meridian compared to the tensile meridian (see, e.g., [249] and [98]). A suitable scaling factor is described by the William-Warnke formulation in dependence on the Lode angle θ [250]:

$$R_3(\theta, Q(\hat{p})) = \frac{2(1 - Q^2) \cos(\theta) + (2Q - 1) \sqrt{4(1 - Q^2) \cos^2(\theta) + 5Q^2 - 4Q}}{4(1 - Q^2) \cos^2(\theta) + (1 - 2Q)^2} \quad (4.7)$$

for $0 \leq \theta \leq 60$. R_3 depends on \hat{p} to reflect the brittle-to-ductile transition (see Page 36):

$$0.5 < Q = Q(\hat{p}) = Q_0 + B\hat{p} \leq 1 \quad (4.8)$$

Q_1 and Q_2 have values $Q_1 = R_3(\pi/6)$ for the shear meridian and $Q_2 = R_3(0) = Q(\hat{p})$ for the tensile meridian. Q_0 and B are parameters derived experimentally.

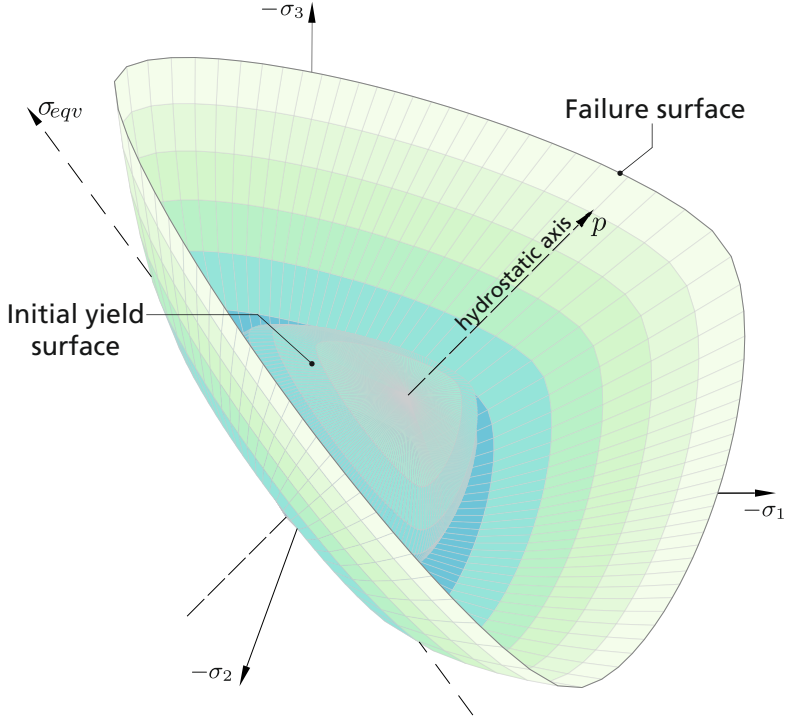


Figure 4.3: Failure surface of the RHT model and virgin elastic limit ($\epsilon_{pl}^* = 0$, "Initial yield surface").

Strain rate dependency

Strain-rate enhancement is considered by the factor F_R :

$$F_R(\dot{\epsilon}_{eff}, \hat{p}) = \begin{cases} F_R^c & 3\hat{p} \geq F_R^c \\ F_R^c - \frac{3\hat{p} - F_R^c}{F_R^c + F_R^t f_t} (F_R^t - F_R^c) & F_R^c > 3\hat{p} \geq -F_R^t \hat{f}_t \\ F_R^t & -F_R^t \hat{f}_t > 3\hat{p} \end{cases} \quad (4.9)$$

Superscripts 'c' and 't' stand for compression and tension and $F_R^{c,t}(\dot{\epsilon}_{eff}, \hat{p})$ can be defined following different suggestions. In the original formulation, the form of the CEB Bulletin 187 [251] was used, but meanwhile a large number of different fit functions have been proposed (reference [109] contains an exhaustive overview). In the simulations documented herein, the compressive function of the CEB Bulletin and the tensile fit of *Malvar* et al. are applied [134]. The functions are detailed in Appendix A.4. Note that in the implementation, the increase in $\dot{\epsilon}_{eff}$ between two cycles is limited to a maximum of 20 % to prevent oscillations. Furthermore, the current version in SOPHIA employs the *total* effective strain rate $\dot{\epsilon}_{eff} = \sqrt{2/3} \dot{\epsilon} : \dot{\epsilon}$ for evaluation and not the effective *plastic* strain rate $\dot{\epsilon}_{eff}^{pl}$, as is done in Autodyn and LS-Dyna.

Hardening regime

Yield of the material occurs already before the stress state is beyond the failure surface. Since the latter is experimentally the most accessible limit state, the RHT incorporates the current elastic limit of the undamaged material by scaling this surface radially by a factor $F_e(\hat{p}, \varepsilon_{pl}^*, \dot{\epsilon}_{eff})$. Additionally, the elastic state is restricted to higher pressures by considering a cap factor $F_c(\hat{p})$:

$$\sigma_y|_{D=0} = f_c \hat{\sigma}_f(\hat{p}/F_e) R_3 F_e F_c \quad (4.10)$$

The scaling factor F_e interpolates between the elastic limit parameters $g_c(\varepsilon_{pl}^*)$ and $g_t(\varepsilon_{pl}^*)$, depending on the normalized effective plastic strain, ε_{pl}^* :

$$F_e(\hat{p}, \varepsilon_{pl}^*, \dot{\epsilon}_{eff}) = \begin{cases} g_c & 3\hat{p} \geq F_R^c g_c \\ g_c - \frac{3\hat{p} - F_R^c g_c}{F_R^c g_c + F_R^t g_t \hat{f}_t} (g_t - g_c) & F_R^c g_c > 3\hat{p} \geq -F_R^t g_t \hat{f}_t \\ g_t & -F_R^t g_t \hat{f}_t > 3\hat{p} \end{cases} \quad (4.11)$$

To define this value, consider an uniaxial loading of a specimen beyond its elastic limit. Let the strain after initial yield be decomposed into an elastic portion ε_e^h and a plastic contribution ε_{pl}^h . The elastic component of the after-yield-strain is defined as the difference between the initial failure surface, divided by the slope of the uniaxial stress-strain diagram:

$$\varepsilon_{el}^h = \frac{\sigma_f(1 - F_{e,0} F_c)}{3G} \quad (4.12)$$

with $F_{e,0}$ being the scaling factor for the case $\varepsilon_{pl}^* = 0$. The material parameter Ψ_h is used to determine the plastic strains up to failure by:

$$\varepsilon_{pl}^h = \varepsilon_{el}^h(\Psi_h - 1) = \frac{\sigma_f(1 - F_{e,0}F_c)}{3G}(\Psi_h - 1) \quad (4.13)$$

In contrast to the formulation in [246], stiffness degradation is not considered here. The normalized plastic strain is determined now by relating the current effective plastic strain ε_{pl}^{eff} to the plastic strain at failure ε_{pl}^h :

$$\varepsilon_{pl}^* = \min \left[\frac{\varepsilon_{pl}^{eff}}{\varepsilon_{pl}^h}, 1 \right] \quad (4.14)$$

The elastic limit parameters read then with $g_{c,0}$ and $g_{t,0}$ ⁴⁴:

$$g_c(\varepsilon_{pl}^*) = (1 - g_{c,0})\varepsilon_{pl}^* + g_{c,0} \quad (4.15)$$

$$g_t(\varepsilon_{pl}^*) = (1 - g_{t,0})\varepsilon_{pl}^* + g_{t,0} \quad (4.16)$$

The cap function F_c limits the elastic regime to ensure that stress states above the pore crush pressure \hat{p}_c lead consistently to irreversible deformation:

$$F_c(\hat{p}) = \begin{cases} 0 & \hat{p} \geq \hat{p}_c \\ \sqrt{1 - \left(\frac{\hat{p} - \hat{p}_u}{\hat{p}_c - \hat{p}_u} \right)^2} & \hat{p}_c > \hat{p} \geq \hat{p}_u \\ 1 & \hat{p}_u > \hat{p} \end{cases} \quad (4.17)$$

With \hat{p}_u being the lower cap threshold pressure, defined as

$$\hat{p}_u = \frac{F_R^c g_c}{3} \quad (4.18)$$

\hat{p}_c is the maximum pressure reached.⁴⁵

⁴⁴ Note that this notation deviates both from the original version and the reformulated version of *Borrval* et al. It expresses the attempt to yield a consistent and more accessible notation than hitherto.

⁴⁵ In case of the default combination with the $p-\alpha$ equation of state, $\hat{p}_c(\alpha)$ is the current, porosity dependent, pore crush pressure.

Residual strength surface

As a second limit surface, the residual strength surface is defined by a polynomial function, similar to the failure surface, but depending only on pressure:

$$\hat{\sigma}_r(\hat{p}) = \begin{cases} A_f \hat{p}^{n_f} & \hat{p} > 0 \\ 0 & \hat{p} \leq 0 \end{cases} \quad (4.19)$$

with material parameters A_f and n_f .

Damage

Once the stress state exceeds the failure limit $\hat{\sigma}_f$, that is, as soon as $\varepsilon_{pl}^* = 1$, softening is described using a scalar damage value D . It is defined by normalizing the accumulated effective plastic strains by a pressure-dependent allowable plastic strain ε_{pl}^f , adopted from the HJ model⁴⁶ [155]:

$$D = \sum \frac{\Delta \varepsilon_{pl}^{eff}}{\varepsilon_{pl}^f} \text{ if } \varepsilon_{pl}^* = 1. \quad (4.20)$$

$$\varepsilon_{pl}^f = \max \left[D_1 (\hat{p} - (1 - D) \hat{p}_t)^{D_2}, \varepsilon_{pl}^m \right] \quad (4.21)$$

D_1 and D_2 are again free material parameters. A minimum allowable plastic strain, ε_{pl}^m , was introduced by *Holmquist* et al. to suppress fracture caused by low magnitude tensile waves and is set to 1 % by default. D ranges from 0 to 1 and is used to interpolate between the failure and the residual limit surface:

$$\sigma_y = f_c [(1 - D) \hat{\sigma}_f - D \hat{\sigma}_r] \quad (4.22)$$

⁴⁶ The HJ-model includes a component related to the plastic volumetric strain since concrete loses cohesion during void collapse. Since they state that the majority of damage will be due to deviatoric plastic strain, this contribution has not been incorporated into the RHT model. Plastic compaction is, on the other hand, reflected if a $p-\alpha$ equation of state is used.

In current implementations of the model in Autodyn and LS-Dyna, an artificial pressure degradation ("spall failure") is implemented to mimic softening if the pressure is below the Hugoniot tensile limit:

$$\hat{p} = \max [(1 - D) \hat{p}_t, \hat{p}] \quad (4.23)$$

Current yield limit and yield function

Summarizing the previous paragraphs, the current yield limit can be condensed to the following form:

$$\sigma_y = f_c \begin{cases} \hat{\sigma}_f(\hat{p}/F_e) R_3 F_e F_c & \varepsilon_{pl}^* \leq 1 \quad (D = 0) \\ (1 - D) \hat{\sigma}_f - D \hat{\sigma}_r & 0 < D \leq 1 \quad (\varepsilon_{pl}^* = 1) \end{cases} \quad (4.24)$$

In its standard formulation, the model utilizes a von Mises yield function:

$$\Phi_{vM} = \sqrt{J_2} - \sigma_y(p, \dot{\varepsilon}_{eff}, \theta, \varepsilon_{pl}^{eff}) \quad (4.25)$$

The flow rule is non-associative and leads to a simple scaling of the deviatoric stresses [28, 226]. Finally, note that the RHT model in SOPHIA is implemented by explicit forward integration; i.e. if history variables, e.g., the plastic strain, are needed to determine the current yield stress, values of the last cycle are used.

4.2.2 Critique on the RHT model

Although its application has been very successful in several scenarios, shortcomings in the formulation have been noted over the years. Besides some undesired behavior in specific stress and loading combinations, especially the deficiency of modeling plain concrete was reported very early in [252].⁴⁷ Later on *Tu et al.* investigated the RHT Autodyn implementation thoroughly, proposed some improvements, and in 2010 furnished the issues further and demonstrated advances beyond simple parameter fitting [253]. *Hartmann* as well investigated the

⁴⁷ In detail: *Hansson* stated that the RHT model delivers satisfying results in the case of a hard steel impactor penetrating an unreinforced concrete target if the concrete is strongly confined [252, p. 108]. On the other hand, he observes less accurate behavior if the failure mode is dominated by tensile cracking.

model intensely in his dissertation [218], which later led to a new concrete model with strong similarities to the RHT model [154]. Furthermore, *Schuler* as well as *Tawadrous et al.* proposed modifications [254, 255]. Summarizing the points of critique risen in the mentioned works, the following list emerges:

1. The model exhibits unrealistic long softening branches in tension and compression.
2. Insufficient consideration of strain rate effects.
3. Unphysical stress paths for some specific scenarios, such as biaxial compression and triaxial extension.⁴⁸
4. A too less sensitive tensile region, respectively, implausible failure under pure mode I.⁴⁹
5. The model is not regularized. Therefore, the dissipated fracture energy depends on the size of the elements.
6. No damage occurs due to hydrostatic compression.⁵⁰
7. The mass-based mixing rule for determining properties for the $p - \alpha$ equation of state might be wrong and better replaced by a volume-based rule.

These issues are valid points of critique, but some of them are more hypothetically relevant and will rarely influence the simulation results in practice.⁵¹ The most

⁴⁸ For triaxial extension, the stress will be kept constant, after reaching the limit value \hat{p}_t , since no plastic flow occurs in the absence of deviatoric stresses. Pseudo-softening ("spall-failure") occurs only if the damage factor increases due to accumulating plastic strains.

⁴⁹ This issue has been demonstrated in the thesis of *Bach* [256]. He modeled the compact tensile specimen from [149] and found shear-dominated failure – elicited by the von Mises flow hypothesis. Additionally, SHB spallation tests have been simulated by *Häußler-Combe et al.* with three different concrete models, among them the RHT model [257]. Simulations with this model were inferior with regard to the free surface velocity results, whereas – in contrast to experiments – even no spallation was found in comparable set-ups in [255].

⁵⁰ A fact that especially *Schuler* brought up. In fact, if no deviatoric stresses occur, compression of the material does not cause damage, as irreversible compaction in these cases is accounted for in the decrease in porosity α through the $p - \alpha$ EoS. *Schuler* proposed to formulate damage as a function of the deviatoric and the spherical stress state $D = f(\sigma^D, p)$ [254]. However, this formulation was never extensively tested and *Schuler* himself used it only in some demonstration cases, where compression was not the dominant stress state [254]. Later, *Nöldgen* resorted to this approach, while reformulating the model for fiber-reinforced ultra-high-performance concrete [6]. Since his anisotropic formulation differs in several aspects from the standard RHT description, an evaluation is quite difficult. The model formulated by *Hartmann et al.* incorporates a comparable approach [154].

⁵¹ E.g., results are not very sensitive regarding the properties of the solid EOS, derived by the mixing rule. As a second example, pure triaxial extension is a very rare stress state, as *Tu et al.* themselves admit [258, p. 1076]. Clearly, one should strive for a comprehensive model

important aspect with regard to the objectives pursued in this thesis is the inferior behavior under tensile loading. As a remedy, an improved yield criterion is proposed as follows.

4.2.3 Formulation of an improved yield criterion for brittle failure

For quasi-brittle materials, such as concrete, the von Mises hypothesis does not adequately describe tensile failure, and a criterion based on the maximum principal stress is much more appropriate. A first attempt to combine such a criterion with a von Mises-based flow rule for compressive stress states has been made by *Feenstra* et al. [151]. They combined a Rankine criterion with a Drucker-Prager model as a simple but adequate model for concrete under static loading; an approach that was repeated for mesoscale simulations in [259]. Briefly after the RHT development, *Clegg* et al. implemented a Rankine criterion in Autodyn as an optional supplement to the material models. Since then, the combination of this “crack-softening” option together with the RHT (or equivalents in other implementations) has been repeatedly applied to concrete under dynamic loading and generally delivers better results than the pure RHT model, e.g., [256, 258, 261]. However, this option still lacks features such as rate enhancement. Therefore, the following section describes in detail the augmentation of the RHT model by a rate-dependent, regularized Rankine criterion and some minor corrections of the model formulation.

Yield function

The principal stress criterion is formulated in the context of classical numerical plasticity. In the present case, it is advantageous to formulate it in tensorial notation and not – as usual – in Voigt notation. The yield function Φ_R reads:

$$\Phi_R = \sigma_I - \sigma_y(\dot{\epsilon}, \epsilon_{pl}) \mathbf{I} = 0 \quad (4.26a)$$

$$\sigma_y(\dot{\epsilon}, \epsilon_{pl}) = F_{R,0}(\dot{\epsilon}_{eff}) f_t(\epsilon_{pl}) \quad (4.26b)$$

that is capable of matching all possible stress states with satisfying results. But not rarely, improved parameter fits already yield adequate solutions; see, e.g., [258] and [256].

σ_I is the principal stress tensor, with the implicit understanding that the principal stresses σ_i are sorted ($\sigma_1 \geq \sigma_2 \geq \sigma_3$). σ_y is the current yield strength, $\dot{\epsilon}$ the strain rate tensor, ϵ_{pl} the tensor of plastic strains and $F_{R,0}$ the above defined function to account for strain rate enhancement; f_t is the current (static) tensile strength, while \mathbf{I} signifies the identity tensor. The subscript "0" in $F_{R,0}$ denotes the fact that this factor is evaluated only once during initial yielding and kept constant thereafter.⁵² Note that equation (4.26a) defines three individual, uncoupled equations for each principal stress component, assuming that there is no influence on yielding by interaction (in contrast to, e.g., the formulation in [259]⁵³). For the elastic domain $\mathcal{E} = \{\sigma \mid \Phi_R < 0\}$ the standard linear-elastic constitutive law is applied: $\sigma = \Lambda : \epsilon$ with Λ being the fourth order elasticity tensor.

Flow-rule

The current strain state is established by:

$$\epsilon^{(n)} = \epsilon_{el}^{(n-1)} + \Delta\epsilon^{(n)} \quad (4.27)$$

If the corresponding "trial"-stress state $^{tr}\sigma^{(n)} = \Lambda : \epsilon^{(n)}$ exceeds the elastic domain, that is, if $\Phi_R > 0$, the stress state has to be mapped back to an admissible state, and the strain increment is split into an elastic and a plastic increment:

$$\epsilon^{(n)} = \epsilon^{(n-1)} + \Delta\epsilon_{el}^{(n)} + \Delta\epsilon_{pl}^{(n)} \quad (4.28)$$

The admissible (projected) stress state then reads:

$$\sigma^{(n)} = ^{tr}\sigma^{(n)} - \Lambda : \Delta\epsilon_{pl}^{(n)} \quad (4.29)$$

and – with the assumption of isotropic behavior:

$$\sigma^{(n)} = ^{tr}\sigma^{(n)} - \left(2G\Delta\epsilon_{pl}^{(n)} + 3K \operatorname{tr}(\Delta\epsilon_{pl}^{(n)})\mathbf{I} \right) \quad (4.30)$$

⁵² There are several reasons for this choice, but the most important one is that after deformation localizes, the strain rate increases strongly in the affected elements, thus rendering the damaged material very strong and preventing proper softening.

⁵³ There, a vector norm $\|\sigma_I\|$ is calculated with the individual principal strains σ_i , in which a component is considered only if $\sigma_i > 0$. The yield criterion is then $\Phi_R = \|\sigma_I\| - \sigma_y$. This criterion delivers a rounded yield surface at the intersection of the three limit planes, which might bring a numerical advantage, depending on the implementation.

To determine the unknown plastic strain increment, the following discrete flow rule is defined (see [28] for details):

$$\Delta \boldsymbol{\varepsilon}_{pl}^{(n)} = \Delta \gamma \mathbf{N} \quad (4.31)$$

in which $\Delta \gamma$ is a scalar value, expressing the magnitude of the increment and \mathbf{N} a tensor, assigning the direction of the plastic flow. If equation (4.31) is inserted into equation (4.30), resorting to the definition of the yield function and the split into deviatoric and hydrostatic strain yields:

$$\boldsymbol{\sigma}_I = \boldsymbol{\sigma}_I^{tr} - \Delta \gamma (2G \mathbf{N}_D + 3K \text{tr}(\mathbf{N}) \mathbf{I}) \quad (4.32)$$

$\mathbf{N}_D = \mathbf{N} - 1/3 \text{tr}(\mathbf{N}) \mathbf{I}$ is the deviatoric projection of \mathbf{N} , $\text{tr}(\mathbf{N})$ its trace, and \mathbf{I} again the identity tensor.

In this work, associative flow is assumed for the Rankine criterion, that is, the direction of the plastic strain increments corresponds to the normal vector of the yield surface \mathbf{e}_I . Consider first the case, that only $\sigma_1 > \sigma_y$. For this condition, the normal vector reads $\mathbf{e}_1 = [1, 0, 0]^T$ and $\mathbf{N} = \mathbf{e}_1 \otimes \mathbf{e}_1$. Equation (4.32) can then be written for all three directions:

$$\begin{aligned} \sigma_1 &= \sigma_1^{tr} - \Delta \gamma (4/3G + K) \\ \sigma_2 &= \sigma_2^{tr} + \Delta \gamma (2/3G - K) \\ \sigma_3 &= \sigma_3^{tr} + \Delta \gamma (2/3G - K) \end{aligned} \quad (4.33)$$

For the general case, three plastic multipliers are defined:

$$\Delta \boldsymbol{\varepsilon}_{pl}^{(n)} = \sum_{j=1}^3 \Delta \gamma_j \mathbf{N}_j \quad (4.34)$$

Following the steps described above, one yields – with the definitions $\Delta \boldsymbol{\gamma} = [\Delta \gamma_1, \Delta \gamma_2, \Delta \gamma_3]^T$, $a_a = 4/3G + K$, $a_b = -2/3G + K$, as well as

$$\mathbf{A} = \begin{bmatrix} a_a & a_b & a_b \\ a_b & a_a & a_b \\ a_b & a_b & a_a \end{bmatrix}$$

– the compact form of the stress update equations:

$$\boldsymbol{\sigma}_I = \boldsymbol{\sigma}_I^{tr} - \mathbf{A} \Delta \boldsymbol{\gamma} \quad (4.35)$$

In contrast to the von Mises criterion used in the RHT model, the associative flow in the case of the Rankine criterion yields a pressure change, as soon as plastic flow occurs. Thus, the criterion can cover softening inherently and no artificial “spall criterion” is necessary.

Softening

The yield strength in equation (4.26b) is formulated in dependence on plastic strains to consider softening.⁵⁴ Besides a linear law [260], several authors apply bi-linear laws, e.g., [258, 262, 263] or simple exponential ones [151, 264, 265]. In the present work, the more complex exponential law derived by *Reinhardt* et al. and *Hordijk* et al. is used, which is based on a wide experimental basis and has the advantage that it not only approximates zero but exactly delivers $f_t(\delta_c) = 0$. It reads [76, 266]:

$$f_t(\delta) = f_{t,0} \left\{ \left[1 + \left(\frac{c_1 \delta}{\delta_c} \right)^3 \right] \exp \left(-\frac{c_2 \delta}{\delta_c} \right) - e^{-c_2} (1 + c_1^3) \frac{\delta}{\delta_c} \right\} \quad (4.36)$$

The dimensionless values $c_1 = 3$ and $c_2 = 6.93$ are given in [76]. Figure 4.4 compares the different softening laws with data from literature for mortar and concrete. The softening law is based on a scalar-valued crack opening δ , which does not have a direct counterpart in the plasticity framework. Therefore, a crack strain is defined, based on the plastic strain increments in direction of the principal axes \mathbf{e}_I :

$$\Delta \epsilon_{pl} = \Delta \gamma_1 \mathbf{e}_1 \otimes \mathbf{e}_1 + \Delta \gamma_2 \mathbf{e}_2 \otimes \mathbf{e}_2 + \Delta \gamma_3 \mathbf{e}_3 \otimes \mathbf{e}_3 \quad (4.37)$$

If the flow occurs only in the direction of the first principal axes (i.e. $\Delta \gamma_2 = \Delta \gamma_3 = 0$), let $\Delta \epsilon_{cr}$ be:

$$\Delta \epsilon_{cr} = \Delta \epsilon_{pl_{1,1}} \quad (4.38)$$

⁵⁴ An initial *hardening* is not considered, although hardening is experimentally observed starting at stress limits of approximately $0.7f_t$. However, the strain increment corresponding to the hardening regime is often so small that it has been passed within one or two steps, rendering a hardening effect negligible.

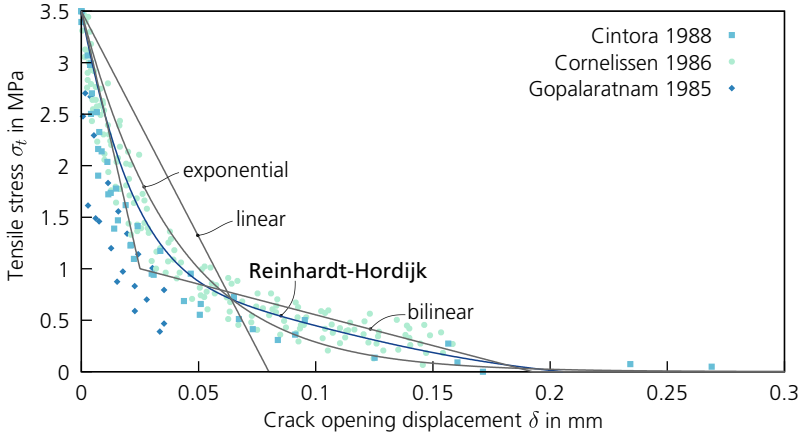


Figure 4.4: Different softening-laws for similar fracture energy together with data points from literature [264, 265, 267].

The index “1,1” designates the first coefficient of the first row and column of the plastic strain increment tensor. For the general case:

$$\Delta \varepsilon_{cr} = \sqrt{\frac{2}{3}} \|\Delta \varepsilon_{pl}\| \quad (4.39)$$

Based on the crack strain, a crack opening can be defined if an appropriate characteristic length l_c is available:

$$\delta = \varepsilon_{cr} l_c, \quad \delta_c = \varepsilon_{cr,c} l_c \quad (4.40)$$

The critical crack opening, δ_c , is derived from the input values for the initial tensile strength and the fracture energy G_F . Considering

$$G_F = \int_0^{\delta_c} f_t(\delta) d\delta \quad (4.41)$$

it follows for the Reinhardt-Hordijk law with the default values for c_1 and c_2 :

$$\delta_c = 5.136 \frac{G_F}{f_{t,0}} \quad (4.42)$$

Crack initiation and energy regularization

For the transformation from plastic crack strain to a crack opening, the characteristic length l_c was introduced. This length is also used to transform the fracture energy G_F (energy per crack area) into a specific energy g_F (energy per volume), which is dissipated in each element. This should ensure – at least in theory – that the energy dissipated in elements of varying size accounts for the different volumes/crack areas. The simple relationship reads

$$g_F = \frac{G_F}{l_c} \quad (4.43)$$

and is a major requirement for mesh objectivity. This principle is known as “regularization” and several proposals to determine l_c can be found in the literature. In 2D simulations, this length can be interpreted as the width of a crack band, see [79, 268]. Unfortunately, for 3D, no ad hoc or directly intuitive definitions are available. The most simple and, therefore, most commonly applied method is to take the cube root of the volume of the elements [153, 254, 258, 260]. More sophisticated proposals are, among others, the projection method [268] or the approach developed by *Barzegar* et al. There, the length of a line pointing along a fictive crack plane, bounded by upper and lower element facets is used [269]. *Oliver* introduced an elegant procedure in which a continuous linear function is integrated, which has a value of 1 at the nodes of this and a value of 0 at the nodes on the other side of a fictive crack plane. The approach was slightly modified by *Govindjee* et al. to be applicable for 3D elements as well [271].

An even more intricate, but on the other hand very intuitive approach has been proposed by *May* et al. [272]. They construct a fictive crack plane with the first principal stress direction as normal and the central point of the element as base point; see the sketch in Figure 4.5. Subsequently, the cutting points with all relevant element edges are calculated; the resulting polygon constitutes the “crack surface”. Together with the element’s volume, the characteristic length can be determined. Although this approach is elaborate, the intuitive concept and reasoning are convincing. Since this calculation must be performed only once in each element that has reached the yield stress, the effort is acceptable. No rotation of the crack coordinate system is considered.⁵⁵

⁵⁵ *May* et al. keep the plane over the entire simulation and use as crack opening only the projected part of the plastic strains in the direction of the initial crack opening. In the

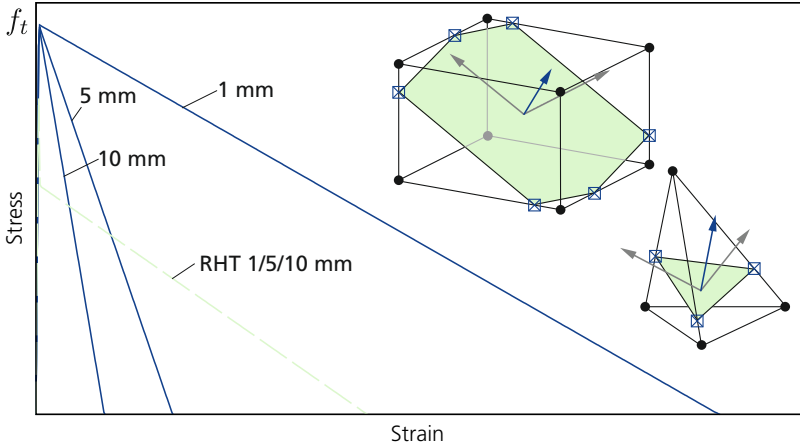


Figure 4.5: Stress-strain-diagram of single element tests of different sizes under confined tension. The standard RHT model dissipates for each element size the same specific fracture energy g_F – and is therefore highly mesh dependent. With regularization in the Rankine-criterion, the total fracture energy $G_F = g_F/l_c$ remains constant. The inlays sketch schematically the approach of the fictive crack planes, detailed in [272] (crack opening is normal to the plane and indicated by the blue vectors).

Considerations concerning strain rate enhancement and fracture energy

Several authors repeatedly question the employed strain rate enhancement in the RHT model for different reasons [218, 252, 255, 258]. Yet an unambiguous point is not made. For example, *Tu et al.* criticize the *DIF* scaling and maintain that the strain rate effects are *overestimated* in the current formulation, whereas *Hartmann*, likewise discontented with the implemented form, asserts an *underestimation*. These two positions amply illustrate the degree of variability in the concept of strain rate enhancement. Indeed, the large scatter in the experimental results, the different fit functions available and the ambiguity in interpreting this effect, promote a certain indisposition regarding the *DIF*-concept in its current form. In fact, one may ask whether a simple multiplication of the limit strength with a scalar empirical factor is sufficient to resemble the complex material behav-

implementation used here, the crack plane is generated only to determine l_c . After this value is known, the crack plane is no longer used.

ior reflected. Several researchers already use viscoplastic formulations, in which the limit strength is not changed, but the amount of plastic flow depends on the loading rate, e.g., [159, 212, 271]. Although again material parameters that have to be fitted by experiments are introduced, considering time inherently in the plasticity routines simply appears to be a more physical way. Nevertheless, such an approach is not (yet) incorporated into the RHT model, and the former empirical DIF equations are used herein as well.

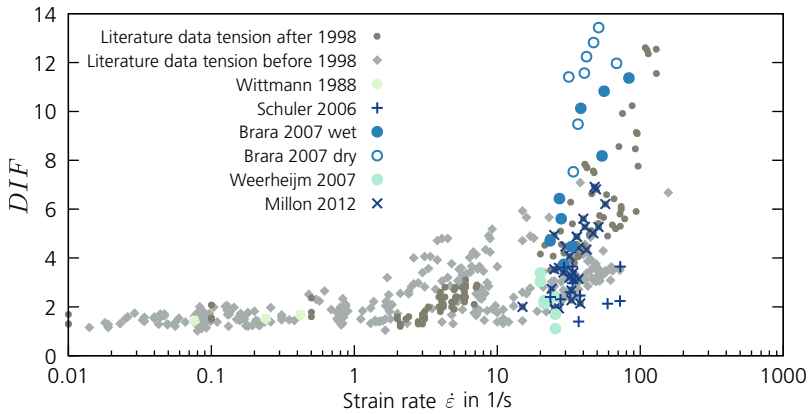


Figure 4.6: Measured fracture energy under dynamic loading (colored symbols) and data for DIF_t for comparison (gray).

Regarding a potential strain rate enhancement of the fracture energy, no consensus exists. The CEB model code declared in 1990, that the available data is too incomplete to establish a reliable function and there have been only a few attempts to improve the situation since then. One of the first works, where the fracture energy has been measured in conjunction with the strain rate, appears to be reference [263]. In this study, an enhancement of fracture energy with increasing strain rate was measured, but the rates considered are rather low. Higher rates have been achieved with split SHB specimens in spallation configuration, conducted by *Schuler et al.* [273]. Later, *Weerheijm et al.*, as well as *Brara et al.*, contributed more data with comparable set-ups [87, 274]. Especially *Weerheijm et al.* elaborate on the problem and postulate a limit value of dynamic fracture energy in the order of 250 J/m^2 . They further maintain that the increase is not comparable to the strength increase, but is caused by the same sources. This is

consistent with the work of *Wittmann* et al., who measured a stronger increase in the fracture energy compared to the strength [263].

Regarding the scarce data and the strong scatter⁵⁶ it is very difficult to settle the matter. Figure 4.6 shows the data of the sources mentioned together with yet unpublished values from an internal report with a set-up similar to that used by *Schuler* et al. ("Millon 2012" [277]). Data for DIF_t from the literature are also plotted in gray. From this figure, one can conclude that the energy enhancement is not limited, contrary to *Weerheijm* et al., and – more important – that the enhancement is not too different with respect to the strength increase. The data for the fracture energy de facto fits well with the second data group for the tensile strength enhancement. Again, the question arises of whether this is a material property or a "system value". Numerical results published in [140, 149] and [201] – replicating experimental results without fracture energy enhancement in the material model – prefer to find the answer in the latter option. The work of *Knell* et al. tends in the same direction. While it clearly shows that a tensile *strength* enhancement is necessary to obtain realistic results, the experiments were best replicated with a static fracture energy [143]. Consequently, it is advocated here to take the static value as input parameter. Since the fracture energy is a derived value and depends in the classical traction-separation laws on the tensile strength and the critical crack opening, a static fracture energy can only be maintained by downscaling the critical crack opening with DIF_t .

There is another issue related to fracture energy, which is entailed with a very fine discretization, as is the case in the mesoscale simulations carried out. The fracture energy is generally dissipated not in a single discrete crack, but in the fracture process zone (FPZ) – a region with multiple microcracks, crack interaction, and so forth. In standard experiments for the determination of the fracture energy, such as the three-point bending test, the work applied is typically related to the projected fracture surface of the final macrocrack, thereby contributing the total energy to one macrocrack only. Consequently, the smeared crack approach is strictly valid only for discretizations, where the size of a single element size encompasses the entire FPZ [79, 278], leading to rather large elements around three times the largest inclusion. In finer discretizations, the FPZ spreads over multiple elements; hence, each element should have a *local* fracture energy.

⁵⁶ *Banthia* et al. even claimed a sixteen-fold increase in fracture energy, measured in dynamic three-point bending tests on plain concrete specimens [275], whereas *Weerheijm* et al. postulates an upper limit of 2.5! However, the numbers of *Banthia* et al. are potentially the result of quasi-static assumptions in a dynamic environment; see [276].

Together, all elements should – in a simulation comparable to the standard test – dissipate the *global* measured energy.

Combining RHT and Rankine failure surfaces

The Rankine criterion copes only with tensile-dominated stress states. For arbitrary states, the RHT model should be used as before. The overlay of both criteria can be achieved by adapting the multi-surface plasticity approach. A resolute realization has been described, e.g., in [259] or [151]. A less sophisticated alternative is a “bifurcation” analysis, as explained in [6] with respect to reference [260]. For a given stress state, with its unique angle of similarity, the interception between the RHT and the Rankine yield surface is determined. Then, the pressure state of this point is compared with the trial pressure and the appropriate criterion is taken.

The SOPHIA implementation takes an even more pragmatic way: In each step, the Rankine criterion is checked first. If $\Phi_R > 0$, plastic flow occurs. Afterwards, the RHT criterion is checked with the updated stresses as well, and potentially a second plastic flow might occur. However, this will only happen in rare cases. Most trial stress states are expected to distinctly activate the Rankine or the RHT criterion. At least for the tensile-dominated problems considered in this study, the stress state is unambiguous. However, future applications to other problems should go along with careful evaluation and potential improvements.

A slight modification of the RHT yield surface in the tensile regime is necessary to distinctly activate Rankine plastic flow near the Hugoniot tensile limit and reads:

$$\hat{\sigma}_f = \begin{cases} A (\hat{p} - \hat{p}_0)^n & 3\hat{p} \geq F_R \\ \frac{3F_R(\hat{p} - \hat{p}_t)}{F_R - 3\hat{p}_t} & F_R > 3\hat{p} \geq \hat{p}_t \\ 0 & \hat{p}_t > \hat{p} \end{cases} \quad (4.44)$$

The Rankine criterion is only activated for stress states with Lode angles up to approximately 35° and low pressures. Figure 4.7 shows the meridian plot of both criteria, while Figure 4.8 presents the combined criterion in the principal stress space.

By combining both criteria, the role of the damage parameter ε_{pl}^m is now limited to compressive stress states. Originally invented to control premature damage from

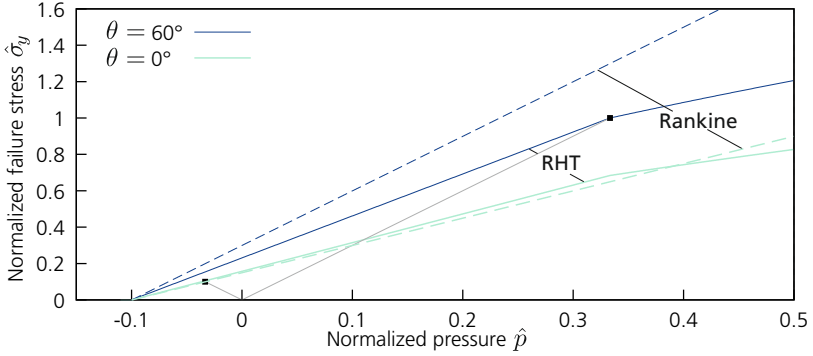


Figure 4.7: RHT failure meridian for compression ($\theta = 60^\circ$) and tension ($\theta = 0^\circ$) with the added Rankine limit. In the compressive regime, the RHT model yields continuously lower limit values. The gray lines mark the stress path of uniaxial compression, respectively tension.

rarefaction waves, the value controls in the original formulation the dissipated fracture energy. For the Rankine criterion, a damage value D_R is defined as the ratio of the dissipated to the available fracture energy:

$$D_R = \frac{G_f}{G_{f,0}} \quad (4.45)$$

A total damage \mathcal{D} from both criteria is determined by superposing the values from each criterion:

$$\mathcal{D} = \min [D + D_R, 1] \quad (4.46)$$

Pre-damage due to shear failure (RHT criterion) is considered in the Rankine criterion by reducing the critical crack opening:

$$\delta_c(D) = \delta_{c,0}(1 - D) \quad (4.47)$$

This relation ensures that the material does not have tensile strength if it has already reached the residual failure surface under compression, i.e. $D = 1$.

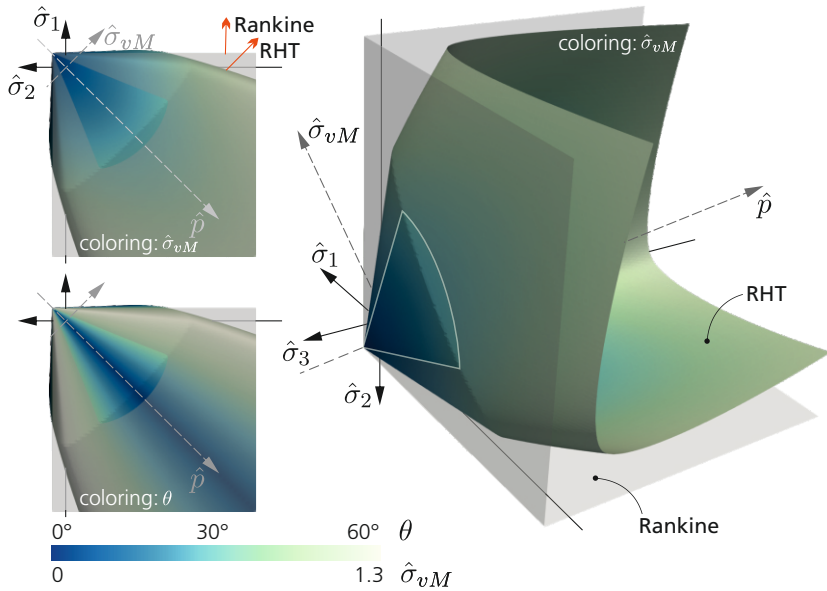


Figure 4.8: Failure envelope of the RHT model with added Rankine criterion in the principal stress space. Left: Plots in the rendulic plane highlight the stress regime, where the Rankine criterion is more strict. Two red arrows indicate the direction of plastic flow (top).

4.2.4 Correction of the residual failure surface

Tu et al. observed some implausible stress-strain paths in specific situations [253, 258]. Especially for confined tensile stress states, softening is not observed, but on the contrary, the yield stress increases between ultimate failure and residual surface. Furthermore, a simple unconfined pressure test does not eventually lead to zero stress but keeps the failure stress constant at roughly $\hat{\sigma}_f = 2/3$ after reaching the residual surface. The reason for this undesired and nonphysical behavior is the lack of R_3 in the formulation of the residual strength surface.

Hence, following [258], R_3 is now considered to prevent higher residual than ultimate stress under tension:

$$\hat{\sigma}_r(\hat{p}, \theta) = \begin{cases} A_f \hat{p}^{n_f} R_3(\theta, \hat{p}) & \hat{p} \geq 1/3 \\ \kappa_0 \hat{p} R_3(\theta, \hat{p}) & 0 < \hat{p} < 1/3 \\ 0 & \hat{p} \leq 0 \end{cases} \quad (4.48)$$

with κ_0 being the failure stress for $\hat{p} = 1/3$: $\kappa_0 = 3A_f (1/3)^{n_f}$. The piecewise-defined function furthermore ensures that the intersection of the polynomial and the linear part is directly below the unconfined uniaxial compressive stress at $\hat{p} = 1/3$. The assumption for this function is that the outer confinement can only be maintained for pressures $\hat{p} > 1/3$. Although this assumption is true for uniaxial cases, it is not true for biaxial or triaxial cases with very light confinement. It is questionable, however, whether this limitation is relevant in practice.

4.2.5 Equation of state

Recalling the compiled observation concerning the failure of concrete in Chapter 3, one may postulate two basic failure modes for concrete: Mode I cracking on the microscale – as underlying failure mechanism in un- or low confined stress states – and pore compaction in confined situations. The first effect is reflected in the RHT model by the added Rankine criterion; together with the idealization on the mesoscale, it should (at least theoretically) cope with all stress states with low confinement. Pore compaction, on the contrary, is traditionally considered by an appropriate EoS. In most cases, a Mie-Grüneisen or a polynomial EOS, augmented with a porosity term α – hence labeled “ p – α EOS” – is well suited to describe the compaction path of the porous concrete [41, 279]. Since in this work mainly tensile-dominated stress states are considered, the RHT model is combined here with a linear EOS only. Indeed, even the p – α EOS implements for

default parameters a linear expansion term, albeit augmented by the porosity, which is neglected here. The EOS then reads⁵⁷:

$$p = K \varepsilon_{v,el} \quad (4.49)$$

It should be noted that the implementation of the $p - \alpha$ EOS could improve the description of the mortar, but has not yet been done due to the evolving complexities with the associative yield of the Rankine criterion.

4.3 Validation examples

This chapter will close with three validation cases for the detailed mesomechanical modeling approach of concrete described above. Two small-scale examples will be used to demonstrate: (a) correct crack propagation properties, such as inclination and branching phenomena, and (b) accurate development of defined fragments together with proper velocities. A medium-scale experiment will then be simulated to highlight the actual possibility of depicting gross fragmentation. The models are generated using a modified, very efficient Take-and-Place algorithm with a Fuller aggregate size distribution and meshed afterwards with linear tetrahedral elements by the open-source software GMSH [280]. Appendix A.1 describes the process.

As detailed in the first section of this chapter, a hybrid approach is used to model the behavior of concrete on the mesoscale: A smeared crack model with erosion for the mortar matrix and cohesive zone elements for the ITZ.⁵⁸ In this thesis, the CZE developed by *Knell* and *Durr* are used [225, 281]. A rate-independent linear traction-separation law is employed for the CZE together with a combined failure

⁵⁷ The formulation deviates from the classical form found, e.g., in [41]:

$$p = K \left(\frac{\rho}{\rho_0} - 1 \right)$$

In this form, the EOS equates $\varepsilon_v = \frac{\rho}{\rho_0} - 1$, which is valid for infinitesimal strains [28], but relates the pressure to the *whole* volumetric strain, including the plastic strains. This violates the fundamental assumptions of numerical plasticity in which the admissible stress state corresponds to an *elastic* strain state only.

⁵⁸ For computational efficiency, the meso domain is divided into several partitions (see Section 6.2). However, nodesplit is not allowed for nodes on partition boundaries to circumvent the intricacies involved in synchronizing the split between partitions.

criterion for tensile and shear tractions (refer to one of the above-mentioned works for detailed information).

One difficulty remains, namely the choice of relevant material parameters. In this respect, the above mentioned critique of *Kim* et al. that the mesoscale approach requires material parameters, which are simply unknown, or at least not well known, is partly justified [209]. Some values are experimentally hardly accessible and assumptions based on engineering judgment have to be made. Although the hereafter described experiments used all slightly different concrete receipts, only one parameter set will be used for all simulations. While there is surely room for improvement of some parameters, it will be seen that this single set can cover a wide range of phenomena and loading intensities – although not yet carefully tuned and based mainly on average values taken from different literature sources. This observation thereby underlines the basic postulate of multiscale analysis that the individual material model becomes less important, as long as the interaction between the phases is resolved. The full parameter set is discussed and reported in Appendix A.6.

4.3.1 Crack propagation and branching: compact tension specimen

Figure 4.9 shows the set-up for a direct tension test on compact, pre-notched concrete specimens, conducted by *Ožbolt* et al. [149]. As shown in the figure, the $200 \times 200 \times 25 \text{ mm}^3$ specimen was held on the upper side of the notch by a steel frame and loaded by a similar frame on the opposite side. Both frames have been affixed to the specimen before loading. The displacement-controlled tests were conducted with different displacement rates to investigate the phenomenon of crack branching above a certain rate, which was reported to lie between 2 and 3 m/s. The concrete used had a compressive strength of $f_c = 53 \text{ MPa}$, a tensile strength of $f_t = 3.8 \text{ MPa}$ and a maximum grain size of 8 mm.

Two different displacement rates, namely $v_A = 0.49$ and $v_B = 4.3 \text{ m/s}$ are simulated for five realizations each, i.e. five different generations of the specimen with arbitrary aggregate positions. The smallest modeled inclusion is 2 mm, the largest 8 mm, following a Fuller distribution with exponent $n = 0.5$. A total porosity of 10 % is considered, while only pores between 2 and 4 mm are explicitly modeled. Roughly 15 000 spherical aggregates are contained, representing a total aggregate content of 65 %. The displacement rate is applied at the bottom

nodes of the circular section and increased linearly within the first 0.2 ms until the target value is reached and then kept constant, see Figure A.6 on Page 223; the degrees of freedom of the nodes at the top of the model, are fixed in vertical direction only, as indicated in Figure 4.9. No further constraints have been applied. The steel frames and the concrete specimen are connected by shared nodes. Employed material parameters for the improved RHT model and input values for the cohesive zone elements are discussed in Appendix A.6 and listed concisely in Tables A.2 to A.4.

Figure 4.10 shows the crack pattern of the five virtual specimens for the higher loading rate. The coloring corresponds to the amount of crack opening δ . Elements are eroded if a crack opening of $\delta_E = 0.5$ mm is reached. However, they already lose their stiffness at δ_c , which is much lower than this threshold. A value of 0.5 mm is reported in [273] to be the lower limit for a crack to be visible in a light microscope and was therefore chosen as an intuitive threshold value.

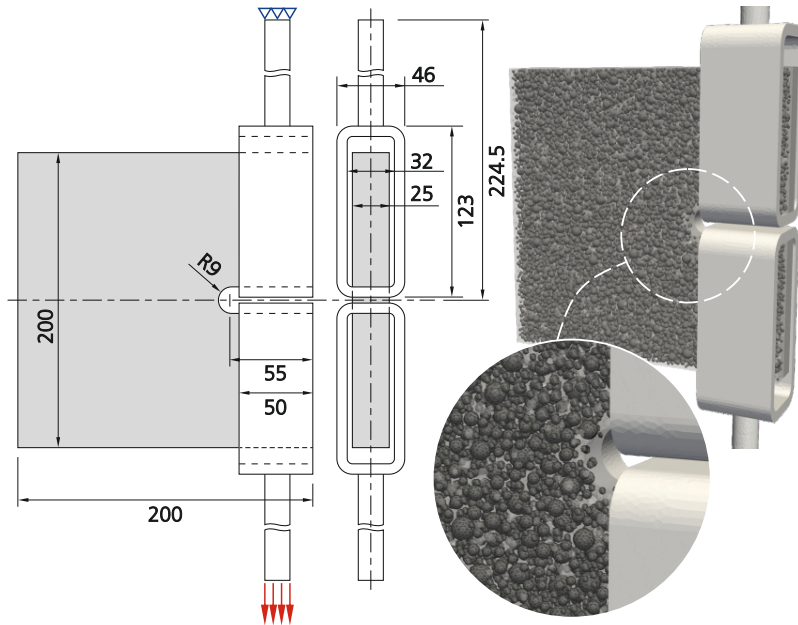


Figure 4.9: Set-up of compact specimens under direct tension tests, acc. to [149] with FE model.

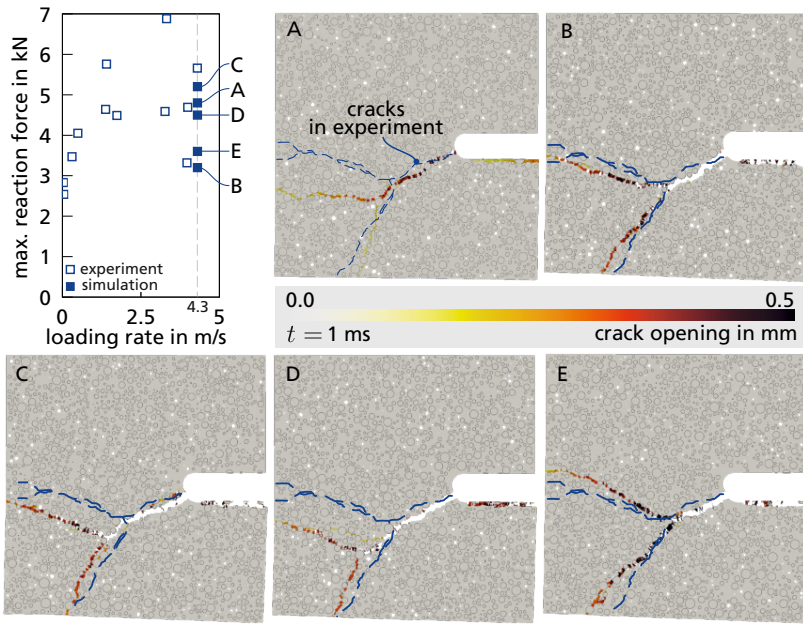


Figure 4.10: Maximum reaction force from experiment and simulation (top left), as well as crack patterns for the high loading rate (slice through the 3D specimen).

Cracks observed in the experiments are overlaid in Figure 4.10 as dark blue, dashed lines. Especially specimens B and E match the experimental result almost perfectly – bearing in mind that the cracks of only one specimen are reported in [149]. All specimens exhibit the correct crack initiation point together with appropriate branching of the crack and very comparable inclinations of the two subcracks. The maximum reaction force is plotted on the top left. This parameter has been found to be very sensitive and subject to high scatter. However, the simulated values fit well in the experimental range. Crack propagation velocity is investigated in [149] with snapshots of high-speed cameras and reported to be initially roughly 835 m/s, slowing down to 480 m/s before branching occurs. The upper branch continues with 387, the bottom one with 444 m/s for the high loading rate. The criteria was a crack opening of 0.1 mm. Trying to conduct this analysis with the FE results by evaluating crack plots at constant time rates, ranges for the velocity are estimated to be 785–1155 m/s for the initial crack,

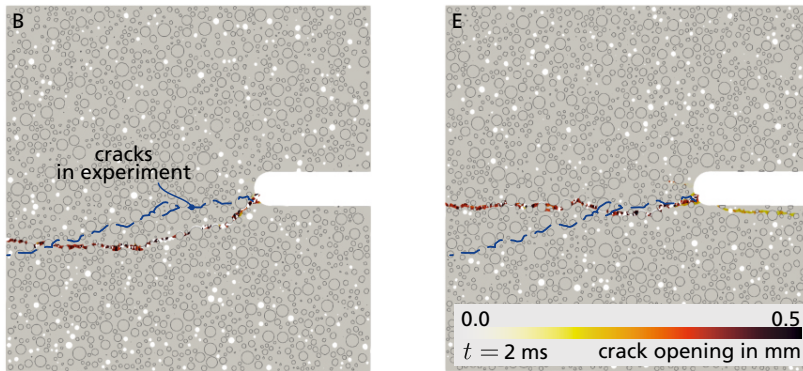


Figure 4.11: Crack patterns of two virtual specimens for the reduced loading rate (slice through the 3D specimen). The two shown cases are representative for all five models.

and 370–566 m/s for the two emerging cracks.⁵⁹ Crack patterns for the low displacement rate are shown in Figure 4.11 for two chosen specimens only. No crack branching appears, and the crack approximates well the experimental pathway.

4.3.2 Fragment velocities and momentum transfer: SHB spallation example

Experiments on the Split-Hopkinson-Bar (SHB) are well suited to investigate material behavior at high strain rates, up to approximately 100 1/s. Data for the rate enhancement of concrete has been generated in the past years predominantly with SHB set-ups. For example, *Schuler et al.* investigated standard concrete (presumably C30/37 grade with a maximum aggregate diameter of 8 mm) in a spallation configuration [273]. The specimen – a cylinder with a diameter of 75 mm and a length of 250 mm – is secured with adhesives to a long aluminum bar. An impactor hits this incident bar and a compressive pulse propagates through the bar. When the pulse reaches the free rear end of the

⁵⁹ It should not be concealed that these numbers depend on the chosen crack criterion of $\delta = 0.1$ mm for the analysis. If a less rigid criterion is taken, e.g., the elements failure point, the crack velocity remains constant at approximately 800 m/s in all cases.

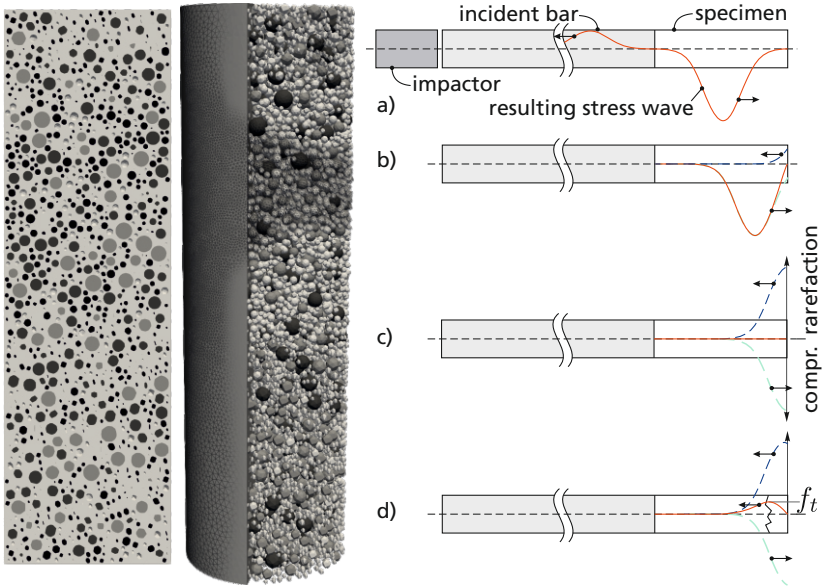


Figure 4.12: Left: Virtual SHB specimen; Right: Principle of wave propagation in the SHB spallation configuration: a) The incoming compressive pulse traverses the interface between incident bar and specimen and is partly reflected into the bar and partly transmitted into the specimen; b) The right-running wave approaches the rear surface and is reflected as rarefaction wave. Dashed lines show the incoming and reflected theoretic wave, while the solid line is the actual net stress state; c) Incoming and reflected waves annihilate each other and the specimen is – for a moment – stress-free; d) Now the rarefaction wave supersedes the incoming wave and the resulting (left-running) wave is a tensile wave. As soon as the stress level of this wave reaches the material’s tensile strength, fracture occurs.

sample, it is reflected as a rarefaction wave. The beginning reflection interferes with the still-incoming compressive pulse, engendering an increasing net tensile stress. Eventually, the strength of the material is exceeded and cracking occurs (see Figure 4.12, right). The newly generated (inner) surfaces again reflect the rarefaction wave, and a characteristic wave profile can be observed in the velocity signal of the rear surface, measured, e.g., with a laser interferometer. The typical drop in the wave profile is called “pull-back velocity”, v_{pb} , and can be used to derive the dynamic strength of the specimen.

A typical model used in the simulation is shown in Figure 4.12, left. Again, aggregates between 2 and 8 mm are considered with a total aggregate content of 70 %. Three different porosities, 0 %, 10 % and 20 %, are investigated. The porous samples are modeled by discretely resolving pores between 2 and 4 mm. The distributions are generated again with the Fuller curve with $n = 0.5$. Material parameters are the same as in the previous section and listed in Tables A.2 to A.4. The meshing is graded such that a finer mesh prevails in the region where most cracking is expected. As input signal, a velocity is calculated from the measured strain in the incident bar by $v_i = -c_b \bar{\varepsilon}_b$, with c_b being the speed of sound of the incident bar and $\bar{\varepsilon}_b$ the average strain from four tests. The strain gauge was placed 400 mm in front of the specimen but the signal is nevertheless applied in the simulation at the nodes of the specimens front surface. No further constraints are considered. Schuler et al. conducted tests with different impact velocities and hence loading intensities, which were labeled as “loading stages” 1 to 3. Here, only loading stages 2 and 3 are simulated. Figure A.5 on Page 223 documents the employed velocity input signal for these stages.

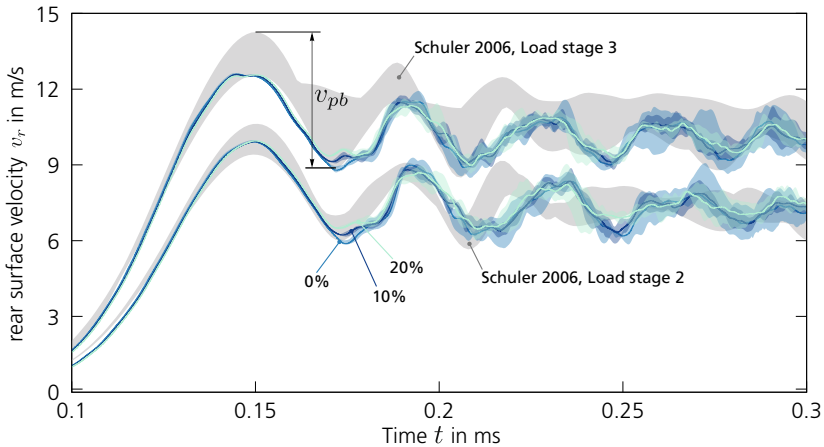


Figure 4.13: Rear surface velocity of SHB specimens with different porosity and loading. For each load stage and each porosity level, five samples have been simulated. The average velocity from these runs is plotted as solid line, while the shaded background marks the whole range of results from [273].

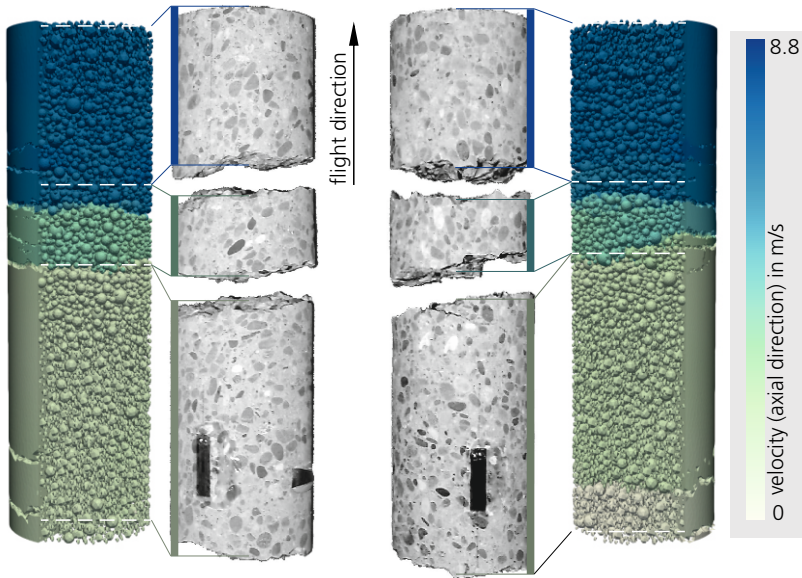


Figure 4.14: Comparison of fragment size between experiment and simulation for two virtual samples with 10 % porosity in loading stage two. Discontinuities in the velocity field highlight the crack planes. Note that photographs and simulation snap-shots exhibit the same scale.

Figure 4.13 shows the rear surface velocity. The range of experimental results for the two loading stages is indicated by the gray-shaded area. For each porosity level, five distinct virtual specimens have been simulated. The line plotted is the respective average value, the colored shading gives the range of results. This scatter is the sole result of the stochastic heterogeneity in the virtual samples.

Several points should be highlighted: For load stage two, all three porosities yield very good results. As expected, the pore-free specimen exhibits the highest, and the model with 20 % porosity the lowest strength. The 10 % specimen delivers here the best results, fitting completely within the experimental range. The scatter within one porosity series is small until approximately 0.2 milliseconds, indicating only slight differences in the fracture. Most importantly – the final velocity of the rear fragment fits very well into the experimental range, indicating a comparable momentum transfer in simulation and experiment.

For load stage three, results are in the lower range of the experimental findings but still acceptable. Here, the overall strength is slightly too low. Furthermore, one observes already a drop in inclination in the velocity profile shortly before the maximum is reached. Consequently, the maximum is less than the expected average of the four test results. There are two issues that potentially even intertwine: First, in the model, slight matrix damage is observable even before the reflected wave fractures the virtual sample distinctly. Second, the conversion and appliance of the input signal presuppose only elastic behavior. That this might in reality not be the case, especially for high rates as here, has already been conjectured in Section 3.2.2. Still, the results are acceptable and the final velocity of the rear fragment is in the experimentally observed range, although on the lower limit.

Regarding the fragmentation of the samples, Figure 4.14 gives the velocity field at $t = 1$ ms of two specimens with 10 % porosity under load stage two. Discontinuities in the field mark distinct fragments. Compared to the test results – displayed are samples 17 and 26 from [273] – the agreement in fragment size is convincing.

4.3.3 Fragment mass distribution: air shock driven fragmentation

Experiments focusing on fragmentation are rare. Even more scarce are tests with quantitative data. In terms of data collection and evaluation, the tests by *Bewick* et al. stand out. They conducted several series of shock tube tests with small- and large-scale specimens of glass, concrete, and concrete masonry [9, 282, 283]. Manual fragment collection and different image analysis techniques were used to determine the mass and velocity distribution of the fragments. Unfortunately, only selected results are published – seriously hampering the thorough exploitation of the test series. Nevertheless, two tests are chosen and simulated in the following. Both tests have been conducted in a small diameter shock tube with different loading intensities and two different slab thicknesses. The principal set-up is shown in Figure 4.15. The slab is fixed between the shock tube and a metal plate with a circular opening. The strength of the concrete samples are given with $f_c = 21.8$ MPa and $f_t = 2.9$ MPa for test 30 and $f_c = 33.7$ MPa and $f_t = 3.6$ MPa for test 36. Crushed limestone aggregates with a maximum diameter of 9.5 mm have been used in both samples.

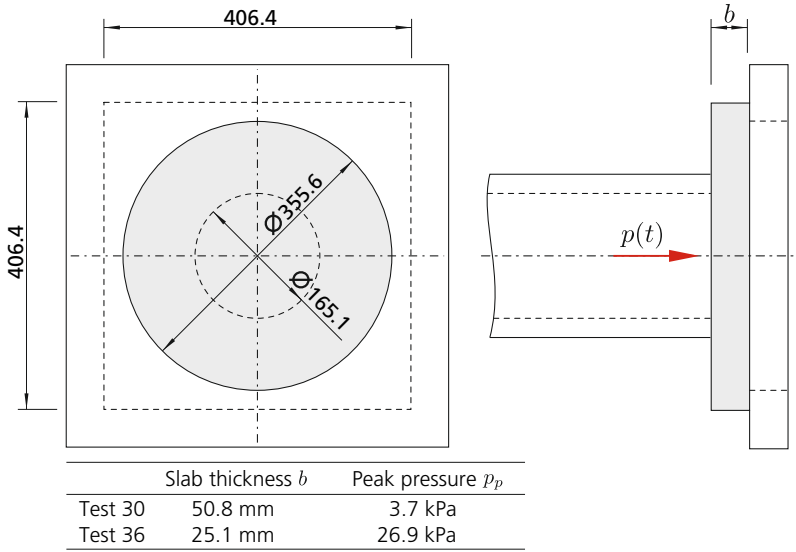


Figure 4.15: Set-up of the shock tube tests, acc. to [9, 282].

For the FE model, only the slab is modeled. The total amount of aggregates is 74 %, modeled in this case with a smallest diameter of 3 up to 9.5 mm, following the Fuller curve with $n = 0.5$. A porosity of 20 % in total was considered with explicit modeling of pores between 3 and 4 mm. The material parameters are again the same as in the previous section, refer to Tables A.2 to A.4 in the appendix. Although concrete strength was reported to differ between the two tests, only one parameter set is used in the simulation. A time history curve, as given in [282] and documented in Figure A.7, Page 224, is taken as pressure input. It is applied to element facets within a 165.1 mm diameter around the center of the plate. Instead of modeling the constraint by the metallic plate, a simple translational boundary in the orthogonal direction is defined at the slab's rear side at all nodes lying on a circle with the appropriate radius.

Figure 4.16 shows the crack pattern of the two tests as snapshots of the high-speed recording. Comparable simulation results are shown in Figure 4.17. For the standard value of $G_F = 30 \text{ J/m}^2$ the number of cracks is obviously underestimated in the case of low pressure loading (left). Reducing this value to 5 J/m^2

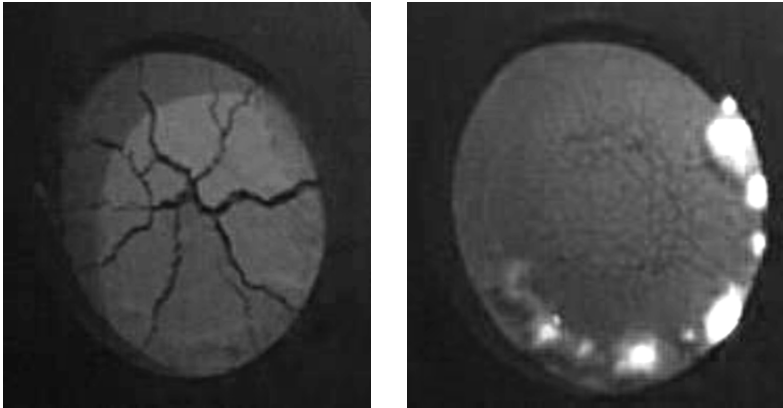


Figure 4.16: Snap-shots from high-speed-video for two tests: no. 30 ($p_p = 3.7$ MPa, $b = 50.8$ mm) and no. 36 ($p_p = 26.9$ MPa, $b = 25.1$ mm, refer to Figure 4.15) from [9, 282]. The point in time is unknown.

improves the results considerably, refer to the small inset. The overall trend that cracking increases with loading is clearly discernible.

The diagram in Figure 4.18 shows the development of individual fragments for the high-pressure test 36. Five simulations have been performed for this test, with a different virtual specimen each ("A" to "E"). Shown in the figure is the average with the min/max values from these simulations. After 5 ms the fragmentation is almost complete. Since fragments emerge due to erosion of elements, the second curve in this diagram is of peculiar interest. It shows the total mass within the model. In the current implementation, the mass of nodes is only deleted if the node itself is completely disconnected. On average 13 % of the total mass vanishes during fragmentation, which is an acceptable value. In the experiments, only 65 % of the mass was recovered although even debris pieces with a mass down to 0.005 g were physically collected (corresponding roughly to spheres with a diameter of 0.8 mm!).

Figure 4.19 shows the break-up of specimen "A" at different points in time and highlights the emergence of a large number of fragments of varying sizes. Although the total number of fragments collected was considerably higher in the tests than in the simulation, their mass distribution, as compared in Figure 4.20,

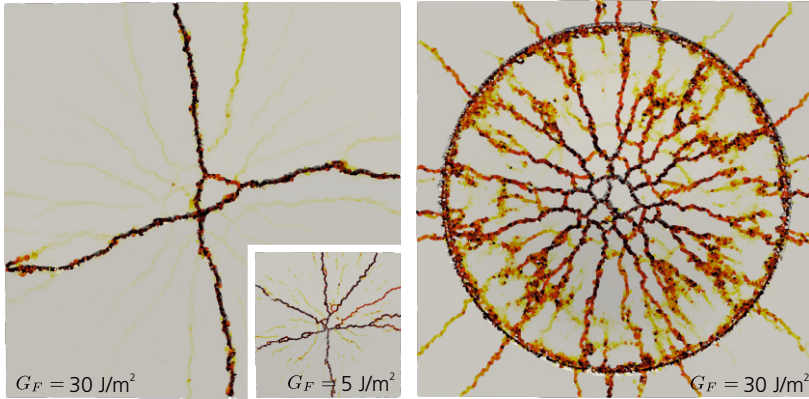


Figure 4.17: Snap-shots from simulation for test no. 30 (left, at 1.5 ms) and no. 36 (right at 0.5 ms, specimen “A”), as in Figure 4.16. In all shown application examples, a fracture energy of 30 J/m^2 was used. With this value, however, the number of cracks is underestimated for the low pressure. There, a value of 5 J/m^2 (inlay, left) delivers much better results.

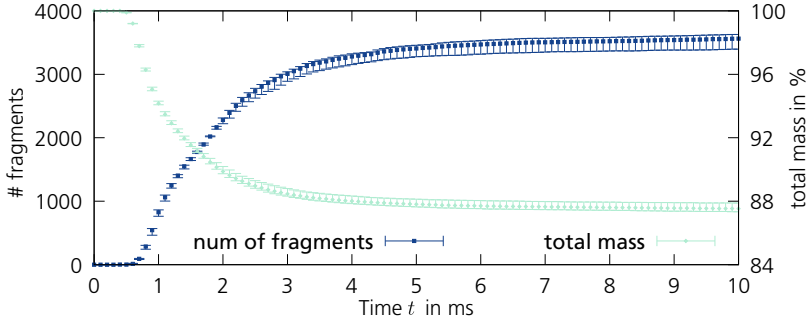


Figure 4.18: Number of fragments and total model mass over time. Average value with min/max values from five virtual specimens.

agrees satisfactorily. Unfortunately, the raw data of the experimental values plotted are not available and the authors report a nonuniform bin definition in their evaluation. Therefore, the simulation results could not be ordered in the same bins. However, the general trend of an exponential distribution in the central mass range is clear. Although the scaling is logarithmic, the probability

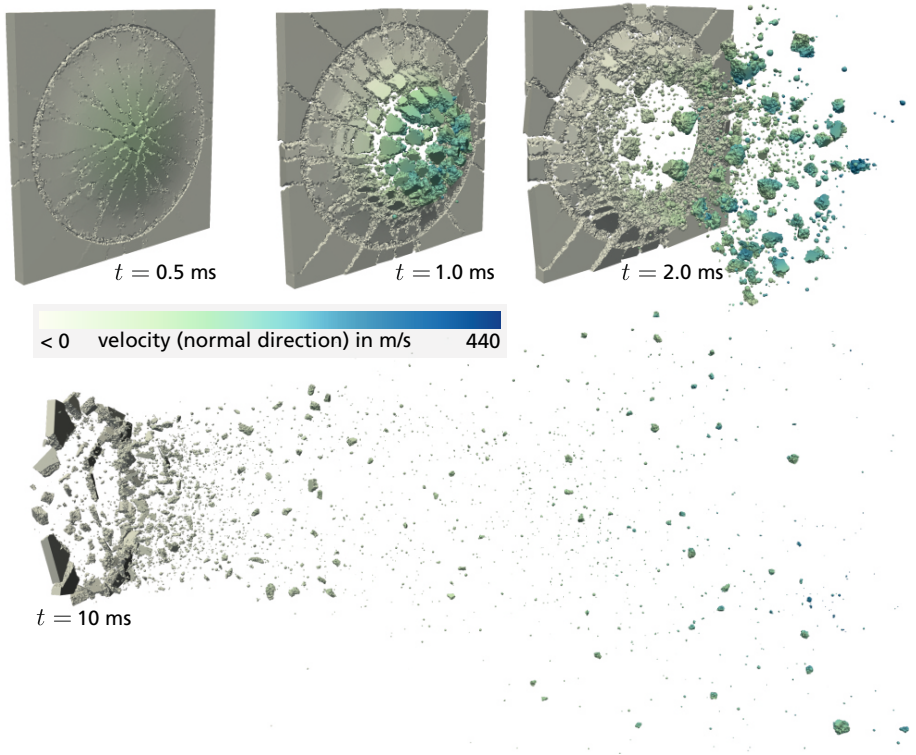


Figure 4.19: Development of fragments at distinct point in times, virtual specimen A.

densities in the range of approximately 0.8 to 10 g match the experimental results well. On the other hand, the simulation underestimates the number of very small pieces and overestimates fragments with higher mass, which are more harmful from a safety perspective. Surely one has to consider that some side effects, such as secondary breaking after initial impact on the ground and rebound, are not covered in the simulation. Overall, the results are very satisfying, and one does not need too much imagination to ponder about further improvements by a more careful fitting of material parameters.

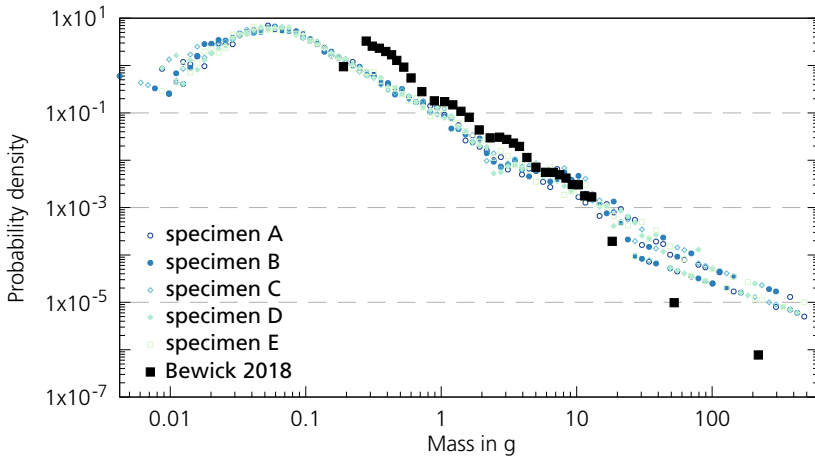


Figure 4.20: Debris mass distribution for test 36. Experimental values (black) and values from five simulations.

4.4 Summary and way forward

The preceding work has outlined an efficient approach for modeling the fracture and debris ejecta of concrete under dynamic loading. Although there is still room for improvement, the foregoing results have shown that the major features of fragmentation are satisfactorily covered: Correct crack paths and branching, accurate fragment sizes and velocities, and an overall fragment distribution with conforming characteristics compared to experiments. It was shown that with this approach results are derived, which are up today incomparable and usable to analyze the effects of debris throw on a new level.

Nevertheless, especially for indoor detonation, it is known that the confined space, its energy dissipation capacity, and potential vent openings have a major implication on the actual pressure distribution and consequently on the fragments initial conditions. It follows that in some situations not only regions of interest have to be considered but also surrounding structures. Depending on the rise time of the pressures, they may not only influence the pressure but may also be an important constraint to the meso domain. Chapter 5 will now turn to the question of how the two scales can be combined efficiently and accurately.

5 Formulation of a multiscale framework for wave propagation codes⁶⁰

The previous chapter closes with the remark that it might be necessary to not only focus on a small to medium-sized meso domain, but that the surrounding structure might influence the mechanical behavior of the region of interest. While explosions in confined spaces are the basic motivation to do so, a coupling of two scales with wave propagation on both might be helpful not only for the specific objective pursued in this thesis but for several other situations. Consider, for example, the use of high-strength polyethylene in human safety vests. If fired on in experiments, the actual penetration process is very local and features several mechanical processes on a lower material scale. Yet the overall ballistic performance depends as well on a membrane stress state due to the gross deformation. In order to decrease computational efforts, one might conceive to model the local effects on a microscale, whereas the membrane forces are considered by a connected macro domain. More generally, every engineer has to cope with the fact that some regions of a model are more important than others. Reducing time and costs by combining different mesh sizes is an important aspect of numerical analysis, hence a coupling of two disparate meshes has always a benefit in itself. Yet for the consideration of wave propagation on both scales, together with the ability to model fragmentation, no current coupling seems to be efficient enough. After reviewing some of the prominent concepts in literature, an existing coupling is outlined, followed by the proposal of a novel coupling scheme. Although the coupling will be applied here to concretes macro- and mesoscale, the more general term “microscale” will be used in the following to designate the lower material scale.

⁶⁰ Some of the content of this chapter, notably sections 5.1 and 5.3, have already been published in [284]. They are here rephrased and expanded.

5.1 Review of multiscale approaches

Taking a bird's eye view, multiscale analysis may be divided into three basic categories; see Figure 5.1: (a) hierarchical, (b) concurrent, and (c) mixed methods. The latter are often very particular solutions and will not be discussed further. *Hierarchical* methods are sometimes more broadly referred to as “indirect”, “information-passing”, “sequential”, “serial” or “parameter-passing” [285, 286], and – depending on the field – as “coarse-graining” [287]. The term *concurrent* is in some works replaced by “direct”, “embedded”, “integrated”, or “hand-shaking” methods [163]. In the following, only some remarkable representatives of the underlying ideas will be mentioned, together with concepts closely related to this work.⁶¹ As this thesis focuses only on numerical approaches, analytical homogenization techniques will be completely omitted.

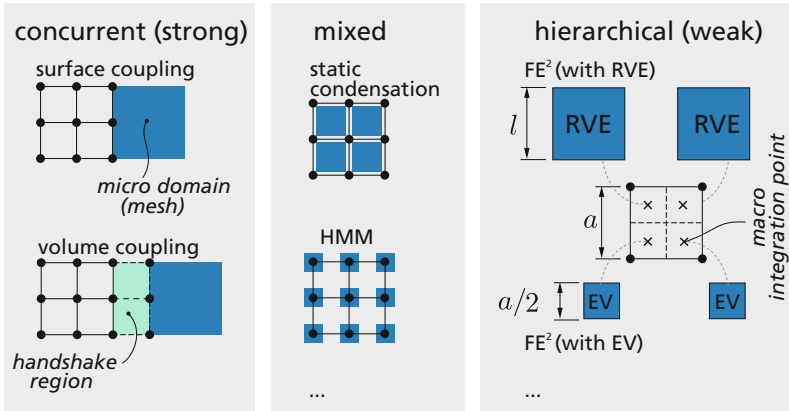


Figure 5.1: Rough overview over the basic multiscale categories. In concurrent strategies, schemes differ mainly between surface and volume coupling, whereas for mixed approaches a variety of different schemes exist. Exemplified adumbrated are only static condensation and the heterogeneous multiscale method (HMM) [289]. For hierarchical methods, only the most famous candidate, the FE^2 class, is shown. Most of these approaches are based on the definition of RVEs, with the notable exception of the works of Gitman et al., who employs equivalent volumes (EV) [290].

⁶¹ Reference [288], a book chapter by Horstemeyer, is to the author's knowledge currently still the most comprehensive broad review of multiscale methods, covering over 300 references from different disciplines and may be a good starting point for interested readers.

5.1.1 Hierarchical approaches

Hierarchical methods rely on the homogenization of the microscale response, which is then infused into the macroscale. The least flexible of these schemes is a fully hierarchical coupling, where the microscale response is precalculated for multiple load cases and stored in a response map [291–293], or employed to determine a yield surface [171]. If a certain load regime is reached, the precalculated solution is used. In more advanced schemes, the microscale can be calculated on the fly if a relevant load case is detected, which was not processed beforehand.

The most common hierarchical processes are semi-concurrent methods that homogenize the micromodel on the fly. If both scales are discretized by finite elements, these approaches are labeled FE^2 -methods, a term coined by *Feyel* [294, 295]. The main idea is that a representative volume element (RVE), representing the microscale, is attached to each material point on the macroscale – which corresponds to Gaussian integration points in the context of finite elements (see the schematic sketch in Figure 5.1, right). Typically, the deformation gradient is passed down from the macroscale to the RVE in which the structural response of the heterogeneous material is calculated. Afterwards, homogenized parameters – generally stresses and strains averaged according to the condition of Hill [296] – are passed back to the macroscale. Differences between the methods consist mainly in the way how the deformation state is applied, how the microscale is homogenized, and whether only first- or even higher-order variables are passed between the scales. Examples are, e.g., [297–300] for first-order and [301] for a second-order FE^2 -method. These methods are well suited not only to derive the bulk behavior of a material, but were used extensively to determine the traction-separation law of cohesive zones on the macroscale, e.g., [200, 302–307]. The reader is referred to the review papers by [308] and [309, 310], which give a detailed and extensive overview of multiscale methods and current examples.

Hierarchical schemes have the decisive advantage that they often inherit a strong parallel characteristic. It is hence very easy to implement full parallel algorithms that exploit modern High-Performance Computing capabilities. On the other hand, especially FE^2 approaches exhibit two serious disadvantages: If softening – or more generally damage – shall be described as part of the material response, one major premise is the validity of the RVE, which means that the observed material behavior is independent of the size of the observation window. *Gitman* et al. have demonstrated that a RVE no longer exists as soon as strain localization

occurs, and therefore the use of RVEs in the nonlinear analysis of this material class fails to deliver objective results [311]. This fact is supported, among others, in [312] and [313]. Since damage develops in general over all length scales, *Geers et al.* state more broadly that such processes violate the principle of separation of scales [310], which is an important presupposition of the validity of standard FE² techniques.⁶²

A second disadvantage, especially with regard to wave propagation on both scales and the focus on concrete, is the size of the RVEs in hierarchical approaches. The propagation of (shock) waves on the macroscale limits the *maximum* element size on this scale to resolve the almost discontinuous pressure jump at the wave-front. On the other hand, the RVE size is bound to a *minimum* size [319]: The RVE should have a size l (refer to Figure 5.1) which leads to a homogeneous macroscopic behavior for a considered response function. *Lacy et al.* note that the size of a representative observation window may be different, depending on the response function considered, with sizes for the resolution of functions connected to damage at the upper end [320]. In this regard, *Bažant et al.* measured the width of the fracture process zone of concrete [321]. They found a corresponding width of the process zone of around 2.7 times the maximum aggregate size. Later *Weerheijm et al.* gave an estimate of the fracture process zone in dynamic tensile tests approximately 3 times the maximum aggregate size [87], while the initial suggestion in [169] was 4 times the largest inhomogeneity. Since a RVE should encompass the fracture process zone, this value indicates a minimum size for a RVE. For an arbitrary standard concrete with a maximum aggregate size of, e.g., 16 mm, this would lead to a RVE size of at least $l = 43.2$ to 64 mm. Considering wave propagation, two investigations maintain that an RVE should even have a minimum edge length of approximately 70 mm to reflect homogeneous properties [104, 218]. However, in practical situations, the preferred edge length

⁶² Two solutions exist to mitigate this problem: Several authors split the microscale response into a discontinuous and a homogeneous bulk portion and thereby retain objectivity of the results [287, 306, 312–315]. *Nguyen et al.* have shown that the existence of an objective RVE can be maintained when applying this technique [316]. However, it seems that these concepts are hardly applicable for cases with multiple, even intersecting cracks, as is the case for brittle materials under high dynamic loading. The second remedy is to abstain from the application of a RVE and to couple an equivalent volume to the underlying material point, as suggested by *Gitman* in [290, 317, 318]. Instead of a RVE with an arbitrary size, this approach refers to models on the microscale that encompass a volume equal to the volume the corresponding macro integration point represents, Figure 5.1, right. Yet this method then comes close to concurrent coupling approaches, where the macro volume is replaced by the micro volume. The main difference is that the coupled volumes proposed by *Gitman* are independent of each other and information is exchanged only with its attached macroscale material volume (represented by an integration point).

of macro element a is generally around $a \approx 20 \dots 30$ mm. But representing each integration point of the macro mesh with a RVE larger than the macro element edge length would lead to virtually overlapping material regions, which introduces simply much more (unnecessary) computational effort than the use of equivalent volumes. This is acceptable as long as the computational costs for the solution of the microscale problem are low due to an implicit solution scheme, although even this is by some authors disputed for practical cases, see, e.g., [291]. As soon as an explicit scheme is applied, the overall computational time will be unnecessarily high, especially in three dimensions. Therefore, concurrent approaches may be a better alternative and have historically been the choice for dynamic problems.

5.1.2 Concurrent approaches

In order to discuss concurrent approaches, consider a continuous body Ω , which is divided into a macro domain Ω_M and a micro domain Ω_m : $\Omega = \Omega_M \cup \Omega_m$, as shown in Figure 5.2, left. For $\mathbf{x}_I = \mathbf{x}_i$, each domain has an interface Γ to the other domain. In this context, capital-letter subscripts denote from now on entities on the macro and small subscripts refer to the micro domain (swapping to superscripts might sometimes be necessary to make room for other subscripts).

Most concurrent methods apply one of two options: Either the domains abut each other and *surfaces* are coupled, or the domains overlap in a finite interface region and, consequently, *volumes* are coupled. The latter is often applied in atomic to continua (ATC) couplings, where regions of interest are modeled with molecular dynamics (MD) and an attached FE-domain enlarges the total domain. The overlapping regions are commonly referred to as “handshake” or “bridging” regions, e.g., [322, 323]. In these references, weighted energy functionals of the subdomains in the handshake region are linearly superposed. A similar approach, but at a more structural level, is pursued in the “Arlequin-method” [324, 325], a versatile concept that yields appealing results for different problems, including dynamic applications [326, 327].

“Domain decomposition” schemes are often able to cope with different scales, disparate meshes, and even different time scales. Therefore, they may be well classified under concurrent methods. An example of a classical decomposition technique worth mentioning with regard to the umbrella term “volume coupling” is the alternating Schwarz algorithm, which has actually been occasionally applied

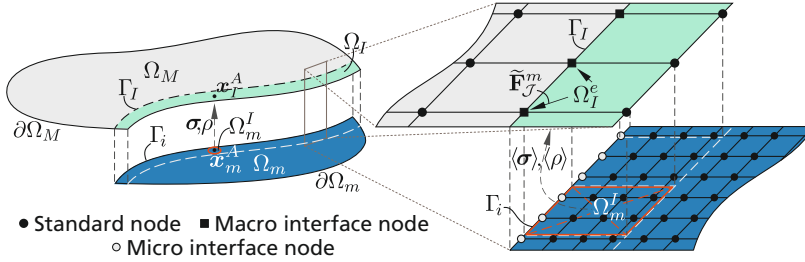


Figure 5.2: Split of body Ω into a macro Ω_M and a micro domain Ω_m . Each domain has an interface Γ to the other domain with $\mathbf{x}_I = \mathbf{x}_i$. For the coupling developed here, the macro domain is slightly enlarged by an interface region Ω_I , which overlaps partly the micro domain. A point \mathbf{x}_I^A in the interface region receives its variable values by averaging a finite material portion Ω_m^I around its coincident counterpart \mathbf{x}_m^A in the micro domain. Right: Detail of discretized domains. The averaged values are transferred to the interface elements and deliver proper forces to the macro domain. Figure from [284].

to multiscale problems, e.g., [328]. In this algorithm, the continuity conditions at the interface are fulfilled by iteratively solving the subdomains together with special interface conditions in a small, overlapping regime. In [329], this method was applied to linear transient ATC problems without iterations by carefully choosing the interface operators.

As the second major class, *surface coupling* is employed in different works. Here, the domain boundaries are adjacent to each other, and continuity has to be ensured between the contiguous domains. The differential formulation of the momentum balance for the split body then reads (neglecting body forces):

$$\rho_M \ddot{\mathbf{u}}_M - \nabla \cdot \boldsymbol{\sigma}_M = \mathbf{0} \text{ in } \Omega_M \quad (5.1a)$$

$$\rho_m \ddot{\mathbf{u}}_m - \nabla \cdot \boldsymbol{\sigma}_m = \mathbf{0} \text{ in } \Omega_m \quad (5.1b)$$

$$\dot{\mathbf{u}}_m = \dot{\mathbf{u}}_M \text{ on } \Gamma \quad (5.1c)$$

Boundary conditions at the body's boundary $\partial\Omega$ may be defined, such as prescribed displacements \mathbf{u}^e on $\partial\Omega^u = \partial\Omega_M^u \cup \partial\Omega_m^u$, tractions \mathbf{t}^e on $\partial\Omega^t = \partial\Omega_M^t \cup \partial\Omega_m^t$ with $\partial\Omega = \partial\Omega^t \cup \partial\Omega^u$, $\partial\Omega^t \cap \partial\Omega^u = \emptyset$ and $\partial\Omega_M^u \cap \partial\Gamma_I =$

$\emptyset, \partial\Omega_m^u \cap \partial\Gamma_i = \emptyset, \partial\Omega_M^t \cap \partial\Gamma_I = \emptyset, \partial\Omega_m^t \cap \partial\Gamma_i = \emptyset$, together with initial conditions in the domain:

$$\mathbf{u}_M = \mathbf{u}_M^e \text{ on } \partial\Omega_M^u, \mathbf{u}_m = \mathbf{u}_m^e \text{ on } \partial\Omega_m^u, \quad (5.2a)$$

$$\mathbf{t}_M = \mathbf{t}_M^e \text{ on } \partial\Omega_M^t, \mathbf{t}_m = \mathbf{t}_m^e \text{ on } \partial\Omega_m^t, \quad (5.2b)$$

$$\dot{\mathbf{u}}_M(t_0) = \dot{\mathbf{u}}_m(t_0) = \mathbf{0}, \mathbf{u}_M(t_0) = \mathbf{u}_m(t_0) = \mathbf{0} \text{ in } \Omega \quad (5.2c)$$

A natural choice to enforce condition (5.1c) is the application of Lagrange multipliers (LM). Indeed, they are widely used in this context, e.g., in the mortar element method [330, 331], and in several domain decomposition concepts. Examples are the FETI framework [332, 333] or references [38, 334, 335]. Local multipliers are used to couple domain boundaries together with a global interface in [336, 337] and are applicable (as are the aforementioned works) to combine two or more scales, disparate meshes, and even different time scales [38, 337]. Less flexible but feasible is the direct formulation of constraint equations, as in [198, 308].

5.1.3 Wave propagation in multiscale methods

A large portion of recent *hierarchical* multiscale methods found in the literature consider quasi-static problems, which are solved by standard implicit methods. Only a few approaches include the transmission and propagation of waves, which is necessary for the consideration of high dynamic loading. Souza et al. model in this context the behavior of composite structures [298, 338, 339] and Karamnejad et al. are concerned with the wave propagation in concrete [315]. However, both methods presuppose that the wavelength of the transmitted signal is substantially larger than the local micro length scale, which allows a quasi-static solution of the boundary value problem on the microscale. Later, the approach in [315] was extended by including inertia effects on the microscale [340]. Nevertheless, transient stresses on the microscale are not considered in this reference. Snozzi applies a multiscale method to determine the cohesive traction-separation law for concrete and solves both scales with explicit time integration [306]. Even there, wave propagation through the bulk material is not considered, since only the cohesive laws at macrocracks are of interest.

As a remarkable exception, the work of Knap et al. should be mentioned [341]. This contribution aims not to solve a particular problem at hand, but rather to

establish a general, abstract framework for a hierarchical solution of dynamic problems and focuses on the algorithmic implementation of generic functions, which establish the coupling of two general scales. The principal functionality of the framework is demonstrated in the paper by simulating a Taylor impact test. However, the authors admit that the solution is very costly, thereby underlying the above reasoning that hierarchical schemes are currently not attractive candidates for coupling in wave propagation problems.

Concurrent couplings are – in contrast – often used for the investigation of dynamic scenarios. Indeed, most of the references mentioned above inherently deal with dynamic problems. In these schemes, wave propagation is naturally allowed and does not add an extrinsic level of difficulty. Instead, only the case of reflections at the interface due to incompatible wave lengths has to be handled – an issue to be discussed in more detail later in Section 5.4. As mentioned above, material failure can be considered on a lower scale without difficulties. Even cracks that cross the interface can be approximated with some success, as will be shown in the last application example, Section 6.3. Consequently, the concept of concurrent multiscale techniques seems to be the most appropriate candidate for the analysis of interest.

Given the large number of already available solutions, one may legitimately raise the question of whether one of these might not be applicable to the aim of this thesis. Yet most of these concepts rely on LM in either way. Admittedly, LM are an attractive numerical instrument since they fulfill the continuity condition exactly, thereby delivering an accurate solution of the discretized equation of motion. But, as will be seen below, they necessitate the solution of a global system of equations. However, recalling the remarks in Chapter 2: the basic advantage of hydrocodes is the direct solution scheme. Storing large matrices and solving global systems of equations abandon the attractive gist of these codes and slow them down considerably. Bearing in mind the huge computational effort needed to solve only the meso domain in the examples shown in Chapter 4, one should strive for a solution that is as efficient as possible. Translated in a comprehensible claim: The coupling should add as few additional operations as possible – per cycle and as a whole. This is the aim pursued in the development of a weak staggered concurrent coupling, which will be detailed in Section 5.3. Beforehand, an already existing surface coupling based on LM is briefly described to highlight its characteristics in case of explicit time integration and to prepare the basis of a comparison with the new development.

5.2 An existing coupling based on Lagrange multipliers

LM are regularly used in the context of the FEM to fulfill certain additional constraints, such as imposed displacements or the coupling of degrees of freedoms (DOF) [29]. For the coupling of two domains, in the following, the generic decomposition approach described by *Combescure* et al. [38, 334], will be adapted to nonlinear wave propagation problems in two domains.

The body Ω (Figure 5.2) may initially be undivided. The reference problem for this body is then defined as: “Find the solution of the displacement field, \mathbf{u} , and the stress field, $\boldsymbol{\sigma}$, which satisfy the boundary conditions, dynamic equilibrium and constitutive material laws” [342]. The weak form of the problem may be derived by formulating the continuous Lagrange-functional for the discretized body:

$$\mathcal{L}(\mathbf{u}, \dot{\mathbf{u}}) = \frac{1}{2} \dot{\mathbf{u}}^T \mathbf{M} \dot{\mathbf{u}} - \Phi(\mathbf{u}) + \mathbf{R}^T \mathbf{u} \quad (5.3)$$

As before, \mathbf{u} is the vector of displacements, \mathbf{M} the mass matrix and \mathbf{R} the vector of external forces; $\Phi(\mathbf{u})$ denotes the strain energy density. To consider additional constraints, such as interfaces between subdomains, let \mathbf{C} be a coupling matrix and $\boldsymbol{\lambda}$ the vector of LM, which can be interpreted as forces in the following. The energy contribution of the LM is $\mathcal{L}_{\boldsymbol{\lambda}}(\mathbf{u}) = \boldsymbol{\lambda}^T \mathbf{C} \mathbf{u}$, which can be added to the functional stated above [38]. Let Ω_M now be a macro domain, discretized with $n_{\mathcal{E}}^M$ finite elements \mathcal{E} and $n_{\mathcal{N}}^M$ nodes \mathcal{N} . Likewise, Ω_m shall be an adjoining micro domain, discretized with $n_{\mathcal{E}}^m$ finite elements and $n_{\mathcal{N}}^m$ nodes. Elements on the microscale are assumed to be much smaller than those in the macro domain. The interface is hence defined by n_i nodes on the micro, and n_I nodes on the macro domain, $n_i \gg n_I$. Let further, for later discussion, denote the dimension of the problem with d , where $d = 2$ for \mathbb{R}^2 and 3 for \mathbb{R}^3 . The number of degrees of freedom per domain is hence $n_{DOF} = dn_{\mathcal{N}}$.

Writing the Lagrange functional for both domains, and applying the principle of least action, delivers an expression for the total problem (see [343] for a detailed derivation):

$$\mathbf{M}_M \ddot{\mathbf{u}}_M(t) = \mathbf{R}_M(t) - \mathbf{F}_M(t) + \mathbf{F}_I(t) \quad \forall t \in [t_0, t_e] \quad (5.4a)$$

$$\mathbf{M}_m \ddot{\mathbf{u}}_m(t) = \mathbf{R}_m(t) - \mathbf{F}_m(t) + \mathbf{F}_I(t) \quad \forall t \in [t_0, t_e] \quad (5.4b)$$

$$\mathbf{C} \ddot{\mathbf{u}}(t) = \mathbf{0} \quad \forall t \in [t_0, t_e] \quad (5.4c)$$

$$\mathbf{F}_I(t) = \mathbf{C}^T \boldsymbol{\lambda}(t) \quad \forall t \in [t_0, t_e] \quad (5.4d)$$

along with the boundary and initial conditions, equation (5.2), and the combined vector $\ddot{\mathbf{u}} = [\ddot{\mathbf{u}}_M \ \ddot{\mathbf{u}}_m]^T$. The mass matrices are diagonal matrices, as explained in Chapter 2. Obviously, the coupling of both domains is achieved by adding coupling forces \mathbf{F}_I to each domain. This vector is non-empty only for DOF of the interface nodes n_i and n_I .

Combesure et al. formulate their approach flexible with regard to the choice of the kinematic coupling variable at the interface and define $\mathbf{W}_z(t) = \mathbf{W}_z(t - \Delta t) + \alpha_z \ddot{\mathbf{u}}(t)$. In this definition, α_z , $z = 1, 2, 3$, is a time integrator derived from the applied time integration method (e.g., Newmark scheme). If the same time integrator is used on both domains, the choice of the coupling variable does not matter, since in case of, e.g., coupled accelerations, velocities, and displacements are compatible as well. Coupling is now enforced by demanding $\mathbf{C} \mathbf{W}_z = \mathbf{0}$ (refer to equation 5.4c). From that it follows for the definition of the linear coupling matrix: $\mathbf{C} \in \mathbb{R}^{dn_i} \times \mathbb{R}^{d(n_i+n_I)}$, $\mathbf{C} = [\mathbf{C}_M \ \mathbf{C}_m]$, $\mathbf{C}_M \in \mathbb{R}^{dn_i} \times \mathbb{R}^{dn_I}$, $\mathbf{C}_m \in \mathbb{R}^{dn_i} \times \mathbb{R}^{dn_i}$. It shall be filled such that $\mathbf{C} \mathbf{1} = \mathbf{0}$ and $\mathbf{C}_M \mathbf{1} = \mathbf{1}$, as well as $\mathbf{C}_m = -\mathbf{I}$.⁶³ $\mathbf{1}$ is a vector with a suitable length, filled with ones, and \mathbf{I} denotes the identity matrix.

⁶³ To demonstrate the coefficients of the matrix, consider a 1D system with two macro DOF u_1^M and u_2^M . Five micro DOF should be coupled to the system, with micronodes 3 and 7 being coincident to the two macronodes. Micronodes 4, 5 and 6 are equally spaced between. The coupling is then enforced by:

$$\mathbf{C} \mathbf{u} = \begin{bmatrix} 1 & 0 & -1 & 0 & 0 & 0 & 0 \\ 0.75 & 0.25 & 0 & -1 & 0 & 0 & 0 \\ 0.5 & 0.5 & 0 & 0 & -1 & 0 & 0 \\ 0.25 & 0.75 & 0 & 0 & 0 & -1 & 0 \\ 0 & 1 & 0 & 0 & 0 & 0 & -1 \end{bmatrix} \begin{bmatrix} u_1^M \\ u_2^M \\ u_3^m \\ u_4^m \\ u_5^m \\ u_6^m \\ u_7^m \end{bmatrix} = \mathbf{0}$$

In the leapfrog scheme, velocities are the primary solution variable. Therefore, the case of $z = 2$ is considered below. For this case, simply $\alpha_2 = \Delta t$ (the index z and time variable (t) will be omitted in the following and the shortcut notation $\mathbf{W} = \mathbf{W}_2(t)$ defined. Furthermore, all expressions are formulated at cycle (n) – only values at a *different* step are explicitly marked).

With $\mathbf{W} = [\mathbf{W}_M \ \mathbf{W}_m]^\top$, the EoM for the coupled system in matrix notation reads:

$$\begin{bmatrix} \mathbf{M}_M & \mathbf{0} & \mathbf{C}_M^\top \\ \mathbf{0} & \mathbf{M}_m & \mathbf{C}_m^\top \\ \mathbf{C}_M & \mathbf{C}_m & \mathbf{0} \end{bmatrix} \begin{bmatrix} \ddot{\mathbf{u}}_M \\ \ddot{\mathbf{u}}_m \\ \lambda \end{bmatrix} = \begin{bmatrix} \mathbf{R}_M - \mathbf{F}_M \\ \mathbf{R}_m - \mathbf{F}_m \\ \mathbf{C}\mathbf{W}/\Delta t \end{bmatrix} \quad (5.5)$$

Defining combined matrices for both domains:

$$\mathbf{M} = \begin{bmatrix} \mathbf{M}_M & \mathbf{0} \\ \mathbf{0} & \mathbf{M}_m \end{bmatrix}, \quad \ddot{\mathbf{u}} = \begin{bmatrix} \ddot{\mathbf{u}}_M \\ \ddot{\mathbf{u}}_m \end{bmatrix}, \quad \mathbf{F}_\Sigma = \begin{bmatrix} \mathbf{R}_M - \mathbf{F}_M \\ \mathbf{R}_m - \mathbf{F}_m \end{bmatrix}$$

gives the EOM in compact form as:

$$\begin{bmatrix} \mathbf{M} & \mathbf{C}^\top \\ \mathbf{C} & \mathbf{0} \end{bmatrix} \begin{bmatrix} \ddot{\mathbf{u}} \\ \lambda \end{bmatrix} = \begin{bmatrix} \mathbf{F}_\Sigma \\ \mathbf{C}\mathbf{W}/\Delta t \end{bmatrix} \quad (5.6)$$

Introducing

$$\mathbf{M}_{LH} = \begin{bmatrix} \mathbf{M} & \mathbf{C}^\top \\ \mathbf{C} & \mathbf{0} \end{bmatrix}$$

equation (5.6) can be solved by inverting \mathbf{M}_{LH} :

$$\begin{bmatrix} \ddot{\mathbf{u}} \\ \lambda \end{bmatrix} = \mathbf{M}_{LH}^{-1} \begin{bmatrix} \mathbf{F}_\Sigma \\ \mathbf{C}\mathbf{W}/\Delta t \end{bmatrix} \quad (5.7)$$

\mathbf{M}_{LH} is constant. Consequently, the costly inversion has to be done only at the beginning of the computation. Furthermore, it suffices to assemble equation (5.7) only for the coupled DOF and to solve all others independently with the standard EOM (equation 2.8). Then it follows for the size of the matrix \mathbf{M}_{LH} : $\mathbf{M}_{LH} \in \mathbb{R}^{d(2n_i+n_I)} \times \mathbb{R}^{d(2n_i+n_I)}$ and the vector $[\mathbf{F}_\Sigma \ \mathbf{C}\mathbf{W}]^\top \in \mathbb{R}^{d(2n_i+n_I)}$. The *additional* effort per cycle consists then in collecting the coefficients of the right-hand vector in equation (5.6) along with the matrix multiplication $\mathbf{C}\mathbf{W} \in \mathbb{R}^{dn_i}$ and the subsequent multiplication with \mathbf{M}_{LH}^{-1} .

For the naive implementation of a matrix multiplication of two matrices $\mathbf{A} \in \mathbb{R}^l \times \mathbb{R}^m$ and $\mathbf{B} \in \mathbb{R}^m \times \mathbb{R}^n$ the number of necessary operations is of order $\mathcal{O}(mnl)$. Therefore, in the worst case, the necessary operations for establishing the vector $\mathbf{C}\mathbf{W}$ is of order $\mathcal{O}(d^2 n_i (n_i + n_I))$ and – with the subsequent multiplication with \mathbf{M}_{LH}^{-1} – of total order $\mathcal{O}(d^2 [(2n_i + n_I)^2 + n_i (n_i + n_I)])$. Considering the fact that usually $n_i \gg n_I$, one can neglect n_I and finally gets $\mathcal{O}(5d^2 n_i^2)$.

Combes et al. propose a further simplification, leading to an additional reduction in the dimensions of the matrices. The system given in equation (5.6) is split into a *free* problem – the individual solution of the uncoupled subdomains – and a *constraint* system, presuming $\ddot{\mathbf{u}} = {}^f\ddot{\mathbf{u}} + {}^l\ddot{\mathbf{u}}$. The *free* problem then reads:

$$\begin{bmatrix} \mathbf{M} & \mathbf{0} \\ \mathbf{0} & \mathbf{0} \end{bmatrix} \begin{bmatrix} {}^f\ddot{\mathbf{u}} \\ \mathbf{0} \end{bmatrix} = \begin{bmatrix} \mathbf{F}_\Sigma \\ \mathbf{0} \end{bmatrix} \quad (5.8)$$

From $\mathbf{C}\mathbf{W} = \mathbf{0}$ it follows that $\mathbf{C}^f\ddot{\mathbf{u}} = -\mathbf{C}^l\ddot{\mathbf{u}}$. Recalling that the velocities are centered at the half time step, one can write $\mathbf{W}^{(n+1/2)} = \mathbf{W}^{(n-1/2)} + \Delta t \ddot{\mathbf{u}}^{(n)}$ and formulate the *constraint* problem:

$$\Delta t \begin{bmatrix} \mathbf{M} & \mathbf{C}^\top \\ \mathbf{C} & \mathbf{0} \end{bmatrix} \begin{bmatrix} {}^l\ddot{\mathbf{u}} \\ \boldsymbol{\lambda} \end{bmatrix} = \begin{bmatrix} \mathbf{0} \\ \mathbf{C}(\mathbf{W}^{(n-1/2)} + \Delta t {}^f\ddot{\mathbf{u}}) \end{bmatrix} \quad (5.9)$$

This approach allows for an independent, parallel solution of both domains, without considering the coupling. After the free accelerations, ${}^f\ddot{\mathbf{u}}$, are determined, the constraint (or “link”) accelerations, ${}^l\ddot{\mathbf{u}}$, have to be calculated, which are a correction to the free accelerations. From the first equation of the matrix system, equation (5.9), follows: ${}^l\ddot{\mathbf{u}} = -\mathbf{M}^{-1}\mathbf{C}^\top\boldsymbol{\lambda}$. Inserting this expression in the second row $\Delta t \mathbf{C}^l\ddot{\mathbf{u}} = \mathbf{C}(\mathbf{W}^{(n-1/2)} + \Delta t {}^f\ddot{\mathbf{u}})$, delivers:

$$\Delta t \mathbf{C}\mathbf{M}^{-1}\mathbf{C}^\top\boldsymbol{\lambda} = -\mathbf{C}(\mathbf{W}^{(n-1/2)} + \Delta t {}^f\ddot{\mathbf{u}}) \quad (5.10)$$

Defining the constant interface operator $\mathbf{H} = \mathbf{C}\mathbf{M}^{-1}\mathbf{C}^\top$, $\mathbf{H} \in \mathbb{R}^{dn_i} \times \mathbb{R}^{dn_i}$, allows rewriting equation (5.9):

$$\Delta t \begin{bmatrix} \mathbf{M} & \mathbf{C}^\top \\ \mathbf{0} & \mathbf{H} \end{bmatrix} \begin{bmatrix} {}^l\ddot{\mathbf{u}} \\ \boldsymbol{\lambda} \end{bmatrix} = \begin{bmatrix} \mathbf{0} \\ -\mathbf{C}(\mathbf{W}^{(n-1/2)} + \Delta t {}^f\ddot{\mathbf{u}}) \end{bmatrix} \quad (5.11)$$

Solving for λ then yields:

$$\lambda = -\frac{1}{\Delta t} \mathbf{H}^{-1} \mathbf{C} \left(\mathbf{W}^{(n-1/2)} + \Delta t^f \ddot{\mathbf{u}} \right) \quad (5.12)$$

It is not necessary to actually determine λ . Instead, inserting the above solution into ${}^l\ddot{\mathbf{u}} = -\mathbf{M}^{-1} \mathbf{C}^T \lambda$, yields the final expression for the unknown constraint accelerations:

$${}^l\ddot{\mathbf{u}} = -\frac{1}{\Delta t} \mathbf{M}^{-1} \mathbf{C}^T \mathbf{H}^{-1} \mathbf{C} \left(\mathbf{W}^{(n-1/2)} + \Delta t^f \ddot{\mathbf{u}} \right) \quad (5.13)$$

Defining $\mathbf{H}_0 = -\mathbf{M}^{-1} \mathbf{C}^T \mathbf{H}^{-1} \mathbf{C}$ one finally gets:

$${}^l\ddot{\mathbf{u}} = \frac{1}{\Delta t} \mathbf{H}_0 \left(\mathbf{W}^{(n-1/2)} + \Delta t^f \ddot{\mathbf{u}} \right) \quad (5.14)$$

\mathbf{H}_0 again is a constant matrix, which has to be evaluated only once at the start of the calculation. It is of size $d(n_i + n_I) \times d(n_i + n_I)$ and by dn_i rows and columns smaller as \mathbf{M}_{LH} above. The number of operations to solve equation (5.14) therefore is in the worst case $\mathcal{O}(d^2(n_i + n_I)^2)$. However, depending on the number of DOFs, the inversion of \mathbf{H} to yield \mathbf{H}_0 might not be trivial, and might even – considering very large models – not be able to be stored in the main memory.

Conclusion The LM coupling, as described above, allows the coupling of two disparately meshed domains in a proper algorithm. Matrix inversions of constant, sparse matrices have to be executed only at the beginning – as long as the interface topology remains unchanged during simulation! But as soon as erosion or nodesplit occurs in the interface region, computational efforts shoot up: The coupling matrix \mathbf{C} has to be enlarged, as well as \mathbf{M} , followed by re-assembling and inverting \mathbf{H} . Especially the latter operation is very costly and takes – depending on the problem size, of course – a substantial amount of time and memory.⁶⁴ Similarly, matrix multiplications are, in general, of non-linear

⁶⁴ Test runs with large 3D application examples, comparable to the one shown in Section 6.3, have been aborted after one day. Within this time, the matrix inversion has not yet succeeded. Surely, the choice of the decomposition algorithm from the C++ Eigen Library used, might not have been the best, but it was the fastest from previous (smaller) tests. In the same time, the weak staggered coupling, to be introduced in the next section, has already passed several thousand cycles.

order and disproportionately increase the necessary time per cycle with increasing problem size.

5.3 Development of an efficient weak staggered coupling

As an alternative, in the following, a “weak staggered” (WS) coupling is proposed.⁶⁵ It exhibits similarities to schemes commonly used in fluid/structure interaction (FSI) problems, see, e.g., [344, 345]. In staggered FSI problems, the compatibility condition, equation (5.1c), is enhanced by the requirement of stress equilibrium at the interface:

$$\boldsymbol{\sigma}_m \cdot \mathbf{n}_{\Gamma_i} = -\boldsymbol{\sigma}_M \cdot \mathbf{n}_{\Gamma_I} \text{ on } \Gamma \quad (5.15)$$

with \mathbf{n}_{Γ} denoting the normal vector of the interface Γ pointing outward the domain. Whereas the fluid exerts pressure on the embedded solid structure, which consequently moves and delivers a new boundary back to the fluid, this concept is applied here to two solid domains with disparate meshes. More specifically, the macro interface velocity is applied as a boundary condition to the micro interface. The microscale, in turn, delivers tractions to the macro interface, reflecting the resistance of the microscale against deformation, i.e. its stiffness. In a pure macro homogenization, these “tractions” are nothing else than the internal forces of the adjacent macro element (see equation (2.7)). However, in the case of disparate meshes, there is no direct connection and consequently no forces to be summed up at the nodes. To determine proper forces, virtual macro elements are spanned over the micro domain in an additional interface domain Ω_I , partially overlapping the micro and adjoining the macro domain at the common boundary Γ_I , see Figure 5.2 (right) on Page 108. These virtual elements retrieve their stress state from the underlying microscale and thereby transform the current microscale stiffness in the vicinity of the domain border into forces applicable to the macro interface nodes.

⁶⁵ In the review introducing this chapter, a basic distinction was made between “hierarchical” and “concurrent” multiscale methods. However, *Belytschko et al.* distinguish between “weak” and “strong” coupling strategies, where the terms apply to the quality of momentum transfer between the different scales [287]. On the contrary, the term “weak” here expresses the fact that no exact equilibrium between the two scales is sought in each cycle and has nothing to do with momentum transfer. Referring to the latter, the coupling should be classified as “strong”.

Although the interface domain Ω_I can be considered as a bridging domain, there is an important difference to classical bridging or handshake domains since no common energy functional is used. Accordingly, its displacement field does not influence the micro displacement field (except for the interface points) but instead is *defined* by the micro field. Points in this region will be forced to correspond to the movement of the underlying micro domain. A very similar approach was described in [346] in a coupled atomistic and discrete dislocation approach. In this ATC coupling, interface atoms are influenced through a non-local potential by neighboring atoms in a “pad” region, a finite atomistic regime protruding the FE continuum. While the pad atoms are fixed by the movement of the underlying FE domain, the FE interface nodes are determined by the interface atoms, and no common energy functional is employed. Indeed, as the authors note, there is no well-defined energy functional for the coupled system in this case, what – on the other hand – does not matter since “a well-defined energy is not a requirement” ([346, p. 762]). Furthermore, references [347] and [348] describe an approach to couple finite elements with a meshless peridynamics formulation, which exhibits close analogies both to reference [346] and the concept employed here. Again, an interface region consisting of finite elements is used in which peridynamic nodes are embedded. They receive the corresponding displacement field from the finite elements, while coupling forces of each node are added to the surrounding FE-nodes.

In contrast to LM coupling, the staggered solution only approximates the stress equilibrium at the interface, since σ_m in equation (5.15) will be replaced by an averaged micro stress $\langle \sigma_m \rangle$. Nevertheless, the results are very satisfying, as long as this averaged stress state is not too far away from the actual local micro stress state, refer to the examples in Chapter 6. On the other hand, this concept is computationally very efficient. It retains the direct character of the solution scheme, no global system of equations has to be solved, and the number of additional floating point operations is linear with respect to the number of entities on the interface. In fact, the whole approach is strongly motivated by the attempt to follow the solution cycle as closely as possible. Besides keeping the hydrocodes’ efficiency, the implementation is straightforward. It leaves the main core of the solver kernel almost untouched, whereas the LM coupling necessitates a much heavier change. Consequently, the WS coupling can be incorporated into existing hydrocodes with moderate effort. Moreover, topology changes on the interface, e.g., due to cracking, are handled with ease and memory requirements remain more or less the same as without coupling. As a final remark, it should be noted that both scales may be even solved by completely different codes by a simple exchange of forces and velocities, rendering the concept very versatile.

5.3.1 Governing equations

Writing the weak form of the continuous problem, equation (2.4), for the three domains defined in Figure 5.2 delivers simply:

$$\int_{\Omega_M} \delta \mathbf{u} \cdot \rho_M \ddot{\mathbf{u}}_M d\Omega_M + \int_{\Omega_M} \nabla \delta \mathbf{u} : \boldsymbol{\sigma}_M d\Omega_M - \int_{\partial\Omega_M} \delta \mathbf{u} \cdot \mathbf{t}_M d\partial\Omega_M = \mathbf{0} \quad (5.16a)$$

$$\int_{\Omega_I} \delta \mathbf{u} \cdot \rho_I \ddot{\mathbf{u}}_I d\Omega_I + \int_{\Omega_I} \nabla \delta \mathbf{u} : \boldsymbol{\sigma}_I d\Omega_I - \int_{\partial\Omega_I} \delta \mathbf{u} \cdot \mathbf{t}_I d\partial\Omega_I = \mathbf{0} \quad (5.16b)$$

$$\int_{\Omega_m} \delta \mathbf{u} \cdot \rho_m \ddot{\mathbf{u}}_m d\Omega_m + \int_{\Omega_m} \nabla \delta \mathbf{u} : \boldsymbol{\sigma}_m d\Omega_m - \int_{\partial\Omega_m} \delta \mathbf{u} \cdot \mathbf{t}_m d\partial\Omega_m = \mathbf{0} \quad (5.16c)$$

along with the standard initial and boundary conditions already mentioned above (see equation (5.2)) and the compatibility constraint $\dot{\mathbf{u}}_m = \dot{\mathbf{u}}_M$ on Γ_i . For the interface domain, likewise the following conditions hold: $\mathbf{u}_I = \mathbf{u}_I^e$ on $\partial\Omega_I^u$, $\mathbf{t}_I = \mathbf{t}_I^e$ on $\partial\Omega_I^t$, $\dot{\mathbf{u}}_I(t_0) = \mathbf{u}_I(t_0) = \mathbf{0}$ in Ω_I , $(\partial\Omega_I^u \cup \partial\Omega_I^t) \cap \Gamma_I = \emptyset$. The microstructural constituents define the material behavior on the microscale. Referring to the previous chapter, in the case of concrete, this is the mortar matrix and the aggregates, but for now an arbitrary microstructure is in view. Assuming that the material behavior of these constituents is known, the stresses can be described as a function of the strain tensor $\boldsymbol{\varepsilon}_m$ and potentially other state and material parameters $\boldsymbol{\beta}_m$: $\boldsymbol{\sigma}_m = f(\boldsymbol{\varepsilon}_m, \boldsymbol{\beta}_m^1, \boldsymbol{\beta}_m^2, \dots)$.

Splitting the last term of equation (5.16b) in tractions on $\partial\Omega_I \setminus \Gamma_I$ and tractions on Γ_I exerted by the macro domain on the interface domain (refer to equation (5.15)), one can reformulate:

$$\int_{\Omega_I} \delta \mathbf{u} \cdot \rho_I \ddot{\mathbf{u}}_I d\Omega_I + \int_{\Omega_I} \nabla \delta \mathbf{u} : \boldsymbol{\sigma}_I d\Omega_I - \int_{\partial\Omega_I \setminus \Gamma_I} \delta \mathbf{u} \cdot \mathbf{t}_I d\partial\Omega_I - \int_{\Gamma_I} \delta \mathbf{u} \cdot \mathbf{t}_I d\Gamma_I = \mathbf{0} \quad (5.17)$$

Isolating now the integral over Γ_I , presupposing a similar split of the last term with a different sign for the Γ_I -integral due to Newton's third law and inserting its expression in equation (5.16a), and noting further that $\partial\Omega_{MI} = (\partial\Omega_M \cup \partial\Omega_I) \setminus \Gamma_I$, yields for the combined domain $\Omega_{MI} = \Omega_M \cup \Omega_I$:

$$\begin{aligned} \int_{\Omega_M} \delta \mathbf{u} \cdot \rho_M \ddot{\mathbf{u}}_M d\Omega_M + \int_{\Omega_I} \delta \mathbf{u} \cdot \rho_I \ddot{\mathbf{u}}_I d\Omega_I + \int_{\Omega_M} \nabla \delta \mathbf{u} : \boldsymbol{\sigma}_M d\Omega_M \\ + \int_{\Omega_I} \nabla \delta \mathbf{u} : \boldsymbol{\sigma}_I d\Omega_I - \int_{\partial\Omega_{MI}} \delta \mathbf{u} \cdot \mathbf{t}_{MI} d\partial\Omega_{MI} = \mathbf{0} \end{aligned} \quad (5.18)$$

As mentioned above, the region Ω_I is not a common material region with its own material behavior. Rather, it receives its state parameters from the underlying micro domain. Therefore, it is designated as “virtual” domain. Density and stress are derived by averaging these values in a micro volume portion with finite size $\Omega_m^I \subseteq \Omega_m$, depending on the coordinate of a material point \mathbf{x}_I in the interface domain (refer to Figure 5.2, left): $\boldsymbol{\sigma}_I(\mathbf{x}) = \langle \boldsymbol{\sigma}_m(\mathbf{x}) \rangle$ and $\rho_I(\mathbf{x}) = \langle \rho_m(\mathbf{x}) \rangle$. A volume averaging operation of the variable under consideration is expressed by the brackets:

$$\langle \circ \rangle = \frac{1}{|\Omega_m^I|} \int_{\Omega_m^I} \circ d\Omega_m^I \quad (5.19)$$

By prescribing the averaged variables to the interface domain Ω_I , it reflects the density and stress state of the micro domain in the vicinity of the interface. Consequently, the macro points on the interface Γ_I receive the influence of the micro domain. As for the kinematics, material points of the interface domain are simply prescribed to follow their initially corresponding material point in the micro domain: $\dot{\mathbf{u}}_I = \dot{\mathbf{u}}_m$ in $\Omega_I \setminus \Gamma_I$, closely following the work in [346]. If discretized, Ω_I reduces to nothing more than a slight extension of the macro mesh into the micro domain. Ω_m^I is then simply the volume covered by each protruding element; see Figure 5.2, right. It should be highlighted already here that this additional domain provides simply a numerical framework to determine and apply proper forces for the macro interface nodes. If Ω_I is suitably discretized by a single element row, it can be almost eliminated from the system, and only the additional mass at the interface nodes remains to be considered.

5.3.2 Discretization

The discretization of both domains with finite elements \mathcal{E} is similar to the one mentioned for the LM coupling, yielding in total $n_{MI} = n_M + n_I$ nodes \mathcal{N} in the combined macroscale domain Ω_{MI} and n_m nodes on the microscale. (A detailed derivation of the matrices representing the problem is given in [284] and is not repeated here for the sake of brevity.) The semi-discretized problem reads then for Ω_{MI} :

$$\mathbf{M}_{MI} \ddot{\mathbf{u}}_{MI} = \mathbf{R} - \mathbf{F}_M - \tilde{\mathbf{F}}_m \quad (5.20)$$

together with the boundary condition $\mathbf{u}_{MI} = \mathbf{u}^e$ for nodes on $\partial\Omega_{MI}^u$ and the initial conditions $\dot{\mathbf{u}}_{MI}(t_0) = \mathbf{u}_{MI}(t_0) = \mathbf{0}$ in Ω_{MI} . The vector $\tilde{\mathbf{F}}_m$ denotes the internal forces of elements in the discretized interface region Ω_I . With reference to Chapter 2.4, the mass matrix is diagonalized by lumping the mass of the

elements at the nodes. The nodal assembly can now be decomposed into nodes completely within Ω_M : \mathcal{N}_M ; nodes completely in Ω_I : \mathcal{N}_I ; and nodes lying on the interface Γ_I : $\mathcal{N}_{\mathcal{I}}$. Due to the fact that $\tilde{\mathbf{F}}_m$ has no entries for nodes \mathcal{N}_M and $\mathbf{F}_M = \mathbf{0}$ for nodes \mathcal{N}_I , equation (5.20) becomes:

$$\begin{bmatrix} \mathbf{M}_M & \mathbf{0} & \mathbf{0} \\ \mathbf{0} & \mathbf{M}_{\mathcal{I}} & \mathbf{0} \\ \mathbf{0} & \mathbf{0} & \mathbf{M}_I \end{bmatrix} \begin{bmatrix} \ddot{\mathbf{u}}_M \\ \ddot{\mathbf{u}}_{\mathcal{I}} \\ \ddot{\mathbf{u}}_I \end{bmatrix} = \begin{bmatrix} \mathbf{R}_M \\ \mathbf{R}_{\mathcal{I}} \\ \mathbf{R}_I \end{bmatrix} - \begin{bmatrix} \mathbf{F}_M \\ \mathbf{F}_{\mathcal{I}}^M \\ \mathbf{0} \end{bmatrix} - \begin{bmatrix} \mathbf{0} \\ \tilde{\mathbf{F}}_{\mathcal{I}}^m \\ \tilde{\mathbf{F}}_I^m \end{bmatrix} \quad (5.21)$$

The vector $\mathbf{F}_{\mathcal{I}}^M$ contains the internal forces of the elements belonging to the *macro* domain, but being attached to the interface nodes, $\mathcal{N}_{\mathcal{I}}$, whereas $\tilde{\mathbf{F}}_{\mathcal{I}}^m$ holds the forces of elements attached to $\mathcal{N}_{\mathcal{I}}$ but lying in the *interface* domain. These are the actual coupling forces derived from the underlying microscale. Since the kinematic state of the nodes \mathcal{N}_I lying *in* the interface is taken directly from the appropriate positions in the micro domain, the last line of equation (5.21) has not to be solved and can be elided. Equation (5.21) then reduces to the final form of the semi-discretized momentum balance of the macro domain:

$$\begin{bmatrix} \mathbf{M}_M & \mathbf{0} \\ \mathbf{0} & \mathbf{M}_{\mathcal{I}} \end{bmatrix} \begin{bmatrix} \ddot{\mathbf{u}}_M \\ \ddot{\mathbf{u}}_{\mathcal{I}} \end{bmatrix} = \begin{bmatrix} \mathbf{R}_M \\ \mathbf{R}_{\mathcal{I}} \end{bmatrix} - \begin{bmatrix} \mathbf{F}_M \\ \mathbf{F}_{\mathcal{I}}^M \end{bmatrix} - \begin{bmatrix} \mathbf{0} \\ \tilde{\mathbf{F}}_{\mathcal{I}}^m \end{bmatrix} \quad (5.22)$$

Comparing equation (5.22) with the semi-discretized EOM of a standard domain (e.g. equation (2.8)), the difference is in the additional force term and the fact that the masses of the interface nodes, $\mathcal{N}_{\mathcal{I}}$, now contain a portion of the virtually attached region.

No peculiarities have to be considered for the micro domain – discretized with nodes \mathcal{N}_m within the domain Ω_m and nodes \mathcal{N}_i lying on the interface Γ_i :

$$\mathbf{M}_m \ddot{\mathbf{u}}_m = \mathbf{R}_m - \mathbf{F}_m \quad (5.23)$$

with the additional boundary condition $\dot{\mathbf{u}}_i = \phi(\dot{\mathbf{u}}_{\mathcal{I}}, \mathbf{x}_i)$ on Γ_i , where ϕ is a linear interpolation function (Section 5.3.4). Supplying the boundary condition $\mathbf{u}_m = \mathbf{u}^e$ for nodes on $\partial\Omega_m^e$ and the initial conditions $\dot{\mathbf{u}}_m(t_0) = \mathbf{u}_m(t_0) = \mathbf{0}$ in Ω_m , an independent initial boundary value problem is achieved for the micro domain.

Writing now the complete problem at once, for easier comparability with the LM based approach, equation (5.4), delivers:

$$\mathbf{M}_M \ddot{\mathbf{u}}_M = \mathbf{R}_M - \mathbf{F}_M - \tilde{\mathbf{F}}_{\mathcal{J}}^m \quad (5.24a)$$

$$\mathbf{M}_m \ddot{\mathbf{u}}_m = \mathbf{R}_m - \mathbf{F}_m \quad (5.24b)$$

$$\dot{\mathbf{u}}_m = \dot{\mathbf{u}}_M \quad (5.24c)$$

Note that the “linking forces” on the *micro* domain are “replaced” by the compatibility condition. Furthermore, all three lines in the above-written system are independent – but have to be solved in a specific sequence. Finally, the linking forces, $\tilde{\mathbf{F}}_{\mathcal{J}}^m$, are determined by a simple loop over some micro elements, with linear complexity only.

5.3.3 Establishing the virtual interface domain

The interface domain is necessary to derive the linking forces $\tilde{\mathbf{F}}_{\mathcal{J}}^m$ at the macro interface nodes. It is established by adding virtual nodes, $\tilde{\mathcal{N}}_I$, within the micro domain. Using these nodes, virtual elements $\tilde{\mathcal{E}}$ are defined, Figure 5.3. These entities are labeled “virtual” since they simply retrieve their state parameter directly by reference to the micro domain, i.e. $\tilde{\mathbf{u}}_I = f(\mathbf{u}_m)$ and $\tilde{\boldsymbol{\sigma}}_I = \langle \boldsymbol{\sigma}_m \rangle$. In the case of the virtual nodes, they are connected to an underlying microscale node if a coincident node exists. Otherwise, they are connected to an underlying micro element at the beginning of the simulation.⁶⁶

Standard linear shape functions $\tilde{\mathbf{N}}(\boldsymbol{\xi})$ are used in the virtual elements. The matrix

$$\tilde{\mathbf{B}} = \frac{\partial \tilde{\mathbf{N}}}{\partial \boldsymbol{\xi}} \tilde{\mathbf{J}}^{-1} \quad (5.25)$$

serves as discrete gradient operator for the elements. In this expression, $\tilde{\mathbf{J}}$ is the Jacobian matrix built with the coordinates of $\mathcal{N}_{\mathcal{J}}$ and $\tilde{\mathcal{N}}_I$ and $\tilde{\mathbf{N}}$ the matrix of shape functions; $\boldsymbol{\xi}$ are the local (elemental) coordinates of the integration point

⁶⁶ Using the shape functions of this element, the position of the virtual node in the local (element) coordinate system is determined and stored. Having this original position at hand, in each cycle the current position can be derived by recourse to the shape functions and the elements’ nodal values.

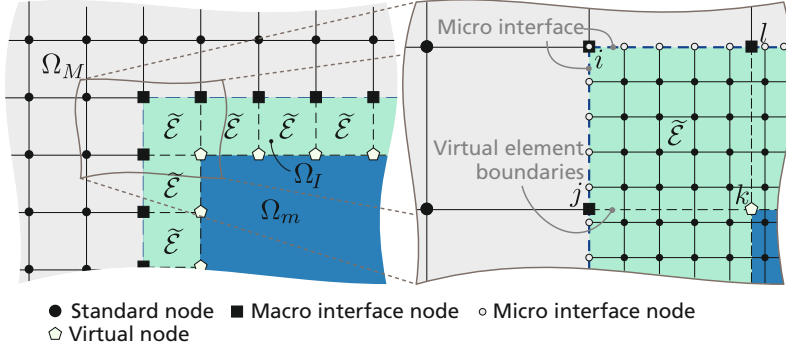


Figure 5.3: Left: The interface domain Ω_I is defined by one element row adjoining the interface, with a resolution similar to the elements size of the macro domain. The virtual elements $\tilde{\mathcal{E}}$ overlapping the micro domain are defined by the macro interface nodes $\mathcal{N}_{\mathcal{I}}$ (black squares) and virtual nodes $\tilde{\mathcal{N}}_I$ (polygons). Right: Detailed view on the overlay of the virtual and the micro mesh. Figure from [284].

under consideration. In this thesis, only hexahedral macro/virtual elements are used, but the approach can be extended to other elemental shapes if necessary.

5.3.4 Interface coupling procedure

In order to prescribe the macro interface movement to the micro interface, a linear interpolation of the velocity is used: $\dot{\mathbf{u}}_i^{(n+1/2)} = \phi\left(\dot{\mathbf{u}}_{\mathcal{I}}^{(n-1/2)}, \mathbf{x}_i^{(n-1)}\right)$, refer to Figure 5.4, left. Together with the linear shape functions of the macro element, the application of a linear function ensures strict compatibility between the domains. Let $\tilde{\mathbf{u}}_k$ denote the vector of the velocity of the k -th virtual elements' nodes $q = 1 \dots 8$: $\tilde{\mathbf{u}}_k = [\dot{\mathbf{u}}_k^1 \dot{\mathbf{u}}_k^2 \dots \dot{\mathbf{u}}_k^8]^\top$. The interpolation for each micro interface node i within the bounds of the virtual element k can then be performed with the following relation:

$$\dot{\mathbf{u}}_i = \tilde{\mathbf{N}}_k^\top(\xi_i, \eta_i, \zeta_i) \tilde{\mathbf{u}}_k \quad (5.26)$$

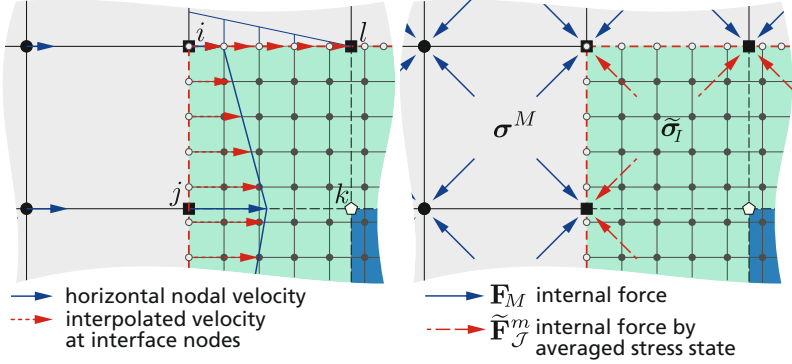


Figure 5.4: Left: Interpolation of the macro interface nodal velocities gives the initial velocity at the micro interface nodes at beginning of each cycle. In the illustrated case, node l still has zero velocity, which leads to the decreasing, linear slope between nodes i and l . Right: The averaged stress state in the micro domain covered by each virtual element is used to determine proper forces for the macro interface nodes.

with $\tilde{\mathbf{N}}_k = [\tilde{N}_k^1 \tilde{N}_k^2 \dots \tilde{N}_k^8]^\top$ and

$$\tilde{N}_k^q(\xi_i, \eta_i, \zeta_i) = \frac{1}{8} (1 + \xi^q \xi_i) (1 + \eta^q \eta_i) (1 + \zeta^q \zeta_i) \quad (5.27)$$

being the vector with the linear shape functions of the nodes q evaluated at the (local) coordinates ξ, η, ζ of the micro node i in the virtual element. For this operation, these coordinates have to be available. They can be determined once during set-up by solving the underlying nonlinear inverse isometric mapping problem; refer to [347] for details. For the velocity of the nodes q , defining the virtual element under consideration, the following conventions are used: If these nodes are interface nodes, then simply $\tilde{\mathbf{u}}_k^q = \dot{\mathbf{u}}_{\mathcal{J}}$ holds; for nodes within the micro domain: $\tilde{\mathbf{u}}_k^q = f(\dot{\mathbf{u}}_m)$, see footnote 66.

The fact that $\dot{\mathbf{u}}_{\mathcal{J}}^{(n-1/2)}$ is known is a beneficiary property of the Leapfrog algorithm and cannot be presupposed for other time integration schemes. For other schemes, more complex staggering procedures, as detailed in the context of fluid/structure interaction, e.g., [344, 349], should be principally adaptable.

5.3.5 Averaging the micro model

The initial boundary value problem of the microscale is fully defined as soon as the initial velocities are applied on the micro domain interface nodes and the solution cycle can be executed for this domain. Once the cycle has been completed, the stress state in the virtual elements is used to derive appropriate forces for the macro interface nodes, $\mathcal{N}_{\mathcal{J}}$. At each integration point g of each virtual element k , the stress state of the $\tilde{n}_{g,\varepsilon}^m$ underlying (attached) micro domain elements is averaged, by applying equation (5.19) in a discretized form, where V_e is the volume of each evaluated micro element:

$$\tilde{\sigma}_{k,g}^I = \langle \sigma_m \rangle_{k,g} \approx \frac{1}{\tilde{V}_{k,g}^s} \sum_{e=1}^{\tilde{n}_{g,\varepsilon}^m} \sigma_e^m V_e \quad (5.28)$$

In this work, \tilde{V}^s in equation (5.28) is equal to the sum of the volumes of the micro elements considered.⁶⁷ If the presence of, e.g., initial voids or emerging cracks shall be considered, a more appropriate definition of \tilde{V}^s may be applicable. The thus averaged stress state is afterwards used to evaluate the internal forces of the virtual element using a discretized form of equation (2.7), with standard Gaussian integration and weight factors $a_{\cdot,\cdot}$ at integration point g of the virtual element k :

$$\tilde{\mathbf{F}}_{\mathcal{J},k}^m = \sum_{g=1}^{n_g} \tilde{\mathbf{B}}_{k,g}^\top \langle \sigma_m \rangle_{k,g} \det \tilde{\mathbf{J}}_{k,g} a_{g,x} a_{g,y} a_{g,z} \quad (5.29)$$

Equation (5.29) thus expresses an average resistance force of the microscale against deformation. The forces are finally added to the macro interface nodes and considered during the macro cycle, see Figure 5.4, right. Recalling that, in general, $\partial \mathbf{F} / \partial \mathbf{u} = \mathbf{K}$, one can interpret the averaging step as related to static condensation approaches, e.g., [350, 351], since it simply delivers an averaged stiffness $\langle \mathbf{K} \rangle$ for the covered micro volume.

In the current study, all elements are one-integration point elements, and the occurrence of hourglass modes is controlled by considering hourglass forces. However, in the virtual macro elements one central integration point is used as well, but in this case no hourglass forces are considered. Since the outer virtual nodes (the ones not on the interface) are fixed within the micro domain,

⁶⁷ Each micro element covered by a virtual element is initially assigned to the nearest integration point of the virtual element.

unphysical distortions cannot occur and there is no need to control these modes. Besides that, no significant effect of the number of integration points within the virtual elements was observed in test simulations.

Once all forces have been collected, the macro model can complete its solution cycle and determine new accelerations, velocities, and finally positions at its nodes \mathcal{N}_M and $\mathcal{N}_\mathcal{T}$. Having computed these values, the time is advanced by one time step, and the process starts over again. The flowchart of one cycle is schematically given below, Figure 5.5, together with an illustration of the marching solution and a comparison between staggered and LM based coupling. An algorithmic outline of the serial solution of one cycle is given in Algorithm 2.

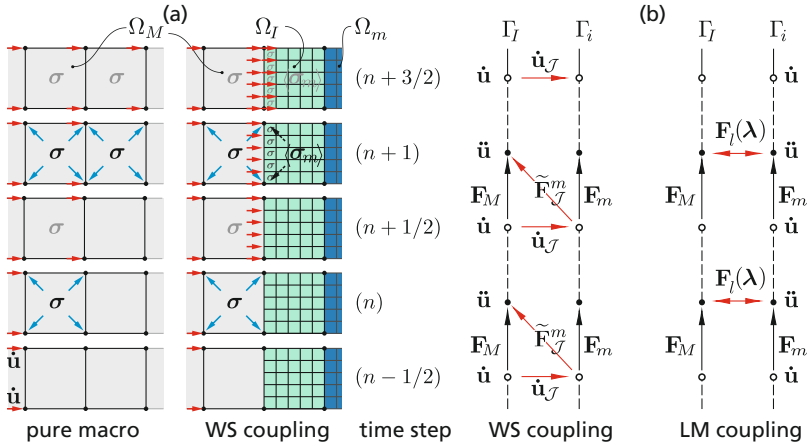


Figure 5.5: (a): Schematic sketch of the marching solution in time of the herein described scheme. A wave propagates from left to right. From the velocities at the nodes, the strain rate and subsequently the stress state is derived in each full time step (n). The forces due to the stress state lead to updated nodal velocities at the next half time step. Note that the force vectors are for illustration purposes only and do not indicate a specific direction. (b): Comparison of the proposed staggered scheme and a surface coupling based on Lagrange multipliers, as exemplified in [38], based on the Leapfrog time integration. Figure from [284].

Algorithm 2 Serial solution of micro and macro domain for one cycle from (n) to $(n + 1)$. Additional operations introduced by the coupling are colored in blue.

```

Use  $\dot{\mathbf{u}}_{\mathcal{J}}^{(n+1/2)}$  to interpolate BC on  $\mathcal{N}_i$ , eq. (5.26)
for  $\forall \mathcal{E}_m$  do      ▷ Standard hydrocode update for all micro domain elements
    Update matrices
    Determine  $\sigma_m$ 
    Calculate  $\mathbf{F}_m$ 
end for
for  $\forall \mathcal{N}_m$  do
    update  $\ddot{\mathbf{u}}_m, \dot{\mathbf{u}}_m, \mathbf{u}_m$ 
end for
for  $\forall \tilde{\mathcal{E}}$  do      ▷ Process the virtual elements
    Update matrices
    determine  $\tilde{\sigma}$ 
    Calculate  $\tilde{\mathbf{F}}^m_{\mathcal{J}}$ 
end for      ▷ Micro domain update finished
for  $\forall \mathcal{E}_M$  do      ▷ Standard update of macro domain elements
    Update matrices
    Determine  $\sigma_M$ 
    Calculate  $\mathbf{F}_M$ 
end for
for  $\forall \mathcal{N}_M$  do
    update  $\ddot{\mathbf{u}}_M, \dot{\mathbf{u}}_M, \mathbf{u}_M$ 
end for
Add  $\tilde{\mathbf{F}}^m_{\mathcal{J}}$  to all  $\mathcal{N}_{\mathcal{J}}$       ▷ Consider the micro domain contribution
for  $\forall \mathcal{N}_{\mathcal{J}}$  do
    update  $\ddot{\mathbf{u}}_{\mathcal{J}}, \dot{\mathbf{u}}_{\mathcal{J}}, \mathbf{u}_{\mathcal{J}}$ 
end for      ▷ Macro domain update finished

```

5.3.6 Estimation of efficiency

Extra effort for coupling For the LM approach, two aspects for the coupling have been identified: Inverting matrix \mathbf{H} and solving equation (5.14) each cycle with the worst case of $\mathcal{O}(d^2(n_i + n_{\mathcal{J}})^2)$ floating point operations. For the WS coupling, again two operations are necessary, but this time both in each time step: Interpolation of the velocities at the interface and averaging of the stress state. The first operation is of order $\mathcal{O}(d(n_i + n_{\mathcal{J}})/\mathcal{P})$, the second of

$\mathcal{O}(n_{\mathcal{E}}^i/\mathcal{P})$, with \mathcal{P} being the number of processors used and $n_{\mathcal{E}}^i$ the number of micro domain elements in the interface region. Both operations are of linear order, and although $n_{\mathcal{E}}^i > (n_i + n_{\mathcal{J}})$ for fine meshes, this effect should be perceptible eventually. Additionally, a costly matrix inversion is never necessary. The fact that \mathcal{P} is mentioned in this estimation should highlight that the operation can be parallelized straightforwardly and scales very well; see Section 6.2.3.

Communication efforts Although the parallel implementation of the coupling will be briefly introduced not before Chapter 6, already here, under the deliberation of efficiency, the necessary communication between the two domains shall be succinctly reflected. For the discussion, assume that macro and micro domains are solved on a different CPU. Pretending that equation (5.13) for the LM coupling is solved by the macro processor, the free accelerations of the micro interface nodes have to be communicated to the macro process. Afterwards, the link accelerations have to be sent back. Presuming that for each node in \mathbb{R}^3 one integer ID (or vector index) and three float components have to be sent each, in total 28 bytes are necessary for each node in each communication step. The total data to be communicated within one solution time step adds then to $2n_i \times 28$ bytes. In the WS coupling the velocities of the nodes of the virtual interface elements (macro interface nodes and virtual nodes) have to be available on the microscale process, whereas the forces to the macro interface nodes and the positions of the virtual nodes are communicated back. Assuming that there is one row of elements for the interface, i.e. $n_{\widetilde{\mathcal{N}}_I} = n_{\mathcal{J}}$, the total amount of data in one time step is $4n_{\mathcal{J}} \times 28$ bytes. The theoretical difference hence is a $\Delta = (2n_i - 4n_{\mathcal{J}}) \times 28$ bytes higher amount of data in the LM coupling, indicating a strong increase for fine meshes where $n_i \gg n_{\mathcal{J}}$.

Summary Comparing LM and WS coupling in view of additional operations and introduced communication efforts shows that the WS coupling offers advantages in both aspects. The additional operations are of linear order only, are easily parallelized, and scale well, as will be shown in Section 6.2. Only data of the macro interface nodes have to be communicated between the domains, indicating small message sizes and fast communication. It should not be dismissed, however, that the LM coupling benefits from compilers tuned to optimize matrix multiplication operations. In HPC settings, communication between processes is handled by suitable hardware, and the additional data size with respect to the WS coupling is perceivable only in the case of large models. Furthermore, the LM coupling

allows a full parallel solution of both domains, whereas in the WS coupling the macro interface nodes cannot be integrated before the microscale problem is fully solved. Yet the main disadvantage of the LM coupling remains the inversion of \mathbf{H} at $t = 0$ and each time the topology changes, which – in contrast – does not pose a challenge for the WS coupling.

5.4 Abating pathological wave reflections

A well-known corollary of coupling domains with disparate meshes (or element skew angle and formulation) are pathological wave reflections at the interface [352–354]. This pathology occurs if the wave propagates from the fine into the coarse domain and contains frequencies higher than the latter is able to resolve. This section discusses this phenomenon and proposes an ameliorating solution, which adapts a current formulation of a selective perfectly matched layer to the proposed WS coupling.

To highlight the problem consider a one-dimensional rod of length $l = 300$ mm with linear elastic material behavior and the following initial and boundary

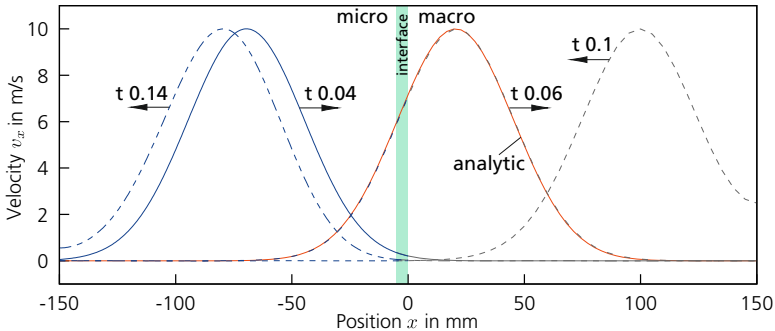


Figure 5.6: Wave propagation from micro- to macroscale in 1D. The pulse is induced at $x = -150$ mm and propagates from left to right. The velocity of all nodes in the bar are plotted here at different time points (denoted by t , the arrow indicates the current propagation direction). “Blue” positions are in the micro, “gray” in the macro domain. Figure from [284].

conditions: $u(x, t_0) = 0$, $\dot{u}(x, t_0) = 0$, $\dot{u}(x = -150, t) = v_b(t)$. The rod is evenly divided into a micro and a macro domain, with the interface ranging from $-5 \leq x \leq 0$. Points $x < -5$ belong to the micro domain, all points $x > 0$ to the macro domain. In the micro domain, elements with length $e_m = 0.5$ mm and on the macro $e_M = 5$ mm are used. A Gaussian pulse with a superimposed sinusoidal signal with angular frequency ω_1 if $A_1 \neq 0$, defines the applied velocity $v_b(t)$ at $x = -150$:

$$v_b(t) = (A_0 + q(t)) e^{-\left(\frac{t-2.5\beta}{\beta}\right)^2}, \quad q(t) = A_1 \sin(\omega_1 t) \quad (5.30)$$

with $\beta > 0$ being a parameter that determines the width of the pulse. If $t > 2.5\beta$ and, consequently, $v_b(t) \rightarrow 0$, the condition is removed. The analytic solution for a right-propagating elastic wave for $0 \leq t < x/c$ is simply achieved by replacing t by $t - x/c$ in equation (5.30), with c being the wave propagation speed, $c_s = \sqrt{E/\rho}$.

The velocity in the bar is plotted in Figure 5.6 for $A_1 = 0$ at distinct points in time. An almost perfect agreement to the analytic solution is yielded (compare the dashed and the solid line for $t = 0.06$). Note that in this case the result is almost identical to the one achieved with a model, where the domains are simply adjoined at one single node (not shown).

Consider now the case of $A_1 \neq 0$. The simulation results are plotted in Figure 5.7. While the low-frequent signal crosses the interface, the high-frequent portion is reflected. One can easily show that there is a cutoff frequency ω_c^h , marking the limit that can be resolved by a 1D discretization with node distance h , see, e.g., [335] or [355]. As mentioned above, this issue occurs within *any* attempt to combine two different domains, and is – more or less – independent of the actual coupling mechanism.

Of course, such behavior is not desired, although the effects on the overall solution may be low, depending on the problem. In the following, an overview of existing mitigation strategies will be given. After that, one special concept will be discussed in detail since it will subsequently be adapted to be incorporated into the WS coupling.

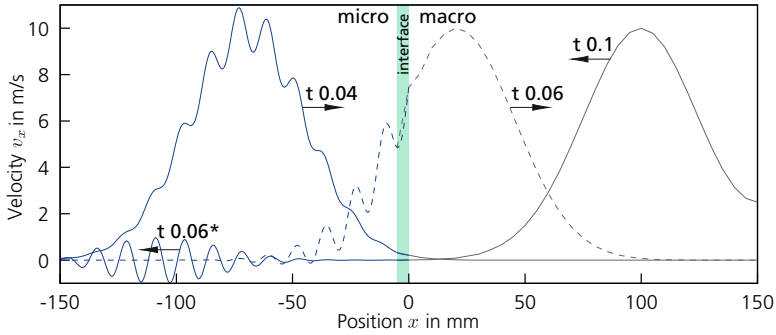


Figure 5.7: Wave propagation from micro to macro in 1D. The superimposed high frequent portion of the signal is reflected at the interface. The wave portion labeled with $t = 0.06^*$ is the high frequency portion reflected at the interface. Figure from [284].

5.4.1 Remedies in literature

The problem of spurious wave reflections on an interface between disparate discretizations is of special concern for ATC couplings. Besides the fact that the scale jump in these cases is pronounced, the reflected wave introduces spurious energy and consequently heats up the atomistic region, such that the results may be totally useless [356, 357]. If larger scales are considered, reflected waves still disturb the solution but may be in an acceptable range – which is of course different from application to application. Most of the mitigation strategies available for this problem can be assigned to one of three general categories: (i) reducing the nodal spacing at the interface, (ii) applying absorbing boundary conditions of some kind, and (iii) designing an absorbing interface layer. As an example for the first category, one can allude to the already mentioned MAAD method by *Abraham* et al. [163, 322]. With a refined mesh in the handshake region, featuring element sizes comparable to the atomic spacing, the occurrence of strong reflections is successfully eliminated but renders the solution very inefficient. The use of transition elements to connect two FE meshes belongs similarly to this category.

The literature dealing with the simulation of wave propagation in unbounded domains contains examples from the second and third rubrics. In practice, unbounded domains translate in simulation to large but bounded problems, and there is a need to eliminate reflections from the now existent domain border. This

may be achieved by applying specific absorbing boundary conditions, e.g., [358, 359]. Closely related are, for instance, the so-called “optimal boundary matching conditions” for a finite difference based coupling scheme detailed in reference [356].

Absorbing layers integrated in the coupling interface have been the subject of several contributions. They refer back to the “Perfectly Matched Layer” (PML) concept, detailed in [360]. In this approach, the domain is surrounded by a medium with (almost) perfect impedance matching but dissipating properties. Originally invented in the context of electromagnetism, it was adapted to simulations of elastic waves in [361, 362]. Meanwhile, several works have picked up the broad idea of an absorbing layer, especially in MD-FE couplings [357, 363, 364].⁶⁸

5.4.2 The SPML approach of *Marchais* et al.

Of special interest to this work is the so-called “Selective Perfectly Matched Layer” (SPML) approach, introduced by *Marchais* et al. [335]. The classical PML technique applies a damping term to each DOF of the whole model. Since the damping term depends on the position of each node, only DOF within the filtering layer, or filtering zone, $\Omega_{\mathcal{F}}$, receive effective damping. For all other nodes, the term equals zero. In the work of *Marchais* et al., only the EOM of the nodes within the filtering zone is altered and furnished with a damping term. The authors entitle their adaption of the PML concept “selected” since the intention is to damp out only specific frequencies in the micro displacement field, namely those that cannot be resolved by the coarser mesh. On the contrary, *all* frequencies are absorbed in the classical PML method. However, although they seem to be the first to use the term SPML, the underlying idea is comparable to the works discussed above. The notable difference is the application of the technique to two FE domains and not to different *numerical* domains, such as a FE and a MD domain. This feature makes this work especially relevant for the current study.

The filtering zone is a finite region of the micro domain, abutting the interface and featuring an additional, overlaying macro discretization – very similar to the interface domain used in the WS coupling. *Marchais* et al. split the *micro*

⁶⁸ As an example of a special, dissipating interface design, the work of *Ben Dhia* et al. should be mentioned [326]. In this reference, it was shown that a dissipative scheme in the “gluing zone” of the Arlequin method filters out the incompatible contribution from the refined domain, without further specifying the dissipative scheme.

displacement field $\mathbf{u}_{\mathcal{F}}$ in this zone into a “compatible macro displacement”, \mathbf{u}_M , and an additional “unique microscale displacement”, \mathbf{u}_m : $\mathbf{u}_{\mathcal{F}} = \mathbf{u}_m + \mathbf{u}_M$. Individual contributions are determined by complementary operators:

$$\mathbf{u}_{\mathcal{F}}(t) = \mathbf{u}_m(t) + \mathbf{u}_M(t) = \mathbb{P}_m \mathbf{u}_{\mathcal{F}}(t) + \mathbb{Q}_M \mathbf{u}_{\mathcal{F}}(t), \quad \mathbb{P}_m = \mathbf{I} - \mathbb{Q}_M \quad (5.31)$$

In the context of the preceding sections, the additional usage of the terms “macro” and “micro” may be confusing. Here, it is important to note that *each DOF of each micro node in the filtering zone* has the above-mentioned contributions in its displacement – even if no macro discretization exists. The “compatible macro displacement” part is the ratio, which *might* be resolved at the position of the considered node in an overlaying (fictive or real) macro element, see Figure 5.8. In other words: the macro contribution of a node in the micro domain is the displacement of this node, which is “compatible” to a real or fictive macro discretization at this position. Therefore, the cumbersome terms “unique microscale displacement” and “compatible macro displacement” might best express the intended meaning and will be used from now on. To avoid confusion, the sans-serif symbols m/M are used for the unique microscale and compatible macro displacement.

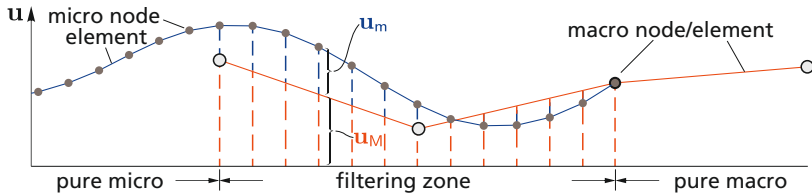


Figure 5.8: Split of the displacement of micro nodes in the filtering zone into a contribution unique of the micro domain and a part which conforms to an overlaying – fictive or real – macro mesh.

To derive a partially damped formulation of the problem, the unique microscale and the compatible macro displacement field may be expressed by the modal basis of the problem at hand and the definitions

$$\mathbf{u}_M(t) = \sum_{j=1}^{n_M} \alpha_j(t) \phi_j \quad \mathbf{u}_m(t) = \sum_{j=n_M+1}^n \alpha_j(t) \phi_j \quad (5.32)$$

in which $\alpha_j(t)$ denotes the time functions related to the eigenmodes ϕ_j . $n = n_M + n_m$ is the total number of DOF. The eigenmodes up to n_M are those of the

compatible macro field, whereas all larger modes belong to the unique microscale field (n_m). Considering the split of the displacement field, the EOM may be finally expressed by $n + 1$ independent ordinary differential equations for each time function α_j of the form (see [335] for details):

$$\ddot{\alpha}_j(t) + \omega_j^2 \alpha_j(t) = 0 \quad \forall j \text{ in } [1, n] \quad (5.33)$$

with ω_j being the j -th eigenfrequency, corresponding to the j -th eigenmode ϕ_j . The authors now modify this equation by adding a damping term with the aim to reach $\lim_{t \rightarrow \infty} \mathbf{u}_m(t) \rightarrow \mathbf{0}$:

$$\ddot{\alpha}_j(t) + \omega_j^2 \alpha_j(t) = \begin{cases} 0 & j \leq n_M \\ -2f_d \dot{\alpha}_j(t) - f_d^2 \alpha_j(t) & j > n_M \end{cases} \quad (5.34)$$

The individual solutions of the above equation for $j > n_M$ are then

$$\alpha_j(t) = A_j e^{-f_d t} e^{i\omega_j t} \quad (5.35)$$

exhibiting a signal decay exponentially with rate $-f_d$, with $f_d > 0$. Consequently, the EOM in the filtering zone may be written in its standard form as:

$$\mathbf{M}\ddot{\mathbf{u}}(t) + \mathbf{F} - \mathbf{R} + 2f_d \mathbf{M}\mathbb{P}_m \dot{\mathbf{u}}(t) + f_d^2 \mathbf{M}\mathbb{P}_m \mathbf{u}(t) = \mathbf{0} \text{ in } \Omega_{\mathcal{F}} \quad (5.36)$$

Note that by applying the microfield projector \mathbb{P}_m in the last two terms, only the unique microscale contribution is affected by the damping.

The main issue is now to find formulations for this projector, which successfully partitions the displacement field into unique micro and compatible macro contribution. A natural choice is to derive this matrix simply by using a linear combination of the eigenmodes. However, this requires the solution of (at least) the first n_M eigenmodes. If these have to be derived only once, this formulation is a feasible way to derive the splitting operator. But the eigenmodes actually depend on the mesh configuration and the current stiffness. Ergo: if the mesh becomes distorted during the simulation or the stiffness changes due to nonlinear material behavior, the splitting operator has to be derived repeatedly, which may be – at the long run – very costly and inefficient.

In addition to a projector defined on a wavelet basis, which should not be discussed here, *Marchais* et al. propose a third variant: a definition based on the

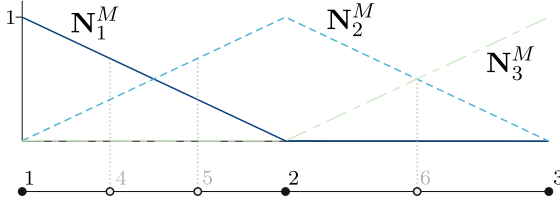


Figure 5.9: A 1D macro mesh (solid points) overlaid by a micro mesh together with linear shape functions of the macro mesh.

shape functions of the macro filtering zone. The compatible macro displacement part is thereby defined as

$$\mathbf{u}_M = \mathbb{N}_M \mathbf{d}_M, \quad \mathbb{N}_M = [\mathbf{N}_M^1 \mathbf{N}_M^2 \dots \mathbf{N}_M^{n_M}] \quad (5.37)$$

Matrix \mathbb{N}_M consists of the shape functions \mathbf{N}_M^j of the overlying macro (filtering) zone, evaluated for each node, and \mathbf{d}_M is defined as the (unknown) projection of \mathbf{u}_F on the macro discretization. To illustrate the assignment of \mathbb{N}_M , consider the simple 1D model in Figure 5.9 with six DOF, three of them belonging to the micro mesh. Then $\mathbf{u}_M = [u_M^1 u_M^2 u_M^3 u_M^4 u_M^5 u_M^6]^\top$ in which u_M^4 , u_M^5 and u_M^6 are the portions of the macro displacement field at the three micro nodes. Evaluating the linear shape functions of the macro mesh at all nodal positions yields:

$$\begin{bmatrix} u_M^1 \\ u_M^2 \\ u_M^3 \\ u_M^4 \\ u_M^5 \\ u_M^6 \end{bmatrix} = \begin{bmatrix} 1 & 0 & 0 \\ 0 & 1 & 0 \\ 0 & 0 & 1 \\ 2/3 & 1/3 & 0 \\ 1/3 & 2/3 & 0 \\ 0 & 1/2 & 1/2 \end{bmatrix} \begin{bmatrix} d_M^1 \\ d_M^2 \\ d_M^3 \end{bmatrix}$$

The unknown vector \mathbf{d}_M can be derived by minimizing the gap between the global and the macro kinetic energy, which finally leads to the following definition of the projection operator (see [335] for the detailed derivation):

$$\mathbb{P}_m = \mathbf{I} - \mathbb{N}_M \mathbf{M}_M^{-1} \mathbf{N}_M^\top \mathbf{M} \quad (5.38)$$

This definition may then be used in equation (5.36). It should be noted that the application of this projector necessitates the solution of the EOM as a whole,

that is, the individual rows of equation (5.36) are no longer independent, as is the case in the simple direct solution scheme (see Chapter 2). This means that the efficiency of this scheme is lost as soon as such a projector is applied. If the LM based approach detailed above is used to couple both domains, the coupling matrix \mathbf{C} now contains *all* DOF in the filtering zone, not only the ones on the interface – an enormous rank increase! Consequently, the inversion of \mathbf{H}_0 takes even longer. In order to apply equation (5.36) in the WS coupling, a pragmatic and less stringent mathematical approach is suggested to determine the unique microscale contribution, which will be detailed in the following paragraphs.

5.4.3 Adaption of the SPML approach to the WS coupling

For the application of the SPML approach, the split of the displacement field within the filtering zone $\Omega_{\mathcal{F}}$ is necessary. *Marchais* et al. achieve this by applying operator \mathbb{P}_m on the total displacement field $\mathbf{u}_{\mathcal{F}}^{(n)}$. But since the operator works simultaneously on several entries of $\mathbf{u}_{\mathcal{F}}^{(n)}$, a common solution of a system of equations is necessary. Therefore the use of such an operator shall be dismissed for the adaption to the WS coupling with its Leapfrog time integration scheme and a different approach is taken. The aim is to isolate the unique microscale displacements of the micro domain nodes within the filtering zone, which then can be damped out. To do so, note first the triviality:

$$\mathbf{u}_m^{(n)} = \mathbf{u}_{\mathcal{F}}^{(n)} - \mathbf{u}_M^{(n)} \quad (5.39)$$

Hence, if one has the total deformation of the microscale nodes and a suitable displacement field of a macro discretization within the filtering zone, one can easily determine the unique microscale contribution by a simple subtraction. Again, the employment of virtual elements, as already introduced above, will lead exactly to such a displacement field. For the WS concept, there is already one row of elements that protrudes from the micro mesh. If one adds one further (or more) rows of virtual “filter elements”, $\tilde{\mathcal{E}}_{\mathcal{F}}$, a filtering zone is established.⁶⁹ Now the nodes of these new virtual elements – the “filter” nodes $\mathcal{N}_{\mathcal{F}}$ – are integrated as standard macro nodes, with the necessary forces derived again by averaging

⁶⁹ It is not possible to use the already existing interface region, since the virtual nodes (the ones within the micro domain, not those on the interface) retrieve their kinematic state by direct recourse to the micro domain (Section 5.3.3), thus their state *contains* the unique microscale displacement at their position.

the stress state of the underlying micro domain.⁷⁰ The resulting displacement field within these elements is then a pure macro field, $\tilde{\mathbf{u}}_{\mathcal{F}}$, influenced by the stress state of the micro domains, see Figure 5.10.

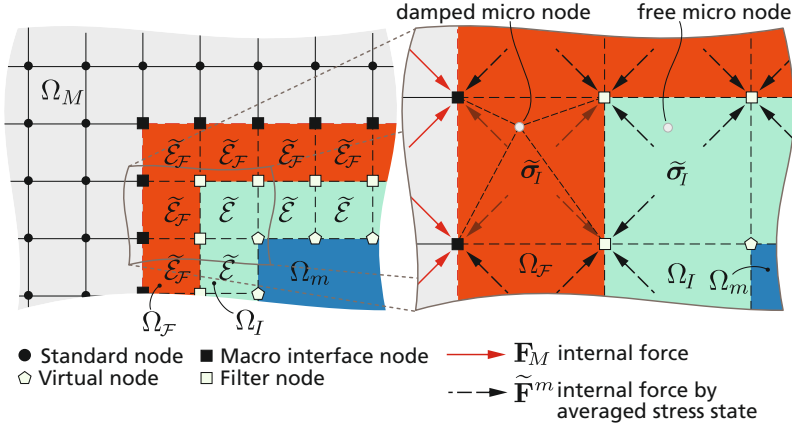


Figure 5.10: Schematic view of the coupling set up with damping. An additional filter zone (red) is inserted between macro (grey) and interface domain (green). The filter nodes receive forces from the averaged micro domain by the virtual filter elements $\tilde{\mathcal{E}}_{\mathcal{F}}$ and are integrated similar to standard macro nodes. Micro nodes lying within the filtering zone receive damping, nodes within the interface domain not.

To derive now the compatible macro displacement for each micro node within the filtering zone, again linear shape functions of the virtual elements are used and equation (5.37) can be applied – with the important difference, that \mathbf{d}_M is replaced by the now known displacements of the “filter” nodes $\mathcal{N}_{\mathcal{F}}$ ⁷¹:

$$\mathbf{u}_M^{(n-1)} = \mathbb{N}_M \tilde{\mathbf{u}}_{\mathcal{F}}^{(n-1)} \quad (5.40)$$

⁷⁰ In contrast to the partially fixed interface elements, the filter elements are prone to hourglass modes if only one integration point is used. In these cases, therefore, four integration points in 2D and eight for 3D should be used in these elements; volumetric locking is excluded, since no ordinary material model is used to determine the stress state.

⁷¹ This leads to the trivial definition of the projector operator: $\mathbb{P}_m = \mathbf{I} - \mathbb{N}'_M$, in which $\mathbb{N}'_M = [\mathbb{N}_M \mathbf{0} \dots \mathbf{0}]$ is the matrix of macro shape functions, extended by n_m zero columns to yield a size of $n \times n$ (\mathbb{N}_M is of size $n \times n_m$ only).

Note that due to the time integration scheme, the kinematic variables in $(n - 1)$ have to be used.⁷² Since $\mathbb{N}_{M_{i,j}} = \mathbf{0}$ for micro nodes outside of their overlying virtual element, it is simpler to evaluate the unique microscale contribution for the micro nodes covered in each virtual element k individually, following the same procedure as for the interface coupling, equation (5.26). Having $\mathbf{u}_M^{(n)}$ for each micro node at hand ($\mathbf{u}_M^{(n-1/2)}$ is retrieved similarly), equation (5.39) is solved and the damping can be applied during integration of the velocities:

$$\dot{\mathbf{u}}_m^{(n+1/2)} = \dot{\mathbf{u}}_m^{(n-1/2)} + \Delta t \ddot{\mathbf{u}}_m^{(n)} \underbrace{- 2f_d \Delta t \dot{\mathbf{u}}_m^{(n-1/2)} - f_d^2 \Delta t \mathbf{u}_m^{(n-1)}}_{\text{damping}} \text{ in } \Omega_{\mathcal{F}} \quad (5.41)$$

The acceleration is still derived without damping as $\ddot{\mathbf{u}}_m^{(n)} = \mathbf{M}_m^{-1}(\mathbf{R}_m^{(n)} - \mathbf{F}_m^{(n)})$. Displacements are afterwards integrated by equation (2.37b). Admittedly, this approach is pragmatic and less stringent than the concept detailed in [335]. There, the compatible macro displacement field and the unique microscale contribution are derived by working on the direct coupled total displacement field, whereas here the displacement field of the (macro) filter elements does not influence the displacement field of the covered micro domain elements within the same timestep. But since the damping decays the signal over several time steps, this is of inferior importance. Indeed, the following examples show that the amplitudes of the pathological reflections are damped out to a high and satisfactory degree.

The damping factor f_d has units of [1/s] and its optimal value is problem-dependent. As detailed in [335], the filtering zone could be enlarged by several rows of elements, and both values – the value of f_d and the width of the filtering layer – affect the solution. Although some rough recommendations are mentioned in [335], optimal values must be determined by trial.

For implementational reasons, the filter nodes are handled as being part of the macro domain. As will be detailed in the next chapter, macro- and microscale are processed by different computational units. Since the macro velocities of the interface and the filter nodes have to be communicated to the microscale, the communication overhead is considerably increased if damping is activated. Whereas for the unfiltered approach, $4n_{\mathcal{J}} \times 28$ bytes have to be considered (refer to Page 127), the demand increases to $(4n_{\mathcal{J}} + n_{\mathcal{F}}) \times 28$ bytes.

⁷² This has to be done in the original SPML approach as well if applied to the Leapfrog scheme, and is no particularity of the WS coupling.

Examples of the applied SPML approach in the WS coupling

Figure 5.11 shows the 1D simulation performed already at the beginning of this section, but now with damping. A strong reduction of the amplitude of the reflected signal is clearly seen.

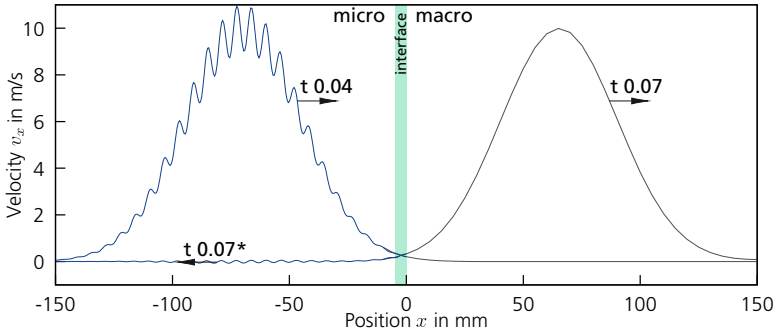


Figure 5.11: The above-mentioned 1D example, repeated with the SPML approach. Compare to Figure 5.7 for the undamped solution. Here, the reflected amplitude is reduced by nearly 95 %.

As a second example, consider a linear-elastic 2D bar under plane strain. Overall, it has a length of 600 mm and a width of 25 mm; the micro domain ranges from $-300 < x < 0$ and the macro correspondingly from $0 \leq x \leq 300$. Elements with edge length $e_M = 12.5$ mm are used for the macro domain, whereas the micro domain is much finer discretized, featuring elements with an edge length of $e_m = 0.78125$ mm. Figure 5.12 displays the velocity profile in the micro domain, while the fringe plot shows the velocity contour at $t = 1.58$ ms. One simulation is undamped; in a second run, the SPML approach was activated with $f_d = 450$ 1/s. The differences in the amplitude of the reflected portion are clearly observable. In this case, the reduction is about 85 % – less than in the 1D example but still high. With view of the kinetic energy of the micro domain, the damping dissipates more than 98 %. *Marchais* et al. show that their SPML approach is theoretically capable of dissipating 99 % of the pathological reflections, which can be achieved by a suitable combination of the layer width and the damping value. Theoretically, an increase of f_d should lead to a higher dissipation rate, but two things should be remembered: First, a too high value of f_d would eventually lead to a noticeable impedance mismatch, and, second, f_d

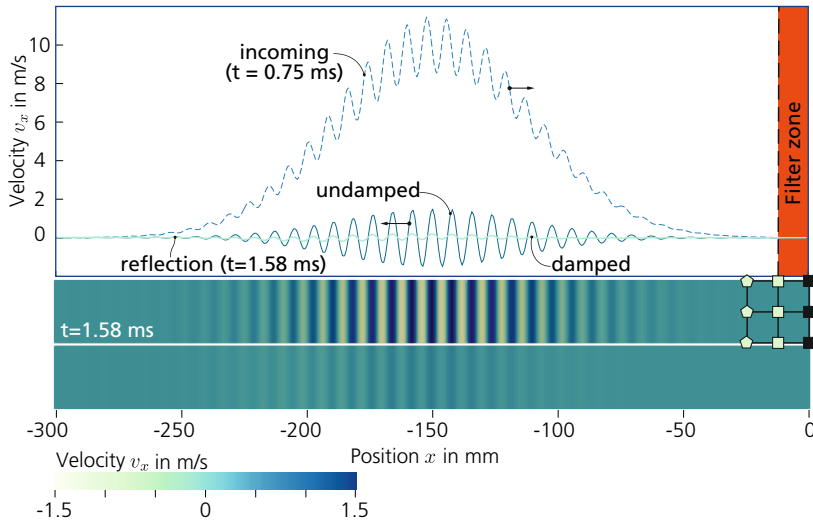


Figure 5.12: Velocity profile of a 2D bar under plane strain, with a wave running from the micro into the macroscale (left to right, macro domain not shown). Without damping, the high-frequency content is reflected at the interface, whereas the SPML approach damps out most of the pathological reflections.

is linked to the frequency content of the signal and should therefore be chosen with regard to the loading signal characteristics. In fact, increasing the value leads again to a higher amplitude of the reflected signal, and the chosen value seems to be close to the optimum.

A second simulation with an additional filter element row was conducted. In this case, $f_d = 300$ 1/s leads to the highest dissipation, reducing the initial amplitude by 90 %. A third filter element and $f_d = 200$ 1/s decreases the amplitude still further, but the additional dissipation rate is relatively low compared to the case of one filtering zone.

6 Validation and application of the weak staggered coupling and outlook on trajectory determination

This chapter is intended to demonstrate the applicability of the developed WS coupling together with the mesomechanical modeling approach. After the comparison of chosen 2D simulations between the LM based and the WS coupling, the parallel and efficient implementation of the latter for large 3D models will be discussed. Subsequently, an internal explosion in a small, confined chamber serves as a final application example, while the detailed determination of fragment trajectories to derive a safety map highlights the benefit of the approach and closes the chapter.

6.1 Validation examples and comparison between coupling approaches

Example simulations demonstrating correct wave propagation with the WS coupling in 3D have already been shown in [284]. Here, only 2D examples will be reported to directly compare the WS and the LM coupling.

6.1.1 Example 1 – homogeneous microscale

As a first example, consider the homogeneous two-dimensional bar with length $l = 1000$ mm and height $h = 50$ mm, shown in Figure 6.1, top. The macro

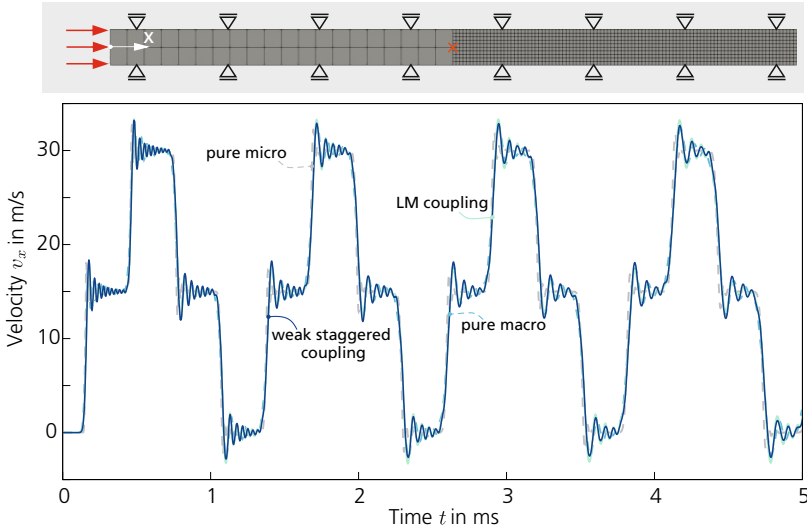


Figure 6.1: Velocity history of a central node (red "x" in model). Comparison of different simulations.

discretization features an element edge length of $e_M = 25$ mm, the micro domain is meshed with elements of size $e_m = 3.125$ mm. On the left boundary of the model, a velocity constraint is applied with $v_0(t) = 15$ m/s, whereas nodes on top and bottom are fixed in orthogonal direction, promoting a plain strain state. For comparison, the problem is additionally simulated with a pure macro and with a pure micro discretization, whereas for the coupling, the rear half of the geometry is replaced by the micro domain. A simple linear elastic material model is used for the whole model, with $G = 6.17$ GPa, $K = 15.4$ GPa and $\rho = 2.194$ g/cm³. Moderate viscous damping with parameters $\zeta_L = 0.01$, $\zeta_Q = 0.1$ has been activated in all runs.

The velocity history of a central node on the interface is shown in the diagram, Figure 6.1. As a result of the instantaneous velocity change on the left side, strong oscillations occur around the theoretical value. These are a direct consequence of the spatial discretization and would occur in every simulation with comparable spatial and time resolution [365]. In fact, all four simulations show more or less the same velocity development. The coupling results fit well between the pure meso

and pure macro results, although differences are in general hardly discernible. Most importantly: The results of the LM coupling and the WS coupling are almost equivalent, with slightly stronger overshooting in the oscillations brought up by the LM coupling.

6.1.2 Example 2 – heterogeneous microscale

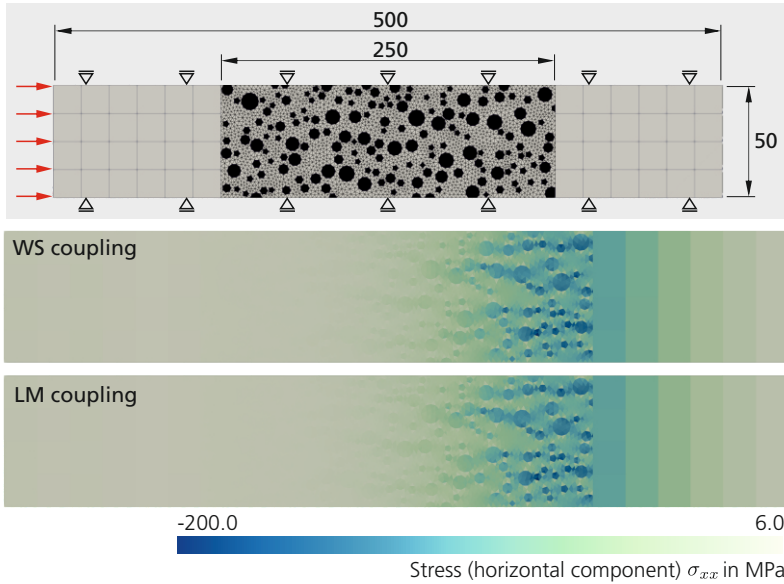


Figure 6.2: Wave propagation through a heterogeneous micro domain with both approaches. Top: Model, bottom: horizontal stress σ_{xx} at $t = 0.1$ ms.

Figure 6.2, top, shows – as a second example – a bar with a heterogeneous micro domain in its center, resulting in two coupling interfaces. The size of the macro elements is again $e_M = 25$ mm, the micro domain is discretized with considerably smaller elements. All elements behave linear elastic, however, with different material properties.⁷³ Boundary conditions are similar to the first example above,

⁷³ Macro: $\rho = 2.194 \text{ g/cm}^3$, $G = 6.17 \text{ GPa}$, $K = 15.4 \text{ GPa}$, Micro: matrix: $\rho = 1.99 \text{ g/cm}^3$, $G = 8.4 \text{ GPa}$, $K = 10.0 \text{ GPa}$; aggregates: $\rho = 2.69 \text{ g/cm}^3$, $G = 31.0 \text{ GPa}$, $K = 41.4 \text{ GPa}$.

whereas the Gaussian pulse, already used for the 1D example in the previous chapter, is applied as velocity boundary at $x = 0$, refer to equation (5.30) on Page 129. The parameters $A_0 = 15$, $A_1 = 0$, $\beta = 0.015$ are used here. Figure 6.2 shows the stress state σ_{xx} at $t = 0.1$ ms – the moment when the peak of the wave just passes the second interface. No differences are observable between the LM based and the WS coupling. For this example, no artificial viscosity was applied. The velocity history of a central node in the micro domain is plotted in Figure 6.3. Again, the development is almost identical, besides stronger overshooting in the saddle points by the LM coupling with increasing problem time.

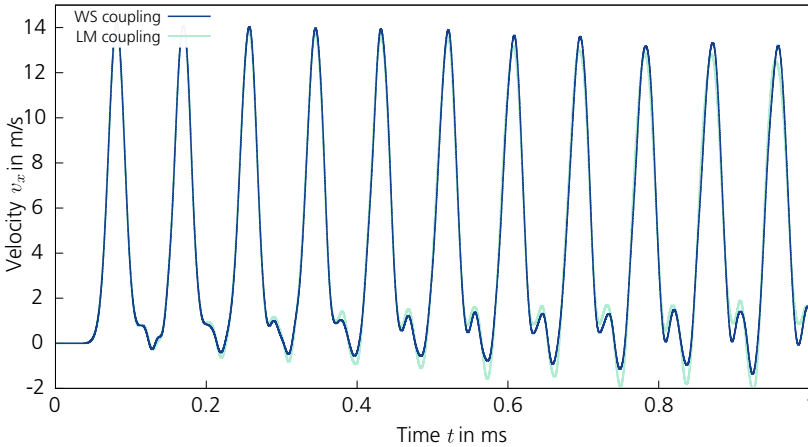


Figure 6.3: Comparison of the velocity history of a node placed at the center of the micro domain.

6.1.3 Example 3 – wave propagation parallel to the interface

A more demanding problem is wave propagation *along* a coupling interface, as exemplified in the two-dimensional bar Figure 6.4, top. The edge lengths of the elements, the material model and the boundary conditions are similar to Example 1. A boundary condition, $v_0(t) = 10$ m/s, is applied at $x = 0$. Figure 6.4 compares the velocity field v_x at different points in time between the two coupling approaches. The wave propagation is more or less identical. Only after

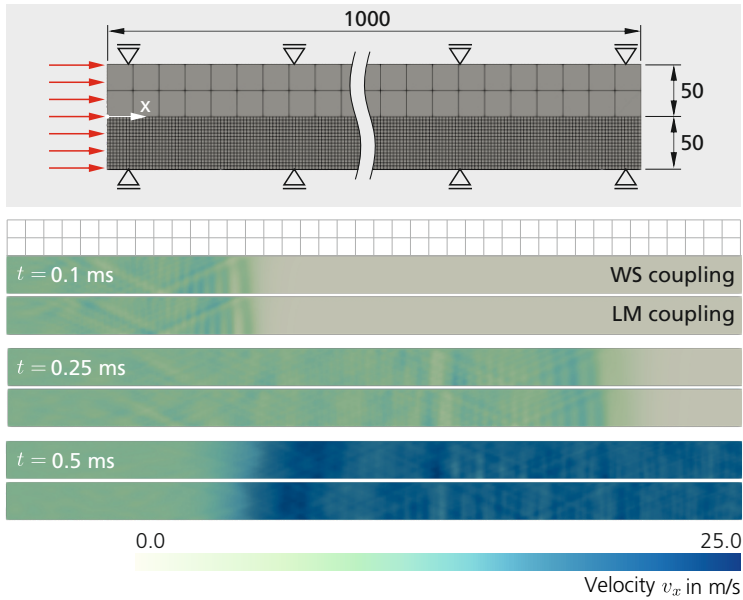


Figure 6.4: Model and velocity field in the micro domain at three distinct points in time. The macro domain is not shown and is only indicated at the top!

some time do slight, negligible differences appear. In the case of LM coupling, already in the first cycle the horizontal interface nodes adjoining the first macro element experience a non-zero velocity, whereas this velocity slowly increases in the WS coupling, as a consequence of the rising stress state in the corresponding virtual elements. Hence, the propagation velocity of the wave is slightly higher in the case of LM coupling. It has to be stated that the LM coupling is more stable if only one integration point is used for the 2D elements. In this case, instabilities occur in the simulations by the WS coupling after some wave passes. The results shown here have been achieved with four integration points. Test runs remained stable in this configuration up to 100 ms. Slight oscillations in the mesh – albeit at the correct global energy level! – are observable only after several wave passes and therefore at problem times, which are irrelevant in most practical cases.

6.1.4 Example 4 – embedded microdomain

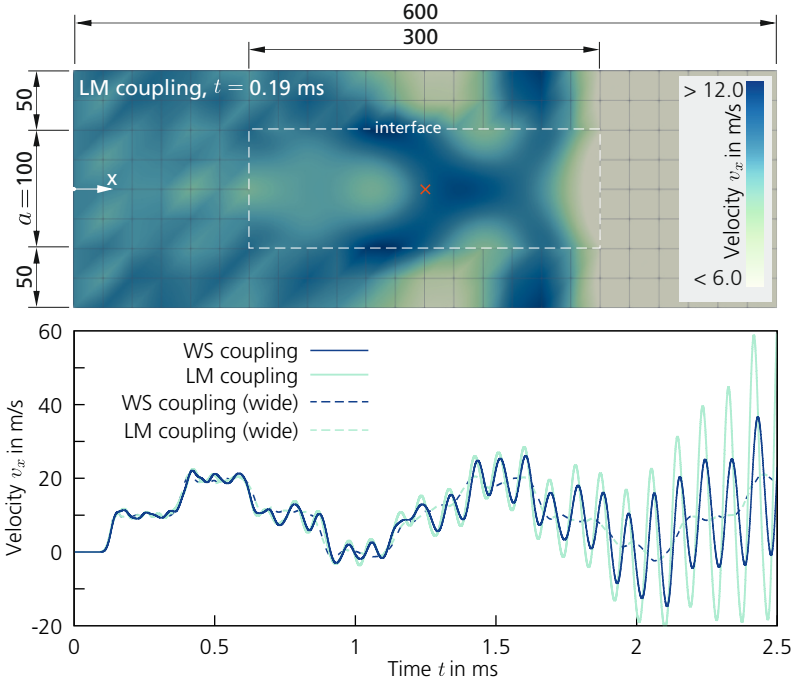


Figure 6.5: Embedded micro domain. Top: Velocity contour plot at $t = 0.19$ ms. Bottom: Velocity history of the central node (red "x" in the contour plot) for a simulation with the small micro domain and one with a significant larger domain.

Finally, the example of a (heterogeneous) micro domain that is completely embedded in the macro domain should be considered. Again, a velocity of $v_0(x = 0, t) = 10$ m/s is applied on the left side, the material model and the remaining boundary conditions are similar to Example 2. Figure 6.5 shows the velocity field at $t = 0.19$ ms along with the dimensions of the model and the velocity of a central node below. For both couplings already in the second wave pass (approximately at 0.7 ms) an increasing oscillation is observable, which aggravates to instability. Yet, this occurs for both couplings, indicating that the set-up is the problem, not the method. Indeed, the reason for the velocity increase is

a difference between the macro and the micro velocity fields, imposed at the interface. Recall from Figure 5.4 (Page 123) that the velocity (for both couplings) is linearly interpolated between two macro nodes and then applied at the micro interface nodes. This results instantaneously in a velocity change of the upper micro interface nodes if node i in Figure 5.4 has a velocity $v_{x,i}^M \neq 0$. Yet, the neighboring micro nodes not on the interface still have $v_x^m = 0$. Consequently, a disturbance propagates down- (and upwards) from the interfaces into the micro domain, although the right-running wave has not yet reached these nodes. This disturbance is already visible in Figure 6.4 for one interface and parallel propagation as diagonal bands in the velocity field. It is clearly observable here as dark “x” in the contour plot, Figure 6.5, top. In this case, the disturbance increases when the up- and downward running waves confront and reflect in the center of the micro domain. In adverse set-ups, such as the one shown, horizontal oscillations occur, which aggravate with time. If, however, the micro domain is enlarged, these effects are inferior and enfeeble with time. The diagram in Figure 6.5 also contains the results of such a simulation, in which the width, a , of the micro domain is significant enlarged to be $a = 400$ mm (labeled “wide”). This simulation remains stable.

Conclusion

The four examples presented demonstrate the equivalence of the novel WS and the established LM based coupling. For the relatively small 2D cases, both simulations show comparable simulation times. It is in 3D, where the WS coupling approach unleashes its potential. The next section details some aspects of the parallel implementation, which is a main ingredient for practical applicability.

6.2 Development of a parallel framework for simulations in 3D

6.2.1 Introduction

Parallel implementation of algorithms generally aims to decrease overall execution time and increase the efficient use of all affected resources. The latter aim

encompasses mainly a balanced workload on all involved processors, which means keeping idle times of individual processing units to a minimum. How well these two aims – total speedup by an increasing number of processes and their efficient use – are achieved depends mostly on how well an algorithm is parallelizable. If it contains inherent sequential sections, the parallelizability is bounded, as is the speedup and the efficiency; a principle known as Amdahl's law.

Especially *hierarchical* multiscale approaches inherently exhibit a parallel structure. The macro domain and every connected RVE are processed on a unique processor, without complications. Since the individual RVE are independent, communication occurs only between each RVE and the macro domain. Things are slightly more complicated in *concurrent* set-ups: There, initially, only two domains exist: a macro and a micro domain. Of course, both can be processed on different computational units, but depending on the problem set-up it is very likely that the micro domain has a much higher number of degrees of freedom than the macroscale. Consequently, the time needed to complete one cycle is significantly higher there. Furthermore – depending on the overall size of the micro domain – it is questionable whether the solution of the complete domain by one processor is feasible at all within rational limits.⁷⁴ It is necessary, therefore, to partition the micro domain itself.

As will be shown in the following, the proposed WS coupling scheme is highly parallelizable and only minor parts of the algorithm are inherently sequential. Furthermore, the scheme is easily adapted to a sub-partitioning of the micro domain – it even supports the decomposition inherently and leads to a very balanced workload. This is in contrast to the standard LM based coupling. Of course, such a coupling can be parallelized as well but is less straightforward. These facts are an important ingredient to the proposed coupling since with current computer power a dynamic solution of large domains discretizing a

⁷⁴ Consider a rather medium-sized wall section of $450 \times 450 \times 200 \text{ mm}^3$, which shall represent the meso structure of concrete. If – for simplicity – one neglects the filling with aggregates and assumes that the whole domain is meshed with regular hexahedron of edge size 2 mm, the overall mesh contains approximately 5×10^6 elements. This is a number that may still be solved by a single processor with a very well vectorized and optimized solution scheme, but is certainly at current capacity limits. If aggregates are involved and consequently tetrahedral elements have to be used, the overall number of elements increases roughly by a factor of seven, see Section 6.3. If one considers a realistic time step of approximately $\Delta t \approx 5 \times 10^{-5} \text{ ms}$ and a total problem time of 10 ms – which alone is the loading time of the blast example, Section 4.3.3 – the whole problem needs 2×10^5 cycles, within each all elements have to be touched multiple times.

micro or meso structure would be impossible. Although parallelization is not a necessary feature of the described coupling, it is nevertheless a necessity for practical application in real problems. Indeed, one may state that the coupling is useful only in the following suggested parallel set-up and does show its advantages only within this framework.

6.2.2 Parallel set-up

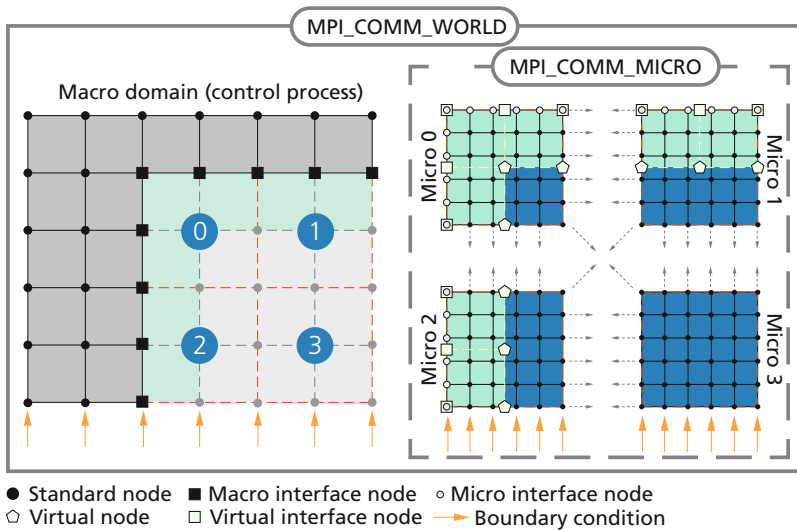


Figure 6.6: The whole model is initially available as macro domain. A part of the macro domain is then replaced by a micro domain (light gray area), which is – in this example – split into four subdomains. Each subdomain is processed on a single process unit. Communication occurs between the micro domain partitions and between the micro domain partitions and the macro domain.

Figure 6.6 shows a schematic set-up of a simple problem. A 2D macro domain (left) should be partially replaced by a micro domain. Then, only the dark gray elements and the black nodes have to be processed in the macro domain, which is taken to be the primary control process. The micro domain is decomposed into four subdomains. Those adjoining the remaining macro domain (here 0, 1,

and 2), represent “interface”-subdomains and have to exchange data with the macro process, whereas subdomain 3 has to communicate only with its peers. Establishing and processing the virtual (macro) elements to provide the forces on the interface is necessary only in the interface-subdomains. In the current implementation, the original macro elements attached to the interface are used to establish the virtual elements in the micro domain. Each interface-subdomain individually communicates its averaged forces $\tilde{\mathbf{F}}_j^m$ with the macro domain. The decomposition of the micro domain in even more subdomains will therefore introduce only negligible more communication between the two domains. Furthermore, the evaluation of the virtual interface elements is done in parallel. More processes available for the micro domain means, therefore, simply a reduction of the individual workload and an increase in the number of processes involved during communication. But still, each micro domain process is responsible for the virtual elements covered in its subpartition and individually sends its averaged forces once to the macro process. This is a significant advantage compared to the LM based coupling. There, the free accelerations have to be collected at one processor, the system of equations, (5.14), established, solved, and the link accelerations distributed back. The solution (i.e. the matrix multiplication) can be parallelized as well, but the optimal choice of processors is here less intuitive.⁷⁵

Once the problem is finally set up, the macro process starts to distribute the velocity of its interface nodes and the micro processes can solve their initial boundary value problem independently. After these processes complete one cycle, the stress state in the virtual elements is averaged, the forces determined and sent to the macro process, where the cycle can be completed subsequently. Algorithm 3 lists the schematic parallel algorithm. It is noteworthy that once the velocities at the macro interface nodes are known to the micro processes, all processes (including the macro process) can solve their domain in parallel. There are only two limitations: (a) the *interface* nodes of the macro domain can be updated only after the micro domain has reached the end of the cycle and provided the appropriate forces, and (b) the boundary nodes of neighbored micro

⁷⁵ Algorithms for a parallel computation of equation (5.14) of course exists, e.g., by using systolic arrays, but this parallelization within the already given parallel set-up is not straightforward. One can think that the matrix operations are distributed to only a number of the micro processes involved, which are idle during the solution of the system of equations anyway. This parallelization will in any case lead to an increase of communication between the partitions. Generally, the speedup is bound and will – after a certain point – not increase further with the number of utilized processes. Furthermore, the optimal number of processors used, strongly depends on the rank of \mathbf{H}_0 , but it is difficult to choose an optimal number beforehand. Finally, the exact structure of \mathbf{H}_0 has a direct effect on the communication penalty; see the appropriate discussions in [366], e.g., pp. 71–73.

domains need information from the appropriate processes before they can be updated.

Algorithm 3 Parallel solution of micro and macro domain for one cycle from (n) to $(n + 1)$. Compare with the serial Algorithm 2 on Page 126. Here, communication efforts are colored in blue.

Micro (Decomposed into \mathcal{P} subpartitions)

```

Receive  $\dot{\mathbf{u}}_{\mathcal{J}}^{(n+1/2)}$ 
Interpolate BC, eq. (5.26)
for  $\forall \mathcal{E}_m^{\mathcal{P}}$  do
    Update matrices
    Determine  $\sigma$ 
    Calculate  $\mathbf{F}_m^{\mathcal{P}}$ 
end for
Communicate  $\mathbf{F}_m^{\mathcal{P}}$  between partitions
for  $\forall \mathcal{N}_m^{\mathcal{P}}$  do
    update  $\ddot{\mathbf{u}}_m, \dot{\mathbf{u}}_m, \mathbf{u}_m$ 
end for
for  $\forall \mathcal{E}^{\mathcal{P}}$  do
    Update matrices
    determine  $\tilde{\sigma}$ 
    Calculate  ${}^{\mathcal{P}}\tilde{\mathbf{F}}_m^m$ 
end for
Send  ${}^{\mathcal{P}}\tilde{\mathbf{F}}_{\mathcal{J}}^m$ 

```

Macro

```

Send  $\dot{\mathbf{u}}_{\mathcal{J}}^{(n+1/2)}$ 

for  $\forall \mathcal{E}_M$  do
    Update matrices
    Determine  $\sigma$ 
    Calculate  $\mathbf{F}_M$ 
end for
for  $\forall \mathcal{N}_M$  do
    update  $\ddot{\mathbf{u}}_M, \dot{\mathbf{u}}_M, \mathbf{u}_M$ 
end for

Receive  ${}^{\mathcal{P}}\tilde{\mathbf{F}}_{\mathcal{J}}^m$  from each partition
for  $\forall \mathcal{N}_{\mathcal{J}}$  do
    update  $\ddot{\mathbf{u}}_{\mathcal{J}}, \dot{\mathbf{u}}_{\mathcal{J}}, \mathbf{u}_{\mathcal{J}}$ 
end for

```

In the given implementation, the broad applicable Message Passing Interface (MPI) protocol is used as underlying mechanism for parallelization and communication [367]. This protocol is independent of the underlying hardware and therefore very versatile. Although the actual communication is implemented by the protocol with special regard to the hardware (e.g., shared or distributed memory, ethernet, infiniband, etc.), these facts remain concealed to the software and enable the program to run later on very different hardware. An inherent feature of this concept is its scalability. Additionally, the OpenMP library (OMP) has been used to further parallelize some code sections on each micro domain partition to further speed up the simulation [368].

With respect to the different mesh sizes, it is obvious that the critical time step of the micro domain is in general much smaller than that of the macroscale.

One might therefore wish to employ subcycling: The micro domain can then complete several cycles with its own time step and only if the sum of these steps yields one time step of the macroscale, the latter is updated as well. Since this problem occurs in any case where different mesh sizes are involved, there exists a distinct scope of literature discussing different options and algorithms. In general, subcycling is possible for the WS coupling as well, but several issues reduce its attractiveness. Only if the solution of the macro domain per step needs more time than the (parallel) solution of the entire micro domain, subcycling yields benefits. Algorithms, requirements, and assumptions are discussed in detail in Appendix A.2.

6.2.3 Exemplified scalability of the WS coupling

To exemplify the scalability of the coupling, consider a simple rectangular model. Starting with a single cubical micro partition of edge size 100 mm, discretized with 512 000 elements, in each subsequent simulation the total micro domain is enlarged by combining an increasing number of this basic micro partition. Each one is processed on an individual CPU-core, but the amount of entities to be processed for the coupling and the size of the data to be shared between macro and micro processes in total increases. Only 100 cycles have been simulated for each case to measure the times spent in the different routines of the cycle. To record meaningful times, each simulation has been repeated five times and the average values are calculated afterwards. All simulations have been conducted on a reserved partition of the HPC cluster at EMI, featuring computenodes with two Intel Xeon Gold 6154 CPUs and 18 cores each. Communication occurs via 56 GBit/s infiniband or shared memory if less than 36 cores are involved. Figure 6.7 shows the results in terms of model size expressed by the number of elements in the micro domain and the average time needed per cycle (determined to be the average value of all processes involved in five runs each). The average time needed for one core to complete one cycle of a single micro partition *without* coupling, that is, a standard simulation of this model, has been used as normalization factor. In fact, two further uncoupled simulations with doubled, respectively, quadruplicated number of elements on the micro partition have been carried out to assess the scaling of the simulations without coupling (“uncoupled” in Figure 6.7 – the point for the quadrupled model lies outside the diagram range). The resulting scaling comes close to an ideal linear scaling: Doubling the model size requires twice as much time; see the dashed line in the diagram.

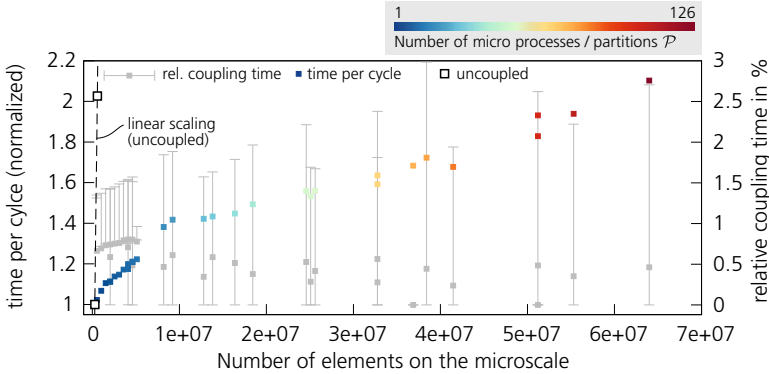


Figure 6.7: Normalized average time per cycle and relative coupling time with growing size of the micro domain. A linear scaling for an uncoupled microscale (standard simulations) is indicated by the dashed line on the diagrams left side.

In contrast, the scaling for the coupled set-up, utilizing MPI in the scheme detailed above, scales ways better. In the extreme, the maximum-sized model with 64 million elements – 125 times more than in the single partition – requires on average only twice as much time for a single cycle! A second data set is plotted in gray on the diagram. These values show the relative time per cycle that the algorithm spends in routines necessary for coupling, namely, interpolation of the interface velocities and averaging of the stress state within Ω_I . Error bars mark the absolute minimum and maximum values measured during the runs. In all cases, the average time needed is below 1 % of the total cycle time, and even in the worst case the maximum value does not exceed 3 %, indicating that the coupling as such is very efficient and does not lead to a perceptible runtime increase. However, not included is the time necessary for *communicating* the values between domains. Essentially, data communication, especially between micro partitions, is responsible for most of the cycle time. Figure 6.8, left, shows the relative time needed to communicate between the individual microscale partitions, which, of course, is independent of the type of coupling. With increasing size, eventually more than 50 % of the total time per cycle is spent here. Besides the increasing amount of data to be communicated, delays occur if some processes are not yet ready to receive data. This delay might be reduced by an improved – but not straightforward – implementation of the communication routines. On the right side, again the necessary time for coupling is plotted, now against the number of microelements covered by the interface

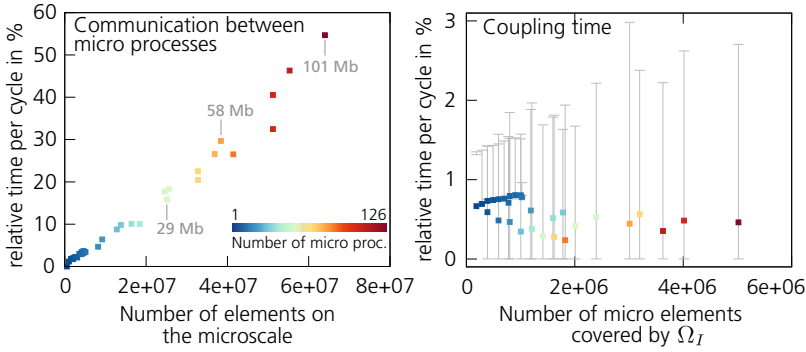


Figure 6.8: Left: Relative time per cycle required for communication between the individual microscale partitions. The necessary amount of data to be communicated is exemplary given for chosen data points. Right: Relative time per cycle required for the coupling routines vs. the number of involved microscale elements.

region Ω_I , $n_{\mathcal{E}}^i$. These elements have to be averaged to determine the interface forces. As can be seen, an increase in these entities does not lead to longer run times, as already conjectured in Section 5.3.6.

This performance analysis highlights that the theoretical considerations regarding the coupling's efficiency are confirmed by an actual measurement. Although the overhead due to communication increases the total time necessary, the actual steps to perform the coupling are very favorable with respect to the total time.

6.3 Application example: internal explosion in a confined chamber

6.3.1 Model and set-up

To demonstrate the applicability of the developments described so far, the case of an internal explosion within a confined chamber is well-suited. The structure shown in Figure 6.9 might resemble a cutout of a test chamber in the chemical industry, a manufacturing site for components containing detonatives, such

as airbags, or a facility to store small amounts of explosives. Potential hazards of debris thrown into adjoining chambers as a consequence of an accidental explosion of the substances involved might be of interest. In this case, the resulting loading of the structure is determined by the fact that the explosion is confined. In contrast to a free-field scenario, several pressure peaks due to a reflection of the first pronounced shock waves are to be expected, followed by a quasi-static “gas-pressure”, p_G . Only if vent openings – either intended or as a result of structural damage – are available, this pressure eventually decreases. The total impulse, hence, is much higher than in a comparable free-field explosion. However, in this example, only an idealized pressure history is used, as indicated in the diagram on the right side of Figure 6.9. It considers only the initial pressure peak and a linear decreasing gas-pressure. In fact, since no reinforcement is included, this structure resembles only a hypothetical case intended to sketch a potential application of the coupling. Future applications should contain reinforcement for realistic structural behavior and a fully coupled fluid/structure interaction to resolve real spatial and time-dependent pressure.

For the demonstration case, the central section of the middle wall is discretized on the mesoscale. Pressure is approximated by the equations of *Kingery* et al. [369]; a second, linear decreasing portion is also considered, representing the diminishing

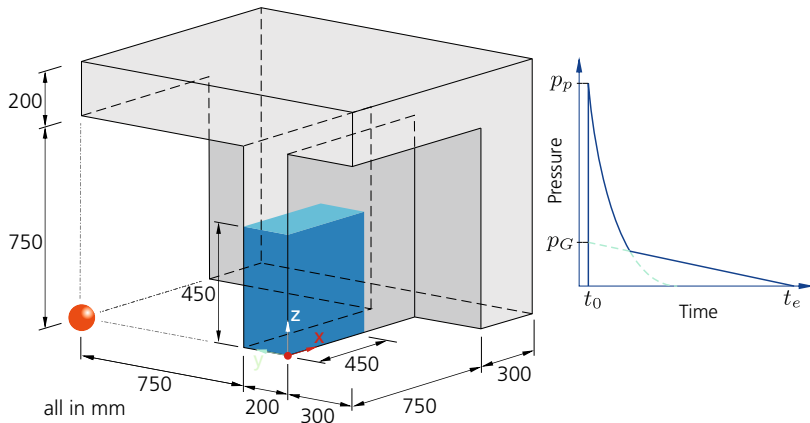


Figure 6.9: Left: Model of a fictive test chamber or storage for explosive substances. The central region of the partition wall is modeled on the micro domain. Right: Idealized pressure history representing an internal detonation.

gas pressure. Values for p_G and t_e have been estimated using empirical data provided in the UFC manual [370]. All planes where the fictive model was “cut-out” of the remaining structure ($x = 0$, $y = 950$, $y = -300$, $z = 0$) have their translational degrees of freedom fixed in the orthogonal direction.

Aggregates between 3 and 16 mm diameter have been considered on the mesoscale, leading in total to 209 243 modeled inclusions (including 38 171 voids). The domain comprises in its pristine state (no cohesive zones active) overall 35 916 639 elements and 6 390 832 nodes. The number of interface nodes on the macroscale is $n_{\mathcal{T}} = 1\,281$, connected to 1 200 virtual elements. Overall $n_i = 42\,257$ nodes establish the micro interface, for which in each cycle the interface velocities have to be interpolated. The virtual elements cover in total $n_{\mathcal{E}}^i = 2\,434\,736$ elements in the micro domain from which an averaged stress state has to be determined in each cycle. In this example, the micro domain is divided into $\mathcal{P} = 72$ subpartitions, 21 of them adjoining the interface. Hence, the interpolation and averaging is carried out in parallel on 21 processes, leaving roughly 115 940 elements for each process to touch – about one-fifth of the total number of elements processed by each CPU core. For comparison: the interface operator \mathbf{H}_0 of the LM coupling would exhibit a size of $134\,457 \times 134\,457$ with slightly more than 45 000 000 non-zero coefficients. Concerning communication between scales, the LM coupling has to send in total roughly 2.3 megabytes between macro and micro processes, the WS coupling only 140 kilobytes.

6.3.2 Results

Figure 6.10 shows two views of the structure at $t = 2$ ms. Colored is the crack opening. The amount of explosives in this case leads to moderate structural damage. In the micro partition, several larger and still connected “clods” dissolve on the rear side. Two distinct cracks propagate from the center diagonally to the upper corner. As a remarkable result, the crack bridging between micro and macro domain should be emphasized here. Each distinct crack on the rear side of the mesoscale is continued in the macro domain – although smeared there in a much larger crack band. In both views, most of the macro elements adjoining the interface exhibit distinct crack openings. It seems that failure in these elements is caused by tensile forces exerted by the mesoscale.

Finally, Figure 6.11 features the velocity field at $t = 2$ ms. For illustrative purposes, the results have been reflected here in the symmetry planes, and the rear side is

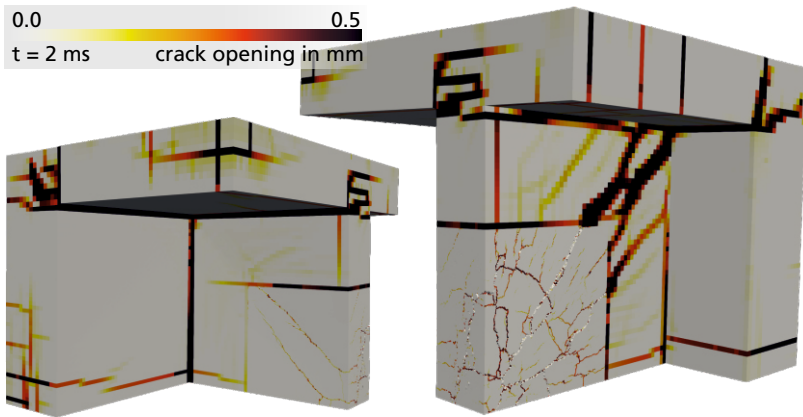


Figure 6.10: Cracks in the wall section. Left: view on loaded side, right: view on rear side.

shown. Discontinuities in the field demarcate individual, larger emerging fragments. The upper view on the side reveals a spallation plane roughly in the middle of the wall, indicating a resulting breach of the wall.⁷⁶

6.3.3 A critical note on remaining limitations

The results shown above clearly envision the possibility of simulating complex and large geometries with an embedded mesoscale description of it. Nevertheless, some challenges still remain and should not be dismissed here.

Besides the already mentioned difficulty of finding proper material parameters for the different phases involved, the mesoscale approach faces the emergence of multiple inner contact surfaces during the simulation. Once the cohesive elements, representing the weak interfacial transition zone, failed due to tension, the aggregates remain freely embedded in the surrounding matrix. Depending on the loading, a closure of the partial gap between aggregate and matrix may occur. The same holds for the matrix failure. As soon as matrix elements are

⁷⁶ Fit functions for breach- and spall thresholds, based on several experiments with reinforced concrete slabs, are given in [371]. These formulas – although not directly transferable – classify the considered scenario slightly above the spall threshold.

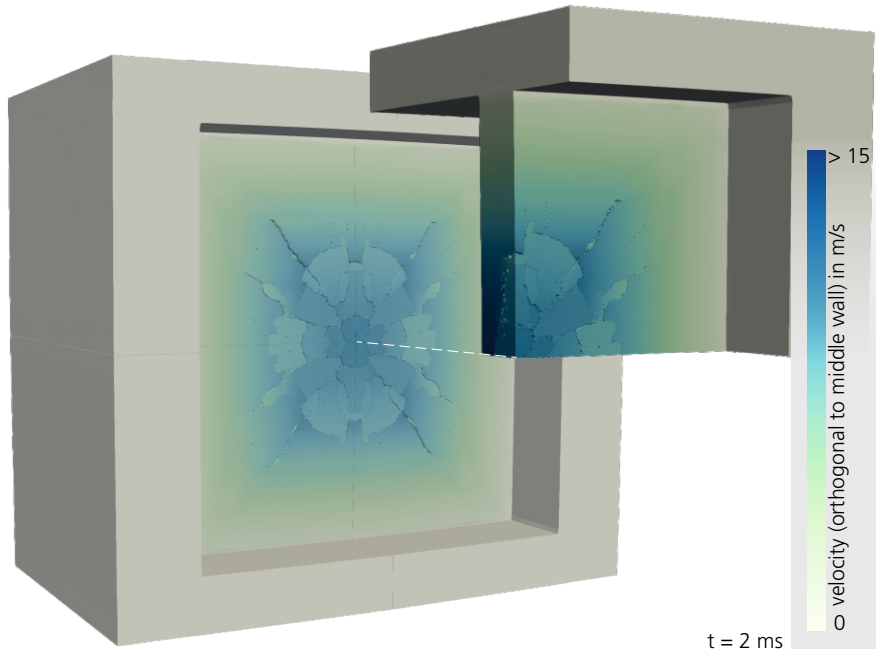


Figure 6.11: Velocity plot with view on the middle-walls rear. Note that only the upper right quarter has been simulated. Results have been reflected at the symmetry-planes for illustration only.

removed from the simulation, free “crack surfaces” arise within the model. Surely, these issues can be handled by a proper contact algorithm without difficulties. However, the algorithm currently implemented in SOPHIA is not able to deal efficiently with the high number of evolving contact surfaces. Hence, no contact was applied in the above simulation. For different loading scenarios this might not be a proper assumption.

Regarding the coupling, the damage aggregation at the interface, as observed above, deserves more investigation. In fact, the appearance of a discontinuity between the two very different scales should not be too surprising and can be expected for any type of coupling. While reiterating that the problem above clearly highlights the accurate propagation of cracks beyond the interface, the

quest for options to further improve the interface behavior is justified. This point is closely related to the question when the coupling should be stopped. If, eventually, the material surrounding the microscale – and the material within the microscale – is highly damaged: is there still an influence of the scales on each other? The current implementation keeps the coupling over the whole time and it is essentially one feature of the WS coupling that it is able to do so. Allowing completely new mesh topologies due to node splitting and element removal at the microscale interface without further considerations or reevaluation of interface operators is a strong argument in favor of this approach. But how and how long this should be appropriately reflected in the averaging procedure of the microscale volume to establish the macro interface forces is still an open question. Yet despite these challenges the coupling surely opens a door towards realistically simulating debris throw. The benefits of such simulations delivering unique fragments in the determination of safety distances is the content of the final section of this chapter.

6.4 Outlook – detailed trajectory determination

This chapter shall close with an outlook on the detailed determination of debris trajectories, the final end of fragmentation simulation. For risk analysis, trajectories are of distinct importance to indicate safety distances and hit probabilities. However, the trajectories strongly depend on the aerodynamic coefficients of the individual pieces, which influence lift, drag, and potentially even rotation and flipping. The equation of motion of a single debris is given by the following coupled differential equations [372], in which the velocity of the fragments $\dot{\mathbf{u}}$ is expressed in terms of two components, v and w , in a generic 2D plane with angle φ to the horizontal, see Figure 6.12:

$$\ddot{u}_v - \frac{A\rho}{2m} (c_D \cos \alpha(\dot{\mathbf{u}}) - (c_L + c_{LA}) \sin \alpha(\dot{\mathbf{u}})) \|\dot{\mathbf{u}}\|^2 = 0 \quad (6.1a)$$

$$\ddot{u}_w - \frac{A\rho}{2m} (c_D \sin \alpha(\dot{\mathbf{u}}) + (c_L + c_{LA}) \cos \alpha(\dot{\mathbf{u}})) \|\dot{\mathbf{u}}\|^2 + g = 0 \quad (6.1b)$$

with A being the projected area of the fragment, ρ and m its density and mass. c_D , c_L and c_{LA} are the coefficients for the drag force, F_D , and the lift force due to translation and auto-rotation, F_L , g is the acceleration of gravity. Note that the wind speed of the environment is already neglected in the equations above. Furthermore, the moment around the pieces' center of gravity, the Magnus-

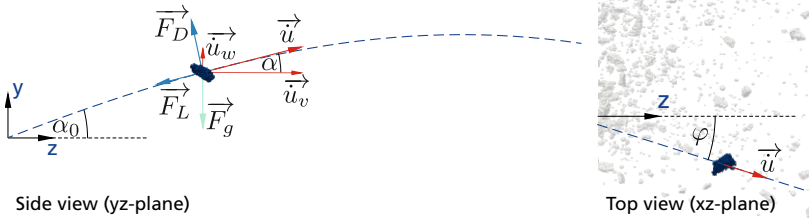


Figure 6.12: Forces acting on a single flying debris piece with velocity \vec{u} . The top view (right) shows additionally the surrounding debris (refer to Section 4.3.3) with strongly irregular shapes.

moment, is omitted here for simplicity as well. α is the current angle between the velocity vector and the ground plane. Equation (6.1) can be solved, e.g., by a Runge-Kutta approach.

For this illustrative example, the mass, initial velocity, and length ratios for each fragment were extracted from the simulation for the final time step. A procedure to track fragments during emergence and not only after some time and distance have passed is surely possible but sophisticated and costly. Moreover, it is doubtful whether such an approach yields a surplus of information since the choice of aerodynamic coefficients is a much more dominating factor. Assuming spherical fragments is too simplistic and results in a gross over-prediction of the flight distances. The detailed resolution of the fragments due to the mesomechanical approach allows more accurate parameters to be applied. On the other hand, exact parameters for the highly irregular and almost arbitrary shaped debris pieces are, of course, unknown. Here, an approach detailed in reference [8] is followed, which seems to be currently the most accurate one to derive realistic aerodynamic coefficients for debris. The authors experimentally derived the drag and lift parameters for several generic debris pieces in wind tunnel tests and proposed interpolation functions based on a sphericity factor and length ratios. With these functions and the actual debris shape from the simulation, individual and hence very realistic coefficients can be determined for each fragment.

With the values for each fragment at hand, the final position and the kinetic energy at impact can be determined. They are plotted for the fragments derived in the third validation example, Section 4.3.3, in the left polar plot of Figure 6.13. For each fragment of the five simulation runs, one point is included in the diagram. The right-hand side of the figure displays the results slightly differently: Major defense standards identify the hit of one piece of debris with more than 79 J

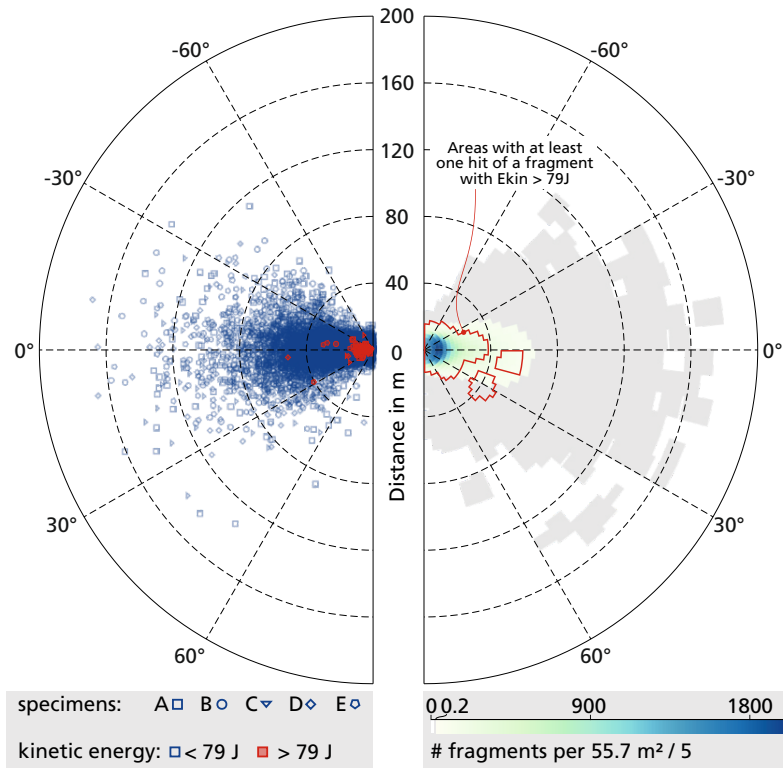


Figure 6.13: Left: Final position of the debris pieces, according to the procedure after [372] for each of the five specimens of the third validation example, Section 4.3.3. Right: Combined fragment density per 55.7 m². A value of 0.2 (gray) corresponds to one piece of debris in one of the five simulations.

within an area of 55.7 m² as critical threshold. Therefore, the graph shows the fragment density per 55.7 m². To achieve this number, for each grid point, the number of fragments in the surrounding, circular area of 55.7 m² is counted. Since five runs have been carried out, the number has to be divided by five. Gray areas, featuring a density of 0.2 fragments per 55.7 m², consequently are those areas hit by one fragment out of five simulations. Areas with at least one hit of a hazardous debris piece are demarcated in the plot, which thereby clearly

outlines critical regions and can be used to define safety distances with high fidelity. Although far from an exhaustive analysis, this map highlights a potential application of the simulation approach employed. That aerodynamic coefficients are determined for each debris piece by considering its actual shape, is – together with a detailed knowledge of its mass and initial velocity vector – surely immensely helpful and forward-looking.

7 Closing remarks

7.1 Main achievements of the present work

Fragmentation of concrete as an important threat emerging from dynamically loaded concrete structures could so far be considered only in experimental works or risk assessments based on probability analysis fueled by empirical data. Given the enormous efforts to conduct the required field tests, a suitable simulation approach would surely considerably advance the possibilities to quantify and mitigate risks due to flying debris. The present work addresses this systematic gap and makes a decisive step toward predictive simulation of debris throw in 3D concrete structures. Two aspects have been combined to a potent approach: (a) a suitable description of concrete on its mesoscale, reflected in an appropriate composition of geometric representation and numerical methods; and (b) the combination of two scales in one model to account for large structures within reasonable computational times.

Until now, the idealization of concrete on its mesoscale – although meanwhile extensively used to investigate and understand the failure behavior of concrete – has to the best knowledge and surprise of the author not been exploited to simulate the emergence of fragments and their quantitative analysis. Surely, the requirements for the model to reach this aim are high but can be tackled. Based on an extensive literature review and the identification of strengths and weaknesses of different approaches, a three-phase system was chosen to describe concrete on this first-order microscale: a homogenized mortar matrix with embedded aggregates, pores, and the consideration of a zero-thickness interfacial transition zone at the matrix-aggregate-boundary. Spherical shapes represent the explicitly modeled aggregates and voids. The resulting models capture the dominant failure modes under dynamic tensile loading and subsequent fragmentation to a fully satisfying degree, while the demands to generate them are well manageable.

Failure of the material is hereby incorporated by a twofold approach: The interfacial transition zone, the weakest link in the material, is properly described by a cohesive zone model. In contrast, a plasticity model is used to consider “cracks” in the matrix and through aggregates – which is much more efficient than handling bulk failure with cohesive zone elements as well. After exceeding a defined criterion, failed elements are removed from the simulation, thus separating the initial continuous body. For a reliable description of the stress-strain behavior of the elements, an existing concrete model, the RHT model, has been improved and furnished with an additional, regularized yield criterion. The latter is based on a rate-dependent principal stress limit and resolves brittle failure more physically than the von Mises yield criterion used so far.

With these assumptions, it is possible to simulate the failure of concrete beyond the occurrence of damage up to the full constitution of fragment clouds in medium-sized models. The achieved results exhibit a degree of detail rarely seen in literature up to now for the considered sample sizes – and are obtained within acceptable computational times. Besides the correct prediction of single crack paths, branching phenomena, and fragment velocities, even the mass distribution of a large number of fragments was simulated to a still satisfying degree; especially if one keeps in mind that only one single material parameter set was applied without extensive parameter fitting. Using the results to determine the expected trajectories of the debris by considering aerodynamic factors based on the actual shape of the individual fragments certainly goes beyond the current state and emphasizes the usefulness of this method.

Beyond an apt description of concrete failure on the mesoscale, this thesis introduces a novel coupling of two finite element domains with disparate discretization. Intended to allow the combination of a refined region with lower scale details in a large model, the coupling expresses a general concept, although the moderate scale difference in concrete lends itself to the application of this method. The approach is based on a small overlapping region, in which the micro domain is averaged to deliver proper forces for the macro interface nodes. In return, the movement of these nodes imposes a boundary condition on the micro interface. Due to its similarity to conventional fluid/structure interaction procedures and their typical staggered scheme, the coupling was labeled “weak staggered coupling”. As a noteworthy feature, the concept retains the direct solution scheme of wave propagation codes and imposes as few additional operations as possible on the overall simulation process. Thereby, it fulfills one driving intention of the development, namely to be as efficient as possible and keep computational costs at a minimum.

A detailed comparison with a conventional coupling based on Lagrange multipliers showed more or less similar results, but several advantages in terms of efficiency and application: The efforts introduced by the coupling are of linear order with respect to the number of coupled entities, and no system of equations has to be solved. Communication between separate domains requires smaller message sizes, additional memory needed is marginal, and the process is easily parallelized and scales impressively. Finally, topology changes on the micro interface, e.g., due to nodesplit or removed elements, are handled intuitively, whereas a complete reevaluation of the coupling matrix, followed by a refactorizing of the interface operator, would be triggered in a Lagrange multiplier based coupling.

Embedding the chosen mesomechanical idealization in a large macroscale model by applying the weak staggered coupling provides a powerful and robust approach to simulate the effects of high dynamic loading on concrete structures and prepares the path toward a new level of risk assessment.

7.2 Topics for further investigation

The present work aimed to establish a basic framework and to clarify which ingredients are necessary for the intended objective. While outlining several of them, certain aspects still need improvement. Some issues are matters of implementation only, but others require yet more research. As in the preceding section, the focus will be first on the material idealization, followed by aspects concerning the coupling.

- Matrix and transgranular failure are modeled within the concept of numerical plasticity. Although this procedure is highly efficient, cracks are smeared over at least one element, and the dissolution of the body into fragments involves erosion of a perceptible amount of volume. Applying the cohesive element approach to bulk failure as well would represent cracks much more realistically and maintain mass and volume. But, as detailed in Chapter 4, the evolving, perpetually changing topology requires immense computational resources and is very error-prone. More research might be dedicated to improved implementations, topology descriptions, and especially nodesplit criteria.

- The role of rate-dependence – not only in the cohesive zone model – seems to be yet not properly understood. Despite the countless efforts to extend the amount of experimental data for the increase factor, it might be more rewarding to focus on a clearer separation of the underlying reasons and especially on guidelines on how and in which modeling paradigm the rate-enhancement should be considered.
- Further on the material side, next steps should involve first of all extensive parametric studies in order to better understand the influence of individual parameters. Besides a deepened understanding of the models behavior, some values for the parameter are still unknown, or at least the degree of scatter is highly uncertain. Parametric studies might reveal on which level further experimental work has to be done to deliver more reliable values.
- The emergence of free inner (contact) surfaces in the mesoscale demands the application of contact algorithms. Knowledge of neighboring elements before element removal or node split should enable smart contact detection algorithms, which might surpass current global strategies regarding computational effort.
- Since only a few experiments dedicated to debris throw with small concrete specimens have been published, there is a strong need to conduct more tests and gather reliable data for direct comparison with simulations. Indeed, this is the only way for growing trust and confidence in the numerical method. That the realization of such tests is immensely difficult has been detailed in the introduction. That they are – nevertheless – tremendously important is equally true.
- Regarding the coupling, the consideration of reinforcement bars is mandatory to give the method relevance in practical situations. In general, it is easy to consider rebars on the microscale by their volumetric representation and with beam-elements in the macro domain. The difficulty involved relates to the additional rotational degrees of freedom of the beam-elements. Averaging the micro domain stress in a virtual “rebar-element” does not naturally entail moments, and additional considerations have to be thoroughly deliberated.
- Furthermore, it seems unavoidable at present that cracks propagate up to the interface. Although they are aptly passed to the macroscale, their existence could be better reflected in the interface behavior. Moreover,

clear criteria defining the appropriateness of information change between material scales with increasing damage at its interfaces should be developed.

- An additional issue concerns the adapted SPML approach: A better understanding of the damping factor, effects of an increased number of filter elements, and the role of the involved material model is required – but only achieved in protracted parameter studies.

Predictive simulation of the fragmentation of concrete in real structures under dynamic loading remains an ambitious challenge. This thesis does not insist on having reached this aim but proposes certainly a promising beginning.

Bibliography

- [1] Forsén, R., R. Berglund, and G. A. Grønsten. "The Effects of Cased Ammunition Explosions Confined in Concrete Cubicles - Kasun-III". In: Department of Defense Explosives Safety Board Seminar (34th) (Portland, Oregon, July 13–15, 2010).
- [2] NATO Standardization Office. *NATO Guidelines for the Storage of Military Ammunition and Explosives*. Dec. 2005.
- [3] Ramin, M. von and A. Stolz. "Debris Throw Model for Accidental Explosions in a Complex Industrial Environment". In: *Chemical Engineering Transactions* 48 (2016), pp. 85–90. DOI: 10.3303/CET1648015.
- [4] Sun, S. et al. "A prediction model for debris scattering in vented gas deflagration". In: *Process Safety and Environmental Protection* 134.3 (2020), pp. 189–196. DOI: 10.1016/j.psep.2019.12.002.
- [5] van der Voort, M. M. et al. "A quantitative risk assessment tool for the external safety of industrial plants with a dust explosion hazard". In: *Journal of Loss Prevention in the Process Industries* 20.4-6 (2007), pp. 375–386. DOI: 10.1016/j.jlp.2007.04.024.
- [6] Nöldgen, M. *Modellierung von ultrahochfestem Beton (UHPC) unter Impaktbelastung: Auslegung eines Hochhauskerns gegen Flugzeuganprall*. Kassel: Kassel University Press GmbH, 2010. ISBN: 9783899588620.
- [7] Wu, Z. et al. "Debris characteristics and scattering pattern analysis of reinforced concrete slabs subjected to internal blast loads—a numerical study". In: *International Journal of Impact Engineering* 131., 10 (2019), pp. 1–16. DOI: 10.1016/j.ijimpeng.2019.04.024.
- [8] Chai, V. et al. "A model for the aerodynamic coefficients of rock-like debris". In: *Comptes Rendus Mécanique* 347.1 (2019), pp. 19–32. DOI: 10.1016/j.crme.2018.10.001.
- [9] Bewick, B. et al. *Fragmentation of Solid Materials Using Shock Tubes. Part 1: First Test Series in a Small-Diameter Shock Tube*. HDTRA1-14-C-0001. San Antonio: Protection Engineering Consultants, Jan. 2017.
- [10] Rouabhi, A. et al. "Continuum modelling of dynamic behaviour and fragmentation of quasi-brittle materials: Application to rock fragmentation by

- blasting". In: *International Journal for Numerical and Analytical Methods in Geomechanics* 29.7 (2005), pp. 729–749. DOI: 10.1002/nag.436.
- [11] Schill, M. and J. Sjöber. "Finite Element simulations of blasting and fragmentation with precise initiation". In: *12th International LS-DYNA Users Conference*. 2012.
- [12] Wang, H. L. and Y. P. Song. "Behavior of mass concrete under biaxial compression-tension and triaxial compression-compression-tension". In: *Materials and Structures* 42.2 (2009), pp. 241–249. DOI: 10.1617/s11527-008-9381-y.
- [13] Pedersen, B. and S. Bless. "Behind-armor debris from the impact of hypervelocity tungsten penetrators". In: *International Journal of Impact Engineering* 33 (2006), pp. 605–614.
- [14] Cullis, I. G. et al. "Numerical simulation of the natural fragmentation of explosively loaded thick walled cylinders". In: *Defence Technology* 10 (2014), pp. 198–210.
- [15] Smith, J. et al. "Discrete modeling of ultra-high-performance concrete with application to projectile penetration". In: *International Journal of Impact Engineering* 65.3 (2014), pp. 13–32. DOI: 10.1016/j.ijimpeng.2013.10.008.
- [16] Johnson, G. R. et al. "Recent epic code developments for high velocity impact: 3D element arrangements and 2D fragment distributions". In: *International Journal of Impact Engineering* 10.1-4 (1990), pp. 281–294. DOI: 10.1016/0734-743X(90)90066-5.
- [17] Johnson, G. R. et al. "An algorithm to automatically convert distorted finite elements into meshless particles during dynamic deformation". In: *International Journal of Impact Engineering* 27 (2002), pp. 997–1013.
- [18] Clayton, J. D. "A model for deformation and fragmentation in crushable brittle solids". In: *International Journal of Impact Engineering* 35 (2008), pp. 269–289.
- [19] Rabczuk, T. and J. Eibl. "Simulation of high velocity concrete fragmentation using SPH/MLSHP". In: *International Journal for Numerical Methods in Engineering* 56.10 (2003), pp. 1421–1444. DOI: 10.1002/nme.617.
- [20] Wu, Y., D. Wang, and C.-T. Wu. "Three dimensional fragmentation simulation of concrete structures with a nodally regularized meshfree method". In: *Theoretical and Applied Fracture Mechanics* 72 (2014), pp. 89–99. DOI: 10.1016/j.tafmec.2014.04.006.
- [21] Collé, A. et al. "An accurate meshless approach to dynamic fragmentation". In: *Proceedings of the LWAG*. 2019, pp. 122–132.
- [22] Trucano, T. G., D. E. Grady, and J. M. McGlaun. "Fragmentation statistics from Eulerian hydrocode calculations". In: *International Journal of Impact*

- Engineering* 10.1-4 (1990), pp. 587–600. DOI: 10.1016/0734-743X(90)90091-9.
- [23] Lim, H. S. et al. *A Review: Numerical Modeling of the Debris Throw of Reinforced Concrete Structures under Internal Explosions*.
 - [24] Weerheijm, J. et al. "Modelling Loading and Break-up of RC Structure due to Internal Explosion of Fragmenting Shells". In: *Proceedings of the 22nd MABS – Military Aspects of Blast and Shock*. Ed. by Proceedings of the 22nd MABS. 2012.
 - [25] Fan, S. C., Q. J. Yu, and C. K. Lee. "Simulation of fracture/breakup of concrete magazine using cohesive element". In: *Materialwissenschaft und Werkstofftechnik* 45.5 (2014), pp. 385–396. DOI: 10.1002/mawe.201400237.
 - [26] Basler & Hofmann AG. *Truemmer- und Splitterwirkung bei Explosionen in Munitionslagern*. TM 364-20. Zürich, Jan. 1, 1980.
 - [27] Altenbach, H. *Kontinuumsmechanik: Einführung in die materialunabhängigen und materialabhängigen Gleichungen*. 3. edition. Berlin Heidelberg: Springer Vieweg, 2015. ISBN: 978-3-662-47069-5.
 - [28] Souza Neto, E. A. d., D. Perić, and D. R. J. Owen. *Computational methods for plasticity: Theory and applications*. Chichester: John Wiley & Sons, 2008. ISBN: 978-0-470-69452-7.
 - [29] Bathe, K.-J. *Finite Elemente Methoden*. Berlin Heidelberg: Springer, 2002. ISBN: 3-540-66806-3.
 - [30] Ta, K. D. and R. J. Rogers. "Control of elastic plane wave dispersion in two-dimensional finite element meshes". In: *Computer & Structures* 21.6 (1985), pp. 1145–1151.
 - [31] Benson, D. J. "Computational methods in Lagrangian and Eulerian hydrocodes". In: *Computer Methods in Applied Mechanics and Engineering* 99.2-3 (1992), pp. 235–394.
 - [32] Belytschko, T. "A survey of numerical methods and computer programs for dynamic structural analysis". In: *Nuclear Engineering and Design* 37.1 (1976), pp. 23–34. DOI: 10.1016/0029-5493(76)90050-9.
 - [33] Belytschko, T., R. L. Chiapetta, and H. D. Bartel. "Efficient large scale non-linear transient analysis by finite elements". In: *International Journal for Numerical Methods in Engineering* 10.3 (1976), pp. 579–596. DOI: 10.1002/nme.1620100308.
 - [34] Hairer, E., C. Lubich, and G. Wanner. "Geometric numerical integration illustrated by the Störmer–Verlet method". In: *Acta Numerica* 12 (2003), pp. 399–450. DOI: 10.1017/S0962492902000144.

- [35] Belytschko, T., N. Holmes, and R. Mullen. "Explicit integration- Stability, solution properties, cost". In: *ASME Applied Mechanics Symposia Series AMD-14* (1975), pp. 1–21.
- [36] Nickell, R. E. "Direct Integration Methods in Structural Dynamics". In: *Journal of the Engineering Mechanics Division* 99.2 (1973), pp. 303–317.
- [37] Dokainish, M. A. and K. Subbaraj. "A survey of direct time-integration methods in computational structural dynamics—I. Explicit methods". In: *Computers & Structures* 32.6 (1989), pp. 1371–1386. DOI: 10.1016/0045-7949(89)90314-3.
- [38] Combescure, A. and A. Gravouil. "A numerical scheme to couple sub-domains with different time-steps for predominantly linear transient analysis". In: *Computer Methods in Applied Mechanics and Engineering* 191.11-12 (2002), pp. 1129–1157. DOI: 10.1016/S0045-7825(01)00190-6.
- [39] Scovazzi, G. et al. "A conservative nodal variational multiscale method for Lagrangian shock hydrodynamics". In: *Computer Methods in Applied Mechanics and Engineering* 199.49-52 (2010), pp. 3059–3100. DOI: 10.1016/j.cma.2010.03.027.
- [40] Anderson JR., C. E. "An Overview of the Theory of Hydrocodes". In: *International Journal of Impact Engineering* 5 (1987), pp. 33–59.
- [41] Hiermaier, S. *Structures Under Crash and Impact*. New York: Springer, 2008. ISBN: 978-0-387-73862-8.
- [42] Malvern, L. E. *Introduction to the mechanics of a continuous medium*. Englewood Cliffs: Prentice-Hall Inc., 1969.
- [43] Hiermaier, S. "Hypervelocity Impact Induced Shock Waves and Related Equations of State". In: *Predictive Modeling of Dynamic Processes: A Tribute to Professor Klaus Thoma*. Ed. by Hiermaier, S. New York: Springer, 2009, pp. 333–348. ISBN: 978-1-4419-0727-1.
- [44] Hiermaier, S. "Numerische Simulation von Impaktvorgängen mit einer Netzfreen Lagrangemethode (Smooth Particle Hydrodynamics)". Dissertation. Neubiberg: Universität der Bundeswehr München, 1996.
- [45] Sauer, M. "Adaptive Kopplung des netzfreien SPH-Verfahrens mit Finiten Elementen zur Berechnung von Impaktvorgängen". Dissertation. Neubiberg: Universität der Bundeswehr München, 2000.
- [46] Mindess, S., J. F. Young, and D. Darwin. *Concrete*. 2nd ed. Upper Saddle River, NJ: Prentice Hall, 2003. ISBN: 0130646326.
- [47] Mehta, P. K. and P. J. M. Monteiro. *Concrete: Microstructure, properties, and materials*. 4. ed. New York, NY: McGraw-Hill Education, 2014. ISBN: 9780071797870.

-
- [48] *Eibl, J. Beton-Kalender 1999*. Vol. 88. Berlin: Ernst & Sohn, 1999. ISBN: 3-433-01424-8.
- [49] *van Mier, J. G. M. Fracture processes of concrete: Assessment of material parameters for fracture models*. New directions in civil engineering. Boca Raton, Fla.: CRC Press, 1997. ISBN: 0849391237.
- [50] *Juenger, M. et al. "Advances in alternative cementitious binders". In: Cement and Concrete Research, 1999, Vol.29(7), pp.1019-1025* 41.12 (2011), pp. 1232–1243. DOI: 10.1016/j.cemconres.2010.11.012.
- [51] *Shahzamanian, M. M. et al. "Representative Volume Element Based Modeling of Cementitious Materials". In: Journal of Engineering Materials and Technology 136.1 (2014), p. 011007.* DOI: 10.1115/1.4025916.
- [52] *Hansen, T. C. "Physical structure of hardened cement paste. A classical approach". In: Materials and Structures 19.6 (1986), pp. 423–436.* DOI: 10.1007/BF02472146.
- [53] *Acker, P., C. Boulay, and P. Rossi. "On the importance of initial stresses in concrete and of the resulting mechanical effects". In: Cement and Concrete Research, 1999, Vol.29(7), pp.1019-1025* 17.5 (1987), pp. 755–764. DOI: 10.1016/0008-8846(87)90038-X.
- [54] *Elices, M. and C. G. Rocco. "Effect of aggregate size on the fracture and mechanical properties of a simple concrete". In: Engineering Fracture Mechanics 75.13 (2008), pp. 3839–3851.* DOI: 10.1016/j.engfracmech.2008.02.011.
- [55] *Wolinski, S. et al. "Influence of aggregate size on fracture mechanics parameters of concrete". In: International Journal of Cement Composites and Lightweight Concrete 9.2 (1987), pp. 95–103.* DOI: 10.1016/0262-5075(87)90025-X.
- [56] *Meddah, M. S., S. Zitouni, and S. Belâabes. "Effect of content and particle size distribution of coarse aggregate on the compressive strength of concrete". In: Construction and Building Materials 24.4 (2010), pp. 505–512.* DOI: 10.1016/j.conbuildmat.2009.10.009.
- [57] *Walker, S. and D. L. Bloem. "Effects of Aggregate Size on Properties of Concrete". In: ACI Journal Proceedings 57.9 (1960), pp. 283–298.* DOI: 10.14359/8021.
- [58] *Cordon, W. A. and H. A. Gillespie. "Variables in Concrete Aggregates and Portland Cement Paste which Influence the Strength of Concrete". In: ACI Journal Proceedings 60.8 (1963), pp. 1029–1050.* DOI: 10.14359/7889.
- [59] *Miled, K., O. Limam, and K. Sab. "A probabilistic mechanical model for prediction of aggregates' size distribution effect on concrete compressive strength". In: Physica A: Statistical Mechanics and its Applications 391.12 (2012), pp. 3366–3378.* DOI: 10.1016/j.physa.2012.01.051.

- [60] Neel, C. "Compaction and Spall of UHPC Concrete Under Shock Conditions". In: *Journal of Dynamic Behavior of Materials* 4.4 (2018), pp. 505–528. DOI: 10.1007/s40870-018-0173-3.
- [61] Birchall, J. D., A. J. Howard, and K. Kendall. "Flexural strength and porosity of cements". In: *Nature* 289.5796 (1981), pp. 388–390. DOI: 10.1038/289388a0.
- [62] Wittmann, F. H. "Structure of concrete with respect to crack formation". In: *Fracture mechanics of concrete*. Ed. by Wittmann, F. H. Developments in civil engineering. Amsterdam: Elsevier, 1983, pp. 43–74. ISBN: 0444421998.
- [63] Scrivener, K. L., A. K. Crumbie, and P. Laugesen. "The Interfacial Transition Zone (ITZ) Between Cement Paste and Aggregate in Concrete". In: *Interface Science* 12.4 (2004), pp. 411–421. DOI: 10.1023/B:INTS.0000042339.92990.4c.
- [64] Zimbelmann, R. "A contribution to the problem of cement-aggregate bond". In: *Cement and concrete research* 15.5 (1985), pp. 801–808. DOI: 10.1016/0008-8846(85)90146-2.
- [65] Liao, K.-Y. et al. "A study on characteristics of interfacial transition zone in concrete". In: *Cement and concrete research* 34.6 (2004), pp. 977–989. DOI: 10.1016/j.cemconres.2003.11.019.
- [66] Hsu, T. T. C. and F. O. Slate. "Tensile Bond Strength Between Aggregate and Cement Paste or Mortar". In: *Journal Proceedings* 60.4 (1963), pp. 465–486. DOI: 10.14359/7863.
- [67] Tasong, W. A., C. J. Lynsdale, and J. C. Cripps. "Aggregate-cement paste interface: Part I. Influence of aggregate geochemistry". In: *Cement and concrete research* 29.7 (1999), pp. 1019–1025. DOI: 10.1016/S0008-8846(99)00086-1.
- [68] Hsu, T. T. C. et al. "Microcracking of Plain Concrete and the Shape of the Stress-Strain Curve". In: *ACI Journal Proceedings* 60.2 (1963). DOI: 10.14359/7852.
- [69] Königsberger, M. et al. "Micromechanics of ITZ-Aggregate Interaction in Concrete Part II: Strength Upscaling". In: *Journal of the American Ceramic Society* 97.2 (2014), pp. 543–551. DOI: 10.1111/jace.12606.
- [70] Guinea, G. V. et al. "The effect of the bond between the matrix and the aggregates on the cracking mechanism and fracture parameters of concrete". In: *Cement and concrete research* 32.12 (2002), pp. 1961–1970. DOI: 10.1016/S0008-8846(02)00902-X.
- [71] Wittmann, F. H., F. Beltzung, and T. J. Zhao. "Shrinkage mechanisms, crack formation and service life of reinforced concrete structures". In:

- International Journal of Structural Engineering* 1.1 (2009), p. 13. DOI: 10.1504/IJSTRUCTE.2009.030023.
- [72] van Mier, J. "Mode I fracture of concrete: Discontinuous crack growth and crack interface grain bridging". In: *Cement and Concrete Research*, 1999, Vol.29(7), pp.1019-1025 21.1 (1991), pp. 1–15. DOI: 10.1016/0008-8846(91)90025-D.
- [73] Scrivener, K. L. and E. M. Gartner. "Microstructural Gradients in Cement Paste Around Aggregate Particles". In: *MRS Proceedings* 114 (1987), p. VII. DOI: 10.1557/PROC-114-77.
- [74] Hordijk, D. A., J. G. van Mier, and H. W. Reinhardt. "Material Properties". In: *Fracture mechanics of concrete structures*. Ed. by Elfgrén, L. RILEM report. London u.a.: Chapman and Hall, 1989, pp. 67–127. ISBN: 0412306808.
- [75] Kühn, T. "Experimentelle Grundlagen für die meso- und makroskopische Modellierung von Beton bei hohen Belastungsgeschwindigkeiten: Eine kritische Beurteilung des Dehnrateneffekts". Dissertation. Dresden: TU Dresden, 2020.
- [76] Hordijk, D. A. "Tensile and Tensile Fatigue Behaviour of Concrete; Experiments, Modelling and Analyses". In: *Heron* 37.1 (1992), pp. 1–79.
- [77] Reinhardt, H. W. "Crack softening zone in plain concrete under static loading". In: *Cement and concrete research* 15.1 (1985), pp. 42–52. DOI: 10.1016/0008-8846(85)90007-9.
- [78] Rots, J. G. "Smeared and discrete representation of localized fracture". In: *International Journal of Fracture* 51 (1991), pp. 45–59.
- [79] Bažant, Z. P. and B. H. Oh. "Crack band theory for fracture of concrete". In: *Matériaux et Constructions* 16.3 (1983), pp. 155–177. DOI: 10.1007/BF02486267.
- [80] Vonk, R. A. "Softening of concrete loaded in compression". Dissertation. Eindhoven: Technische Universiteit Eindhoven, 1992. DOI: 10.6100/IR375705.
- [81] Rots, J. G. et al. "Smeared crack approach and fracture localization in concrete". In: *Heron* 30.1 (1985).
- [82] Mindess, S. and S. Diamond. "Fracture Surfaces of Cement Pastes, Rocks, and Cement/Rock Interfaces". In: *MRS Proceedings* 370 (1994), p. 71. DOI: 10.1557/PROC-370-295.
- [83] Alexander, M. G. et al. "Properties of paste-rock interfaces and their influence on composite behaviour". In: *Matériaux et Constructions* 28.9 (1995), pp. 497–506. DOI: 10.1007/BF02473154.
- [84] Bažant, Z. P. and E. Becq-Giraudon. "Statistical prediction of fracture parameters of concrete and implications for choice of testing standard".

- In: *Cement and concrete research* 32.4 (2002), pp. 529–556. DOI: 10.1016/S0008-8846(01)00723-2.
- [85] Kotsovos, M. D. and J. B. Newman. "A mathematical description of the deformational behaviour of concrete under complex loading". In: *Magazine of Concrete Research* 31.107 (1979), pp. 77–90. DOI: 10.1680/macr.1979.31.107.77.
- [86] van Vliet, M. R. A. and J. G. M. van Mier. "Experimental investigation of concrete fracture under uniaxial compression". In: *Mechanics of Cohesive-frictional Materials* 1.1 (1996), pp. 115–127. DOI: 10.1002/(SICI)1099-1484(199601)1:1<115::AID-CFM6>3.0.CO;2-U.
- [87] Weerheijm, J. and J. van Doormaal. "Tensile failure of concrete at high loading rates: New test data on strength and fracture energy from instrumented spalling tests". In: *International Journal of Impact Engineering* 34.3 (2007), pp. 609–626. DOI: 10.1016/j.ijimpeng.2006.01.005.
- [88] Elmer, W., E. Taciroglu, and L. McMichael. "Dynamic strength increase of plain concrete from high strain rate plasticity with shear dilation". In: *International Journal of Impact Engineering* 45.6 (2012), pp. 1–15. DOI: 10.1016/j.ijimpeng.2012.01.003.
- [89] Rots, J. G. and R. de Borst. "Analysis of Mixed-Mode Fracture in Concrete". In: *Journal of Engineering Mechanics* 113.11 (1987), pp. 1739–1758. DOI: 10.1061/(ASCE)0733-9399(1987)113:11(1739).
- [90] Vile, G. W. "The Strength of Concrete under Short-Term Static Biaxial Stress". In: *The structure of Concrete and its behaviour under load*. Ed. by Brooks, A. E. and K. Newman. 1965, pp. 275–288.
- [91] Stroeve, P. "Some aspects of the micromechanics of concrete". Dissertation. Delft: TU Delft, 1973.
- [92] van Mier, J. "Strain-softening of concrete under multiaxial loading conditions". Dissertation. Technische Hogeschool Eindhoven, 1984. DOI: 10.6100/IR145193.
- [93] Stroeve, P. "A case of compression failure in concrete due to stress release". In: *Fracture mechanics of concrete structures*. Ed. by Wittmann, F. H. Freiburg: AEDIFICATIO Publishers, 1995, pp. 461–470. ISBN: 3-905088-12-6.
- [94] Williams, E. M., S. A. Akers, and P. A. Reed. *Laboratory Characterization of Fine Aggregate Cementitious Material*. ERDC/GSL TR-05-16. US Army Corps of Engineers Engineer Research and Development Center, July 2005.
- [95] Sfer, D. et al. "Study of the Behavior of Concrete under Triaxial Compression". In: *Journal of Engineering Mechanics* 128.2 (2002), pp. 156–163. DOI: 10.1061/(ASCE)0733-9399(2002)128:2(156).

- [96] *Jamet, P., A. Millard, and G. Nahas. "Triaxial behaviour of a micro-concrete complete stress-strain curves for confining pressures ranging from 0 to 100 MPa". In: (Toulouse, May 22–24, 1984). CEA-CONF-7303.*
- [97] *Poinard, C., Y. Malecot, and L. Daudeville. "Damage of concrete in a very high stress state: Experimental investigation". In: *Materials and Structures* 43.1-2 (2010), pp. 15–29. DOI: 10.1617/s11527-008-9467-6.*
- [98] *Launay, P. and H. Gachon. "Strain and Ultimate Strength of Concrete Under Triaxial Stress". In: *American Concrete Institute, Special Publication* 34 (1972), pp. 269–282. DOI: 10.14359/18069.*
- [99] *Dupray, F. et al. "A mesoscopic model for the behaviour of concrete under high confinement". In: *International Journal for Numerical and Analytical Methods in Geomechanics* 33.11 (2009), pp. 1407–1423. DOI: 10.1002/nag.771.*
- [100] *Malécot, Y. et al. "Strength and damage of concrete under high triaxial loading". In: *EJCE* 14 (2010), p. 27. DOI: 10.3166/EJCE.14.777-803.*
- [101] *Williams, E. M., S. A. Akers, and P. A. Reed. *Laboratory Characterization of SAM-35 Concrete*. ERDC/GSL TR-06-15. US Army Corps of Engineers Engineer Research and Development Center, Sept. 2006.*
- [102] *Speck, K. and M. Curbach. "Ein einheitliches dreiaxiales Bruchkriterium für alle Betone". In: *Beton- und Stahlbetonbau* 105.4 (2010), pp. 233–243.*
- [103] *Bažant, Z. P., F. C. Bishop, and T.-P. Chang. "Confined Compression Tests of Cement Paste and Concrete up to 300 ksi". In: *ACI Journal Proceedings* 83.4 (1986), pp. 553–560. DOI: 10.14359/10448.*
- [104] *Riedel, W. *Beton unter dynamischen Lasten. Meso- und makromechanische Modelle und ihre Parameter*. Freiburg i. Br.: Fraunhofer-Verlag, 2004. ISBN: 978-3816763406.*
- [105] *Lu, D. et al. "A nonlinear dynamic uniaxial strength criterion that considers the ultimate dynamic strength of concrete". In: *International Journal of Impact Engineering* 103 (2017), pp. 124–137. DOI: 10.1016/j.ijimpeng.2017.01.011.*
- [106] *Bischoff, P. H. and S. H. Perry. "Compressive behaviour of concrete at high strain rates". In: *Matériaux et Constructions* 24.6 (1991), pp. 425–450. DOI: 10.1007/BF02472016.*
- [107] *Zhang, M. et al. "Further investigation on the dynamic compressive strength enhancement of concrete-like materials based on split Hopkinson pressure bar tests. Part I: Experiments". In: *International Journal of Impact Engineering* 36.12 (2009), pp. 1327–1334. DOI: 10.1016/j.ijimpeng.2009.04.009.*

- [108] Flores-Johnson, E. A. and Q. M. Li. "Structural effects on compressive strength enhancement of concrete-like materials in a split Hopkinson pressure bar test". In: *International Journal of Impact Engineering* 109 (2017), pp. 408–418. DOI: 10.1016/j.ijimpeng.2017.08.003.
- [109] Lu, Y. B. and Q. M. Li. "About the dynamic uniaxial tensile strength of concrete-like materials". In: *International Journal of Impact Engineering* 38.4 (2011), pp. 171–180. DOI: 10.1016/j.ijimpeng.2010.10.028.
- [110] Ortlepp, S. "Zur Beurteilung der Festigkeitssteigerung von hochfestem Beton unter hohen Dehngeschwindigkeiten". Dissertation. Dresden: TU Dresden, 2006.
- [111] Forquin, P. and F. Hild. "A Probabilistic Damage Model of the Dynamic Fragmentation Process in Brittle Materials". In: *Advances in Applied Mechanics Volume 44*. Vol. 44. Advances in Applied Mechanics. Elsevier, 2010, pp. 1–72. ISBN: 9780123808783. DOI: 10.1016/S0065-2156(10)44001-6.
- [112] Zielinski. "Fracture of concrete and mortar under uniaxial impact tensile loading". Dissertation. Delft: TU Delft, 1982.
- [113] Reinhardt, H. W. and J. Weerheijm. "Tensile fracture of concrete at high loading rates taking account of inertia and crack velocity effects". In: *International Journal of Fracture* 51.1 (1991), pp. 31–42. DOI: 10.1007/BF00020851.
- [114] Sharon, Gross, and Fineberg. "Energy dissipation in dynamic fracture". In: *Physical review letters* 76.12 (1996), pp. 2117–2120. DOI: 10.1103/PhysRevLett.76.2117.
- [115] Zhou, F., J.-F. Molinari, and T. Shioya. "A rate-dependent cohesive model for simulating dynamic crack propagation in brittle materials". In: *Engineering Fracture Mechanics* 72.9 (2005), pp. 1383–1410. DOI: 10.1016/j.engfracmech.2004.10.011.
- [116] Yan, D. and G. Lin. "Influence of initial static stress on the dynamic properties of concrete". In: *Cement and Concrete Composites* 30.4 (2008), pp. 327–333. DOI: 10.1016/j.cemconcomp.2007.11.004.
- [117] Grote, D. L., S. W. Park, and M. Zhou. "Dynamic behavior of concrete at high strain rates and pressures: I. experimental characterization". In: *International Journal of Impact Engineering* 25.9 (2001), pp. 869–886. DOI: 10.1016/S0734-743X(01)00020-3.
- [118] Chen, G., Y. Hao, and H. Hao. "3D meso-scale modelling of concrete material in spall tests". In: *Materials and Structures* 48.6 (2015), pp. 1887–1899. DOI: 10.1617/s11527-014-0281-z.

-
- [119] Song, J. H., H. Wang, and T. Belytschko. "A comparative study on finite element methods for dynamic fracture". In: *Computational Mechanics* 42 (2008), pp. 239–250.
- [120] Rossi, P. "A physical phenomenon which can explain the mechanical behaviour of concrete under high strain rates". In: *Matériaux et Constructions* 24.6 (1991), pp. 422–424. DOI: 10.1007/BF02472015.
- [121] Rossi, P. and F. Toutlemonde. "Effect of loading rate on the tensile behaviour of concrete: description of the physical mechanisms". In: *Materials and Structures* 29.2 (1996), pp. 116–118. DOI: 10.1007/BF02486201.
- [122] Reinhardt, H. W., P. Rossi, and J. G. M. van Mier. "Joint investigation of concrete at high rates of loading". In: *Materials and Structures* 23.3 (1990), pp. 213–216. DOI: 10.1007/BF02473020.
- [123] Ross, C. A., J. W. Tedesco, and S. T. Kuennen. "Effects of Strain Rate on Concrete Strength". In: *Materials Journal* 92.1 (1995). DOI: 10.14359/1175.
- [124] Cui, J., H. Hao, and Y. Shi. "Discussion on the suitability of concrete constitutive models for high-rate response predictions of RC structures". In: *International Journal of Impact Engineering* 106 (2017), pp. 202–216. DOI: 10.1016/j.ijimpeng.2017.04.003.
- [125] Cadoni, E. et al. "Strain-rate effect on the tensile behaviour of concrete at different relative humidity levels". In: *Materials and Structures* 34.1 (2001), pp. 21–26. DOI: 10.1007/BF02482196.
- [126] Chen, X., L. Xu, and S. Wu. "Influence of Pore Structure on Mechanical Behavior of Concrete under High Strain Rates". In: *Journal of Materials in Civil Engineering* 28.2 (2016), p. 04015110. DOI: 10.1061/(ASCE)MT.1943-5533.0001380.
- [127] Mayercsik, N. P. et al. "Analysis of Portland cement mortar under impact: A combined material characterization, micromechanics modeling, and dynamic testing approach". In: *Cement and concrete research* 73 (2015), pp. 190–206. DOI: 10.1016/j.cemconres.2015.01.021.
- [128] Piotrowska, E., P. Forquin, and Y. Malecot. "Experimental study of static and dynamic behavior of concrete under high confinement: Effect of coarse aggregate strength". In: *Mechanics of Materials* 92 (2016), pp. 164–174. DOI: 10.1016/j.mechmat.2015.09.005.
- [129] Cotsovos, D. M. and M. N. Pavlović. "Numerical investigation of concrete subjected to high rates of uniaxial tensile loading". In: *International Journal of Impact Engineering* 35.5 (2008), pp. 319–335.
- [130] Weerheijm, J., ed. *Understanding the tensile properties of concrete*. Cambridge: Woodhead Publishing Ltd., 2013. ISBN: 978-0-85709-045-4.

- [131] Cusatis, G. "Strain-rate effects on concrete behavior". In: *International Journal of Impact Engineering* 38.4 (2011), pp. 162–170. DOI: 10.1016/j.ijimpeng.2010.10.030.
- [132] Gary, G. and P. Bailly. "Behaviour of quasi-brittle material at high strain rate. Experiment and modelling". In: *European Journal of Mechanics - A/Solids* 17.3 (1998), pp. 403–420. DOI: 10.1016/S0997-7538(98)80052-1.
- [133] Guo, Y. B. et al. "Response of high-strength concrete to dynamic compressive loading". In: *International Journal of Impact Engineering* 108 (2017), pp. 114–135. DOI: 10.1016/j.ijimpeng.2017.04.015.
- [134] Malvar, L. J. and A. C. Ross. "Review on Strain Rate Effects for Concrete in Tension". In: *ACI Materials Journal* November/December (1998), p. 4.
- [135] Levi-Hevroni, D. et al. "Experimental and numerical investigation on the dynamic increase factor of tensile strength in concrete". In: *International Journal of Impact Engineering* 114 (2018), pp. 93–104. DOI: 10.1016/j.ijimpeng.2017.12.006.
- [136] *Comite Euro-International du Beton. CEB-FIP Model Code*. Lausanne: Thomas Telford, 1990.
- [137] Hao, H. and X. Q. Zhou. "Concrete Material Model for High Rate Dynamic Analysis". In: *Proceedings of the 7th International Conference on Shock & Impact Loads on Structures*. Ed. by Huang, F. L., Q. M. Li, and T. S. Lok. Singapore: CI-Premier PTE, 2007. ISBN: 9789810575908.
- [138] Forquin, P. and B. Lukić. "On the Processing of Spalling Experiments. Part I: Identification of the Dynamic Tensile Strength of Concrete". In: *Journal of Dynamic Behavior of Materials* 4.1 (2018), pp. 34–55. DOI: 10.1007/s40870-017-0135-1.
- [139] Song, Z. and Y. Lu. "Mesoscopic analysis of concrete under excessively high strain rate compression and implications on interpretation of test data". In: *International Journal of Impact Engineering* 46 (2012), pp. 41–55. DOI: 10.1016/j.ijimpeng.2012.01.010.
- [140] van Doormaal, J. C., J. Weerheijm, and L. J. Sluys. "Experimental and numerical determination of the dynamic fracture energy of concrete". In: *Journal de Physique IV (Proceedings)* 04.C8 (1994), pp. C8-501–C8-506. DOI: 10.1051/jp4:1994878.
- [141] Le Nard, H. and P. Bailly. "Dynamic behaviour of concrete: The structural effects on compressive strength increase". In: *Mechanics of Cohesive-frictional Materials* 5.6 (2000), pp. 491–510. DOI: 10.1002/1099-1484(200008)5:6<491::AID-CFM106>3.0.CO;2-R.

-
- [142] Snozzi, L., A. Caballero, and J. F. Molinari. "Influence of the meso-structure in dynamic fracture simulation of concrete under tensile loading". In: *Cement and concrete research* 41 (2011), pp. 1130–1142.
- [143] Knell, S. et al. "Mesoscale simulation of concrete spall failure". In: *The European Physical Journal Special Topics* 206 (2012), pp. 139–148.
- [144] Yilmaz, O. and J.-F. Molinari. "A mesoscale fracture model for concrete". In: *Cement and concrete research* 97 (2017), pp. 84–94. DOI: 10.1016/j.cemconres.2017.03.014.
- [145] Hao, Y. and H. Hao. "Finite element modelling of mesoscale concrete material in dynamic splitting test". In: *Advances in Structural Engineering* 19.6 (2016), pp. 1027–1039. DOI: 10.1177/1369433216630828.
- [146] Ožbolt, J., A. Sharma, and H.-W. Reinhardt. "Dynamic fracture of concrete – compact tension specimen". In: *International Journal of Solids and Structures* 48.10 (2011), pp. 1534–1543. DOI: 10.1016/j.ijsolstr.2011.01.033.
- [147] Toutlemonde, F. "Résistance au choc des structures en béton: du comportement du matériau au calcul des ouvrages". Dissertation. Paris: Ecole Nationale des Ponts et Chaussées, 1994.
- [148] Bischoff, P. H. and S. H. Perry. "Compressive Strain Rate Effects of Concrete". In: *MRS Proceedings* 64 (1985), p. 194. DOI: 10.1557/PROC-64-151.
- [149] Ožbolt, J., J. Bošnjak, and E. Sola. "Dynamic fracture of concrete compact tension specimen: Experimental and numerical study". In: *International Journal of Solids and Structures* 50.25-26 (2013), pp. 4270–4278. DOI: 10.1016/j.ijsolstr.2013.08.030.
- [150] Drucker, D. C. and W. Prager. "Soil mechanics and plastic analysis or limit design". In: *Quarterly of Applied Mathematics* 10.2 (1952), pp. 157–165. DOI: 10.1090/qam/48291.
- [151] Feenstra, P. H. and R. de Borst. "A composite plasticity model for concrete". In: *International Journal of Solids and Structures* 33.5 (1996), pp. 707–730. DOI: 10.1016/0020-7683(95)00060-N.
- [152] Schwer, L. E. and Y. D. Murray. "Continuous Surface Cap Model for Geometrial Modeling: A New LS-DYNA Material Type". In: *7th International LS-DYNA Users Conference*. 2009.
- [153] Malvar, L. et al. "A plasticity concrete material model for DYNA3D". In: *International Journal of Impact Engineering* 19.9-10 (1997), pp. 847–873. DOI: 10.1016/S0734-743X(97)00023-7.
- [154] Hartmann, T., A. Pietzsch, and N. Gebbeken. "A Hydrocode Material Model for Concrete". In: *International Journal of Protective Structures* 1.4 (2010), pp. 443–468. DOI: 10.1260/2041-4196.1.4.443.

- [155] *Holmquist, T. J. and G. R. Johnson. "A computational constitutive model for concrete subjected to large strains, high strain rates, and high pressures". In: 14th International Symposium on Ballistics (Québec, Canada, Sept. 26–29, 1993).*
- [156] *Mazars, J. and G. Pijaudier-Cabot. "Continuum Damage Theory - Application to Concrete". In: Journal of Engineering Mechanics 115.2 (1989).*
- [157] *Grassl, P. and M. Jirásek. "Damage-plastic model for concrete failure". In: International Journal of Solids and Structures 43.22-23 (2006), pp. 7166–7196. DOI: 10.1016/j.ijsolstr.2006.06.032.*
- [158] *Burlion, N. et al. "Compaction and tensile damage in concrete: constitutive modelling and application to dynamics". In: Computer Methods in Applied Mechanics and Engineering 183.3-4 (2000), pp. 291–308. DOI: 10.1016/S0045-7825(99)00223-6.*
- [159] *Gatuingt, F. and G. Pijaudier-Cabot. "Coupled damage and plasticity modelling in transient dynamic analysis of concrete". In: International Journal for Numerical and Analytical Methods in Geomechanics 26.1 (2002), pp. 1–24. DOI: 10.1002/nag.188.*
- [160] *Erzar, B. and P. Forquin. "Experiments and mesoscopic modelling of dynamic testing of concrete". In: Mechanics of Materials 43.9 (2011), pp. 505–527. DOI: 10.1016/j.mechmat.2011.05.002.*
- [161] *Ortiz, M. "A constitutive theory for the inelastic behaviour of concrete". In: Mechanics of Materials 4 (1985), pp. 67–93. DOI: 10.1016/0167-6636(85)90007-9.*
- [162] *Bažant, Z. P. et al. "Microplane Model M4 for Concrete. I: Formulation with Work-Conjugate Deviatoric Stress". In: Journal of Engineering Mechanics (2000), pp. 944–953.*
- [163] *Broughton, J. Q. et al. "Concurrent coupling of length scales: Methodology and application". In: Physical Review B 60.4 (1999), pp. 2391–2403. DOI: 10.1103/PhysRevB.60.2391.*
- [164] *van Mier, J. and M. van Vliet. "Uniaxial tension test for the determination of fracture parameters of concrete: State of the art". In: Engineering Fracture Mechanics 69.2 (2002), pp. 235–247. DOI: 10.1016/S0013-7944(01)00087-X.*
- [165] *Simo, J. C. and J. W. Ju. "Strain- and stress-based continuum damage models—I. Formulation". In: International Journal of Solids and Structures 23.7 (1987), pp. 821–840. DOI: 10.1016/0020-7683(87)90083-7.*
- [166] *Ožbolt, J. and A. Sharma. "Numerical simulation of dynamic fracture of concrete through uniaxial tension and L-specimen". In: Engineering Fracture Mechanics 85 (2012), pp. 88–102. DOI: 10.1016/j.engfracmech.2012.02.013.*

-
- [167] Bede, N. et al. "Dynamic fracture of notched plain concrete beams: 3D finite element study". In: *International Journal of Impact Engineering* 77.6 (2015), pp. 176–188. DOI: 10.1016/j.ijimpeng.2014.11.022.
- [168] Carol, I., C. M. López, and O. Roa. "Micromechanical analysis of quasi-brittle materials using fracture-based interface elements". In: *International Journal for Numerical Methods in Engineering* 52.12 (2001), pp. 193–215. DOI: 10.1002/nme.277.
- [169] Zaitsev, Y. B. and F. H. Wittmann. "Simulation of crack propagation and failure of concrete". In: *Matériaux et Constructions* 14.5 (1981), pp. 357–365. DOI: 10.1007/BF02478729.
- [170] Constantinides, G. and F.-J. Ulm. "The effect of two types of C-S-H on the elasticity of cement-based materials: Results from nanoindentation and micromechanical modeling". In: *Cement and concrete research* 34.1 (2004), pp. 67–80. DOI: 10.1016/S0008-8846(03)00230-8.
- [171] Durr, N., M. Sauer, and S. Hiermaier. "Mesoscale investigation of dynamic fracture in quartzite and sandstone and homogenization to macroscale". In: *International Journal of Solids and Structures* (2018). DOI: 10.1016/j.ijsolstr.2018.04.024.
- [172] Wicklein, M. *Zelluläres Aluminium: Entwicklung eines makromechanischen Materialmodells mittels mesomechanischer Simulation*. Freiburg i. Br.: Fraunhofer Verlag, 2006. ISBN: 3-8167-7018-5.
- [173] Zhou, R., Z. Song, and Y. Lu. "3D mesoscale finite element modelling of concrete". In: *Computers & Structures* 192 (2017), pp. 96–113. DOI: 10.1016/j.compstruc.2017.07.009.
- [174] Schlangen, E. and J. G. M. van Mier. "Simple lattice model for numerical simulation of fracture of concrete materials and structures". In: *Materials and Structures* 25.9 (1992), pp. 534–542. DOI: 10.1007/BF02472449.
- [175] Leite, J., V. Slowik, and H. Mihashi. "Computer simulation of fracture processes of concrete using mesolevel models of lattice structures". In: *Cement and concrete research* 34.6 (2004), pp. 1025–1033. DOI: 10.1016/j.cemconres.2003.11.011.
- [176] Grassl, P. and M. Jirásek. "Meso-scale approach to modelling the fracture process zone of concrete subjected to uniaxial tension". In: *International Journal of Solids and Structures* 47.7-8 (2010), pp. 957–968. DOI: 10.1016/j.ijsolstr.2009.12.010.
- [177] Grassl, P. et al. "Meso-scale modelling of the size effect on the fracture process zone of concrete". In: *International Journal of Solids and Structures* 49.13 (2012), pp. 1818–1827. DOI: 10.1016/j.ijsolstr.2012.03.023.
- [178] Cusatis, G., Z. P. Bažant, and L. Cedolin. "Confinement-Shear Lattice Model for Concrete Damage in Tension and Compression: I. Theory". In:

- Journal of Engineering Mechanics* 129.12 (2003), pp. 1439–1448. DOI: 10.1061/(ASCE)0733-9399(2003)129:12(1439).
- [179] Cusatis, G. and L. Cedolin. "Two-scale study of concrete fracturing behavior". In: *Engineering Fracture Mechanics* 74.1-2 (2007), pp. 3–17. DOI: 10.1016/j.engfracmech.2006.01.021.
- [180] Eliáš, J. et al. "Stochastic discrete meso-scale simulations of concrete fracture: Comparison to experimental data". In: *Engineering Fracture Mechanics* 135 (2015), pp. 1–16. DOI: 10.1016/j.engfracmech.2015.01.004.
- [181] Brara, A. et al. "Experimental and numerical study of concrete at high strain rates in tension". In: *Mechanics of Materials* 33.1 (2001), pp. 33–45. DOI: 10.1016/S0167-6636(00)00035-1.
- [182] Hentz, S., F. V. Donzé, and L. Daudeville. "Discrete element modelling of concrete submitted to dynamic loading at high strain rates". In: *Computers & Structures* 82.29-30 (2004), pp. 2509–2524. DOI: 10.1016/j.compstruc.2004.05.016.
- [183] Azevedo, N. and J. V. Lemos. "Aggregate shape influence on the fracture behaviour of concrete". In: *Structural Engineering and Mechanics* 24.4 (2006), pp. 411–427. DOI: 10.12989/sem.2006.24.4.411.
- [184] Qin, C. and C. Zhang. "Numerical Study of Dynamic Behavior of Concrete by Mesoscale Particle Element Modeling". In: *Seismic Safety Evaluation of Concrete Dams*. Elsevier, 2013, pp. 595–617. ISBN: 9780124080836. DOI: 10.1016/B978-0-12-408083-6.00025-8.
- [185] Nagai, K., Y. Sato, and T. Ueda. "Mesoscopic Simulation of Failure of Mortar and Concrete by 3D RBSM". In: *Journal of Advanced Concrete Technology* 3.3 (2005), pp. 385–402. DOI: 10.3151/jact.3.385.
- [186] Pelessone, D., G. Cusatis, and J. T. Baylot. "Application of the Lattice Discrete Particle Model (LDPM) to Simulate the Effects of Munitions on Reinforced Concrete Structures". In: *International Symposium on the Interaction of the Effects of Munitions with Structures (ISIEMS)* 12.1. 2007.
- [187] Thilakarathna, P. et al. "Mesoscale modelling of concrete – A review of geometry generation, placing algorithms, constitutive relations and applications". In: *Engineering Fracture Mechanics* 231.197–213 (2020), p. 106974. DOI: 10.1016/j.engfracmech.2020.106974.
- [188] Wittmann, F. H., P. E. Roelfstra, and H. Sadouki. "Simulation and analysis of composite structures". In: *Materials Science and Engineering* 68.2 (1985), pp. 239–248. DOI: 10.1016/0025-5416(85)90413-6.

-
- [189] Kwan, A., Z. M. Wang, and H. C. Chan. "Mesoscopic study of concrete II: Nonlinear finite element analysis". In: *Computers & Structures* 70.5 (1999), pp. 545–556. DOI: 10.1016/S0045-7949(98)00178-3.
- [190] Eckardt, S., S. Häfner, and C. Könke. "Simulation of the fracture behaviour of concrete using continuum damage models at the mesoscale". In: *Proceedings. Jyväskylä*, 2004, pp. 1–18. ISBN: 9513918688.
- [191] Häfner, S. et al. "Mesoscale modeling of concrete: Geometry and numerics". In: *Computers & Structures* 84.7 (2006), pp. 450–461. DOI: 10.1016/j.compstruc.2005.10.003.
- [192] Lammi, C. J. et al. "Dynamic Fracture and Dissipation Behaviors of Concrete at the Mesoscale". In: *International Journal of Applied Mechanics* 07.03 (2015), p. 1550038. DOI: 10.1142/S1758825115500386.
- [193] Hain, M. and P. Wriggers. "Numerical homogenization of hardened cement paste". In: *Computational Mechanics* 42.2 (2008), pp. 197–212. DOI: 10.1007/s00466-007-0211-9.
- [194] López, C. M., I. Carol, and A. Aguado. "Meso-structural study of concrete fracture using interface elements. II: Compression, biaxial and Brazilian test". In: *Materials and Structures* 41.3 (2008), pp. 601–620. DOI: 10.1617/s11527-007-9312-3.
- [195] Snozzi, L., F. Gatuingt, and J. F. Molinari. "A meso-mechanical model for concrete under dynamic tensile and compressive loading". In: *International Journal of Fracture* 178 (2012), pp. 179–194.
- [196] Lu, Y., Z. Song, and Z. Tu. "Analysis of Dynamic Response of Concrete Using a Mesoscale Model Incorporating 3D Effects". In: *International Journal of Protective Structures* 1.2 (2010), pp. 197–217.
- [197] Zohdi, T. I. and P. Wriggers. *An introduction to computational micromechanics*. corr. 2. printing. Vol. Vol. 20. Lecture notes in applied and computational mechanics. Berlin: Springer, 2008. ISBN: 9783540774822.
- [198] Eckardt, S. and C. Könke. "Adaptive Damage Simulation of Concrete Using Heterogeneous Multiscale Models". In: *Journal of Algorithms & Computational Technology* 2.2 (2008), pp. 275–298. DOI: 10.1260/174830108784646661.
- [199] Qian, Z. *Multiscale modeling of fracture processes in cementitious materials*. Haveka B. V., 2012. ISBN: 978-94-6186-054-5.
- [200] Palmieri, V. and L. de Lorenzis. "Multiscale modeling of concrete and of the FRP–concrete interface". In: *Engineering Fracture Mechanics* 131 (2014), pp. 150–175. DOI: 10.1016/j.engfracmech.2014.07.027.
- [201] Gatuingt, F., L. Snozzi, and J. F. Molinari. "Numerical determination of the tensile response and the dissipated fracture energy of concrete: Role of the mesostructure and influence of the loading rate". In: *International*

- Journal for Numerical and Analytical Methods in Geomechanics* 37.18 (2013), pp. 3112–3130. DOI: 10.1002/nag.2181.
- [202] Huang, Y. J. et al. "Monte Carlo simulations of meso-scale dynamic compressive behavior of concrete based on X-ray computed tomography images". In: *International Journal of Impact Engineering* 97 (2016), pp. 102–115. DOI: 10.1016/j.ijimpeng.2016.06.009.
- [203] Huang, Y. et al. "2D and 3D homogenization and fracture analysis of concrete based on in-situ X-ray Computed Tomography images and Monte Carlo simulations". In: *Engineering Fracture Mechanics* 163 (2016), pp. 37–54. DOI: 10.1016/j.engfracmech.2016.06.018.
- [204] Contrafatto, L., M. Cuomo, and S. Gazzo. "A concrete homogenisation technique at meso-scale level accounting for damaging behaviour of cement paste and aggregates". In: *Computers & Structures* 173 (2016), pp. 1–18. DOI: 10.1016/j.compstruc.2016.05.009.
- [205] Poinard, C. et al. "Compression triaxial behavior of concrete: the role of the mesostructure by analysis of X-ray tomographic images". In: *European Journal of Environmental and Civil Engineering* 16.sup1 (2012), s115–s136. DOI: 10.1080/19648189.2012.682458.
- [206] Wang, Z. M., A. Kwan, and H. C. Chan. "Mesoscopic study of concrete I: Generation of random aggregate structure and finite element mesh". In: *Computers & Structures* 70.5 (1999), pp. 533–544. DOI: 10.1016/S0045-7949(98)00177-1.
- [207] Wriggers, P. and S. O. Moftah. "Mesoscale models for concrete: Homogenisation and damage behaviour". In: *Finite Elements in Analysis and Design* 42.7 (2006), pp. 623–636. DOI: 10.1016/j.finel.2005.11.008.
- [208] Skarżyński, Ł. and J. Tejchman. "Calculations of fracture process zones on meso-scale in notched concrete beams subjected to three-point bending". In: *European Journal of Mechanics - A/Solids* 29.4 (2010), pp. 746–760. DOI: 10.1016/j.euromechsol.2010.02.008.
- [209] Kim, S.-M. and R. K. Abu Al-Rub. "Meso-scale computational modeling of the plastic-damage response of cementitious composites". In: *Cement and concrete research* 41.3 (2011), pp. 339–358. DOI: 10.1016/j.cemconres.2010.12.002.
- [210] Trawiński, W., J. Bobiński, and J. Tejchman. "Two-dimensional simulations of concrete fracture at aggregate level with cohesive elements based on X-ray CT images". In: *Engineering Fracture Mechanics* 168 (2016), pp. 204–226. DOI: 10.1016/j.engfracmech.2016.09.012.
- [211] Ren, W. et al. "Two-dimensional X-ray CT image based meso-scale fracture modelling of concrete". In: *Engineering Fracture Mechanics* 133 (2015), pp. 24–39. DOI: 10.1016/j.engfracmech.2014.10.016.

-
- [212] Pedersen, R. R., A. Simone, and L. J. Sluys. "Mesoscopic modeling and simulation of the dynamic tensile behavior of concrete". In: *Cement and concrete research* 50 (2013), pp. 74–87. DOI: 10.1016/j.cemconres.2013.03.021.
- [213] Zhou, X. Q. and H. Hao. "Mesoscale modelling of concrete tensile failure mechanism at high strain rates". In: *Computers & Structures* 86.21-22 (2008), pp. 2013–2026. DOI: 10.1016/j.compstruc.2008.04.013.
- [214] Wang, X. F. et al. "Monte Carlo simulations of mesoscale fracture modelling of concrete with random aggregates and pores". In: *Construction and Building Materials* 75 (2015), pp. 35–45. DOI: 10.1016/j.conbuildmat.2014.09.069.
- [215] Zhou, W. et al. "Mesoscopic simulation of the dynamic tensile behaviour of concrete based on a rate-dependent cohesive model". In: *International Journal of Impact Engineering* 95 (2016), pp. 165–175. DOI: 10.1016/j.ijimpeng.2016.05.003.
- [216] Gangnant, A. et al. "Modeling of the quasibrittle fracture of concrete at meso-scale: Effect of classes of aggregates on global and local behavior". In: *Cement and concrete research* 89 (2016), pp. 35–44. DOI: 10.1016/j.cemconres.2016.07.010.
- [217] Riedel, W., T. Wicklein, and K. Thoma. "Shock properties of conventional and high strength concrete: Experimental and mesomechanical analysis". In: *International Journal of Impact Engineering* 35 (2008), pp. 155–171.
- [218] Hartmann, T. "Zur mesomechanischen Modellierung von Beton und ihrer Anwendung zur makromechanischen Modellbildung". Dissertation. Neubiberg: Universität der Bundeswehr München, 2009.
- [219] Tu, Z. and Y. Lu. "Mesoscale modelling of concrete for static and dynamic response analysis -Part 1: Model development and implementation". In: *Structural Engineering and Mechanics* 37.2 (2011), pp. 197–213. DOI: 10.12989/sem.2011.37.2.197.
- [220] López, C. M., I. Carol, and A. Aguado. "Meso-structural study of concrete fracture using interface elements. I: Numerical model and tensile behavior". In: *Materials and Structures* 41.3 (2008), pp. 583–599. DOI: 10.1617/s11527-007-9314-1.
- [221] Bernard, F. and S. Kamali-Bernard. "Numerical study of ITZ contribution on mechanical behavior and diffusivity of mortars". In: *Computational Materials Science* 102 (2015), pp. 250–257. DOI: 10.1016/j.commatsci.2015.02.016.
- [222] Keinde, D. et al. "Effect of the interfacial transition zone and the nature of the matrix-aggregate interface on the overall elastic and inelastic behaviour of concrete under compression: A 3D numerical study". In:

- European Journal of Environmental and Civil Engineering* (2014), pp. 1–10. DOI: 10.1080/19648189.2014.896757.
- [223] Gambarelli, S. and J. Ožbolt. "Dynamic fracture of concrete in compression: 3D finite element analysis at meso- and macro-scale". In: *Continuum Mechanics and Thermodynamics* 32.6 (2020), pp. 1803–1821. DOI: 10.1007/s00161-020-00881-5.
- [224] Bernard, F., S. Kamali-Bernard, and W. Prince. "3D multi-scale modelling of mechanical behaviour of sound and leached mortar". In: *Cement and concrete research* 38.4 (2008), pp. 449–458. DOI: 10.1016/j.cemconres.2007.11.015.
- [225] Knell, S. *A numerical modeling approach for the transient response of solids at the mesoscale*. Freiburg i. Br.: Fraunhofer Verlag, 2011. ISBN: 978-3-8396-0323-9.
- [226] Wilkins, M. L. *Calculation of Elastic-Plastic Flow*. UCRL-7322, Rev. 1. Livermore, CA: Lawrence Radiation Laboratory, University of California, 1969.
- [227] Rots, J. G. "Strain-Softening analysis of concrete fracture specimens". In: *Fracture toughness and fracture energy of concrete*. Ed. by Wittmann, F. H. Developments in civil engineering. Amsterdam: Elsevier, 1986. ISBN: 978-0444427335.
- [228] Rots, J. G. and J. Blaauwendraad. "Crack models for concrete: discrete or smeared? Fixed, multi-directional or rotating?" In: *Heron* 34.1 (1989).
- [229] Jirásek, M. and T. Zimmermann. "Analysis of Rotating Crack Model". In: *Journal of Engineering Mechanics* 124.8 (1998), pp. 842–851. DOI: 10.1061/(ASCE)0733-9399(1998)124:8(842).
- [230] Červenka, J. and V. K. Papanikolaou. "Three dimensional combined fracture–plastic material model for concrete". In: *International Journal of Plasticity* 24.12 (2008), pp. 2192–2220. DOI: 10.1016/j.ijplas.2008.01.004.
- [231] Tailhan, J.-L. et al. "Multiscale probabilistic approaches and strategies for the modelling of concrete cracking". In: *VIII International Conference on Fracture Mechanics of Concrete and Concrete Structures, FraMCoS-8*. Ed. by van Mier, J. and Ruiz, G., Andrade, R.C.Yu, Zhang, X.X. 2013.
- [232] Belytschko, T. and T. Black. "Elastic crack growth in finite elements with minimal remeshing". In: *International Journal for Numerical Methods in Engineering* 45.5 (1999), pp. 601–620. DOI: 10.1002/(SICI)1097-0207(19990620)45:5<601::AID-NME598>3.0.CO;2-S.
- [233] Moës, N., J. Dolbow, and T. Belytschko. "A finite element method for crack growth without remeshing". In: *International Journal for Numerical*

- Methods in Engineering* 46.1 (1999), pp. 131–150. DOI: 10.1002/(SICI)1097-0207(19990910)46:1<131::AID-NME726>3.0.CO;2-J.
- [234] Durr, N. and M. Sauer. "Mesoscale Modeling of Quartzite and Sandstone under Shock Loading: Influence of Porosity and Pressure-dependent Quartz Stiffness on Macroscopic Behavior". In: *Procedia Engineering* 103 (2015), pp. 105–112. DOI: 10.1016/j.proeng.2015.04.015.
- [235] Barenblatt, G. "The mathematical theory of equilibrium cracks in brittle fracture". In: *Adv. Appl. Mech.* 7 (1962), pp. 55–129.
- [236] Dugdale, D. S. "Yielding of steel sheets containing slits". In: *Journal of the Mechanics and Physics of Solids* 8 (1960), pp. 100–104.
- [237] Hillerborg, A., M. Mod  er, and P.-E. Petersson. "Analysis of crack formation and crack growth in concrete by means of fracture mechanics and finite elements". In: *Cement and concrete research* 6.6 (1976), pp. 773–781. DOI: 10.1016/0008-8846(76)90007-7.
- [238] Xu, X.-P. and A. Needleman. "Numerical Simulations of Fast Crack Growth in Brittle Solid". In: *Journal of the Mechanics and Physics of Solids* 42.9 (1994), pp. 1397–1434.
- [239] Camacho, G. T. and M. Ortiz. "Computational Modelling of Impact Damage in Brittle Materials". In: *Int. J. Solids Structures* 33.20-22 (1996), pp. 2899–2938.
- [240] Pandolfi, A. and M. Ortiz. "Solid Modeling Aspects of Three-Dimensional Fragmentation". In: *Engineering with Computers* 14 (1998), pp. 287–308.
- [241] Rossi, P. "Numerical modeling of the cracking using a non-deterministic approach". In: *Fracture toughness and fracture energy*. Ed. by Mihashi, H. Rotterdam u.a.: Balkema, 1989, pp. 383–394. ISBN: 9061919886.
- [242] Hao, H. et al. "Review of the current practices in blast-resistant analysis and design of concrete structures". In: *Advances in Structural Engineering* 19.8 (2016), pp. 1193–1223. DOI: 10.1177/1369433216656430.
- [243] Schwer, L. E. and Y. D. Murray. "A three-invariant smooth cap model with mixed hardening". In: *International Journal for Numerical and Analytic Methods in Geomechanics* 18 (1994), pp. 657–688.
- [244] Denoual, C. and F. Hild. "A damage model for the dynamic fragmentation of brittle solids". In: *Computer Methods in Applied Mechanics and Engineering* 183.3-4 (2000), pp. 247–258. DOI: 10.1016/S0045-7825(99)00221-2.
- [245] Riedel, W., N. Kawai, and K.-i. Kondo. "Numerical assessment for impact strength measurements in concrete materials". In: *International Journal of Impact Engineering* 36 (2009), pp. 283–293.

- [246] *Borrvall, T. and W. Riedel. "The RHT Concrete Model in LS-DYNA". In: 8th International LS-DYNA Conference. 2011.*
- [247] *Riedel, W. "10 years RHT: A review of concrete modelling and hydrocode applications". In: Predictive Modeling of Dynamic Processes: A Tribute to Professor Klaus Thoma. Ed. by Hiermaier, S. New York: Springer, 2009, pp. 143–165. ISBN: 978-1-4419-0727-1.*
- [248] *Grunwald, C. et al. "A general concrete model in hydrocodes: Verification and validation of the Riedel-Hiermaier-Thoma model in LS-DYNA". In: International Journal of Protective Structures 8.1 (2017), pp. 58–85. DOI: 10.1177/2041419617695977.*
- [249] *Ottosen, N. S. "A Failure Criterion for Concrete". In: Journal of the Engineering Mechanics 103.4 (1977), pp. 527–535.*
- [250] *William, K. J. and E. P. Warnke. "Constitutive Model for the Triaxial Behaviour of Concrete". In: Seminar on Concrete Structures Subjected to Triaxial Stresses, IABSE. International Association of Bridge and Structural Engineers, 1975.*
- [251] *Bischoff, P. H. and F.-H. Schlüter. Concrete structures under impact and impulsive loading, Synthesis Report. Comité Euro-Internationale du Béton, 1988.*
- [252] *Hansson, H. Simulation of penetration in normal strength concrete for a projectile with L/D=9. FOI-R-1759-SE. Stockholm: FOI, 2005.*
- [253] *Tu, Z. and Y. Lu. "Evaluation of typical concrete material models used in hydrocodes for high dynamic response simulations". In: International Journal of Impact Engineering 36 (2009), pp. 132–146.*
- [254] *Schuler, H. Experimentelle und numerische Untersuchungen zur Schädigung von stoßbeanspruchtem Beton: Zugl.: München, Univ. der Bundeswehr, Diss., 2004. Freiburg i. Br.: Fraunhofer-Verlag, 2004.*
- [255] *Tawadrous, A. S., D. S. Preece, and J. P. Glenville. "Modification of the RHT model for enhanced tensile response predictions of geologic materials". In: Rock Fragmentation by Blasting. Ed. by Singh, P. K. and A. Sinha. CRC Press, 2012, pp. 309–323. ISBN: 9780429220630.*
- [256] *Bach, A. Stahlbetonbauteile unter kombinierten statischen und detonativen Belastungen in Experiment, Simulation und Bemessung. Vol. Heft Nr. 29. Freiburg i. Br.: Fraunhofer-Verlag, 2017. ISBN: 978-3-8396-1028-2.*
- [257] *Häußler-Combe, U., E. Panteki, and T. Kühn. "Strain rate effects for spallation of concrete". In: EPJ Web of Conferences 94 (2015), p. 04006. DOI: 10.1051/epjconf/20159404006.*
- [258] *Tu, Z. and Y. Lu. "Modifications of RHT material model for improved numerical simulation of dynamic response of concrete". In: International*

- Journal of Impact Engineering* 37 (2010), pp. 1072–1082. DOI: 10.1016/j.ijimpeng.2010.04.004.
- [259] Unger, J. F., S. Eckardt, and C. Konke. "A mesoscale model for concrete to simulate mechanical failure". In: *Computers and Concrete* 8.4 (2011), pp. 401–423. DOI: 10.12989/cac.2011.8.4.401.
- [260] Clegg, R. A., C. J. Hayhurst, and I. Robertson. *Development and Application of a Rankine Plasticity Model for Improved Prediction of Tensile Cracking in Ceramic and Concrete Materials under Impact*.
- [261] Leppänen, J. "Concrete subjected to projectile and fragment impacts: Modelling of crack softening and strain rate dependency in tension". In: *International Journal of Impact Engineering* 32.11 (2006), pp. 1828–1841. DOI: 10.1016/j.ijimpeng.2005.06.005.
- [262] Petersson, P.-E. *Crack growth and development of fracture zones in plain concrete and similar materials*. TVBM-1006. University of Lund, 1981.
- [263] Wittmann, F. H. et al. "Fracture energy and strain softening of concrete as determined by means of compact tension specimens". In: *Materials and Structures* 21.1 (1988), pp. 21–32. DOI: 10.1007/BF02472525.
- [264] Gopalaratnam, V. S. and S. P. Shah. "Softening Response of Plain Concrete in Direct Tension". In: *Journal Proceedings* 82.3 (1985). DOI: 10.14359/10338.
- [265] Cintora, T. "Softening Response of Concrete in Direct Tension". Master Thesis. New Jersey: New Jersey Institute of Technology, 1988.
- [266] Reinhardt, H. W., H. A. W. Cornelissen, and D. A. Hordijk. "Tensile Tests and Failure Analysis of Concrete". In: *Journal of Structural Engineering* 112.11 (1986), pp. 2462–2477. DOI: 10.1061/(ASCE)0733-9445(1986)112:11(2462).
- [267] Cornelissen, H., D. A. Hordijk, and H. W. Reinhardt. "Experimental determination of crack softening characteristics of normalweight and lightweight concrete". In: *Heron* 31.2 (1986), pp. 45–56.
- [268] Jirásek, M. and M. Bauer. "Numerical aspects of the crack band approach". In: *Computers & Structures* 110-111 (2012), pp. 60–78. DOI: 10.1016/j.compstruc.2012.06.006.
- [269] Barzegar, F. and S. Maddipati. "Three-Dimensional Modeling of Concrete Structures. I: Plain Concrete". In: *Journal of Structural Engineering* 123.10 (1997), pp. 1339–1346. DOI: 10.1061/(ASCE)0733-9445(1997)123:10(1339).
- [270] Oliver, J. "A consistent characteristic length for smeared cracking models". In: *International Journal for Numerical Methods in Engineering* 28.2 (1989), pp. 461–474. DOI: 10.1002/nme.1620280214.

- [271] Govindjee, S., G. J. Kay, and J. C. Simo. "Anisotropic modelling and numerical simulation of brittle damage in concrete". In: *International Journal for Numerical Methods in Engineering* 38 (1995), pp. 3611–3633.
- [272] May, M., S. Kilchert, and S. Hiermaier. "3D modeling of fracture in brittle isotropic materials using a novel algorithm for the determination of the fracture plane orientation and crack surface area". In: *Finite Elements in Analysis and Design* 56.12–13 (2012), pp. 32–40. DOI: 10.1016/j.finel.2012.03.001.
- [273] Schuler, H., C. Mayrhofer, and K. Thoma. "Spall experiments for the measurement of the tensile strength and fracture energy of concrete at high strain rates". In: *International Journal of Impact Engineering* 32.10 (2006), pp. 1635–1650. DOI: 10.1016/j.ijimpeng.2005.01.010.
- [274] Brara, A. and J. R. Klepaczko. "Fracture energy of concrete at high loading rates in tension". In: *International Journal of Impact Engineering* 34.3 (2007), pp. 424–435. DOI: 10.1016/j.ijimpeng.2005.10.004.
- [275] Banthia, N. et al. "Impact testing of concrete using a drop-weight impact machine". In: *Experimental Mechanics* 29.1 (1989), pp. 63–69. DOI: 10.1007/bf02327783.
- [276] Weerheijm, J. and I. Vejt. "The dynamic fracture energy of concrete: Review of test methods and data comparison". In: *Fracture mechanics of concrete and concrete structures*. Ed. by Oh, B. H., O. C. Choi, and L. Chung. [United States]: IA-FraMCoS, 2010. ISBN: 978-89-5708-180-8.
- [277] Millon, O. and W. Riedel. *Stochastic Distribution of Concrete Strength*. I-19/11. Efringen-Kirchen: Ernst-Mach-Institut, Fraunhofer, 2012.
- [278] Kong, X. et al. "Modified K&C model for cratering and scabbing of concrete slabs under projectile impact". In: *International Journal of Impact Engineering* 108 (2017), pp. 217–228. DOI: 10.1016/j.ijimpeng.2017.02.016.
- [279] Herrmann, W. "Constitutive Equation for the Dynamic Compaction of Ductile Porous Materials". In: *Journal of Applied Physics* 40.6 (1969), pp. 2490–2499.
- [280] Geuzaine, C. and J.-F. Remacle. "Gmsh: A 3-D finite element mesh generator with built-in pre- and post-processing facilities". In: *International Journal for Numerical Methods in Engineering* 79.11 (2009), pp. 1309–1331. DOI: 10.1002/nme.2579.
- [281] Durr, N. *Mesoscale modeling of dynamic fracture and shock compression in quartzite and sandstone*. Freiburg i. Br.: Fraunhofer-Verlag, 2017. ISBN: 978-3-8396-1319-1.

- [282] Bewick, B. et al. *Fragmentation of Solid Materials Using Shock Tubes. Part 3: Second Test Series in a Small-Diameter Shock Tube*. HDTRA1-14-C-0001. San Antonio: Protection Engineering Consultants, Oct. 2018.
- [283] Bewick, B. et al. *Fragmentation of Solid Materials Using Shock Tubes. Part 2: First Test Series in a Large-Diameter Shock Tube*. HDTRA1-14-C-0001. San Antonio: Protection Engineering Consultants, Dec. 2017.
- [284] Grunwald, C. et al. "A concurrent two-scale coupling for wave propagation using direct solution schemes with explicit time integration". In: *International Journal for Numerical Methods in Engineering* (2021). DOI: 10.1002/nme.6795.
- [285] Fish, J. "Bridging the scales in nano engineering and science". In: *Journal of Nanoparticle Research* 8.5 (2006), pp. 577–594. DOI: 10.1007/s11051-006-9090-9.
- [286] Fish, J. *Practical multiscaleing*. Chichester: Wiley, 2014. ISBN: 9781118534847.
- [287] Belytschko, T. and J. H. Song. "Coarse-graining of multiscale crack propagation". In: *International Journal for Numerical Methods in Engineering* 81.5 (2010), pp. 537–563. DOI: 10.1002/nme.2694.
- [288] Horstemeyer, M. F. "Multiscale Modeling: A Review". In: *Practical Aspects of Computational Chemistry*. Ed. by Leszczynski, J. and M. K. Shukla. Vol. 1. Dordrecht: Springer Netherlands, 2010, pp. 87–135. ISBN: 978-90-481-2686-6. DOI: 10.1007/978-90-481-2687-3_4.
- [289] E, W., B. Engquist, and Z. Huang. "Heterogeneous multiscale method: A general methodology for multiscale modeling". In: *Physical Review B* 67.9 (2003), p. 783. DOI: 10.1103/PhysRevB.67.092101.
- [290] Gitman, I. M., H. Askes, and L. J. Sluys. "A coupled-volume approach to the multi-scale modelling of quasi-brittle materials". In: *Materials Science Forum* 539-543 (2007), pp. 2582–2587.
- [291] Terada, K. et al. "A method of two-scale analysis with micro-macro decoupling scheme: application to hyperelastic composite materials". In: *Computational Mechanics* 52.5 (2013), pp. 1199–1219. DOI: 10.1007/s00466-013-0872-5.
- [292] Takano, N., M. Zako, and Y. Ohnishi. "Macro-micro uncoupled homogenization procedure for microscopic nonlinear analysis of composites". In: *Materials Science Research International* 2.2 (1996), pp. 81–86.
- [293] Temizer, I. and T. I. Zohdi. "A numerical method for homogenization in non-linear elasticity". In: *Computational Mechanics* 40.2 (2007), pp. 281–298. DOI: 10.1007/s00466-006-0097-y.
- [294] Feyel, F. "Multiscale FE2 elastoviscoplastic analysis of composite structures". In: *Computational Materials Science* 16.1-4 (1999), pp. 344–354. DOI: 10.1016/S0927-0256(99)00077-4.

- [295] Feyel, F. "A multilevel finite element method (FE2) to describe the response of highly non-linear structures using generalized continua". In: *Computer Methods in Applied Mechanics and Engineering* 192.28-30 (2003), pp. 3233–3244. DOI: 10.1016/S0045-7825(03)00348-7.
- [296] Hill, R. "Elastic properties of reinforced solids: Some theoretical principles". In: *Journal of the Mechanics and Physics of Solids* 11.5 (1963), pp. 357–372. DOI: 10.1016/0022-5096(63)90036-X.
- [297] Kouznetsova, V., W. A. M. Brekelmans, and F. P. T. Baaijens. "An approach to micro-macro modeling of heterogeneous materials". In: *Computational Mechanics* 27.1 (2001), pp. 37–48. DOI: 10.1007/s004660000212.
- [298] Souza, F. V. and D. H. Allen. "Modeling failure of heterogeneous viscoelastic solids under dynamic/impact loading due to multiple evolving cracks using a two-way coupled multiscale model". In: *Mechanics of Time-Dependent Materials* 14.2 (2010), pp. 125–151. DOI: 10.1007/s11043-009-9099-4.
- [299] Souza, F. V. and D. H. Allen. "Modeling the transition of microcracks into macrocracks in heterogeneous viscoelastic media using a two-way coupled multiscale model". In: *International Journal of Solids and Structures* 48.22-23 (2011), pp. 3160–3175. DOI: 10.1016/j.ijsolstr.2011.07.010.
- [300] Chatzigeorgiou, G., Y. Chemisky, and F. Meraghni. "Computational micro to macro transitions for shape memory alloy composites using periodic homogenization". In: *Smart Materials and Structures* 24.3 (2015), p. 035009. DOI: 10.1088/0964-1726/24/3/035009.
- [301] Kouznetsova, V., M. G. D. Geers, and W. A. M. Brekelmans. "Multi-scale constitutive modelling of heterogeneous materials with a gradient-enhanced computational homogenization scheme". In: *International Journal for Numerical Methods in Engineering* 54.8 (2002), pp. 1235–1260. DOI: 10.1002/nme.541.
- [302] Matous, K., M. Kulkarni, and P. Geubelle. "Multiscale cohesive failure modeling of heterogeneous adhesives". In: *Journal of the Mechanics and Physics of Solids* 56.4 (2008), pp. 1511–1533. DOI: 10.1016/j.jmps.2007.08.005.
- [303] Kulkarni, M. G., K. Matouš, and P. H. Geubelle. "Coupled multi-scale cohesive modeling of failure in heterogeneous adhesives". In: *International Journal for Numerical Methods in Engineering* 84.8 (2010), pp. 916–946. DOI: 10.1002/nme.2923.
- [304] Verhoosel, C. V. et al. "Computational homogenization for adhesive and cohesive failure in quasi-brittle solids". In: *International Journal for Numerical Methods in Engineering* 83.8-9 (2010), pp. 1155–1179. DOI: 10.1002/nme.2854.

-
- [305] Nguyen, V. P. "An enhanced continuous-discontinuous multiscale method for modeling mode-I cohesive failure in random heterogeneous quasi-brittle materials". In: *Engineering Fracture Mechanics* 79 (2012), pp. 78–102. DOI: 10.1016/j.engfracmech.2011.10.005.
- [306] Snozzi, L. "A meso-scale computational approach to dynamic failure in concrete". Dissertation. Lausanne: École Polytechnique Fédérale de Lausanne, 2013.
- [307] Ellis, B. D. et al. "Experimental investigation and multiscale modeling of ultra-high-performance concrete panels subject to blast loading". In: *International Journal of Impact Engineering* 69 (2014), pp. 95–103. DOI: 10.1016/j.ijimpeng.2013.12.011.
- [308] Unger, J. F. and S. Eckardt. "Multiscale Modeling of Concrete". In: *Archives of Computational Methods in Engineering* 18.3 (2011), pp. 341–393. DOI: 10.1007/s11831-011-9063-8.
- [309] Geers, M., V. G. Kouznetsova, and W. Brekelmans. "Multi-scale computational homogenization: Trends and challenges". In: *Journal of Computational and Applied Mathematics* 234.7 (2010), pp. 2175–2182. DOI: 10.1016/j.cam.2009.08.077.
- [310] Geers, M. G. D. et al. "Homogenization Methods and Multiscale Modeling: Nonlinear Problems". In: *Encyclopedia of computational mechanics*. Ed. by Stein, E., R. de Borst, and T. J. R. Hughes. Vol. 21. Chichester, West Sussex, England and Hoboken, NJ: John Wiley & Sons Ltd, 2018, pp. 1–34. ISBN: 9781119003793. DOI: 10.1002/9781119176817.ecm2107.
- [311] Gitman, I. M., H. Askes, and L. J. Sluys. "Representative Volume: Existence and size determination". In: *Engineering Fracture Mechanics* 76.16 (2007), pp. 2518–2534.
- [312] Belytschko, T., S. Loehnert, and J.-H. Song. "Multiscale aggregating discontinuities: A method for circumventing loss of material stability". In: *International Journal for Numerical Methods in Engineering* 73.6 (2008), pp. 869–894. DOI: 10.1002/nme.2156.
- [313] Coenen, E. W. C. et al. "A multi-scale approach to bridge microscale damage and macroscale failure: A nested computational homogenization-localization framework". In: *International Journal of Fracture* 178.1-2 (2012), pp. 157–178. DOI: 10.1007/s10704-012-9765-4.
- [314] Song, J.-H. and Y.-C. Yoon. "Multiscale failure analysis with coarse-grained micro cracks and damage". In: *Theoretical and Applied Fracture Mechanics* 72 (2014), pp. 100–109. DOI: 10.1016/j.tafmec.2014.04.005.
- [315] Karamnejad, A., V. P. Nguyen, and L. J. Sluys. "A multi-scale rate dependent crack model for quasi-brittle heterogeneous materials". In: *Engi-*

- neering Fracture Mechanics* 104 (2013), pp. 96–113. DOI: 10.1016/j.engfracmech.2013.03.009.
- [316] *Nguyen, V. P. et al.* "On the existence of representative volumes for softening quasi-brittle materials – A failure zone averaging scheme". In: *Computer Methods in Applied Mechanics and Engineering* 199.45-48 (2010), pp. 3028–3038. DOI: 10.1016/j.cma.2010.06.018.
 - [317] *Gitman, I. M.* "Representative volumes and multi-scale modelling of quasi-brittle materials". Dissertation. Delft: TU Delft, 2006.
 - [318] *Gitman, I. M., H. Askes, and L. J. Sluys.* "Coupled-volume multi-scale modelling of quasi-brittle material". In: *European Journal of Mechanics - A/Solids* 27.3 (2008), pp. 302–327. DOI: 10.1016/j.euromechsol.2007.10.004.
 - [319] *Drugan, W. J. and J. R. Willis.* "A micromechanics-based nonlocal constitutive equation and estimates of representative volume element size for elastic composites". In: *Journal of the Mechanics and Physics of Solids* 44.4 (1996), pp. 497–524. DOI: 10.1016/0022-5096(96)00007-5.
 - [320] *Lacy, T. E., D. L. McDowell, and R. Talreja.* "Gradient concepts for evolution of damage". In: *Mechanics of Materials* 31.12 (1999), pp. 831–860. DOI: 10.1016/S0167-6636(99)00029-0.
 - [321] *Bažant, Z. P. and G. Pijaudier-Cabot.* "Measurement of Characteristic Length of Nonlocal Continuum". In: *Journal of Engineering Mechanics* 115.4 (1989), pp. 755–767. DOI: 10.1061/(ASCE)0733-9399(1989)115:4(755).
 - [322] *Abraham, F. F. et al.* "Spanning the continuum to quantum length scales in a dynamic simulation of brittle fracture". In: *Europhysics Letters (EPL)* 44.6 (1998), pp. 783–787. DOI: 10.1209/epl/i1998-00536-9.
 - [323] *Belytschko, T. and S. P. Xiao.* "Coupling Methods for Continuum Model with Molecular Model". In: *International Journal for Multiscale Computational Engineering* 1.1 (2003), p. 12. DOI: 10.1615/IntJMultCompEng.v1.i1.100.
 - [324] *Ben Dhia, H.* "Multiscale mechanical problems: the Arlequin method". In: *Comptes Rendus de l'Académie des Sciences - Series IIB - Mechanics-Physics-Chemistry-Astronomy* 326.12 (1998), pp. 899–904.
 - [325] *Ben Dhia, H. and G. Rateau.* "The Arlequin method as a flexible engineering design tool". In: *International Journal for Numerical Methods in Engineering* 62.11 (2005), pp. 1442–1462. DOI: 10.1002/nme.1229.
 - [326] *Ben Dhia, H. and C. Zammali.* "Level-Sets and Arlequin framework for dynamic contact problems". In: *Revue Européenne des Éléments Finis* 13.5-7 (2004), pp. 403–414. DOI: 10.3166/reef.13.403-414.

-
- [327] Ghanem, A. et al. "Arlequin framework for multi-model, multi-time scale and heterogeneous time integrators for structural transient dynamics". In: *Computer Methods in Applied Mechanics and Engineering* 254 (2013), pp. 292–308. DOI: 10.1016/j.cma.2012.08.019.
 - [328] Mota, A., I. Tezaur, and C. Alleman. "The Schwarz alternating method in solid mechanics". In: *Computational Mechanics* 319.6 (2017), pp. 19–51. DOI: 10.1016/j.cma.2017.02.006.
 - [329] Thirunavukkarasu, S. and M. N. Guddati. "A domain decomposition method for concurrent coupling of multiscale models". In: *International Journal for Numerical Methods in Engineering* 92.11 (2012), pp. 918–939. DOI: 10.1002/nme.4362.
 - [330] Belgacem, F. B. "The Mortar finite element method with Lagrange multipliers". In: *Numerische Mathematik* 84.2 (1999), pp. 173–197. DOI: 10.1007/s002110050468.
 - [331] Bernardi, C., Y. Maday, and F. Rapetti. "Basics and some applications of the mortar element method". In: *GAMM-Mitteilungen* 28.2 (2005), pp. 97–123. DOI: 10.1002/gamm.201490020.
 - [332] Farhat, C. and F.-X. Roux. "A method of finite element tearing and interconnecting and its parallel solution algorithm". In: *International Journal for Numerical Methods in Engineering* 32.6 (1991), pp. 1205–1227. DOI: 10.1002/nme.1620320604.
 - [333] Farhat, C., P.-S. Chen, and J. Mandel. "A scalable Lagrange multiplier based domain decomposition method for time-dependent problems". In: *International Journal for Numerical Methods in Engineering* 38.22 (1995), pp. 3831–3853. DOI: 10.1002/nme.1620382207.
 - [334] Gravouil, A. and A. Combescure. "Multi-time-step explicit-implicit method for non-linear structural dynamics". In: *International Journal for Numerical Methods in Engineering* 50.1 (2001), pp. 199–225. DOI: 10.1002/1097-0207(20010110)50:1<199::AID-NME132>3.0.CO;2-A.
 - [335] Marchais, J., L. Chamoin, and C. Rey. "Wave filtering through a selective perfectly matched layer in multiscale couplings with dynamically incompatible models". In: *International Journal for Numerical Methods in Engineering* 110.8 (2017), pp. 745–775. DOI: 10.1002/nme.5428.
 - [336] Park, K. C. and C. A. Felippa. "A variational principle for the formulation of partitioned structural systems". In: *International Journal for Numerical Methods in Engineering* 47.1-3 (2000), pp. 395–418. DOI: 10.1002/(SICI)1097-0207(20000110/30)47:1/3<395::AID-NME777>3.0.CO;2-9.
 - [337] Subber, W. and K. Matouš. "Asynchronous space-time algorithm based on a domain decomposition method for structural dynamics problems

- on non-matching meshes". In: *Computational Mechanics* 57.2 (2016), pp. 211–235. DOI: 10.1007/s00466-015-1228-0.
- [338] Souza, F. V., D. H. Allen, and Y.-R. Kim. "Multiscale model for predicting damage evolution in composites due to impact loading". In: *Composites Science and Technology* 68.13 (2008), pp. 2624–2634. DOI: 10.1016/j.compscitech.2008.04.043.
- [339] Souza, F. V. and D. H. Allen. "Multiscale modeling of impact on heterogeneous viscoelastic solids containing evolving microcracks". In: *International Journal for Numerical Methods in Engineering* 82 (2010), pp. 464–504. DOI: 10.1002/nme.2773.
- [340] Karamnejad, A. and L. J. Sluys. "A dispersive multi-scale crack model for quasi-brittle heterogeneous materials under impact loading". In: *Computer Methods in Applied Mechanics and Engineering* 278 (2014), pp. 423–444. DOI: 10.1016/j.cma.2014.05.020.
- [341] Knap, J. et al. "A computational framework for scale-bridging in multi-scale simulations". In: *International Journal for Numerical Methods in Engineering* 108.13 (2016), pp. 1649–1666. DOI: 10.1002/nme.5270.
- [342] Guidalt, P. et al. "A two-scale approach with homogenization for the computation of cracked structures". In: *Computers and Structures* 85 (2007), pp. 1360–1371.
- [343] Gravouil, A., A. Combescure, and M. Brun. "Heterogeneous asynchronous time integrators for computational structural dynamics". In: *International Journal for Numerical Methods in Engineering* 102.3-4 (2015), pp. 202–232. DOI: 10.1002/nme.4818.
- [344] Farhat, C. and M. Lesoinne. "Two efficient staggered algorithms for the serial and parallel solution of three-dimensional nonlinear transient aeroelastic problems". In: *Computer Methods in Applied Mechanics and Engineering* 182.3-4 (2000), pp. 499–515. DOI: 10.1016/S0045-7825(99)00206-6.
- [345] Vassen, J.-M. et al. "Strong coupling algorithm to solve Fluid-Structure-Interaction problems with a staggered approach". In: *Proceedings of the 7th European Symposium on Aerothermodynamics*. Ed. by Ouwehand, L. ESA SP. Noordwijk: ESA Communications, 2011. ISBN: 9789292212568.
- [346] Shilkrot, L. E., R. E. Miller, and W. A. Curtin. "Multiscale plasticity modeling: coupled atomistics and discrete dislocation mechanics". In: *Journal of the Mechanics and Physics of Solids* 52.4 (2004), pp. 755–787. DOI: 10.1016/j.jmps.2003.09.023.
- [347] Liu, W. and J.-W. Hong. "A coupling approach of discretized peridynamics with finite element method". In: *Computer Methods in Ap-*

- plied Mechanics and Engineering* 245-246 (2012), pp. 163–175. DOI: 10.1016/j.cma.2012.07.006.
- [348] Jin, S., Y. K. Hwang, and J.-W. Hong. "Coupling of non-ordinary state-based peridynamics and finite element method with reduced boundary effect". In: *International Journal for Numerical Methods in Engineering* 122.16 (2021), pp. 4033–4054. DOI: 10.1002/nme.6691.
 - [349] Piperno, S., C. Farhat, and B. Larrotureau. "Partitioned procedures for the transient solution of coupled aroelastic problems Part I: Model problem, theory and two-dimensional application". In: *Computer Methods in Applied Mechanics and Engineering* 124.1-2 (1995), pp. 79–112. DOI: 10.1016/0045-7825(95)92707-9.
 - [350] Ibrahimbegović, A. and D. Markovic. "Strong coupling methods in multi-phase and multi-scale modeling of inelastic behavior of heterogeneous structures". In: *Computer Methods in Applied Mechanics and Engineering* 192.28-30 (2003), pp. 3089–3107. DOI: 10.1016/S0045-7825(03)00342-6.
 - [351] Hirai, I., B. P. Wang, and W. D. Pilkey. "An efficient zooming method for finite element analysis". In: *International Journal for Numerical Methods in Engineering* 20.9 (1984), pp. 1671–1683. DOI: 10.1002/nme.1620200910.
 - [352] Bažant, Z. P. "Spurious Reflection of Elastic Waves in Nonuniform Finite Element Grids". In: *Computer Methods in Applied Mechanics and Engineering* 16 (1978), pp. 91–100.
 - [353] Liu, J. B., S. K. Sharan, and L. Yao. "Wave motion and its dispersive properties in a finite element model with distortional elements". In: *Computers & Structures* 52.2 (1994), pp. 205–214. DOI: 10.1016/0045-7949(94)90273-9.
 - [354] Mullen, R. and T. Belytschko. "Dispersion analysis of finite element semidiscretizations of the two-dimensional wave equation". In: *International Journal for Numerical Methods in Engineering* 18.1 (1982), pp. 11–29. DOI: 10.1002/nme.1620180103.
 - [355] Jebahi, M. et al. "Multiscale Modeling of Complex Dynamic Problems: An Overview and Recent Developments". In: *Archives of Computational Methods in Engineering* 23.1 (2016), pp. 101–138. DOI: 10.1007/s11831-014-9136-6.
 - [356] E, W. and Z. Huang. "Matching conditions in atomistic-continuum modeling of materials". In: *Physical review letters* 87.13 (2001), p. 135501. DOI: 10.1103/PhysRevLett.87.135501.
 - [357] To, A. C. and S. Li. "Perfectly matched multiscale simulations". In: *Physical Review B* 72.3 (2005). DOI: 10.1103/PhysRevB.72.035414.

- [358] Engquist, B. and A. Majda. "Absorbing Boundary Conditions for the Numerical Simulation of Waves". In: *Mathematics of Computation* 31.139 (1977), p. 629. DOI: 10.2307/2005997.
- [359] Higdon, R. L. "Absorbing boundary conditions for elastic waves". In: *GEOPHYSICS* 56.2 (1991), pp. 231–241. DOI: 10.1190/1.1443035.
- [360] Berenger, J.-P. "A perfectly matched layer for the absorption of electromagnetic waves". In: *Journal of Computational Physics* 114.2 (1994), pp. 185–200. DOI: 10.1006/jcph.1994.1159.
- [361] Hastings, F. D., J. B. Schneider, and S. L. Broschat. "Application of the perfectly matched layer (PML) absorbing boundary condition to elastic wave propagation". In: *The Journal of the Acoustical Society of America* 100.5 (1996), pp. 3061–3069. DOI: 10.1121/1.417118.
- [362] Collino, F. and C. Tsogka. "Application of the perfectly matched absorbing layer model to the linear elastodynamic problem in anisotropic heterogeneous media". In: *GEOPHYSICS* 66.1 (2001), pp. 294–307. DOI: 10.1190/1.1444908.
- [363] Wagner, G. J. and W. K. Liu. "Coupling of atomistic and continuum simulations using a bridging scale decomposition". In: *Journal of Computational Physics* 190.1 (2003), pp. 249–274. DOI: 10.1016/S0021-9991(03)00273-0.
- [364] Liu, W. K. et al. "Bridging scale methods for nanomechanics and materials". In: *Computer Methods in Applied Mechanics and Engineering* 195.13-16 (2006), pp. 1407–1421. DOI: 10.1016/j.cma.2005.05.042.
- [365] Holmes, N. and T. Belytschko. "Postprocessing of finite element transient response calculations by digital filters". In: *Computers & Structures* 6.3 (1976), pp. 211–216. DOI: 10.1016/0045-7949(76)90032-8.
- [366] Bertsekas, D. P. and J. N. Tsitsiklis. *Parallel and distributed computation: Numerical methods*. Vol. 7. Optimization and neural computation series. Belmont, Mass: Athena Scientific, 1997. ISBN: 9781886529014.
- [367] Message Passing Interface Forum. *A Message-Passing Interface Standard: Version 3.1*. Ed. by Message Passing Interface Forum. 2015.
- [368] OpenMP Architecture Review Board. *The OpenMP API specification for parallel programming*. URL: <https://www.openmp.org/> (visited on 09/22/2022).
- [369] Kingery, C. N. and G. Bulmash. *Airblast parameters from TNT spherical air burst and hemispherical surface burst*. ARBL-TR-02555. Aberdeen, 1984.
- [370] Dalton, J. C. et al. *Unified Facilities Criteria (UFC) 3-340-02: Structures to resist the effects of accidental explosions*. USA, 2008.

-
- [371] *Technical Manual - Design and Analysis of Hardened Structures to Conventional Weapons Effects*. DAHSCWEMAN97/TM 5-855-1/AFJMAN 32-1055/NAVFAC P-1080. Washington D.C., Apr. 21, 1997.
- [372] Fan, S. C. et al. "Validation of a flight model for predicting debris trajectory from the explosion of an ammunition storage magazine". In: *Journal of Wind Engineering and Industrial Aerodynamics* 136.2 (2015), pp. 114–126. DOI: 10.1016/j.jweia.2014.11.004.
- [373] Xu, Z., H. Hao, and H. N. Li. "Mesoscale modelling of fibre reinforced concrete material under compressive impact loading". In: *Construction and Building Materials* 26.1 (2012), pp. 274–288. DOI: 10.1016/j.conbuildmat.2011.06.022.
- [374] Andreasen, A. H. M. "Ueber die Beziehung zwischen Kornabstufung und Zwischenraum in Produkten aus losen Körnern (mit einigen Experimenten)". In: *Kolloid-Zeitschrift* 50.3 (1930), pp. 217–228. DOI: 10.1007/BF01422986.
- [375] Zhang, Z. et al. "Three-dimensional mesoscale modelling of concrete composites by using random walking algorithm". In: *Composites Science and Technology* 149 (2017), pp. 235–245. DOI: 10.1016/j.compscitech.2017.06.015.
- [376] Schutter, G. de and L. Taerwe. "Random particle model for concrete based on Delaunay triangulation". In: *Materials and Structures* 26.2 (1993), pp. 67–73. DOI: 10.1007/BF02472853.
- [377] Hsu, T. T. C. "Mathematical Analysis of Shrinkage Stresses in a Model of Hardened Concrete". In: *ACI Journal Proceedings* 60.3 (1963). DOI: 10.14359/7860.
- [378] Wittmann, F. H., H. Sadouki, and T. Steiger. "Experimental and numerical study of effective properties of composite materials". In: *Micromechanics of Concrete and Cementitious Composites*. Ed. by Huet, C. Lausann: Presses Polytechniques et Universitaires Romandes, 1993, pp. 59–82.
- [379] Belytschko, T. and R. Mullen. "Mesh Partitions of Explicit-Implicit Time Integration". In: *Formulations and computational algorithms in finite element analysis*. Ed. by Bathe, K.-J., J. T. Oden, and W. Wunderlich. Cambridge, Mass.: Massachusetts Inst. of Technology, 1977, pp. 673–690. ISBN: 0262021277.
- [380] Belytschko, T., H.-J. Yen, and R. Mullen. "Mixed methods for time integration". In: *Computer Methods in Applied Mechanics and Engineering* 17-18 (1979), pp. 259–275. DOI: 10.1016/0045-7825(79)90022-7.
- [381] Belytschko, T. and Y. Y. Lu. "Explicit multi-time step integration for first and second order finite element semidiscretizations". In: *Computer*

- Methods in Applied Mechanics and Engineering* 108.3-4 (1993), pp. 353–383. DOI: 10.1016/0045-7825(93)90010-U.
- [382] Smolinski, P. "An explicit multi-time step integration method for second order equations". In: *Computer Methods in Applied Mechanics and Engineering* 94.1 (1992), pp. 25–34. DOI: 10.1016/0045-7825(92)90155-D.
- [383] Smolinski, P., T. Belytschko, and M. Neal. "Multi-time-step integration using nodal partitioning". In: *International Journal for Numerical Methods in Engineering* 26.2 (1988), pp. 349–359. DOI: 10.1002/nme.1620260205.
- [384] Smolinski, P., S. Sleith, and T. Belytschko. "Stability of an explicit multi-time step integration algorithm for linear structural dynamics equations". In: *Computational Mechanics* 18.3 (1996), pp. 236–244. DOI: 10.1007/BF00369941.
- [385] Tamma, K. K. and J. F. D'Costa. "A new explicit variable time-integration self-starting methodology for computational structural dynamics". In: *International Journal for Numerical Methods in Engineering* 33.6 (1992), pp. 1165–1180. DOI: 10.1002/nme.1620330605.
- [386] Neal, M. O. and T. Belytschko. "Explicit-explicit subcycling with non-integer time step ratios for structural dynamic systems". In: *Computers & Structures* 31.6 (1989), pp. 871–880. DOI: 10.1016/0045-7949(89)90272-1.
- [387] Daniel, W. J. T. "Analysis and implementation of a new constant acceleration subcycling algorithm". In: *International Journal for Numerical Methods in Engineering* 40.15 (1997), pp. 2841–2855. DOI: 10.1002/(SICI)1097-0207(19970815)40:15<2841::AID-NME193>3.0.CO;2-S.
- [388] Belytschko, T., P. Smolinski, and W. K. Liu. "Stability of multi-time step partitioned integrators for first-order finite element systems". In: *Computer Methods in Applied Mechanics and Engineering* 49.3 (1985), pp. 281–297. DOI: 10.1016/0045-7825(85)90126-4.
- [389] Daniel, W. J. T. "The subcycled Newmark algorithm". In: *Computational Mechanics* 20.3 (1997), pp. 272–281. DOI: 10.1007/s004660050248.
- [390] Daniel, W. J. T. "A study of the stability of subcycling algorithms in structural dynamics". In: *Computer Methods in Applied Mechanics and Engineering* 156.1-4 (1998), pp. 1–13. DOI: 10.1016/S0045-7825(97)00140-0.
- [391] Klepaczko, J. R. and A. Brara. "An experimental method for dynamic tensile testing of concrete by spalling". In: *International Journal of Impact Engineering* 25.4 (2001), pp. 387–409. DOI: 10.1016/S0734-743X(00)00050-6.

- [392] Chen, X., S. Wu, and J. Zhou. "Experimental and modeling study of dynamic mechanical properties of cement paste, mortar and concrete". In: *Construction and Building Materials* 47 (2013), pp. 419–430. DOI: 10.1016/j.conbuildmat.2013.05.063.
- [393] Gopalaratnam, V. S., S. P. Shah, and R. John. "A modified instrumented charpy test for cement-based composites". In: *Experimental Mechanics* 24.2 (1984), pp. 102–111. DOI: 10.1007/BF02324991.
- [394] Lambert, D. E. and C. Allen Ross. "Strain rate effects on dynamic fracture and strength". In: *International Journal of Impact Engineering* 24.10 (2000), pp. 985–998. DOI: 10.1016/S0734-743X(00)00027-0.
- [395] Ross, C. A. et al. "Moisture and Strain Rate Effects on Concrete Strength". In: *ACI Materials Journal* 93.3 (1996). DOI: 10.14359/9814.
- [396] Tedesco, J. W., A. C. Ross, and S. T. Kuennen. "Experimental and Numerical Analysis of High Strain Rate Splitting-Tensile Tests". In: *ACI Materials Journal* 90.2 (1993). DOI: 10.14359/4013.
- [397] Yan, D. and G. Lin. "Dynamic properties of concrete in direct tension". In: *Cement and Concrete Research*, 1999, Vol.29(7), pp.1019-1025 36.7 (2006), pp. 1371–1378. DOI: 10.1016/j.cemconres.2006.03.003.
- [398] Régat, X. and J.-L. Hanus. "Experimental Study of the Dynamic Flexural Strength of Concrete". In: *Experimental Mechanics* 57.3 (2017), pp. 427–442. DOI: 10.1007/s11340-016-0243-1.
- [399] Tsembeles, K. et al. "The Shock Hugoniot Properties of Cement Paste & Mortar up to 18 GPa". In: *AIP Conference Proceedings*. AIP, 2004, pp. 1488–1491. DOI: 10.1063/1.1780520.
- [400] Wu, W. et al. "Measurement of Mechanical Properties of Hydrated Cement Paste Using Resonant Ultrasound Spectroscopy: Measurement of Mechanical Properties of Hydrated Cement Paste Using Resonant Ultrasound Spectroscopy". In: *Journal of ASTM International* 7.5 (2010).
- [401] Ding, Y.-Q. et al. "Determination and Validation of Parameters for Riedel-Hiermaier-Thoma Concrete Model". In: *Defence Science Journal* 63.5 (2013), pp. 524–530. DOI: 10.14429/dsj.63.3866.
- [402] Grady, D. E. and M. D. Furnish. "Hugoniot and release properties of a water-saturated high-silica-content grout". In: *Shock compression of condensed matter*. Ed. by Schmidt, S. C., J. N. Johnson, and L. W. Davison. Amsterdam, New York: Elsevier Science Pub. Co, 1990, pp. 621–624. ISBN: 0444882715.
- [403] Kohees, M., J. Sanjayan, and P. Rajeev. "Stress-strain relationship of cement mortar under triaxial compression". In: *Construction and Building Materials* 220 (2019), pp. 456–463. DOI: 10.1016/j.conbuildmat.2019.05.146.

- [404] Zech, B. and F. H. Wittmann. "A complex study on the reliability assessment of the containment of a PWR - Part II - Probabilistic approach to describe the behaviour of materials". In: *Nuclear Engineering and Design* 48.2-3 (1978), pp. 575–584. DOI: 10.1016/0029-5493(78)90099-7.
- [405] Ritter, R. "Verformungsverhalten und Grenzflaechen von Ultrahochleistungsbeton unter mehraxialer Beanspruchung". Dissertation. TU Dresden.

A Appendix

A.1 Generation of mesomechanical models – geometric representation

Analyzing concrete on the mesoscale necessitates the geometric representation of a near-real concrete sample. This includes two steps: (i) generating a realistic aggregate size distribution and (ii) placing the generated aggregates in the target volume. For the generation of a suitable aggregate size distribution either specific sieve lines or analytical distributions, as the Fuller curve, may be used. In most cases, the distribution is generated first and particles placed afterwards.

Generating the aggregate size distribution

Of course a realistic grading of the modeled aggregates is of importance. Due to its simple mathematical description and the ideal packaging achieved, almost all researchers revert to the Fuller curve for their models, e.g., [118, 191, 200, 207, 214, 373], as is done in this work as well. This cumulative distribution function describes the probability P of a particle having a diameter larger than d and reads – in the general form of *Andreasen* [374]:

$$P(d) = \left(\frac{d}{d_{max}} \right)^n \quad (\text{A.1})$$

with $n = 0.5$ suggested by Fuller and d_{max} as the maximum particle diameter considered. As it shows, this is the lowest value in practice since an even stronger reduction of void content leads to poor workability of the fresh concrete [46].

The here employed process to generate the distribution follows closely the algorithm detailed in reference [207]. In a first step, the diameter range of the

particles is divided in equally-spaced “bins”. Each bin i contains finally particles in the range of $[d_i, d_{i+1}]$. Taking the largest diameter in each bin, the volume, $V_{tot,i}$, is determined, which should be filled by the particles within the current bin. After that, an algorithm generates particles with random diameters, as long as $\sum_{j=1}^{N_i} V_j \leq V_{tot,i}$, with N_i being the number of particles in the bin and V_j the volume of the j -th particle in the bin. For the determination of the particle diameter, the following simple relationship can be used [207]:

$$d = d_{i+1} + \eta(d_i - d_{i+1}) \quad (\text{A.2})$$

where η is a random number in the range $[0, 1]$. This equation generates an even distribution of the diameters, but exhibits slight deviations from the volume distribution, especially at smaller diameters. More accurate results are achieved if the exact inverse cumulative distribution function is used, as given in [191] for the Fuller distribution:

$$d = (\eta (d_i^{n-3} - d_{i+1}^{n-3}) + d_{i+1}^{n-3})^{1/(n-3)} \quad (\text{A.3})$$

Here, n is the Fuller exponent. This equation delivers a nearly perfect agreement with the theoretical distribution, see Figure A.1 for a comparison.

Placing the particles

After the distribution has been generated, the particles have to be placed within the volume. To this end, different strategies were developed in the last years. They may be ordered broadly in (a) Take-and-Place (TaP) derivatives⁷⁷ (b) ap-

⁷⁷ Although sometimes imaginatively relabeled: For example, *Zhang et al.* developed a so called “Random walking algorithm” [375]. In this algorithm, aggregates are placed uniformly distributed in an initial placing layer above the considered volume and are subsequently moved into the target domain, thereby simulating the pouring process. By the random moving down action, aggregates are furthermore fortuitously rotated. The direction of the walking is restricted downwards, but free in the horizontal directions and determined by a fixed step length combined with a random number. After the walking action, a collision check is performed and if a collision is detected, the walking action repeated. Although this algorithm is termed “Random walking algorithm” by the authors, it may be well categorized as a TaP approach, where only the process of determining the initial coordinate is replaced by a more complex process, which has more similarity with the physical manufacturing process, than the random coordinate choice.

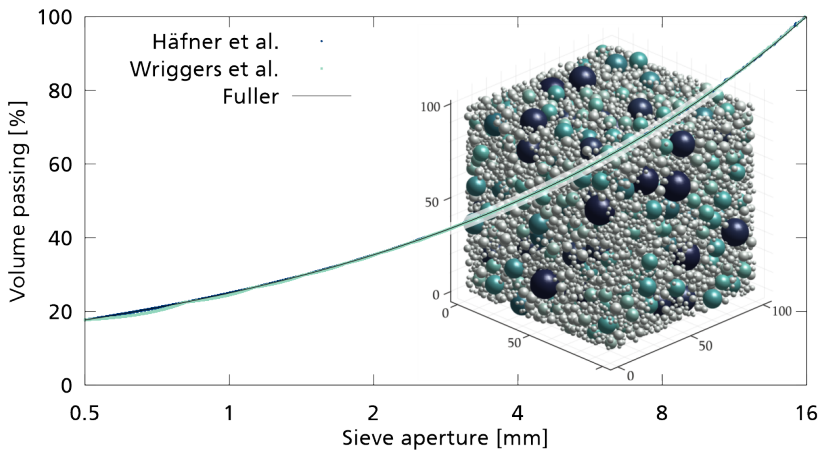


Figure A.1: Comparison of the generated sieve lines with equations (A.2) ("Wriggers et al."), (A.3) ("Häfner et al.") and the Fuller curve, equation (A.1). Each point represents one particle. The distribution fills a cube with edge length of 100 mm, an aggregate volume of 70 % and a diameter range of 0.5 ... 16 mm. The accurate formulation delivers 378 000 particles, the naive one 324 000, a considerable difference of 16 %. Inlet: 3D plot of the particles, though only particles larger than 2 mm are shown.

proaches based on Voronoi diagrams⁷⁸ and (c) completely different approaches, for instance, based on CT images⁷⁹ or distinct singular solutions, e.g., [80].

TaP algorithms are the most widely used approaches, e.g., in [118, 145, 196, 216, 308], likely due to their simplicity and ease of implementation. Especially for spherical aggregates they are highly suited [187]. Therefore, a TaP algorithm is used here as well. Starting with the largest aggregate from the distribution

⁷⁸ E.g., in [59, 195] randomly seeded points in the target volume were used to construct a Voronoi diagram. Aggregates are then formed by shrinking the Voronoi cells, until the specified amount of aggregate volume content is reached. This process has the huge advantage that no intersection checks have to be done and is therefore highly efficient. Furthermore, shapes resembling crushed aggregates are the result. Schutter et al. use Delauny triangles and place aggregates within the triangles [376].

⁷⁹ E.g., reference [202]. Detecting mortar and aggregate phases due to different transmittance, pixels of the different phases were converted to finite elements. A clear advantage is a very realistic representation of the aggregate shape and that no collision checks have to be performed. On the other side, the process is very labor intensive and definitely less efficient as even a naive TaP implementation.

generated in the first step, a random position $\mathbf{x} = \mathbf{x}_{min} + \eta \Delta \mathbf{x}$ for the particles center within the bounds of the target volume is generated and the aggregate placed. \mathbf{x}_{min} is the volume's lower corner and $\Delta \mathbf{x}$ its edge length minus the current particles diameter. After placing, it has to be ensured that the placed aggregate does not overlap with previous arranged aggregates. This may be done by a contact check between the current and all previous put inclusions. If an intersection between the inclusions is found, a new coordinate has to be chosen and the process is repeated until all aggregates are placed. It is obvious that this process includes contact checks of order $\mathcal{O}(N_j^2)$ for each particle (with N_j being the number of already positioned particles), which makes this process very ineffective for a large number of aggregates. Several optimized TaP algorithms have hence be proposed.⁸⁰ Häfner et al. suggested to partition the target volume in subdomains [191]. Once a coordinate is randomly chosen, the intersection check has to be done only with other aggregates of the relevant subdomain, in which the coordinate falls. With a smart division algorithm, the number of potential conflicting aggregates, and correspondingly the number of check operations, can be highly reduced and the TaP algorithm is – even with several thousands of aggregates, such as the example shown in Figure A.1 – highly efficient.

The position of particles is randomly chosen within the bounds of the volume. Strictly speaking, a position is acceptable if the distance e between the center of an inclusion with diameter d and the center of each surrounding particle with diameter d_j fulfills the condition $e \geq 0.5 (d_j + d) \forall j \in N_j$, where N_j is the number of all already placed particles. In real concrete, however, particles are covered with a thin cement layer and do not touch each other. Therefore, e should take a minimum value e_{min} . In the literature, several approaches how to estimate this minimum distance exist, all based on purely pragmatic reasons.⁸¹

⁸⁰ Leite et al., for instance, try to find a new position for the coordinate, once an intersection was found, not by choosing a new random coordinate, but by recourse to a so-called stochastic-heuristic translation and rotation process [175]. The aggregate is slightly moved and translated around its initial coordinate until an intersection-free position is found. Wriggers et al. followed this approach by a similar process [207]. In [173], the standard TaP algorithm is applied only for a certain amount of aggregates to avoid the ineffectiveness for large number of particles. After the initial placing, the model is meshed and the remaining aggregates are generated on basis of the finite elements.

⁸¹ E.g., Schlagen et al. take a ratio of 0.1 of the sum of both particle diameter [174]. This number is based on the theoretical assumption of Hsu, who developed a mathematical model of equally-sized spherical inclusions to estimate the stresses of concrete under shrinkage. Considerations of the packing density in relation to the volume content lead to minimum distance between $0.2 \dots 0.6d$ [377]. The same approach is taken in [144, 208], whereas in

e_{min}	d_{min}	Time in s	part. generated	part. placed	volume in %
0.25	1.0	160	66 603	50 176	93.8
0.25	0.5	2 225	377 893	162 257	90.3
0.1	0.5	434	378 233	356 328	99.2

Table A.1: Comparison of algorithm performance for different fill parameter of a $100 \times 100 \times 100 \text{ mm}^3$ cube. Times have been determined on a standard workstation with one run each only. Only particles with $d_{min} \leq d \leq 16$ are generated. If a particle cannot be placed after 10 000 trials, it is discarded and the next particle will be tried. In case of $d_{min} = 0.5 \text{ mm}$, the standard value of $e_{min} = 0.25 \text{ mm}$ is too restrictive to place all particles successfully.

Actually, the minimum distance between aggregates plays an important role, since it can reduce the available space for placing considerably. Meanwhile, the principal (obvious) relationship between volume ratio and distance between particles has been verified experimentally by *Wittmann* et al. They measured an average distance of 0.56 mm for a low volume content of 30 % and of 0.08 mm for 80 % [378]. *Scrivener* et al. later confirmed an average distance between particles of several hundred microns [63]; *Mindess* et al. gives a range of 75 to 100 μm [46]. In the algorithm developed, a constant input parameter is used as minimum distance, with a default of $e_{min} = 0.25 \text{ mm}$. Table A.1 compares the necessary time and the achieved success to fill a cube with an edge length of 100 mm with an aggregate content of 70 %. Larger voids are handled as particles, which are later subtracted from the remaining matrix.

The resulting algorithm meets all five quality requirements demanded by *Leite* et al. [175]:

1. location of aggregates free from correlation;
2. shape and size of aggregates randomly distributed between limits;
3. spatial distribution should be relatively uniform;
4. size distribution and content should be exactly matched and
5. maximum aggregate content should be comparable to real concrete.

[206] and [207] a variable ratio γ of the smaller of both diameter is used. The initial value for γ is 0.3, but is iteratively reduced if not enough space is available.

A.2 Subcycling

The straightforward implementation of the couplings detailed in Chapter 5, employs the same time step size for the entire model. But often the critical time step Δt_c of the microscale is significantly smaller than that of the macroscale. In order to save computational resources, subcycling in the microscale domain may therefore be desirable. This section introduces the challenges involved with subcycling and discusses the options for the two couplings here presented.

A.2.1 Overview on existing subcycling algorithms

First ideas for subcycling algorithms were developed already in the 1970s. Besides the comparison of explicit-implicit procedures in [379], *Belytschko et al.* suggested an explicit time integration with different time steps for two mesh partitions [380]. The classical term for the first concept (explicit-implicit) is “mixed time integration schemes”, while meanwhile the designation “heterogeneous asynchronous time integration” (HATI) prevails.⁸² In contrast, “multi time integration schemes”, i.e. domains with the same time integration scheme but different time steps, are labeled “homogeneous asynchronous time integration” [343]. It is the latter, which is here synonymously termed as “subcycling”. The multi time integration scheme of *Belytschko et al.* turned out to become the basis of many following developments. Since it highlights the actual problem of subcycling and serves as groundwork for the multi time stepping of the WS coupling as well, it shall be briefly reviewed here.

In the following, the time step of the macro domain, Δt_M , is termed “major time step” in contrast to “minor time step” denoting the time integrator on the micro domain, Δt_m . One major cycle is then the advancement of (n) to $(n + 1)$ with step size Δt_M . Minor cycles fit into the interval between (n) and $(n + 1)$ and are marked as $(n + [j])$, where $[j]$ is a fractional time increment: $[j] = j/p$ and $\Delta t_M = p\Delta t_m$. *Belytschko, Yen, and Mullen* proposed the following decomposed

⁸² See [343], which – besides the thorough theoretical description of the framework – contains an exhaustive review of homogeneous and heterogeneous asynchronous time integrator. Since in this work only homogeneous time integration is of interest, HATI schemes will not be further discussed.

form for the semi-discretized momentum balance of a linear-elastic domain with two different time steps:

$$\begin{bmatrix} \mathbf{M}_M & 0 \\ 0 & \mathbf{M}_m \end{bmatrix} \begin{bmatrix} \ddot{\mathbf{u}}_M \\ \ddot{\mathbf{u}}_m \end{bmatrix} + \begin{bmatrix} \mathbf{K}_M & \mathbf{K}_{Mm} \\ \mathbf{K}_{mM} & \mathbf{K}_m \end{bmatrix} \begin{bmatrix} \mathbf{u}_M \\ \mathbf{u}_m \end{bmatrix} = \begin{bmatrix} \mathbf{R}_M \\ \mathbf{R}_m \end{bmatrix} \quad (\text{A.4})$$

Noting that the major domain should be evaluated only at time step (n) , but the minor domain further at intermediate time steps $(n + [j])$, one may write for the velocities and displacements of the two domains:

$$\dot{\mathbf{u}}_M^{(n+1)} = \Delta t_M \ddot{\mathbf{u}}_M^{(n+1)} + \dot{\mathbf{u}}_M^{(n)}, \quad \dot{\mathbf{u}}_m^{(n+[j+1])} = \Delta t_m \ddot{\mathbf{u}}_m^{(n+[j+1])} + \dot{\mathbf{u}}_m^{(n+[j])} \quad (\text{A.5a})$$

$$\mathbf{u}_M^{(n+1)} = \Delta t_M \dot{\mathbf{u}}_M^{(n+1)} + \mathbf{u}_M^{(n)}, \quad \mathbf{u}_m^{(n+[j+1])} = \Delta t_m \dot{\mathbf{u}}_m^{(n+[j+1])} + \mathbf{u}_m^{(n+[j])} \quad (\text{A.5b})$$

For the sake of readability, the Leapfrog time integration is here not spelled out in detail, hence velocities are written to be updated at full time steps using the same time increment as acceleration and displacement; transferring the findings to the more complex case, is, however, only paperwork. Solving equation (A.5b) for the domain with the major time step $\dot{\mathbf{u}}_M^{(n+1)}$ and inserting the result in equation (A.5a) leads to:

$$\ddot{\mathbf{u}}_M^{(n+1)} = \frac{1}{\Delta t_M^2} \mathbf{u}_M^{(n+1)} - \frac{1}{\Delta t_M^2} \mathbf{u}_M^{(n)} - \frac{1}{\Delta t_M} \dot{\mathbf{u}}_M^{(n)} \quad (\text{A.6a})$$

$$\ddot{\mathbf{u}}_m^{(n+[j+1])} = \frac{1}{\Delta t_m^2} \mathbf{u}_m^{(n+[j+1])} - \frac{1}{\Delta t_m^2} \mathbf{u}_m^{(n+[j])} - \frac{1}{\Delta t_m} \dot{\mathbf{u}}_m^{(n+[j])} \quad (\text{A.6b})$$

Inserting the accelerations and displacements at (n) , respectively $(n + [j])$, in equation (A.4) and solving for \mathbf{u} yields finally:

$$\begin{aligned} \mathbf{u}_M^{(n+1)} &= \mathbf{u}_M^{(n)} + \Delta t_M \dot{\mathbf{u}}_M^{(n)} \\ &\quad + \Delta t_M^2 \mathbf{M}_M^{-1} \left(\mathbf{R}_M - \mathbf{K}_M \mathbf{u}_M^{(n)} - \mathbf{K}_{Mm} \mathbf{u}_m^{(n)} \right) \end{aligned} \quad (\text{A.7a})$$

$$\begin{aligned} \mathbf{u}_m^{(n+[j+1])} &= \mathbf{u}_m^{(n+[j])} + \Delta t_m \dot{\mathbf{u}}_m^{(n+[j])} \\ &\quad + \Delta t_m^2 \mathbf{M}_m^{-1} \left(\mathbf{R}_m - \mathbf{K}_{mM} \mathbf{u}_M^{(n+[j])} - \mathbf{K}_m \mathbf{u}_m^{(n+[j])} \right) \end{aligned} \quad (\text{A.7b})$$

It is obvious that equation (A.7a) can be updated at each major cycle (n) independently of equation (A.7b). In contrast, equation (A.7b) contains the position

of the *macro* nodes in Ω_M , $\mathbf{u}_M^{(n+[j])}$, at *minor* cycles $(n + [j])$, which are generally not evaluated at these points in time. The main issue is therefore to provide values for $\mathbf{u}_M^{(n+[j])}$, for which different possibilities are found in literature.

Belytschko et al. interpolate the values $\mathbf{u}_M^{(n+[j])}$ between two major cycles. They found that only a linear interpolation between the positions yields stable results (i.e. $\dot{\mathbf{u}}_M = \text{const}$ between two major cycles) [380]. Later they refined their algorithm in order to enhance implementational aspects and stability [381]. In this latter work, they propose to keep the acceleration at the interface nodes constant, instead of the velocity. Meanwhile, *Smolinski* had developed a subcycling algorithm for a system of parabolic differential equations and proved the stability of this scheme [383]. In further works, the author applied his algorithm to second-order systems [382, 384]. In this scheme, accelerations for the interface nodes for cycles $(n + [j])$ have to be known. The algorithm limits the ratio $\Delta t_M / \Delta t_m$ to an even integer multiple and swaps the sign of the interface accelerations in each minor update, which at the end leads to constant velocities. A variable-time integration scheme based on the conservation form of the equation of motion is presented in [385]. Again, nodes and elements are partitioned in different groups and the equations are solved for each group individually, very similar to reference [32], with constant velocities at the interface.

The algorithms mentioned so far have in common that the ratio between large and small time steps of adjacent nodes has to be whole-numbered and that they assume matching meshes between the domains. An exception to the first condition was developed in [386]. The authors presented a subcycle algorithm for hyperbolic problems based on individual nodal and elemental “clocks”, which trigger an element or a node to update, once its unique time step has been reached. The “clock” concept was later picked up in [381], where the partition of elements and groups was not longer determined by spatial considerations but by the time step solely. If, however, a node belongs to elements of different groups, it remained mandatory that the time step ratio between these groups is again an integer. For all works cited previously, matching meshes between the domains are implied, although the employment of non-boolean coupling matrices in connection with global LM allow for disparate meshes. Hence, LM couplings are a convenient tool for homogeneous (and surely as well heterogeneous) asynchronous time integration – either with global, or, as in [337], with local LM, connecting the domains to a “common-refinement-based-interface”.

Another point to be considered is the order of updates. *Daniel* classifies the above cited algorithms with regard to the update order in three different categories or

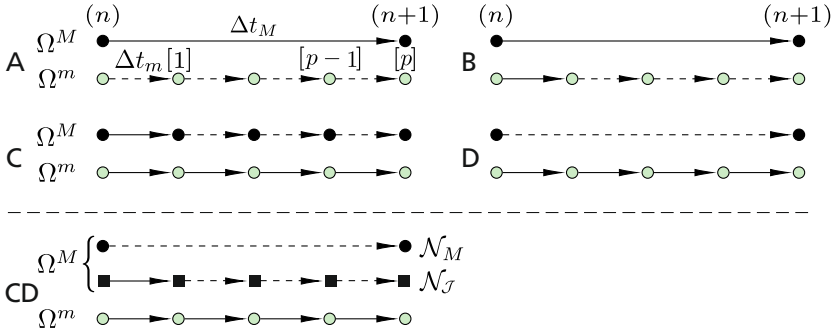


Figure A.2: Different interpretations of explicit-explicit subcycling algorithms (A to C acc. to Daniel [387]). Dashed lines denote steps performed after the steps with continuous lines. Only scheme “B” allows a full parallel solution of both scales. See text for further explanation.

“interpretations”, as shown in Figure A.2 [387]. Algorithms of type “A” update the large domain first and the smaller domain is updated subsequently with the respective minor time step, until the major time has been reached. An example of this type of algorithm is the above mentioned algorithm of Belytschko et al. [380]. Type “B” is a slight improvement since both domains are simultaneously updated, each with its respective time step, and the small domain is subsequently updated for the rest of the major time step. In both algorithms, the interface nodes between Ω_M and Ω_m are assumed to have values dependent on an interpolation between the values of Ω_M at time $t^{(n)}$ and $t^{(n+1)}$ – a major premise taken by almost all authors.

Algorithms of type “C” update the nodes of both domains always with the small time step. However, the *elements* of the large domain are updated only each major time step and values of interface nodes are kept constant for the next subcycles. This algorithm has been criticized in [387] to be unstable and is mentioned here for completeness only.

Algorithms of type “B” are mostly used in current multi step schemes. Yet they have the grave disadvantage, that the macroscale determines the end time $t^{(n+1)}$ of the subcycling and the models may not choose an appropriate time step by their own stability criteria. Indeed, even modern HATI-schemes rely on the knowledge of the number of substeps p in advance. Constant Δt_m are

encountered frequently in linear or moderate non-linear problems, but cannot be presupposed in highly-nonlinear cases and automatic time stepping is mandatory. But then it is very unlikely that $\sum_{j=1}^p \Delta t_{m,j} = \Delta t_M$. Here, it is assumed that the minor time steps are *not* known in advance and that they are allowed to change during a major time step. Then a different update order is necessary. Before discussing this aspect, however, the underlying equations shall be modified first for the case of multi time integration.

A.2.2 Proposed subcycling algorithm for the WS coupling

Although the case of linear elasticity, as written in equation (A.4), elucidates the principle of subcycling algorithms, equations (5.22) and (5.23) are reverted to now for the more general case and the proposed decomposition in a macro and a micro domain. For the subcycling, equation (5.22) is written for cycle (n):

$$\begin{bmatrix} \mathbf{M}_M & \mathbf{0} \\ \mathbf{0} & \mathbf{M}_{\mathcal{J}} \end{bmatrix} \begin{bmatrix} \ddot{\mathbf{u}}_M^{(n)} \\ \ddot{\mathbf{u}}_{\mathcal{J}}^{(n)} \end{bmatrix} = \begin{bmatrix} \mathbf{R}_M^{(n)} \\ \mathbf{R}_{\mathcal{J}}^{(n)} \end{bmatrix} - \begin{bmatrix} \mathbf{F}_M^{(n)} \\ \mathbf{F}_{\mathcal{J}}^{M^{(n)}} \end{bmatrix} - \begin{bmatrix} \mathbf{0} \\ \tilde{\mathbf{F}}_{\mathcal{J}}^{m^{(n)}} \end{bmatrix} \quad (\text{A.8})$$

and equation (5.23) for minor cycle ($n + [j]$):

$$\begin{aligned} \dot{\mathbf{u}}_m^{(n+[j+1/2])} &= \mathbf{M}_m^{-1} \left(\mathbf{R}_m^{(n+[j])} - \mathbf{F}_m^{(n+[j])} \right) \Delta t_{m_h} + \dot{\mathbf{u}}_m^{(n+[j-1/2])} \\ \dot{\mathbf{u}}_i^{(n+[j])} &= \varphi \left(\dot{\mathbf{u}}_{\mathcal{J}}^{(n+[j]-1)}, \mathbf{x}_i^{(n+[j]-1)} \right) \end{aligned} \quad (\text{A.9})$$

Apparently, equation (A.8) can be updated at each major cycle independently of the minor domain. $\tilde{\mathbf{F}}_{\mathcal{J}}^{m^{(n)}}$ is available because the minor domain is updated at the major cycles as well. On the other hand, the minor updates (equation (A.9)) need the velocities of the macro interface nodes, $\mathcal{N}_{\mathcal{J}}$, at ($n + [j + 1/2]$), where the latter designates the half time step of the Leapfrog scheme following the minor step ($n + [j]$). A simple interpolation is sufficient if update order B is used. Then Ω_M is advanced by $p\Delta t_m$ and the interface velocity at the micro domain simply becomes

$$\dot{\mathbf{u}}_i^{(n+[j+1/2])} = \varphi \left(\dot{\mathbf{u}}_{\mathcal{J}}^*, \mathbf{x}_i^{(n+[j]-1)} \right) \quad (\text{A.10})$$

with

$$\dot{\mathbf{u}}_{\mathcal{J}}^* = (1 - [j])\dot{\mathbf{u}}_{\mathcal{J}}^{(n-1/2)} + \frac{[j]}{p}\dot{\mathbf{u}}_{\mathcal{J}}^{(n+1/2)} \quad (\text{A.11})$$

In this case the expression for the internal forces of the virtual elements in line two of equation (A.8) has to be modified to be (compare with equation (5.29)):

$$\tilde{\mathbf{F}}_{\mathcal{J}}^{m(n)} = \frac{1}{\Delta t_M} \sum_{j=1}^p \varepsilon \tilde{\mathbf{F}}_{\mathcal{J}}^{m(n-1+[j])} \Delta t_m^{(n-1+[j])} = \frac{\tilde{\mathbf{I}}_{\mathcal{J}}^{m(n)}}{\Delta t_M} \quad (\text{A.12})$$

Here, the summation expression gives the *momentum*, $\tilde{\mathbf{I}}_{\mathcal{J}}^{m(n)}$, of the averaged forces over the whole macro cycle and ensures momentum balance between the domains. By division with the major time step, a force is obtained at major cycle (n) , which can be added to the macro interface nodes. But, as explained above – this order presupposes constant and foreknown minor step sizes. If this is not the case, one can only update Ω_m first. Only when this domain has completed one major cycle, Ω_M is updated as well – an update order sketched as “D” in Figure A.2. Here, the sum of (potentially non-constant) minor time steps determines the final major time step, however, by guaranteeing that the latter is bound by the critical time step $\Delta t_{M,c}$.

But how should $\dot{\mathbf{u}}_{\mathcal{J}}^{(n+[j+1/2])}$ now be determined for application at the micro domain interface? Reaching major step (n) in the leapfrog-scheme presupposes the velocities at $(n+1/2)$. That means that macro velocities at a future point in time are available for the micro domain if $(n+[j+1/2]) < (n+1/2)$. However, $(n+1/2)$ has been determined in the *last* major cycle with $\Delta t_m^{(n-1)}$. Hence, there is no guarantee that this value falls exactly in the half interval of the *current* major step! Courageously ignoring the potential mismatch, one option now is simply to use these interface velocities. Thereby the two domains can be handled completely independent, which is an advantage from an implementational point of view since communication between the scales can then be reduced to the major cycle. But even then – how should the velocities $\dot{\mathbf{u}}_i^{(n+[j+1/2])}$ be interpolated without knowing p beforehand? Should one guess p (which might surely be often possible) or should one keep $\dot{\mathbf{u}}_i$ simply constant over the macro time step? The first option is as dissatisfying as the latter, which leads to notable discontinuities in the interface velocities between the last minor of a major and the following first minor step. Both options may work in specific situations, but are surely prone to inaccuracy and instability.

A better update scheme is displayed in Figure A.2 as “CD”. Here, the micro domain and the macro interface nodes are updated each subcycle $[j]$. Macro *interior* nodes and elements are updated each major step only, as shown in Figure A.3. This algorithm does not necessitate interpolations and the interface

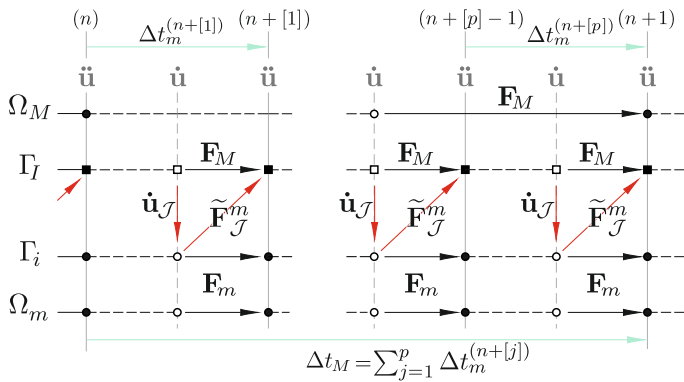


Figure A.3: Subcycling update scheme CD: Macro interface nodes are updated each minor time step as well.

conditions are always accurately fulfilled.⁸³ As a serious disadvantage of this scheme, one has to mention the fact that it necessitates the consecutive solution of both domains. Only after Ω_m has reached the full cycle, Ω_M can be updated as well, since only then the real time step is known. Theoretically, this scheme has only an advantage if the solution of the macro domain needs more time than the (parallel) solution of the micro domain; a condition which is likely only for very large macro domains. Otherwise the scheme should be even slower than the one without subcycling.

A.2.3 Subcycling of the LM approach

Subcycling for the LM coupling expressed in the form originally proposed by *Gravouil et al.*, relies again on the linear interpolation of the velocities and the LM of the major time step, which was shown to deliver a stable time integration

⁸³ As *Belytschko, Yen, and Mullen* remarked in [380], this is – in the strict sense – only correct for a subcycle number less than two, since in each further subcycle, the nodes in the major domain that are connected to elements with interface nodes would be affected by the updated velocities of the interface nodes. Thus the change of the macro interface velocity propagates theoretically with each minor cycle by one element further into the macro domain. In test simulations, however, the loss of accuracy when treating only the interface nodes has been found to be negligible.

Algorithm 4 Subcycling procedure; detailed is one major step from (n) to $(n+1)$ with $[p]$ subcycles. $\mathcal{E}_{\mathcal{J}}$ are the macro elements attached to the interface nodes $\mathcal{N}_{\mathcal{J}}$. Refer to Algorithm 2 on Page 126 for a detailed view of one standard cycle and an expansion of operations, which are here abbreviated by “Solve domain”.

Micro	Macro
while $t + [j]\Delta t_m \leq t + \Delta t_M$ do Receive $\dot{\mathbf{u}}_{\mathcal{J}}^{(n+[j]/2)}$ Interpolate BC, eq. (5.26) Solve domain for $(n + [j])$ for $\forall \tilde{\mathcal{E}}$ do Update matrices Determine $\tilde{\boldsymbol{\sigma}}$ Calculate $\tilde{\mathbf{F}}_I^m$ end for Send $\tilde{\mathbf{F}}_I^m$ end while	Send $\dot{\mathbf{u}}_{\mathcal{J}}^{(n+[1]/2)}$ for $\forall \mathcal{E}_{\mathcal{J}}$ do Calculate $\mathbf{F}_{\mathcal{J}}^M$ end for Receive $\tilde{\mathbf{F}}_I^m$ With $\Delta t_M = \Delta t_m$: for $\forall \mathcal{N}_{\mathcal{J}}$ do update $\ddot{\mathbf{u}}_{\mathcal{J}}, \dot{\mathbf{u}}_{\mathcal{J}}, \mathbf{u}_{\mathcal{J}}$ end for With $\Delta t_M = [p]\Delta t_m$: Solve domain, except $\mathcal{N}_{\mathcal{J}}$

for arbitrary Newmark parameter [334]. The subcycling can be included simply by modifying matrix \mathbf{H} (Page 114) to be:

$$\hat{\mathbf{H}} = \Delta t_M \mathbf{C}_M \mathbf{M}_M^{-1} \mathbf{C}_M^{\top} + \Delta t_m \mathbf{C}_m \mathbf{M}_m^{-1} \mathbf{C}_m^{\top} \quad (\text{A.13})$$

Furthermore, \mathbf{W} and $\boldsymbol{\lambda}$ have to be replaced by

$$\mathbf{W}^{(n+[j+1])} = \mathbf{W}^{(n)} (1 - [j]) + [j] \mathbf{W}^{(n+1)} \quad (\text{A.14a})$$

$$\boldsymbol{\lambda}^{(n+[j+1])} = \boldsymbol{\lambda}^{(n)} (1 - [j]) + [j] \boldsymbol{\lambda}^{(n+1)} \quad (\text{A.14b})$$

and equation 5.12 is modified to read

$$\hat{\mathbf{H}} \boldsymbol{\lambda}^{(n+[j+1])} = - \left(\mathbf{C}_m \mathbf{W}_m^{(n+[j+1])} + \mathbf{C}_M \mathbf{W}_M^{(n+[j+1])} \right) \quad (\text{A.15})$$

The linking forces become $\mathbf{F}_l^M = \mathbf{C}_M \boldsymbol{\lambda}^{(n+1)}$ and $\mathbf{F}_l^m = \mathbf{C}_m \boldsymbol{\lambda}^{(n+[j+1])}$. Note, that the interface operator depends on the time step of *both* scales (contained in $\hat{\mathbf{H}}$, equation (A.13)). Although one may define $\hat{\mathbf{H}} = \Delta t_M \hat{\mathbf{H}}_M + \Delta t_m \hat{\mathbf{H}}_m$, with the constant matrices $\hat{\mathbf{H}}_M$ and $\hat{\mathbf{H}}_m$, the solution of the global interface problem has to be done at each minor cycle. Exact equilibrium is achieved of course only at major time steps.⁸⁴ As a last remark, it should be noted that the approach necessitates the solution of the macro domain first, in order to allow the interpolation of the interface kinematic quantities. Consequently, this presupposes an update scheme type B. The latter allows for a full parallel solution of both domains, but again faces the problem of pre-determining the time steps of the minor scale.

A.2.4 Stability of subcycling

Generally, stability proofs are based on spectral stability analysis or by showing that the physical energy is bounded. Whereas the first approach has been applied to mixed time integration and first-order schemes, e.g., [383, 388], it is very sophisticated and energy considerations are preferred for multi time, second-order and nonlinear cases [38, 334, 343]. A combination of spectral stability analysis together with an energy consideration is applied to a multi time stepping second-order scheme in [384]. Here, a Newmark- β time integration scheme is considered. For the staggered coupling, neither approach can be applied due to the involved complexity and the fact that no energy functional exists. Nevertheless, without giving a detailed proof, *Belytschko* et al. argued that the stability of their algorithm is most likely achieved if each domain respects its own standard stability criterion [381]. Since (apart from the order of updates in which the nodal and elemental variables is performed) the here proposed scheme is essentially identical to the algorithm in [381] with constant interface velocities, one may assume that the same standard criteria will (at least in practical situations⁸⁵) lead to a comparable stability. However, one major difference to these algorithms is the fact, that not only the time scale of the domains exhibits

⁸⁴ Later, versions satisfying the equilibrium at minor steps have been developed. See [343] and references within.

⁸⁵ Unfortunately, *Daniel* later showed that the algorithm of *Belytschko* et al. is actually stable only in a statistical sense; that is, cases where instabilities occur theoretically exist. Yet since the occurrence of these cases decrease with increasing number of DOF of nodal groups with different time steps, they are unlikely to be encountered in practical calculations and one should presume "practical" stability for real systems [389, 390].

disparity, but that non-matching interfaces are present here as well. Especially in case of interfaces parallel to the wave propagation, the emergence of instabilities is observed. Although not initiated, they are proliferated by active subcycling.

A.3 Cement reaction

Chemical name	Chemical formula	Shorthand notation	Weight in %
Tricalcium silicate	3CaO SiO ₂	C3S	55
Dicalcium silicate	2CaO SiO ₂	C2S	18
Tricalcium aluminate	3CaO Al ₂ O ₃	C3A	10
Tetracalcium aluminoferrite	4CaO Al ₂ O ₃ Fe ₂ O ₃	C4AF	8
Calcium sulfate dihydrate (gypsum)	CaSO ₄ 2H ₂ O	CSH ₂	6

A.4 Strain rate enhancement formulas

Different proposals have been made for the strain rate enhancement scaling function. The version proposed in [104] and implemented in Autodyn reads:

$$F_R^{c,t}(\dot{\epsilon}_{eff}) = \left(\frac{\dot{\epsilon}_{eff}}{\dot{\epsilon}_0^{c,t}} \right)^{\beta_{c,t}} \quad (\text{A.16})$$

Symbols 'c' and 't' designate the respective variable for compression or tension. The exponent is defined as

$$\beta_c = \frac{1}{5 + 3f_c/4}, \quad \beta_t = \frac{1}{10 + f_c/2} \quad (\text{A.17})$$

with f_c in MPa. Later, the second, steeper branch, as observed in the data, has been proposed in [245]:

$$F_R^{c,t}(\dot{\epsilon}_{eff}) = \begin{cases} \left(\frac{\dot{\epsilon}_{eff}}{\dot{\epsilon}_0^{c,t}} \right)^{\alpha_{c,t}\beta_{c,t}} & \dot{\epsilon}_{eff} \leq \dot{\epsilon}_{eff}^{c,t} \\ \xi_{c,t} \sqrt[3]{\dot{\epsilon}_{eff}} & \dot{\epsilon}_{eff} > \dot{\epsilon}_{eff}^{c,t} \end{cases} \quad (A.18)$$

This version has been implemented in LS-Dyna [246]. There, the default values for $\beta_{c,t}$ are given as

$$\beta_c = \frac{4}{20 + 3f_c}, \quad \beta_t = \frac{2}{20 + f_c}, \quad \alpha_c = \alpha_t = 1 \quad (A.19)$$

However, these definitions actually differ from the ones found in the CEB Bulletin, where one finds:⁸⁶

$$\begin{aligned} \beta_c &= \frac{1}{5 + 9f_c/10}, & \beta_t &= \frac{1}{10 + 6f_c/10} \\ \alpha_c &= 1.026, & \alpha_t &= 1.016 \\ \log \xi_c &= 6.156\beta_c - 2, & \log \xi_t &= 7.112\beta_t - 2.33 \\ \dot{\epsilon}_0^c &= 30 \times 10^{-6} \text{1/s}, & \dot{\epsilon}_0^t &= 3 \times 10^{-6} \text{1/s} \end{aligned}$$

$\dot{\epsilon}_p^{c,t}$ is given to be 30 1/s in [136]. These values have been implemented in the SOPHIA Version of the RHT model.

For the tensile regime, however, it was reported that the version detailed above agrees well with *theoretic* models [134], but is too high with respect to *experimental* data for tensile loading. Therefore, *Malvar* et al. modified the function to read (tension only):

$$F_R^t(\dot{\epsilon}) = \begin{cases} \left(\frac{\dot{\epsilon}}{\dot{\epsilon}_0^t} \right)^{\beta_t^M} & \dot{\epsilon}_p \leq 1 \\ \xi_t^M \sqrt[3]{\frac{\dot{\epsilon}}{\dot{\epsilon}_0^t}} & \dot{\epsilon}_p > 1 \end{cases} \quad (A.21)$$

⁸⁶ $\xi_{c,t}$ has to be determined such that an intersection of the two functions in equation (A.18) at $\dot{\epsilon}_{eff}^{c,t}$ is ensured, from which follows that $\xi = (1/\dot{\epsilon}_p^{c,t})^{(1/3)}(\dot{\epsilon}_0^{c,t}/\dot{\epsilon}_0^{c,t})^{\beta_{c,t}}$. Originally, this variable was expressed in the 187 CEB Bulletin to be $\log \xi_c = 6\beta_c - 0.492$ and $\log \xi_t = 7\beta_t - 0.492$ together with $\dot{\epsilon}_{eff}^{c,t} = 30 \text{ 1/s}$. In this form it has been published in [245], however, with a slight inconsistency. For these values, the first line in equation (A.18) has to be modified to read $(\dot{\epsilon}_{eff}/\dot{\epsilon}_0^{c,t})^{a_{c,t}\beta_{c,t}}$ with the factor $a_c = 1.026$ and $a_t = 1.01$. With $a_{c,t} = 1$, as written above, the intersection of the two branches would be at $\dot{\epsilon}_{eff}^{c,t} = 28.7948 \text{ 1/s}$.

$$\begin{aligned}\beta_t^M &= 1/(1 + 8f_c/10) \\ \log \xi_t^M &= 6\beta_t^M - 2 \\ \dot{\varepsilon}_0^t &= 1 \times 10^{-6} 1/s\end{aligned}$$

As a further alternative, Hao et al. proposed the following fit for tensile loading [137]:

$$F_R^t(\dot{\varepsilon}) = \begin{cases} 1.0 & \dot{\varepsilon} < 10^{-4} \\ 2.06 + 0.26 \log \dot{\varepsilon} & 10^{-4} \leq \dot{\varepsilon} < 1 \\ 2.06 + 2.0 \log \dot{\varepsilon} & \dot{\varepsilon} > 1 \end{cases} \quad (\text{A.23})$$

In the simulations shown in this thesis, the compressive branch of the CEB formulation and the Malvar formula for tension is used. None of these formulations limit the DIF with respect to high strain rates. Although no data exist for higher rates (and it is debatable whether it is even possible to measure such data for tension) in this work the DIF_t is limited to $F_{R,max}^t = 15$, following [105] and the general recommendation to limit the DIF_t in [145]. Otherwise, very high-rates in the fine discretization lead to an unnatural high strength of the matrix and prevents damage. The role of the rate enhancement and a proper idealization in the plasticity algorithm certainly needs more research.

Figure A.4 details the available data for the DIF together with the mentioned fit functions.

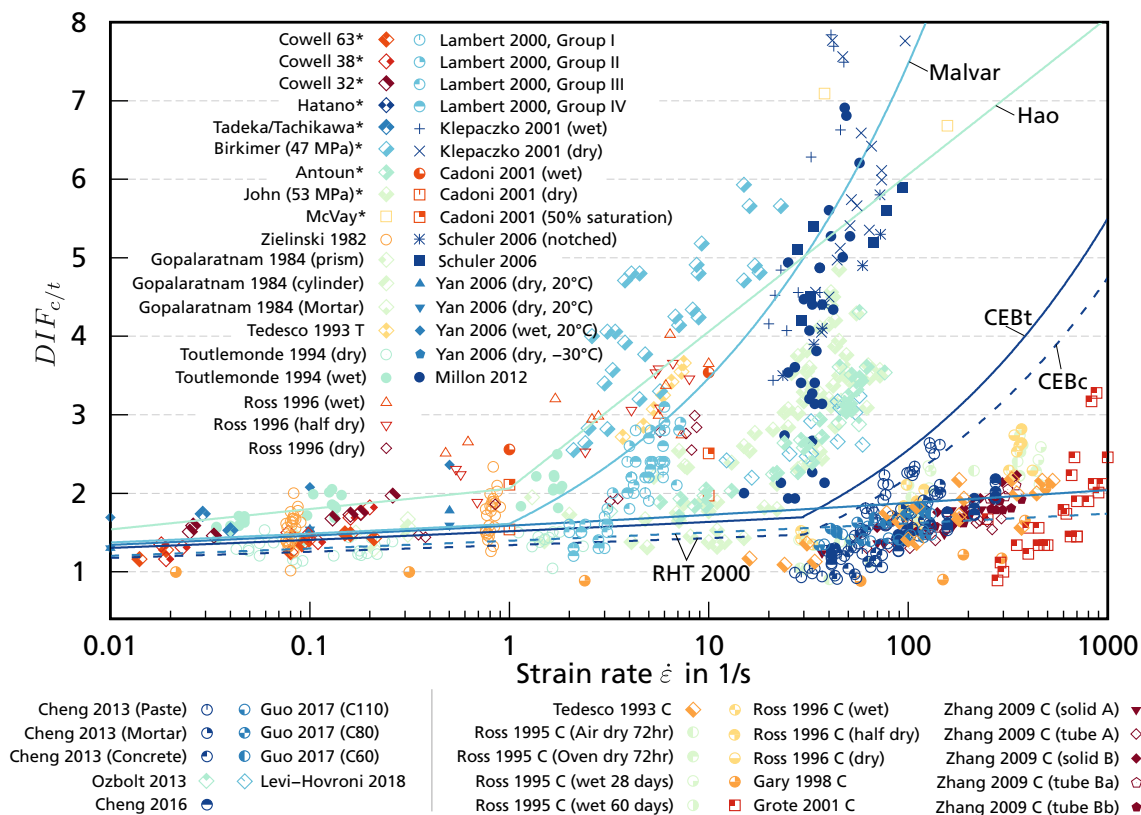


Figure A.4: Experimental values from literature for tensile and compressive (marked by "C" in the legend) strength increase. Only DIF values below 8 are shown. The only data set featuring higher values is the one in [391], these data points can be deciphered in the overview plot, Figure 3.7 on Page 40. Data marked with an asterisk are taken from the review paper [134] and referenced therein. All other data are from [107, 112, 117, 123, 125, 126, 132–135, 147, 149, 273, 391–398].

A.5 Loading conditions of the validation examples

The following figures document the applied velocity, respectively pressure histories used for the simulation of the validation examples in Chapter 4.

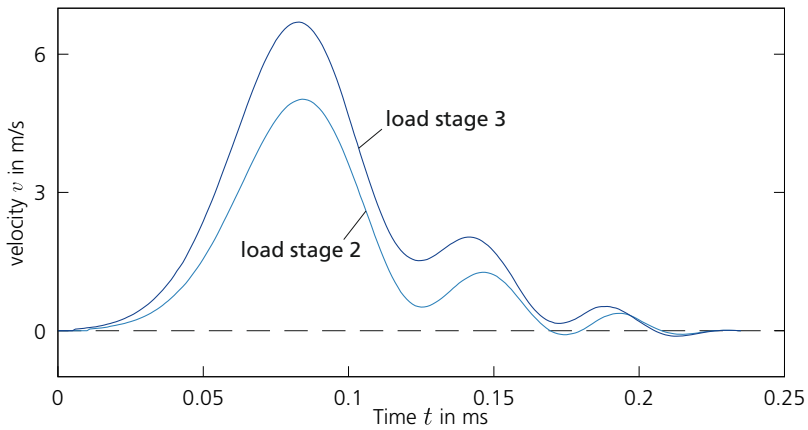


Figure A.5: Velocity signal used as input for the SHB simulations in Section 4.3.2 as derived from the strain signals in the incident bar.

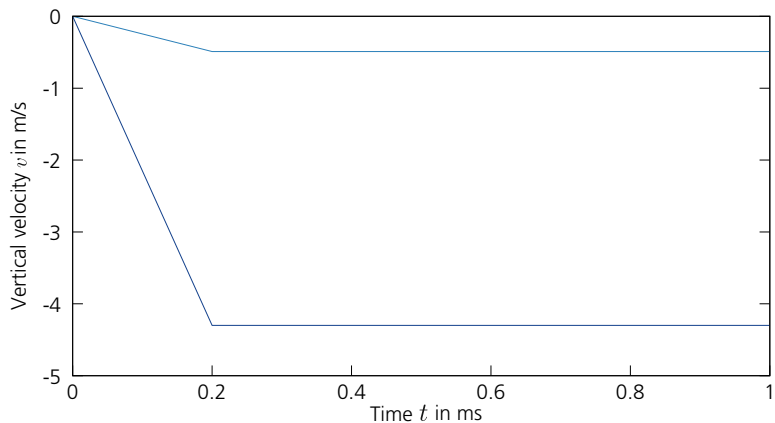


Figure A.6: Velocity applied at the bottom nodes of the steel rod in the simulation of the compact tension tests, Section 4.3.1.

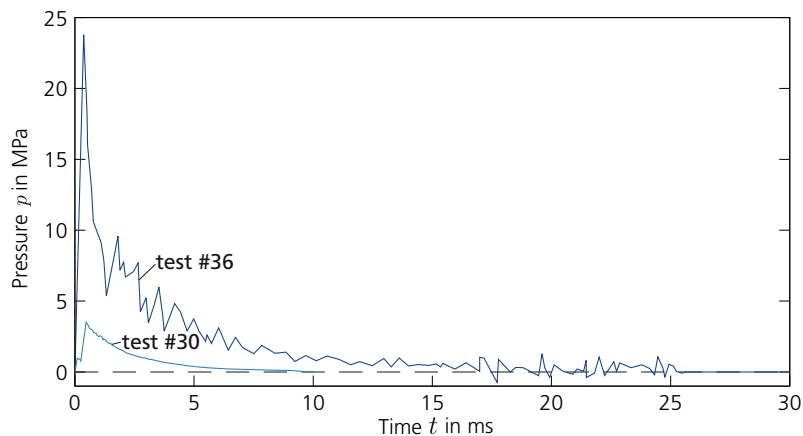


Figure A.7: Pressure histories for the shock tube validation example, Section 4.3.3. The data has been digitized from figures given in [9, 282].

A.6 Material parameter for the mesomechanical simulations within this work

A.6.1 RHT model parameter for mortar matrix

The mortar matrix is a composite of the hardened cement paste with fine aggregates, i.e. sand and additives. Generally, one may assume that mortar behaves similarly as concrete and it seems therefore to be a justified hypothesis to start with the standard parameter set for concrete as basis. Literature reporting mortar properties is not too abundantly and often only some parameter are given. Furthermore, the receipts vary and the experimental scatter is high. The following overview mentions only deviating parameters from the standard concrete model as given in [248].

Elastic properties

Several works mention the elastic properties of mortar, however with very high scatter. Especially between mechanical and ultrasonic testing large differences appear, see Figure A.8. Values have been taken more close to the ultrasonic measurements to be:

$$E = 24.3 \text{ GPa} \quad G = 10.3 \text{ GPa}$$

it follows

$$\nu = 0.179 \quad K = 12.6 \text{ GPa}$$

The density was taken as average from [104, 399, 402] to be

$$\rho_0 = 2.08 \text{ g/cm}^3$$

These values deliver a bulk speed of sound of $c_{b,0} = 2461 \text{ m/s}$.

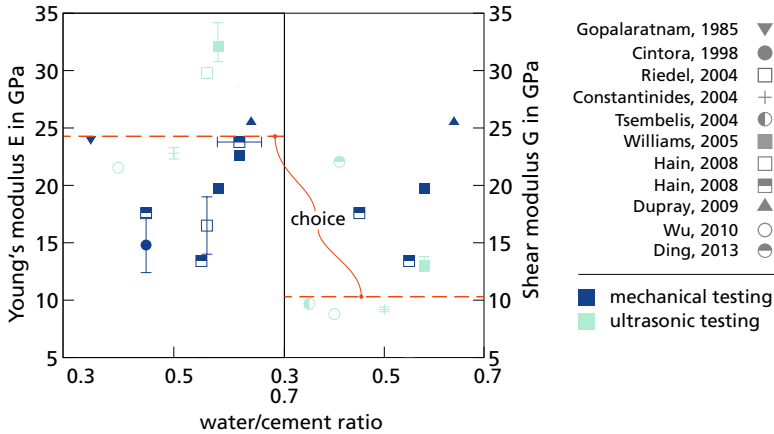


Figure A.8: Young's and shear modulus. Values from literature [94, 99, 104, 170, 193, 264, 265, 399–401] and actual choice.

Strength parameter

Uniaxial compressive strength Values for the uniaxial compressive strength of mortar as mentioned in literature are shown in Figure A.9. Again, the scatter is very high. With increasing w/c a reduction of f_c is observable. A value of

$$f_c = 48.0 \text{ MPa}$$

is chosen, which might be a justified choice for w/c values in the plotted range.

Uniaxial tensile strength The uniaxial tensile strength is plotted in Figure A.10. The choice of $f_t = 3.5 \text{ MPa}$ is on the upper range of the available data, but still well supported. With this value:

$$\hat{f}_t = 0.073$$

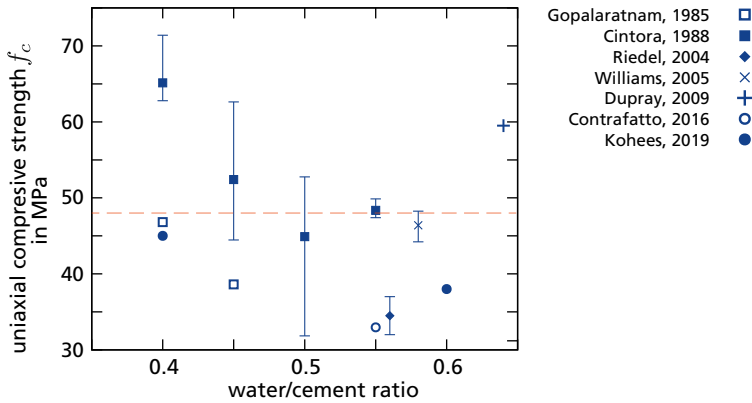


Figure A.9: Literature values for mortar compressive strength [94, 99, 104, 204, 264, 265, 403].

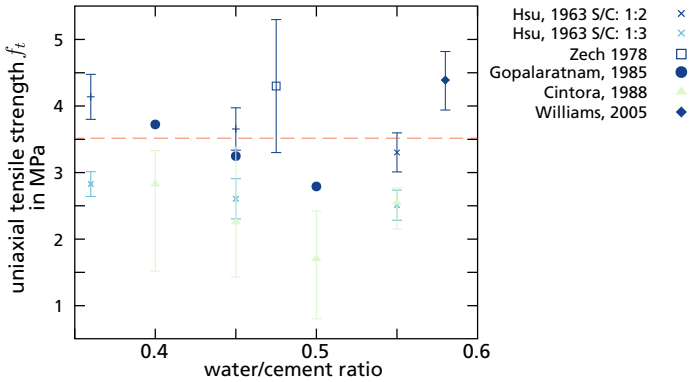


Figure A.10: Literature values for mortar uniaxial tensile strength [68, 94, 264, 265, 404].

Compressive meridian Only few data exits for the compressive meridian data, especially towards higher pressure. Figure A.11 shows the available data, along with data for concrete. The failure meridian based on the standard C30/37 pa-

parameter set is plotted as dashed line ("RHT C30"). A new fit has been determined by a nonlinear Levenberg-Marquardt fit. The resulting parameter are:

$$A = 2.13$$

$$n = 0.63$$

and fit well for both, the concrete data and the mortar values.

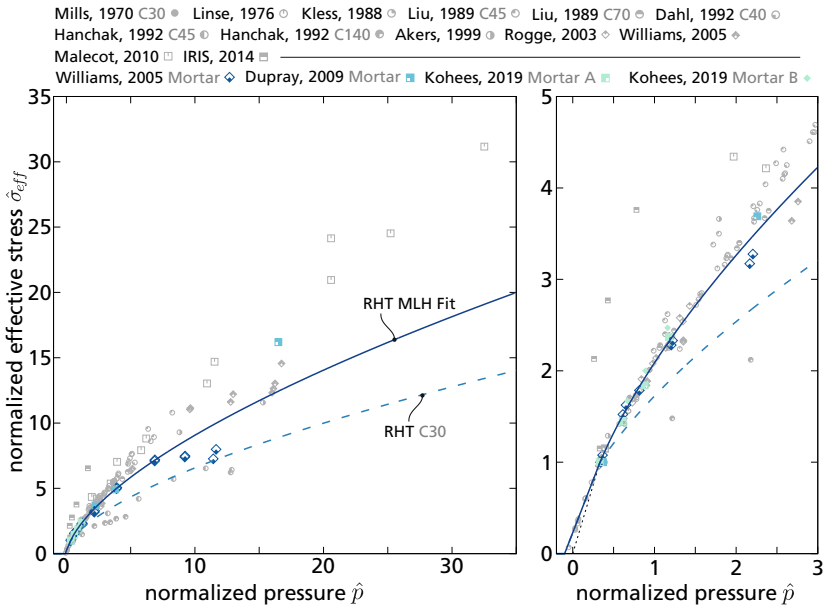


Figure A.11: Compressive meridian of the RHT model together with literature values for mortar (colored symbols) and concrete (grey symbols) strength. Line "RHT C30" marks the meridian with the standard parameter. A new fit ("RHT MLH Fit") is here proposed, which is well suited for concrete *and* mortar. Data for concrete is compiled and referenced in [405], data for mortar is from [94, 99, 403].

Additional parameter for the Rankine criterion

The only additional value for the Rankine criterion is the fracture energy. Scatter for this value is again extraordinarily high, as illustrated by the two test series from *Cintora* and *Gopalaratnam et al.*, plotted in Figure A.12 together with a least square fit. The distribution follows roughly a Weibull distribution (right view) and has an arithmetic value of $\overline{G_F} = 75$ N/m (as compared to 112 N/m for standard concrete [84]). However, as elaborated on in Section 4.2.3, this value is not necessarily the correct one to be applied to the individual elements. Rather the total energy dissipated in a simulation comparable to the standard testing procedure should yield the average value. For the individual elements, a much smaller value, here taken to be $G_F = 30$ N/m, is appropriate and yields satisfying results.

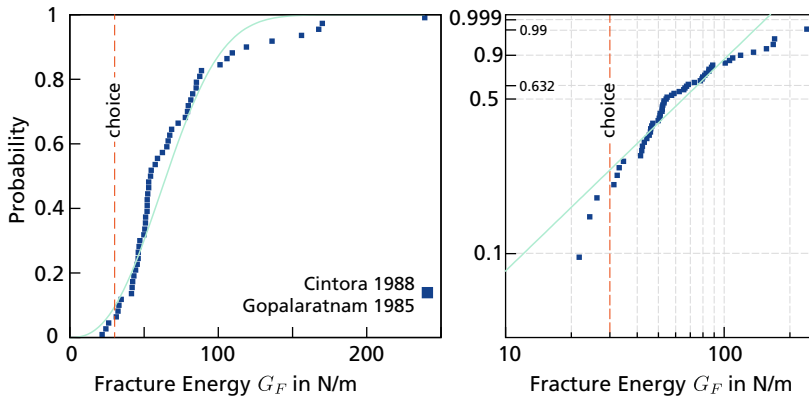


Figure A.12: Literature values for mortar fracture energy plotted as cumulative probability plot. Right: Plot with Weibull scaling. Data from [264, 265].

The complete parameter set for mortar is listed in Table A.2:

Parameter	Symbol	Value	Unit
Shear modulus	G	10.3	GPa
Bulk modulus	K	12.6	GPa
Initial Density	ρ_0	2.08	g/cm ³
Cylindrical compressive strength	f_c	48.0	MPa
Normalized tensile strength	\hat{f}_t	0.073	–
Fracture energy	G_F	30	N/m
Failure surface parameter	A	2.13	–
Failure surface exponent	n	0.63	–
Triaxiality parameter	Q_0	0.6805	–
Brittle-to-ductile parameter	B	0.0105	–
Elastic to plastic strain factor	Ψ_h	1.36	–
Onset on hardening compression	$g_{c,0}$	0.627	–
Onset on hardening tension	$g_{t,0}$	1.0	–
Residual strength surface parameter	A_f	2.13	–
Residual strength surface exponent	n_f	0.63	–
Damage parameter	D_1	0.04	–
Damage exponent	D_2	1.0	–
Minimum strain to failure	ε_{pl}^m	0.01	–

Table A.2: Summary of the RHT material parameter for mortar.

A.6.2 Aggregate material model

Aggregates are herein considered to represent an intrusive igneous rock, such as granite. Most of the parameter have been taken from concretes standard set, except a much higher compressive strength, fracture energy and fit parameter for the failure surface. The values are documented in Table A.3. A linear failure law (refer to Figure 4.4) was employed for the aggregates and in all cases (compression and tension) the CEB formulation for strain rate enhancement used. Furthermore, the simple cube-root regularization was applied in aggregate elements. As the

work of *Snozzi et al.* shows, the material parameter of the aggregates are – in tensile dominated failure – of inferior importance [142].

Parameter	Symbol	Value	Unit
Shear modulus	G	31.0	GPa
Bulk modulus	K	41.4	GPa
Initial Density	ρ_0	2.67	g/cm ³
Cylindrical compressive strength	f_c	220.0	MPa
Normalized tensile strength	\hat{f}_t	0.1	–
Fracture energy	G_F	360	N/m
Failure surface parameter	A	2.3	–
Failure surface exponent	n	0.79	–
Triaxiality parameter	Q_0	0.6805	–
Brittle-to-ductile parameter	B	0.0105	–
Elastic to plastic strain factor	Ψ_h	2.0	–
Onset on hardening compression	$g_{c,0}$	0.7	–
Onset on hardening tension	$g_{t,0}$	0.53	–
Residual strength surface parameter	A_f	2.3	–
Residual strength surface exponent	n_f	0.79	–
Damage parameter	D_1	0.04	–
Damage exponent	D_2	1.0	–
Minimum strain to failure	ε_{pl}^m	0.01	–

Table A.3: Summary of the RHT material parameter for “hard” aggregates.

A.6.3 ITZ data

For the ITZ, a relatively simple, rate-independent cohesive zone model was applied [225, 281]. Only three parameter are necessary to describe its behavior: Tensile strength, shear strength and fracture energy. As already mentioned, detailed values for these parameter are not available or include high scatter. Most researchers therefore prefer to use strength values of approximately 50 % of mortars strength [219]. Here, estimates of the dynamic strength are used.

For the simulation of the SHB specimen and the shock tube sample, a value of $f_t = f_s = 9$ MPa was applied. The lower strain rate regime at the compact specimen tension test was considered by a reduced strength. For *all* simulations, a fracture energy similar to mortar was employed for the cohesive zone elements. Table A.4 summarizes the values.

Example	$f_t = f_s$ in MPa	G_F in N/m
Ožbolt, $v_A = 0.49$, Section 4.3.1	3	30
Ožbolt, $v_B = 4.3$, Section 4.3.1	5	30
Schuler, Section 4.3.2	9	30
Bewick, Section 4.3.3	9	30
Hooked wall, Section 6.3	9	30

Table A.4: Summary of the applied input parameter for the cohesive zone elements of the application examples.